Measurement Variability and Model Uncertainty in Mountain Permafrost Research

---

Dissertation

zur

Erlangung der Naturwissenschaftlichen Doktorwürde

(Dr. sc. nat.)

vorgelegt der

Mathematisch-naturwissenschaftlichen Fakultät

der

Universität Zürich

von

Stefanie Gubler

von

Baden AG

Promotionskomitee

Prof. Dr. Wilfried Haeberli (Vorsitz)

Dr. Stephan Gruber (Leitung der Dissertation)

Prof. Dr. Ross S. Purves

Zürich 2013

Abstract

Permafrost is lithosphere material that stays at or below zero degree Celsius during more than two consecutive years. Due to its purely thermal definition, and since it is a subsurface phenomenon, permafrost studies often include resource-intense measurement campaigns. For example, permafrost evolution is monitored by ground temperature measurements obtained from deep boreholes, and permafrost distribution is often measured using temperature-recording devices deployed few centimeters below the ground surface. While deep boreholes are costly, measurement campaigns comprising hundreds of spatially-distributed near-surface devices require great human effort. Hence, permafrost measurements are often complemented with empirical or physically-based models. Before such models can be used for prediction or decision making, they should be evaluated to quantify the accuracy and the inherent uncertainty of the modeled output.

Distribution and extent of permafrost in mountain regions is strongly influenced by topographic and other environmental variables, for example ground properties. This high variability requires spatially-distributed measurements for model development, i.e., for calibration and validation. In this thesis, ground surface temperatures were measured spatially-distributed at 39 locations (called footprints) representing the main topographic conditions and different ground cover types around the mountain Corvatsch in the Upper Engadine, Switzerland, during a three-year period. From these measurements, three variables that are suitable to validate mountain permafrost models could be derived: the mean annual ground surface temperature, the day of snow disappearance, and the snow ripening date. The influence of the topographic attributes and ground cover type on the three variables was quantified using multiple linear regression. We found that changes in the mean annual ground surface temperature due to slope, aspect, and ground cover type at one elevation correspond to changes in elevational distances of 1000 m. Ten measurement devices, randomly distributed at each of the 39 footprints, allowed quantification of measurement variability at a small scale. This resulted in differences of up to 2.5°C in mean annual ground surface temperature and up to three weeks in the melting and ripening dates within certain footprints. This

fine-scale variability should be taken into account when evaluating spatially-distributed models with point measurements, or when used for decision making.

This variability indicates that physically-based mountain permafrost models should be evaluated at locations representing different environmental factors that influence permafrost occurrence. In this thesis, the parametric sensitivities and uncertainties of one physically-based permafrost model were quantified systematically at locations covering elevations from 500 to 4000 m, different slopes and all aspects as well as six different ground cover types. In total, 52 parameters were analyzed, including different physical as well as model specific parameters. Errors due to model discretization parameters, such as the time step and discretization of the ground column, were quantified. The setting allowed quantification of the range of model sensitivities that must be expected when modeling permafrost in mountain regions. Model sensitivities and errors vary strongly in the environmental setting, underlining the importance of systematic and representative model analyses.

Several short- and longwave downward radiation parameterizations were evaluated primarily to increase the accuracy of modeled radiative fluxes in impact models applied in Switzerland. The uncertainties of the parameterizations were quantified, and the results were implemented in the model mentioned above.

Contents

Part I Synopsis

Part II Publications

Part III Appendix

List of Figures

List of Tables

Acronyms

APIM	Alpine Permafrost Index Map
ASRB	Alpine Surface Radiation Budget
BTS	Bottom Temperature of Snow
DEM	Digital Elevation Model
DMIP	Distributed Model Intercomparison Project
EB	Energy Balance
EISMINT	European Ice Sheet Modeling INiTiative
FAST	Fourier Analysis Sensitivity Testing
GCM	Global Circulation Model
GCOS	Global Climate Observing System
GCT	Ground Cover Type
GEOtop	Distributed energy- and mass-balance model
GIS	Geographic Information Systems
GLUE	Generalized Likelihood Uncertainty Estimation
GST	Ground Surface Temperature
GT	Ground Temperature
GTN-P	Global Terrestrial Network for Permafrost
iButton	Tiny temperature logger
LIDAR	LIght Detection And Ranging
MAAT	Mean Annual Air Temperature
MAGT	Mean Annual Ground Temperature
MAGST	Mean Annual Ground Surface Temperature
MBD	Mean Biased Deviance
MC	Monte Carlo
MCMC	Monte Carlo Markov Chain
MD	Melt-out Day of snow
MeteoSwiss	Federal Office of Meteorology and Climatology
MO	Monin-Obukhov parameterization
PDF	Probability Density Function

PERMAKART	Permafrost Map of Switzerland
PERMEBAL	Permafrost and Energy Balance
Permos	Swiss Permafrost Monitoring Network
RCM	Regional Circulation Model
RD	Snow Ripening Date
RMSD	Root Mean Squared Deviance
SwissMetNet	Swiss Meteorological Network
SnowMIP	Snow Models Intercomparison Project
TEBAL	Topography and Energy Balance
UTL	Universal Temperature Logger
WB	Water Balance
WEqT	Winter Equilibrium Temperature

Symbols

T	Temperature [$^{\circ}\mathrm{C}$]
T_a	Air temperature [$^{\circ}\mathrm{C}$]
T_s	Ground surface temperature [$^{\circ}\mathrm{C}$]
T_z	Ground temperature at depth z [$^{\circ}\mathrm{C}$]
r_h	Relative humidity [%]
p_v	Water vapor pressure [hPa]
z	Depth [mm]
t	Time [s]
P	Period of temperature wave [a]
A_s	Surface temperature amplitude [$^{\circ}\mathrm{C}$]
SDR	Shortwave downward radiation [$\mathrm{W\,m^{-2}}$]
I_0	Solar radiation at the top of the atmosphere [$\mathrm{W\,m^{-2}}$]
τ	Atmospheric attenuation coefficient due to Rayleigh scattering (τ_r), water vapor (τ_w), ozone (τ_o), aerosols (τ_a), uniformly mixed gases (τ_g) and clouds (τ_c)
α_A	Ångström wavelength exponent
β_A	Ångström turbidity coefficient
O_3	Ozone [mm]
LDR	Longwave downward radiation [$\mathrm{W\,m^{-2}}$]
LUR	Longwave upward radiation [$\mathrm{W\,m^{-2}}$]
ϵ	Clear-sky (ϵ_{cl}) and all-sky (ϵ_{all}) emissivity
σ_{SB}	Stefan-Boltzmann constant [$\mathrm{W\,m^{-2}K^{-4}}$]
R_{net}	Net radiation [$\mathrm{W\,m^{-2}}$]
Q_h	Sensible heat flux [$\mathrm{W\,m^{-2}}$]
Q_{le}	Latent heat flux [$\mathrm{W\,m^{-2}}$]
Q_m	Melt energy [$\mathrm{W\,m^{-2}}$]
Q_g	Ground heat flux [$\mathrm{W\,m^{-2}}$]
α	Surface albedo of snow (α_s) or ground (α_g)
K_T	Thermal conductivity [$\mathrm{W\ m^{-1}\ K^{-1}}$]

C	Volumetric heat capacity [$\mathrm{J\ m^{-3}\ K^{-1}}$]
κ	Thermal diffusivity [$\mathrm{m^2\,s^{-1}}$]
K_h	Hydraulic conductivity [mm $\mathrm{s^{-1}}$]
α_{vG}	Parameter of water retention curve [$\mathrm{mm^{-1}}$]
n_{vG}	Parameter of water retention curve
ψ	Suction potential [$\mathrm{mm^{-1}}$]
θ_s	Saturated water content of the ground
θ_r	Residual water content of the ground
T_0	Temperature threshold for rain ($T_{r,0}$) or snow ($T_{s,0}$) [$^\circ$C]
df_s	Snow deformation rate [%]
$d_{s,cut}$	Snow density cut-off [$\mathrm{kg\,m^{-3}}$]
$s_{w,irr}$	Irreducible water saturation of snow
r	Ground (r_g) or snow (r_s) aerodynamical roughness [mm]
$c_{s,r}$	Ground-snow roughness threshold [mm]
v_s	Snow viscosity [$\mathrm{Ns\,m^{-2}}$]
ϵ	Emissivity of ground (ϵ_g) or snow (ϵ_s)
c_α	Extinction parameter snow albedo [mm]
z_f	Depth above which water drains laterally [mm]
T_i	Initial ground temperature [$^\circ$C]
$r_{h_{min}}$	Minimal value of relative humidity [%]
v_{min}	Minimal wind velocity value [$\mathrm{m\,s^{-1}}$]
tol_h	Heat equation tolerance [$\mathrm{J\,m^{-2}}$]
tol_r	Richard's equation tolerance [mm]
dt	Time discretization [s]
swe_m	Maximal snow water equivalent in boundary layers [mm]
n_b	Number of bottom snow layers
n_m	Number of middle snow layers
n_t	Number of top snow layers
z_{max}	Total depth of ground column [mm]
dz_{min}	Thickness of uppermost ground layer [mm]
b	Ground depth growth rate
h_w	Sensor height of wind velocity measurement [m]
h_T	Sensor height of temperature measurement [m]
c_P	Correction factor for precipitation
Γ_P	Precipitation lapse rate
Γ_T	Temperature lapse rate [$^\circ\mathrm{C\ km^{-1}}$]
Γ_{DT}	Dew temperature lapse rate [$^\circ\mathrm{C\ km^{-1}}$]
Y_i	Model output
θ_j	Model parameter

$s_{i,j}$	Sensitivity of model output Y_i to parameter θ_j
$v_{i,j}$	Total variance of model output Y_i due to changes in parameter θ_j
$\mathrm{L}(Y;\Theta)$	Likelihood function of parameters Θ given the observations Y
$\mathrm{p}(\Theta)$	Probability distribution of model parameters Θ
$\mathcal{U}(\min,\max)$	Uniform distribution
$\sigma(X)$	Standard deviation of random variable X
$\mu(X)$	Mean value of random variable X
$\mathrm{Var}(X)$	Variance of random variable X
$\mathrm{E}(X)$	Expected value of random variable X
$\mathrm{Cov}(X,Y)$	Covariance of random variables X and Y
R^2	Coefficient of determination

Part I

Synopsis

1 Introduction

1.1 Motivation and problem description

Permafrost is defined as lithosphere material that stays at or below zero degrees Celsius during two consecutive years (*Muller*, 1947, *Brown and Péwé*, 1973, *Washburn*, 1979). It exists in cold regions at high latitudes and/or at high elevation areas like the Swiss Alps. In such mountain regions, ground temperatures (GT) vary strongly within small distances since the importance of influencing processes varies under the different topographic conditions. In the northern hemisphere, north exposed slopes for example receive only little solar radiation and are therefore significantly colder than nearby south facing slopes (*Gruber et al.*, 2003, 2004b). Further, the complex influence of snow on the ground thermal regime, and its high spatial variability, alter GTs within small distances in mountain regions (*Keller and Gubler*, 1993). The study of mountain permafrost hence calls for spatially-distributed measurements that are complemented with models at appropriate scales.

Before being used for applications, a model must be corroborated to fit its intended use (*Rykiel*, 1996). Models are often validated at single locations due to lack of spatially-distributed data (*Kirchner et al.*, 1996) and due to computational constraints. However, unless a systematic model validation is performed, it remains unclear whether the model performs well within the whole modeling domain. That is of special con-

cern if a model is applied within highly variable terrain as encountered in mountain areas. To assess a model's validity under differing environmental conditions, spatially-distributed measurements sampled along the major environmental factors are required. The uncertainties and sensitivities of mountain permafrost models most likely vary at differing locations due to the changing relevance of processes. This in turn requires systematic sensitivity and uncertainty analyses performed at locations representing the range of topographic and other environmental variables typically encountered in the modeling domain, i.e. in high mountain areas.

Models complement measurements by providing a theoretical framework for research, or by making spatio-temporal predictions of phenomena that cannot be measured (*Wainwright and Mulligan*, 2004). The combination of measurements with models is common in environmental research to gain insights in system functioning. Measurements are used as model drivers and serve for validation. If a measurement is used as ground truth, the question of whether it represents the same quantity as the model output is important (*Gupta et al.*, 2005). The stochastic variability of influence quantities plays an important role when measurements are used for model driving or validation. In environmental models, the simulation environment is often represented by a digital elevation model (DEM), while model validation is performed with a point measurement. In mountain permafrost research, for example, simulated ground temperature is validated with a point measurement taken within one grid cell of the DEM. The representativeness of the temperature measurement as well as the exact depth at which the temperature measurement is taken add to model errors. Replicated measurements are needed to quantify measurement uncertainty due to fine-scale environmental variability.

Installation and maintenance of measurement devices often need great human and monetary resources. Effective and efficient measurements are required to gain the greatest benefit (*Gupta et al.*, 2008) to optimize the cost-benefit function of the measurement campaign. Measurement campaigns are planned and conducted according to the observational system model that is based on the conceptual and perceptual understanding of the phenomena under investigation (*Gupta et al.*, 2008). Systematic quantification of model uncertainties and sensitivities has the potential to detect and quantify knowledge gaps, and thereby optimizing future measurement campaigns.

In summary, permafrost is highly variable and its occurrence is governed by processes that have varying relevance in mountain regions. It reacts sensitively to changes in inputs and boundary conditions and is driven by highly non-linear processes such as the freezing and thawing of liquid water in the active layer. Mountain permafrost is hence a phenomenon suitable as a case study for assessing the variability of measurements and model uncertainties in a highly heterogeneous setting.

1.2 Aim and objectives

The overall aim of this thesis is to study the combined effectiveness of measurements and models in quantifying transient and spatially-heterogeneous environmental phenomena in mountain regions. A first step into this direction is to study measurement variability and model uncertainty related to mountain permafrost and to quantify the influence of topographic and environmental variability on model evaluation. The outcomes provide a discussion basis to optimize the joint use of measurements and models within the area of mountain permafrost research. These findings can be transferred to other research fields. To reach this goal, the following objectives are defined:

1. Design a measurement campaign providing data that:

   (a) allows quantification of measurement variability in mountain regions and

   (b) provides a basis for systematic mountain permafrost model validation.

   Systematic validation of mountain permafrost models requires ground temperature measurements distributed along the typical characteristics of mountain regions. At the coarse scale representing a mountain, topography determining the energy balance as well as the ground cover strongly influence ground temperatures. There is a need for a dataset of relevant quantities distributed along the environmental factors that determine permafrost occurrence in mountain regions. Within typical resolutions of DEMs (e.g. 10 or 25 m) used in mountain permafrost research, local ground properties such as moisture and snow distribution influence the ground thermal regime. Replication of measurements at the scale of a DEM grid cell is required to obtain insights into the stochastic variability of the data used for decision making and model validation.

2. Validate parameterized meteorological input data and quantify the uncertainties of the parameterizations.

   Time series of quantities such as air temperature, relative humidity, precipitation, global shortwave (SDR), and downward longwave radiation (LDR) are often used to drive environmental models. They determine the energy balance, the hydrology, and other processes at the Earth's surface and subsurface. The variables air temperature, relative humidity, and global SDR are commonly measured at ordinary meteorological stations in Switzerland. The uncertainty of these quantities can be attributed to the precision and the accuracy of the measurement device, which are often provided by the manufacturer. However, measurements of LDR are scarce and hence, LDR is parameterized in impact models. There is a need to

calibrate these LDR parameterizations to increase their accuracy and to quantify their uncertainty in order to propagate them through impact models.

3. Evaluate a physically-based permafrost model and quantify the influence of environmental variability on model evaluation.

   The processes influencing permafrost vary strongly in mountain environments. The outputs of physically-based models, as well as model uncertainties, sensitivities, and model errors change considerably along topographic and other environmental gradients. The energy- and mass-balance model GEOtop (*Rigon et al.*, 2006) is a potential mountain permafrost model incorporating many permafrost relevant processes. So far, there is a need for in-depth evaluation of GEOtop to assess its ability to reproduce permafrost conditions such that the model can be used operationally for decision making. One objective is to evaluate the suitability of GEOtop for mountain permafrost investigations. The high environmental variability encountered in mountains requires a systematic model evaluation approach.

4. Optimize the efficiency and the effectiveness of jointly used measurements and models.

   The design of measurement campaigns is often based on the conceptual understanding of the system functioning to measure quantities at locations and at times where they seem relevant (*Gupta et al.*, 2008). The combination of the conceptual understanding with a systematic model evaluation has the potential to quantitatively determine locations and times when models, and hence our physical knowledge implemented in mathematical formulae, contain the greatest uncertainties and/or errors. The determination of locations, times, and variables for which knowledge gaps are greatest may modify the way measurement campaigns are conducted and help optimize campaigns based on quantitative arguments.

1.3 Approach

The approach of this thesis spans field measurements and computer modeling. A measurement campaign on spatially-distributed ground surface temperatures (GST) was conducted. GST is an economic and relevant quantity in mountain permafrost research since it determines the thermal state of the ground (e.g. *Hoelzle et al.*, 2003). The dataset consisting of 390 GST time series serves as the basis to quantify the influence of environmental variability on permafrost relevant quantities like the mean annual GST (MAGST), the melt-out day of snow (MD) and the beginning of snow melt respectively

the snow-ripening date (RD). Measurement variability is analyzed on two scales, the coarse scale comprising the area of a mountain, and the fine scale representing a grid cell of a typical DEM used in mountain permafrost modeling (i.e., 10 m), using multiple linear regression analysis.

The physically-based model GEOtop (*Rigon et al.*, 2006) incorporates many processes relevant in mountain permafrost. The model is evaluated systematically at a variety of locations covering the range of environmental variability typically found in the Alps. The measurements mentioned above could be used as ground truth to validate the model. In a separate, preliminary study, several longwave downward radiation parameterizations are calibrated and the uncertainties of modeled downward clear-sky short- and all-sky longwave radiation are quantified. The findings are implemented in GEOtop.

The results from the two analyses are integrated to discuss possibilities of optimizing measurement campaigns based on systematic model evaluation.

1.4 Structure of the thesis

The thesis comprises a short paragraph summarizing the results (Part I) and four publications produced during this thesis (Part II). Chapter 2 of Part I provides the background information necessary to understand the current state of research and the research gaps that lead to the conducted work. A brief summary of the essence and the needs that evolve from the current state of research are presented after each section of the chapter. It provides an overview of mountain permafrost research including measurement and modeling approaches and discusses different model evaluation techniques developed in fields like hydrology and meteorology. In Chapter 3, the measurements conducted within this thesis, derived variables, as well as analyzing tools are presented together with details on the investigated physically-based models. Chapter 4 summarizes the results published in the four publications. The last chapters summarize the main contributions and insights gained in the thesis and provides an outlook on future research.

2 Background

2.1 Mountain permafrost

2.1.1 Definition and characteristics

Permafrost is lithosphere material that remains at temperatures of maximally zero degree Celsius for at least two consecutive years (*Muller*, 1947, *Brown and Péwé*, 1973, *Washburn*, 1979). Except for its geomorphological expression through features like rock glaciers, permafrost is invisible because of its purely thermal definition and its being a subsurface phenomenon. Permafrost ground must not necessarily contain ice. Permafrost can exist at any place where the mean annual air temperature (MAAT) is below zero degrees Celsius (e.g., *Haeberli et al.*, 2010), but it is also observed at isolated locations for MAAT above the freezing point (*Delaloye et al.*, 2008). Since the upper part of the ground normally thaws in summer, the *permafrost body* is generally bounded from above by the so-called *active layer* consisting of seasonally-frozen ground. In flat areas and steady state conditions, the mean annual ground temperature (MAGT) increases with depth due to the geothermal heat flow. The permafrost thickness is the distance between the *permafrost table* and the *permafrost base*. The thermal offset as observed for different ground types such as block fields can result in lower ground temperatures at

the permafrost table than in the active layer (e.g., *Burn and Smith*, 1987, *Osterkamp and Romanovsky*, 1999, *Gruber and Haeberli*, 2007).

Permafrost occurs in cold climate regions, e.g. in Alaska, Canada, and Russia. It has gained attention due to infrastructure projects, such as pipe lines or mining activities in permafrost areas and the release of methane resulting in a positive warming feedback in the climate system (e.g., *Woo et al.*, 1992, *Nelson and Anisimov*, 1993, *Koster et al.*, 1994, *Kwong and Gan*, 1994). In high-latitude regions, permafrost occurrence depends mainly on air temperature. It is classified as *continuous* if 90–100%, *discontinuous* if 50–90%, *sporadic* if 10–50% and *isolated* if 0–10% of the land area are estimated to be permafrost (*Heginbottom et al.*, 1993, *Brown et al.*, 1997). This classification led to the map of the International Permafrost Association (IPA) for high latitudes. At mid latitudes, permafrost exists at high elevations such as the Alps, where its occurrence and distribution patterns are mainly determined by elevation and solar radiation (*Haeberli*, 1975, *Keller*, 1992, *Hoelzle*, 1996). Permafrost occurring in mountain regions characterized by great topographic variability is referred to as *mountain permafrost* (*Gruber and Haeberli*, 2009). Due to the high topographic variability found in mountain areas (c.f. *Keller*, 1992, *Hoelzle*, 1996), a permafrost classification as in the IPA map on air temperature alone is not useful in high mountain areas (*Etzelmüller et al.*, 2001a). To investigate mountain permafrost, a combination of temperature measurements from boreholes and spatially-distributed measurements at the surface can be used to drive and validate empirical and physically-based models (e.g., *Haeberli*, 1975, *Hoelzle et al.*, 1993, *Keller et al.*, 1998, *Gruber*, 2005, *Boeckli et al.*, 2012a). Sections 2.2 and 2.3 discuss advances in mountain permafrost measurements and models in more detail.

2.1.2 Relevance

Approximately 1–3% of the total area of the Alps are estimated to contain permafrost (*Boeckli et al.*, 2012b, probabilistic index >0.5). In the Alps, permafrost is 10 to several 100 m deep (*Haeberli*, 1992, *Luethi and Funk*, 2001, *PERMOS*, 2007), and the active layer is few meters thick (*PERMOS*, 2007). An increase in active layer thickness under warming conditions can lead to slope instabilities (*Gruber and Haeberli*, 2007) and trigger rock falls and chain reactions, such as debris flows (*Harris et al.*, 2001b, *Gruber et al.*, 2004a, *Gruber and Haeberli*, 2007, *Fischer*, 2009). High-cost installations, such as the protection dams above Pontresina, Upper Engadine, Switzerland, protect people and infrastructures from permafrost hazards. Other than natural hazards, infrastructure built in permafrost, such as cable car stations or restaurants, need special adaptation caused by ground settling or ground moving due to permafrost degradation (c.f. *Haeberli*, 1992, *Haeberli et al.*, 1997, *Harris et al.*, 2001b, *Gruber and Haeberli*, 2007, *Bommer*

et al., 2010), which indicates the relevance of mountain permafrost on human livelihoods. Further, water supply in Asia (*Bolch and Marchenko*, 2006, *Woo et al.*, 2008) and formation of Alpine landscapes (*Barsch*, 1971, *Haeberli et al.*, 2006) are other examples of the relevance of mountain permafrost.

2.1.3 Governing processes at different spatial scales

Mountain permafrost is a phenomenon that is governed by different processes at and below the Earth's surface, that operate at different spatial scales (*Etzelmüller et al.*, 2001a, *Hoelzle et al.*, 2001, *Gruber*, 2005): on the *continental scale* (e.g., the Alps) climate is the governing factor determining air temperature, solar radiation and precipitation patterns. Topography plays a major role on a *regional scale* (e.g., the Corvatsch mountain) determining the amount of solar radiation through geometric effects, differences in air temperature, and snow redistribution by avalanches and wind. At the *local scale* (e.g., the size of a typical grid cell of a DEM of 10 or 25 m resolution), the ground material, availability of water, and the snow distribution determine the available energy and the heat conduction in the ground. In this thesis, the variability of ground surface temperatures is studied at the scale of a mountain referred to as the *coarse scale*, and the *fine scale* of a grid cell of $10 \times 10\,\mathrm{m}^2$.

At the coarse scale, permafrost is influenced by air temperature, solar radiation (*Hoelzle*, 1996) and snow (e.g., *Keller and Gubler*, 1993, *Bernhard et al.*, 1998, *Ishikawa*, 2003, *Luetschg et al.*, 2008, *Hasler et al.*, 2011b) (Fig. 2.1). Air temperatures change with a lapse rate of approximately $-6.5^{\circ}\mathrm{C\,km}^{-1}$. The amount of direct solar radiation warming the ground is primarily influenced by the aspect and the slope. Southern exposed slopes receive more solar radiation in the northern hemisphere. Therefore, permafrost occurs at lower elevations on northern exposed slopes (*Haeberli*, 1975). The energy exchanged at the Earth's surface and heat conduction into or out of the ground determines the thermal state of the ground and thereby permafrost occurrence (*Smith*, 1975, *Ohmura*, 1982, *Williams and Smith*, 1989, *Gavrilowa*, 1988). The surface radiation balance $R_{net}[\,\mathrm{Wm}^{-2}]$ is:

$$R_{net} = SDR \cdot (1 - \alpha) + LDR - LUR, \tag{2.1}$$

where SDR is the shortwave downward radiation and LDR and LUR are the downward respectively upward longwave radiation components. The amount of reflected shortwave radiation is determined by the surface albedo α. SDR is determined by latitude and geometric effects in mountain regions, and LDR and LOR are determined by air respectively ground temperature and emissivity. The surface energy balance can be written as:

$$Q_g = R_{net} - Q_h - Q_{le} - Q_m. \tag{2.2}$$

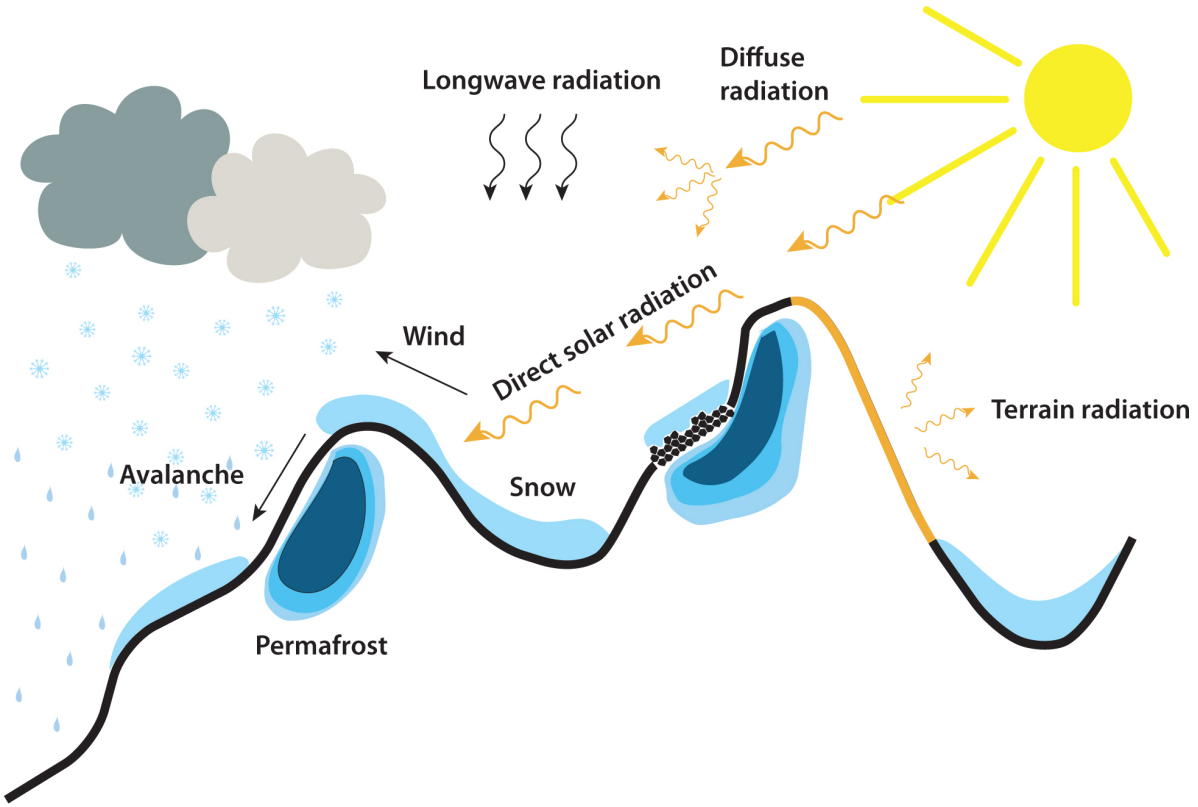

Figure 2.1: *Solar radiation, redistribution of snow and air temperature determine the presence or absence of permafrost in mountain regions at the regional scale. These processes are influenced by geometric effects and elevational gradients. Ground temperatures may vary within small distances due to differences in ground cover, local snow distribution and shading effects.*

On the right side of the equation, Q_h is the turbulent flux of sensible heat and Q_{le} determines the turbulent flux of latent heat, Q_g is the ground heat flux, and Q_m is the required energy to melt snow, if present, in $\mathrm{W\,m^{-2}}$.

In addition to air temperature and radiation, snow distribution and depth influence ground temperatures strongly (*Vonder Mühll et al.*, 1998, *Zhang et al.*, 2001, *Luetschg et al.*, 2008). Due to its low thermal conductivity, a snow cover of more than 50 to 80 cm thickness insulates the ground from cold air in winter and preserves summer heat in the ground (*Smith*, 1975). If the snow cover is relatively thin, its high albedo results in a reflecting of most of the incoming solar radiation, which results in a relative cooling of the ground (*Keller and Gubler*, 1993). The amount of energy needed to melt snow results in a counter-intuitive cooling of the active layer in spring. Topography and land forms

play a major role determining redistribution of snow in mountain regions. Typically in spring, wet snow avalanches redistribute snow from steep slopes to more shallow locations such as natural depressions. There, snow may last during the whole summer and insulates the ground from the warm air temperatures. Hence, permafrost may occur at locations of long lasting snow, whereas near-by steeper sites at higher elevations may be permafrost-free (*Haeberli*, 1975). In general, perennial snow patches indicate the presence of permafrost. At mountain ridges, snow is typically blown away. Further, it does not accumulate in steep rock walls. High elevation, north exposed rock walls and ridges exhibit favorable conditions for permafrost occurrence. In summary, the timing of the snow influences ground temperatures (GT) strongly. Since snow has a high inter-annual variability, and since its influence on GTs is complex, modeling snow is a key step for predicting short-term variability in mountain permafrost.

Heat penetrates the ground mainly through conduction, but also through advective processes such as circulation of air and water in the ground (*Gruber and Haeberli*, 2007, *Hasler et al.*, 2011a). The conductive heat flux Q_g in the ground is proportional to the temperature gradient, i.e.:

$$Q_g = -K_T \frac{\partial T}{\partial z}, \tag{2.3}$$

where K_T is the thermal conductivity $[\mathrm{Wm^{-1}K^{-1}}]$, i.e. the ability of the ground to conduct heat, T is temperature [°C] and z is depth $[\mathrm{mm}]$. Changes of the heat flux Q_g with depth result in changes of the temperature in time:

$$\frac{\partial T}{\partial t} = -\frac{1}{C}\frac{\partial Q}{\partial z}, \tag{2.4}$$

where C is the volumetric heat capacity $[\mathrm{Jm^{-3}K^{-1}}]$ of the ground determining the amount of energy needed to increase the temperature of one cubic meter of the ground by one Kelvin. The differential equation describing the heat conduction is (*Ingersoll et al.*, 1948, *Carslaw and Jaeger*, 1959, *Lunardini*, 1981, *Williams and Smith*, 1989):

$$\frac{\partial T}{\partial t} = \frac{K_T}{C}\frac{\partial^2 T}{\partial z^2} = \kappa \frac{\partial^2 T}{\partial z^2}, \tag{2.5}$$

where $\kappa := \frac{K_T}{C}$ is the thermal diffusivity $[\mathrm{m^2s^{-1}}]$. An analytic solution of the heat conduction (assuming constant heat capacity and thermal conductivity, and a sinusoidal surface temperature $T_s(t) = A_s \sin(2\pi t/P)$) is given by (c.f. *Ingersoll et al.*, 1948):

$$T_{z,t} = \overline{T_z} + A_s \exp^{(-z\sqrt{\pi/\kappa P})} \cdot \sin\left(\frac{2\pi t}{P} - z\sqrt{\pi/\kappa P}\right), \tag{2.6}$$

where A_s is the temperature amplitude [°C] at the ground surface, P is the period of the temperature wave (one year), $\overline{T_z}$ is the mean annual GT (MAGT) at depth z, and t

is the time. The term $A_s \exp^{(-z\sqrt{\pi/\kappa P})}$ is the temperature amplitude at depth z. The exponential term indicates the diminishing temperature amplitude with depth. Analytic solutions of Eq. 2.5 exist only for a limited set of idealized conditions (*Lunardini*, 1981), and therefore the heat conduction must normally be solved numerically (*Riseborough et al.*, 2008).

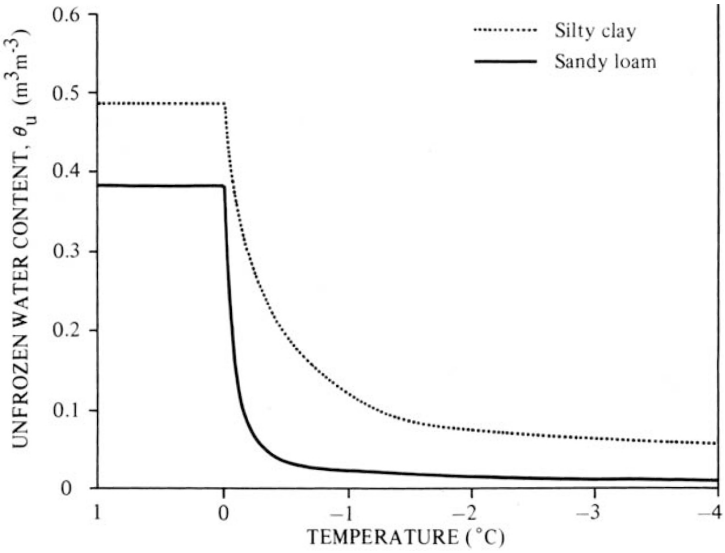

Figure 2.2: *In dependence of pore size, water may remain unfrozen for temperatures below the freezing point. In sandy loam, water almost instantaneously freezes at 0°C, while in the small pores in silty clay, portions of liquid water still exist at -4°C (Williams and Smith, 1989).*

The thermal conductivity and the heat capacity in the ground depend on the composition of the ground (*de Vries*, 1963). Water that changes to ice increases its thermal conductivity by a factor of four (from around 0.5 to 2 $\mathrm{Wm^{-1}K^{-1}}$, and decreases the heat capacity by a factor of two from approximately $4{\cdot}10^6$ to $2{\cdot}10^6$ $\mathrm{Jm^{-3}K^{-1}}$ (e.g., *Williams and Smith*, 1989, *Tsuang*, 2005). When freezing, water releases heat that is equal to the heat needed to raise the temperature of a rock of equal volume by 150°C (*Gold and Lachenbruch*, 1973). In dependence of the radius of the pores in the ground, water may remain unfrozen at temperatures below the freezing point (e.g *Wettlaufer and Worster*, 2006) (Fig. 2.2). The ground freezing characteristics curve relates the amount of unfrozen water to temperature (e.g., *Koopmans and Miller*, 1966, *Fuchs et al.*, 1978, *Dall'Amico*, 2010). One possibility to model the freezing behavior in the ground is to use the van Genuchten equation (*van Genuchten*, 1980) for water retention in pores:

$$\theta(\psi) = \theta_r + \frac{\theta_s - \theta_r}{(1 + (\alpha_{vG}|\psi|)^n_{vG})^{1-1/n_{vG}}}, \tag{2.7}$$

where θ_r the residual and θ_s is the saturated water content (the ground porosity), α_{vG} and n_{vG} are parameters determining the shape of the curve, and ψ is the suction potential [mm^{-1}]. Modeling the freezing of liquid water is essential to study ground temperature evolution.

Essence: Mountain permafrost is relevant because of its influence on hazards such as rock falls and its influence on the stability of infrastructure. It is a phenomenon that is highly variable in mountain regions. At different scales, different processes determine its spatial distribution. Air temperature, precipitation patterns, and climate determine permafrost occurrence at the continental scale. Topography is important at the coarse scale determining solar radiation and air temperature by geometry. Snow patterns and local ground properties like moisture influence the amount of energy reaching and penetrating into the ground at the fine scale. The thermal properties of water change abruptly when freezing occurs, and therefore water in the ground close to the freezing point strongly influences the thermal regime of the ground.

Needs: There is a need for distributed measurements to study the variability of ground temperatures at appropriate scales and to quantify the influence of different processes on mountain permafrost. Validated, physically-based permafrost models that simulate the relevant processes adequately are required to study feed backs and interactions mechanisms, as well as to provide scenarios of mountain permafrost evolution.

2.2 Measuring mountain permafrost

Given that permafrost is purely thermally defined, measuring is essential to investigate its occurrence and evolution. This study basically deals with ground temperature measurements and neglects geophysical approaches to determine the ice content of the ground (e.g., *Vonder Mühll et al.*, 2001, *Hauck et al.*, 2004, *Hilbich et al.*, 2008, 2009), as well as creep measurements (*Wagner*, 1992, *Arenson et al.*, 2002, *Roer et al.*, 2005, *Roer and Nyenhuis*, 2007). Two main approaches to measure ground temperatures exist today (*Haeberli et al.*, 2010): boreholes to monitor ground temperature evolution and the active-layer depth and tiny loggers to study the spatial distribution of the near surface temperature. In this section, diverse ground temperature measurement studies performed in mountain regions are presented and the general terminology concerning measurements and measurement uncertainty is introduced.

2.2.1 Ground temperature measurements

Ground temperatures (GT) measured in boreholes are used to study the evolution of GT in the active layer and the permafrost body. At great depth, the temperatures integrate over large surface areas (*Gold and Lachenbruch*, 1973) and represent the thermal conditions at the ground surface of several decades in the past (*Lachenbruch and Marhsall*, 1986). The longest temperature series in mountain permafrost exist since 1988 in a borehole of 58 m depth in the Murtèl rock glacier at Corvatsch in Switzerland (*Haeberli et al.*, 1988, *Vonder Mühll and Haeberli*, 1990) to document the thermal conditions of creeping permafrost and the creep processes and to analyze the physico-chemical properties of ice and rock mixtures (*Hoelzle et al.*, 2002). A series of boreholes in Europe were installed within the Permafrost and Climate in Europe project (PACE) (*Harris et al.*, 2001a) providing a longitudinal transect of permafrost measurements in European mountains. Today, mountain permafrost is monitored within the climate observing systems, i.e. the Global Terrestrial Network for Permafrost (GTN-P) within the Global Climate Observing System (GCOS). In the Swiss Alps, 27 boreholes at 14 locations monitor GTs within the Swiss Permafrost Monitoring Network (PERMOS), forming part of GTN-P. The borehole measurements are continuously analyzed and related to geophysical measurements and climate. General temperature trends, such as the temperature rise of approximately $0.1\,^{\circ}\mathrm{C\,a^{-1}}$ recorded at the Murtèl rock glacier borehole from 1988 to 1995 (*Vonder Mühll et al.*, 1998) provide insights on the reaction of permafrost to increasing air temperatures. The strong temperature increase stopped in the cold year of 1997, and was not observed later. Differing snow conditions (*PERMOS*, 2009, 2010) as well as phase change may be possible reasons for the nearly constant temperatures in the

Murtèl rock glacier. In southern Norway by contrast, increases of 0.015 to 0.095$^{\circ}\mathrm{C\,a}^{-1}$ were observed during the last ten years and are attributed to higher air temperatures in winter and increasing snow depths (*Isaksen et al.*, 2011). GT increases were also reported in Alaska (*Romanovsky et al.*, 2011). In Switzerland, the recorded temperatures are often very close to zero degree Celsius (e.g., *PERMOS*, 2009, 2010). If the ground temperatures are close to zero degree Celsius, the energy is absorbed as latent heat in ice rich ground (e.g., *Gold and Lachenbruch*, 1973), and hence changes in permafrost conditions cannot be observed in the temperature measurements. Temperature measurements from boreholes are suitable to investigate the temporal evolution of cold permafrost. Since boreholes are very expensive, however they can not be used to study the distribution of mountain permafrost.

Measuring the spatial extent of mountain permafrost is time and cost intense, and difficult due to the remoteness and harsh conditions encountered in permafrost areas (e.g., *Gruber et al.*, 2004c). Distributed GT measurements can only be obtained near the ground surface. A first measurement campaign to determine the spatial distribution of mountain permafrost was conducted by *Haeberli* (1973). He measured the temperature below the snow when the winter ground temperatures are in equilibrium (also called winter equilibrium temperature (WEqT) (e.g., *Schoeneich*, 2011)). Below an isolating snow pack, the ground surface temperature (GST) reflects the thermal state of the ground and can therefore be used as a permafrost indicator. The bottom temperature of snow (BTS) measurements served to develop empirical mountain permafrost distribution models (*Hoelzle et al.*, 1993, *Keller and Gubler*, 1993). However, due to the high inter-annual variability of the snow cover, BTS measurements from one year only are not representative to determine permafrost conditions (*Hoelzle et al.*, 2003, *Brenning et al.*, 2005). Therefore nowadays, tiny loggers such as the universal temperature loggers (UTL) or iButtons are used to study the seasonal and inter-annual behavior of the ground thermal conditions (*Hoelzle et al.*, 1999, 2003, *Gruber et al.*, 2003). GST influences permafrost conditions, and measurements are important to understand the thermal behavior of the active layer (e.g., *Haeberli*, 1985). Since GSTs are the most important causes of temperature changes in depth, they can be used as the upper boundary condition to numerically solve the heat conduction or as a rough indicator of the presence or absence of permafrost. Thermal offsets depending on surface type (e.g., *Burn and Smith*, 1987, *Osterkamp and Romanovsky*, 1999, *Gruber and Haeberli*, 2007, *Hasler et al.*, 2011b) must be accounted for when using GST to determine permafrost distribution.

Hoelzle et al. (2003) distributed eleven tiny loggers at elevations between 2500 and 2700 m covering aspects from SE to NW and different ground cover types (GCT) in the area around the Murtèl rock glacier. Within that measurement setting, GCT most dominantly determined the mean annual GST (MAGST) (*Hoelzle et al.*, 2003). Based on GST mea-

surements in steep rock faces, the differences in MAGST between north and south faces were estimated to be equivalent to almost 1000 m vertical (*Gruber et al.*, 2003, 2004b). That data set focused on steep rock walls to model ground temperatures determined by pure heat conduction since snow accumulation on steep rock walls was assumed to be negligible. A typical GST time series recorded in a permafrost area is depicted in Fig. 2.3. In summer, GST highly correlate with air temperature. That is followed by a dampening of the temperature variability when the first snow falls. In early spring, GTs converge to the WEqT that is measured by the BTS method. The start of snow melt can be observed in a zero-curtain period. Since the temperature of a zero curtain usually is exactly zero degree Celsius, zero curtain periods are often used for post-calibration of temperature measurements.

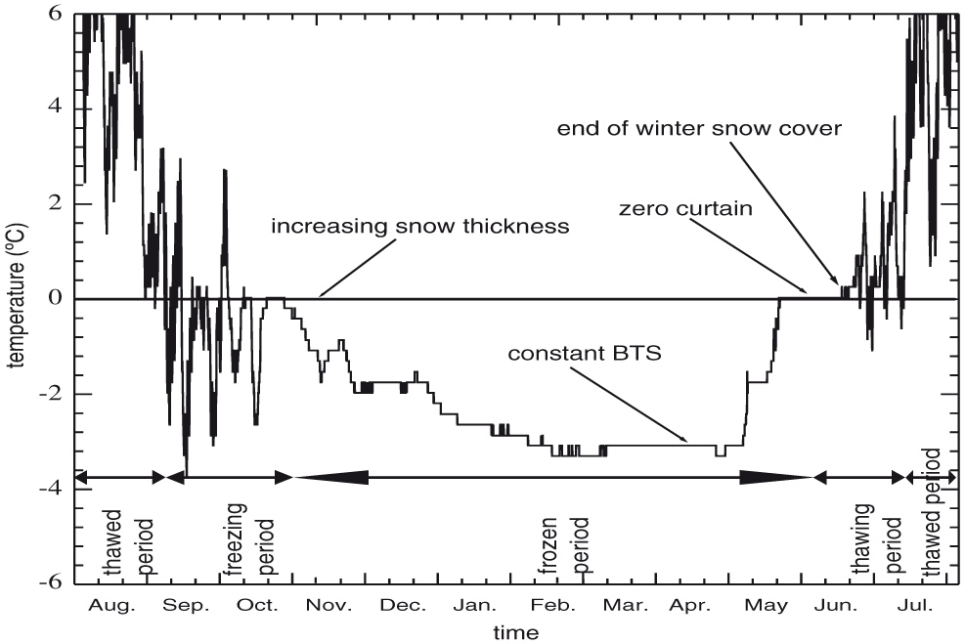

Figure 2.3: *Typical thermal regime at the ground surface (Hoelzle et al., 2003). In summer, GTs correlate with air temperatures and show high daily variability. The onset of snow results in a dampening of the daily GST variance. Under an isolating snow pack, GST reaches an equilibrium state in early spring. Zero curtain periods in spring indicate the beginning of snow melt.*

2.2.2 Measurement uncertainty

If not otherwise mentioned, the definitions follow the "Guide to the expression of uncertainty in measurement" (*JCGM*, 2008) and deal with uncertainty in the measuring

process. The *quantity* (of interest) denotes an attribute of a phenomenon that can be quantified by a value usually consisting of a unit multiplied with a number. The *true* value of a quantity is the value that would be obtained from a perfect measurement, but is indeterminate by nature. A *measurement* is a set of operations to determine the value of a quantity, the particular measured quantity subject to the measurement is called *measurand*. The *error* is the difference between the measured quantity and the true value. Since the true value can never be known, a reference value is needed to estimate the error of a measurement. Measurement errors consist of two components: *random* and *systematic* errors. A random error is the difference of a measurement and the mean of (theoretically) infinitely often repeatedly[1] performed measurements of the same measurand, and is referred to as *precision* of a measurement. Random errors vary unpredictably and come from stochastic spatial and temporal variability of influence quantities. A systematic error is the mean of (theoretically) infinitely often performed measurements minus the true value of the measurand and is often referred to as the *bias*. A bias correction (also called calibration) can in theory eliminate the systematic error. The *trueness* of a measurement is the agreement of a (theoretically) infinite number of measurements and the true value. The *accuracy* of a measurement denotes the agreement between a measurement and the true value of a measurand. Normally, the true value of a measurand is unknown, and thus the accuracy is only a qualitative concept. The *uncertainty* of a measurement is (*JCGM*, 2008, Page 2, 2.2.3):

> a parameter, associated with the result of a measurement, that characterizes the dispersion of the values that could reasonably be attributed to the measurand,

i.e., a parameter enclosing all reasonable values of the measurand. The *uncertainty range* includes both systematic and random effects of a measurement. It is an important measure to describe the quality of a measurement and influences decisions that are based on measurements (*Ramsey and Ellison*, 2007).

As mentioned, quantification of measurement uncertainty is important when the measurements are used for decision making or for model validation (*Monte et al.*, 1996). For example, the iButton-device DS1922L used in this thesis measures temperatures with an accuracy of $0.5^{\circ}\mathrm{C}$ and a resolution of $0.0625^{\circ}\mathrm{C}$, whereas UTL-loggers are accurate to $0.1^{\circ}\mathrm{C}$. Temperature measurement devices can be calibrated in ice baths at zero degrees Celsius. Further, they can be post-calibrated if zero-curtain periods occurred during the measurement period. The random error of the measurement device can be estimated

[1] Measurements taken successively under same conditions including the same measurement device, same location, same person and small time lags.

as the standard deviation of the measurements when temperatures are known to be constant.

An additional source of measurement uncertainty comes from temporal or spatial heterogeneity of the environment. Measurements of ground temperatures are often point measurements (e.g., boreholes). The use of these measurements implicitly assumes that they are representative of their surroundings. However, temperatures may vary considerably due to the fine-scale heterogeneity of properties of the surrounding environment. In fact, spatial variability may account for the largest part of the measurement uncertainty (*Ramsey and Ellison*, 2007). The high environmental variability encountered in mountain regions requires spatially-distributed measurements that cover the main attributes typically found in mountain environments. The question whether a measurement is representative of its surroundings is important when measurements as temperatures in boreholes are used to make general statements on mountain permafrost evolution. A systematic measurement design including fine-scale replication of measurements is of fundamental importance if measurements are used for decision making or model evaluation (Fig. 2.4).

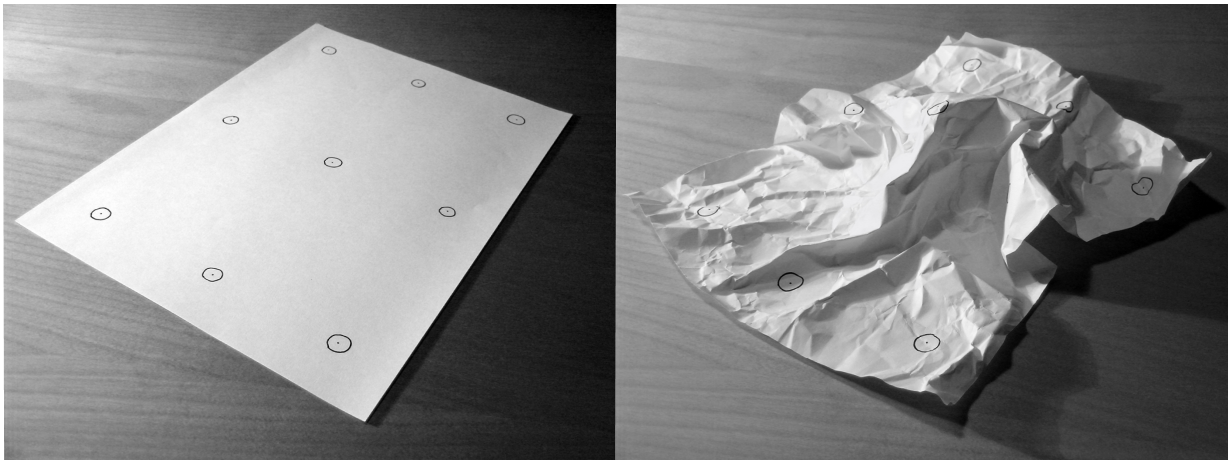

Figure 2.4: *The variability of spatial phenomena increases with increasing heterogeneity of the environment. This is figured here as homogeneous environments in flat terrain (left) versus environmental heterogeneity in mountain regions (right). The spatial variability of measurements, model outputs and model evaluation measures should be considered if used for decision making.*

Essence: Temperature sensors in several deep boreholes continuously measure ground temperatures in the Swiss Alps to monitor the evolution of mountain permafrost and its reaction to climate change. Since 1973, bottom of snow temperatures were used to establish an empirical permafrost model in high mountain areas and are nowadays being replaced by high resolution ground surface temperature measurements. A variety of GST measurements placed within different ground types or covering diverse topographic attributes in steep rock faces exist to serve as a basis for process studies and model validation in mountain permafrost research.
Every measurement is prone to two types of errors: random and systematic. In contrast to random errors, systematic errors can be reduced by calibration. Within a strongly variable environment such as those encountered in the Swiss Alps, natural variability leads to an additional uncertainty in the measured quantity that is relevant for decision making or model validation.

Needs: Ground surface temperatures are an important variable in permafrost research determining the thermal state of the ground. GST measurements are relatively cheap and simple to obtain and have therefore high potential to study permafrost distribution and serve for spatially-distributed model validation. A measurement campaign should cover the environmental variables considered relevant in mountain permafrost studies to guarantee representative measurements at the coarse scale. Replication of measurements within small distances are needed to quantify measurement uncertainty due to environmental variability at the fine scale.

2.3 Modeling mountain permafrost

The high spatial variability encountered in mountain regions and the sparse available measurements require the use of models to obtain a continuous picture of permafrost occurrence and permafrost development (*Etzelmüller et al.*, 2001a). This section provides a short overview of certain models developed for mountain permafrost research.

2.3.1 The purpose of models

An environmental model is a mathematical or conceptual representation of an environmental phenomenon. Mathematical models are widely used in environmental system analyses, physics, economy, etc. Different types, such as data-driven (statistical) or law-driven (physical) models, exist (*Saltelli et al.*, 2008) and generally serve different purposes, such as formulating knowledge or belief of system functioning, communicating knowledge, testing hypothesis, and improving the understanding of underlying processes (e.g., *Wainwright and Mulligan*, 2004). With the increasing power of computational resources, the focus of environmental models has been shifted. For example, the study of the environment is motivated by practical forecasting needs: to understand the impact of events that have not happened yet, to understand the impact of humans on the environment, and to understand the impact of changing environments on human livelihood and behavior (*Wainwright and Mulligan*, 2004). Thus, environmental models are used to predict incidences that affect human livelihood, such as floods, rockfalls, landslides, etc. (*Dorren*, 2003, *Nötzli et al.*, 2006, *Huggel et al.*, 2007, *Schneider*, 2011, *Dorren*, 2012, *Moretti et al.*, 2012) and to provide scenarios of future environments (e.g., *IPCC*, 2007). With respect to climate change, models have an application-driven purpose to inform with politics and economy to communicate and underlie expected changes in the climate and the land use (*Wainwright and Mulligan*, 2004). Especially there, it is important that models are used in a coherent way and that they are not applied out of context. Appropriate model validation and the quantification of model uncertainty become indispensable for such applications (e.g., *Rykiel*, 1996).

In mountain permafrost research, a variety of models of diverse complexities have been developed, ranging from *empirical* (or statistical) permafrost models to reproduce the spatial extent of permafrost over large areas to *physically-based* models that resolve the physical processes influencing the thermal regime of the ground for spatio-temporal prediction (e.g., *Hoelzle et al.*, 2001, *Etzelmüller et al.*, 2001a, *Riseborough et al.*, 2008). Empirical models relate explanatory variables to the quantity of interest. The selection of the explanatory variables is based on the conceptual understanding of underlying physical processes of the modeler. In physically-based models, some processes are parame-

terized, i.e., physically-based models include empirical relationships between variables. Hence, the clear distinction made here between empirical and physically-based models is somewhat artificial. Depending on the question to be answered, computer resources and data availability determine the choice of the applied model (*Riseborough et al.*, 2008). With respect to scale (e.g., Sect. 2.1.3), the processes included in a mountain permafrost model and the question to be studied vary considerably (*Etzelmüller et al.*, 2001b, *Hoelzle et al.*, 2001).

2.3.2 Empirical mountain permafrost models

Knowing the spatial extension of mountain permafrost is relevant for hazard mitigation planning such as constructions against floods or avalanches, or construction of infrastructure for tourism (*Haeberli*, 1992, *Ives and Bovis*, 1978, *Keusen and Haeberli*, 1983, *Wegmann and Keusen*, 1998, *Phillips*, 2000). Based on measurements, empirical models have been developed to simulate permafrost distribution. They relate observed permafrost indicators, such as the bottom temperature of snow, the mean annual ground surface temperature (MAGST) or land forms (e.g. active, relict and inactive rock glaciers) to topoclimatic factors, such as altitude, aspect and slope or mean annual air temperature (MAAT) and direct solar radiation applying statistical tools such as multiple standard linear of logistic regression (*Keller and Gubler*, 1993, *Keller et al.*, 1998, *Gruber and Hoelzle*, 2001, *Lewkowicz and Ednie*, 2004, *Boeckli et al.*, 2012a).

The study by *Haeberli* (1975) resulted in a heuristic permafrost distribution in the Alps. He related the topographic variables altitude, exposition and other topographic factors such as ridges or hill foots to permafrost observations from BTS and GT measurements, geophysical surveys and the temperature of spring water. The so-called rules-of-thumb represent the influence of sensible heat, solar radiation and snow redistribution on permafrost occurrence. According to the rules-of-thumb, permafrost is probable at elevations higher than 2500 m on inclined northern exposed slopes and higher than 3000 m on inclined southern exposed slopes in the Swiss Alps. This model was implemented in GIS using hundreds of BTS measurements resulting in the first permafrost distribution maps of Switzerland PERMAKART (*Keller*, 1992) and PERMAMAP (*Hoelzle*, 1992, *Hoelzle et al.*, 1993). Direct solar radiation is an important input to model permafrost distribution in the Alps (*Hoelzle*, 1992, 1996) and can be derived based on digital elevation models (*Funk and Hoelzle*, 1992). By contrast in southern Norway, a linear relationship between MAAT and MAGT was sufficient to model permafrost. Potential solar radiation was shown to have a minor influence on permafrost occurrence in southern Norway (*Ødegård et al.*, 1996). MAAT at -4°C indicates the lower limit of continuous permafrost (*Ødegård et al.*, 1992, 1996), resulting in continuous permafrost areas above

1700 m for southern Norway. Recently, *Boeckli et al.* (2012a) developed the Alpine Permafrost Index Map (APIM) based on the combination of logistic and linear regression using an Alpine wide rock glacier inventory and rock-logger data. *Boeckli et al.* (2012b) provided the first high-resolution permafrost distribution map for the whole European Alps (Fig. 2.5). Before application, the model was 10-fold cross-validated (*Hand*, 1997). Many other empirical models have been developed (e.g., *Hoelzle*, 1994, *Etzelmüller et al.*, 2001a, *Gruber and Hoelzle*, 2001).

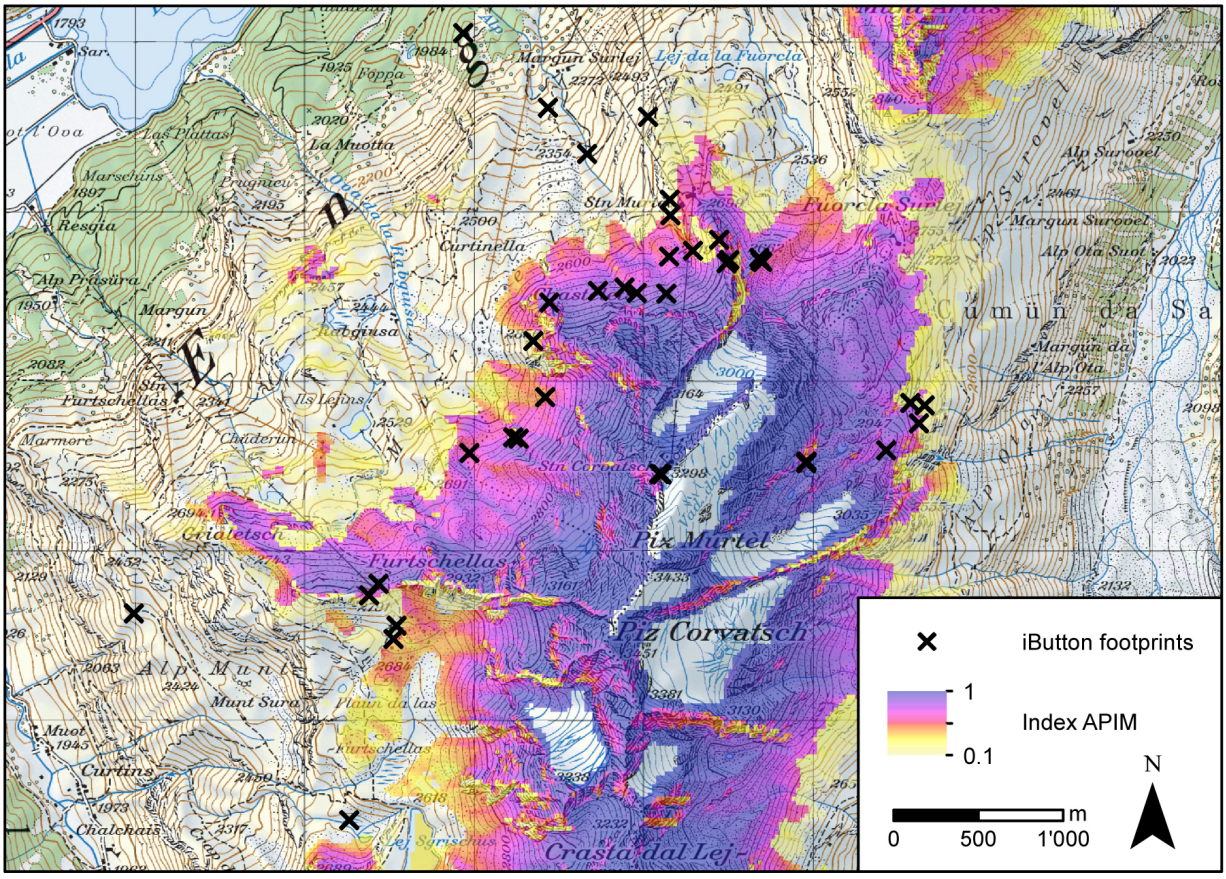

Figure 2.5: *Permafrost distribution map at Corvatsch, Switzerland (Boeckli et al., 2012a) (Courtesy of L. Boeckli and Ch. Gschwend). The crosses indicate the footprints at which GST was measured during this thesis. Map provided by Swisstopo (Resolution 1:50000).*

However, empirical models are often not useful in extrapolating to other regions or for future predictions since they are calibrated to local environments and assume steady-state conditions. Empirical permafrost models do not explicitly treat processes such as the energy balance at the surface or heat transport in the ground, and the transient effect of climate change cannot be modeled. These heuristics are based on absolute values and

must therefore be refined to respond to climatic variation. Similarly, degree-day models used to simulate snow or ice-melt by accounting for relations between air temperature and ablation behave accurately if calibrated to local conditions (e.g., *Sommerfeld et al.*, 1991, *Rango and Martinec*, 1995, *Braithwaite and Zhang*, 2000, *Braithwaite*, 2008). However, they cannot be spatially extrapolated in mountain areas because of variable melt rates, local shading and other topographic effects (e.g., *Hock*, 2003). Further, degree-day models show great inter-annual variability. Nevertheless, these models need only few input variables, are simple to understand and require only little computational effort (c.f. *Etzelmüller et al.*, 2001a). Hence, they are useful tools for many applications.

2.3.3 Physically-based mountain permafrost models

In physically-based (also process-based) permafrost models, the mathematical equations describing the physical processes that influence ground temperatures such as the energy fluxes, snow accumulation, heat conduction, etc. are solved explicitly. Physically-based models are therefore theoretically suitable to be used for spatio-temporal prediction (e.g., *Hoelzle et al.*, 2002) and for climate related sensitivity studies to investigate interactions and feedback mechanisms between processes (*Etzelmüller et al.*, 2001a, *Hoelzle et al.*, 2002). Physically-based models require much input data measured at meteorological stations or provided by general circulation models and incorporate many model parameters. Profound and detailed evaluation of physically-based models is fundamental to trust model outputs (*Rykiel*, 1996) and requires high-quality validation measurements (*Monte et al.*, 1996). Especially in mountain areas, where the topographic variability leads to different sensitivities of individual parameters and processes influencing permafrost, validation measurements are required that cover the range of topographic and environmental variability.

Riseborough et al. (2008) summarizes the use of physically-based models to investigate the temporal and thermal evolution of permafrost and to study the spatial distribution of permafrost at either a variety of single locations, along two-dimensional transects or within a whole geographic region. Nowadays, most permafrost models are applied at single points by one-dimensional transient models (*Riseborough et al.*, 2008) that neglect heat and water exchange between adjacent points. The work by *Nötzli* (2008) is singular in mountain permafrost research since it focuses on ground temperatures in three dimensions, and thereby allows to study the geometric effects of mountain topography on permafrost evolution. The upper boundary condition to the heat conduction can either be obtained from temperature measurements, from freezing and thawing factors accounting for the relation between ground surface temperatures and air temperature (e.g., *Anisimov and Nelson*, 1996, *Smith and Riseborough*, 2002, *Juliussen and Humlum*, 2007,

Etzelmüller et al., 2011, *Hipp et al.*, 2012), or by solving the energy balance at the ground surface explicitly (e.g., *Stocker-Mittaz et al.*, 2002, *Zhang et al.*, 2003, *Gruber*, 2005).

Different physically-based mountain permafrost models have been developed to simulate the energy balance within complex topography such as the model TEBAL (Topography and Energy BALance) (*Gruber et al.*, 2004a, *Gruber*, 2005), which is based on PERMEBAL (Permafrost and Energy Balance) (*Mittaz et al.*, 2002, *Stocker-Mittaz et al.*, 2002). TEBAL was applied to simulate temperatures in steep rock walls neglecting snow and was validated using distributed rock-surface temperatures (*Gruber*, 2005, *Gruber et al.*, 2004b, *Nötzli et al.*, 2007). Models like SNOWPACK, a model originally developed for avalanche warning (*Bartelt and Lehning*, 2002, *Lehning et al.*, 2002a,b), focus on snow evolution and can be used in mountain permafrost research if they are extended by proper ground heat transfer schemes (*Luetschg*, 2004, *Luetschg and Haeberli*, 2005). Other models that solve the heat conduction in the ground are driven with freezing and thawing factors, so called n-factors (e.g., *Juliussen and Humlum*, 2007, *Etzelmüller et al.*, 2011, *Hipp et al.*, 2012). These factors are estimated using the relationship between air temperature and GST. The high inter-annual variability of the snow conditions however introduces great uncertainties in these models. The model GEOtop is a distributed hydrological model (*Bertoldi et al.*, 2006, *Rigon et al.*, 2006, *Endrizzi*, 2007, *Dall'Amico*, 2010) that integrates the energy and mass balance, calculates snow compaction and snow melting processes and accounts for freezing mechanisms in the ground. It is therefore expected to be a suitable tool for transient permafrost modeling in high mountain environments, but has so far not been used for mountain permafrost research.

The neglect of the inter-annual variability of the snow cover (as by the freezing and thawing factors) or the use of empirical parameterizations as well as unknown physical properties of the ground introduce uncertainties in permafrost models. Parametric model uncertainties should be quantified to obtain a degree of confidence in the model output. The high environmental variability in mountain areas additionally challenges model evaluation since parameter sensitivities as well as model errors may vary considerably for different model settings (Fig. 2.4). This requires systematic model evaluation approaches when simulating highly variable phenomena such as mountain permafrost.

Essence: The use of empirical and physically-based models has a long tradition in mountain permafrost research, starting with the rules-of-thumb by W. Haeberli in 1975. Empirical permafrost models relate topoclimatic factors such as MAAT and potential solar radiation derived from DEMs to permafrost indicators such as MAGST or land forms. Empirical models are often used in permafrost distribution maps for large regions such as the Alps. They have the advantage of being simple to understand, require only few input data and are computationally cheap, but they are not suitable to be used at locations where they were not calibrated to (c.f., degree-day models). Physically-based permafrost models incorporate relevant processes, such as the energy balance at the Earth's surface, snow pack evolution and snow melt and heat transfer into the ground. They can be used to improve our physical understanding of relevant processes and to provide scenarios of GT evolution in the past and the future. Physically-based models require more input data and incorporate many parameters that are often not available. They have a broad application range, such as providing scenarios of future environments and can also be used in sensitivity studies to investigate the influence of individual parameters on the phenomenon of interest. Before used for decision making, however, they need to be properly evaluated.

Needs: Different empirical and physically-based models exist that can be used to investigate mountain permafrost distribution and evolution. Before used for decision making, these models should be evaluated including calibration and validation with ground truth data and quantification of model sensitivities and uncertainties. In addition, the high environmental variability in mountain regions requires investigating whether model evaluation performed at single locations is suitable to inform about the model in the whole application domain. There is hence a need to quantify the influence of environmental variability on model evaluation measures.
The physically-based model GEOtop is a potential mountain permafrost model that incorporates many processes relevant for permafrost such as snow accumulation and melting, and the conduction of heat in the ground including freezing and thawing processes in the active layer. Before GEOtop can be used in mountain permafrost studies, it should be evaluated. As mentioned above, model evaluation should represent the main environmental variability encountered in mountain regions to inform about the ability of GEOtop to simulate mountain permafrost.

2.4 Model evaluation

2.4.1 General overview

The most important part in model development certainly consists of developing the perceptual, conceptual and numerical models (Fig. 2.6). The modeler's perceptual and conceptual understanding on influencing processes and interactions form the basis of developing numerical models. To be used for decision making or to detect defects, the numerical model should be evaluated by quantifying its accuracy and the uncertainty of the modeled variable. Hence, the acquisition of driving and validation data forms an integral part of the modeling process.

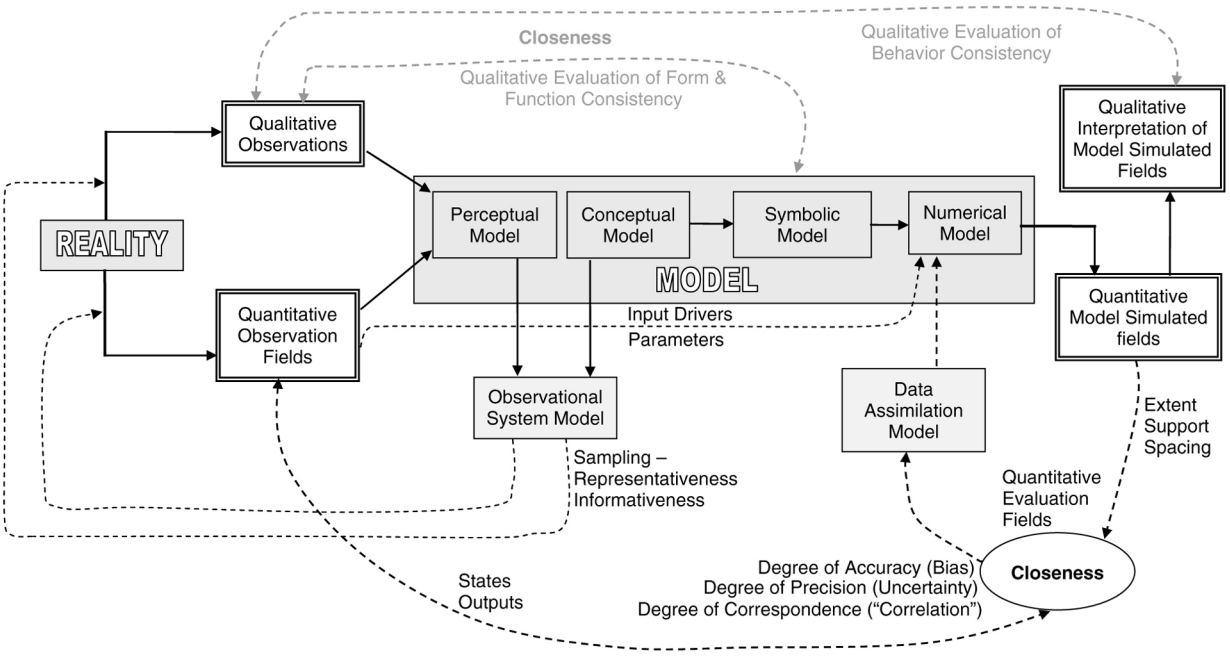

Figure 2.6: *The modeling process consists of model development, acquisition of driving and validation data, and model evaluation (Gupta et al., 2008). The observational system model forms the basis of sampling model input and validation data, and model parameters. Field observations should be representative and informative to ensure appropriate model behavior.*

Getting a complex model running is difficult and, hence, models are often not properly evaluated. The lack of spatially-distributed measurements may be an additional reason for that neglect, as well as the lack of demand by some scientific communities (*Kirchner et al.*, 1996). A model should be tested to meet its intended purpose (*Rykiel*, 1996, *Pilkey and Pilkey-Jarvis*, 2007) with appropriate accuracy (*Saltelli et al.*, 2008, Page 10):

> [...], the quality of a model is largely a function of its fitness for purpose. If modeling is a craft and models cannot be proven true (because of the pervasive nature of uncertainty and the difficulty of separating observation from observer and facts from values), then the modeler has a moral obligation, and indeed it is in the modeler's own practical interest, to be as rigorous as possible when assessing the robustness of model inference. Doing so should produce better and more parsimonious models, and will strengthen the analyst's defense of the results in the case of scientific controversy or public policy debate.

Three conditions should be considered to state that a model behaves properly (*Gupta et al.*, 2005): a) the input-state-output behavior of the model is consistent with the measurements, b) the model predictions are accurate (i.e. they have negligible bias) and precise (i.e. the prediction uncertainty is relatively small), and c) the model structure and behavior are consistent with the scientists understanding of reality. These conditions can be tested by:

1. calibrating and validating the model outputs with measurements to increase and quantify the model's accuracy,
2. quantifying the total output uncertainty coming from uncertainties in input variables, model parameters, modeler's perception, etc.,
3. analyzing how the uncertainty in the model response is apportioned to different parameters.

Environmental research fields like hydrology or meteorology show an established tradition in model evaluation (e.g., *Beven and Binley*, 1992, *Beven*, 1993, *Kavetski et al.*, 2003, *Anderson and Bates*, 2001) and data assimilation to reduce the bias and the uncertainty of modeled outputs for weather predictions (e.g., *Anderson*, 2001, *Young*, 2002, 2003, *Moradkhani et al.*, 2005, *Evensen*, 1994). In cryosphere research, selected studies exist quantifying parametric model uncertainty (*Hebeler and Purves*, 2008, *Hebeler et al.*, 2008, *Machguth et al.*, 2008) or inter-comparing models (*Pellicciotti et al.*, 2005, *Payne et al.*, 2000, *Etchevers et al.*, 2002, 2004). In mountain permafrost research, some model validation studies exist. For example, the empirical permafrost model PERMAKART was compared to almost 4000 BTS measurements showing that the model has a mean elevational error of approximately ± 300 m. The alpine permafrost index map (APIM) (*Boeckli et al.*, 2012b) was evaluated based on the area under the receiver-operating characteristics curve (AUROC) combined with ten-fold cross-validation (*Boeckli et al.*, 2012a). The numerical model TEBAL was validated using 14 rock temperature measurements, resulting in a mean absolute difference of 1.2°C for the modeled and measured ground

temperatures (*Gruber et al.*, 2004c), with similar results obtained by *Nötzli et al.* (2007). A model inter-comparison was done by *Romanovsky et al.* (1997) by comparing three numerical models with analytic solutions of the heat conduction and with measurements. They found that time resolution of maximally one hour and depth resolution in the uppermost meter of the ground column of maximally 20 ,mm ensure accurate model outputs. However, studies investigating the parametric uncertainty and sensitivity of physically-based mountain permafrost models are scarce in mountain permafrost research.

In the following sections, some model evaluation techniques are presented. First, the validation measures used in this thesis are introduced. Then, sensitivity tests and methods to quantify the parametric output uncertainty are presented. Since some of the calibration methods provide calibrated parameters together with uncertainty ranges, they are discussed in the last section.

2.4.2 Validation

Validation aims at testing whether a model fits its intended purpose by comparing model outputs to ground truth measurements (*Rykiel*, 1996). A great variety of model validation measures exist in the literature to estimate the bias, the variation of the errors, or to analyze the general fit by linear regression statistics (e.g., *Nash and Sutcliffe*, 1970, *Reckhow et al.*, 1990, *Smith and Rose*, 1995, *Allen*, 2009). In this work, three out of the six evaluation measures determined by *Stow et al.* (2003) are considered (e.g., *Mayer and Butler*, 1993, *Legates and McCabe*, 1999, *Gueymard*, 2012): the mean biased deviance (MBD), the root mean squared deviance (RMSD) and the coefficient of determination R^2. Deviance is preferred over error to emphasize that the ground truth measurements are also affected by errors (*Gueymard*, 2012). A perfect model fulfills $\mathrm{MBD} = 0$, $\mathrm{RMSD} = 0$ and $\mathrm{R}^2 = 1$. The three measures quantify the accuracy and the precision of the model (*Stow et al.*, 2009). The MBD is:

$$\mathrm{MBD} = \frac{1}{n}\sum_{i=1}^{n}(y_i - x_i), \tag{2.8}$$

where y_i are the modeled and x_i the measured quantities. The RMSD quantifies the scatter of the model prediction:

$$\mathrm{RMSD} = \sqrt{\frac{1}{n}\sum_{i=1}^{n}(y_i - x_i)^2}. \tag{2.9}$$

The correlation coefficient R^2 quantifies the linear relationship between the model output and the measurements:

$$R^2 = (\frac{\mathrm{Cov}(x,y)}{\sigma_x \sigma_y})^2, \tag{2.10}$$

where $\mathrm{Cov}(x,y)$ is the covariance of x and y and σ the standard deviation of the variables. Perfect linear agreement of the model with the measurements is indicated by $R^2 = 1$. However, this agreement does not necessarily correspond to the one-one line since the model outputs may be a multiplication of the measurements with a constant factor. Therefore, visual validation as scatter plots is necessary (e.g., *Stow et al.*, 2009).

In model validation, the question whether a measurement represents the same quantity as the model output arises (*Gupta et al.*, 2005). Before evaluating a model, the quality of the validation data, the representativeness and informativeness of the measurements and a sufficient sampling should hence be guaranteed (*Allen*, 2009). In the modeling process, *Gupta et al.* (2008) includes the formulation of an observational system model (OSM) (Fig. 2.6). The OSM is derived from the perceptual and conceptual understanding of system functioning of the modeler and forms the basis of designing campaigns to collect model driving or validation data and model parameters. The high environmental variability encountered in mountain regions requires *distributed* and *replicated* measurements that represent the environmental conditions which influence the model outputs. Replicated measurements allow quantification of measurement uncertainty due to fine- scale spatial heterogeneity, while distributed measurements are necessary to validate a model under differing environmental conditions. If both measurement and model uncertainties (e.g. Sect. 2.4.4) are quantified, a modeler can test how they relate to each other (Fig. 2.7). Both the mean behavior as well as the spread of the measurement and the model output can be compared. Ideally, model uncertainty lies within the measurement uncertainty (*Stow et al.*, 2009) having a small bias and similar dispersion. In that case, the model uncertainty represents the stochastic variability of a measured quantity accurately.

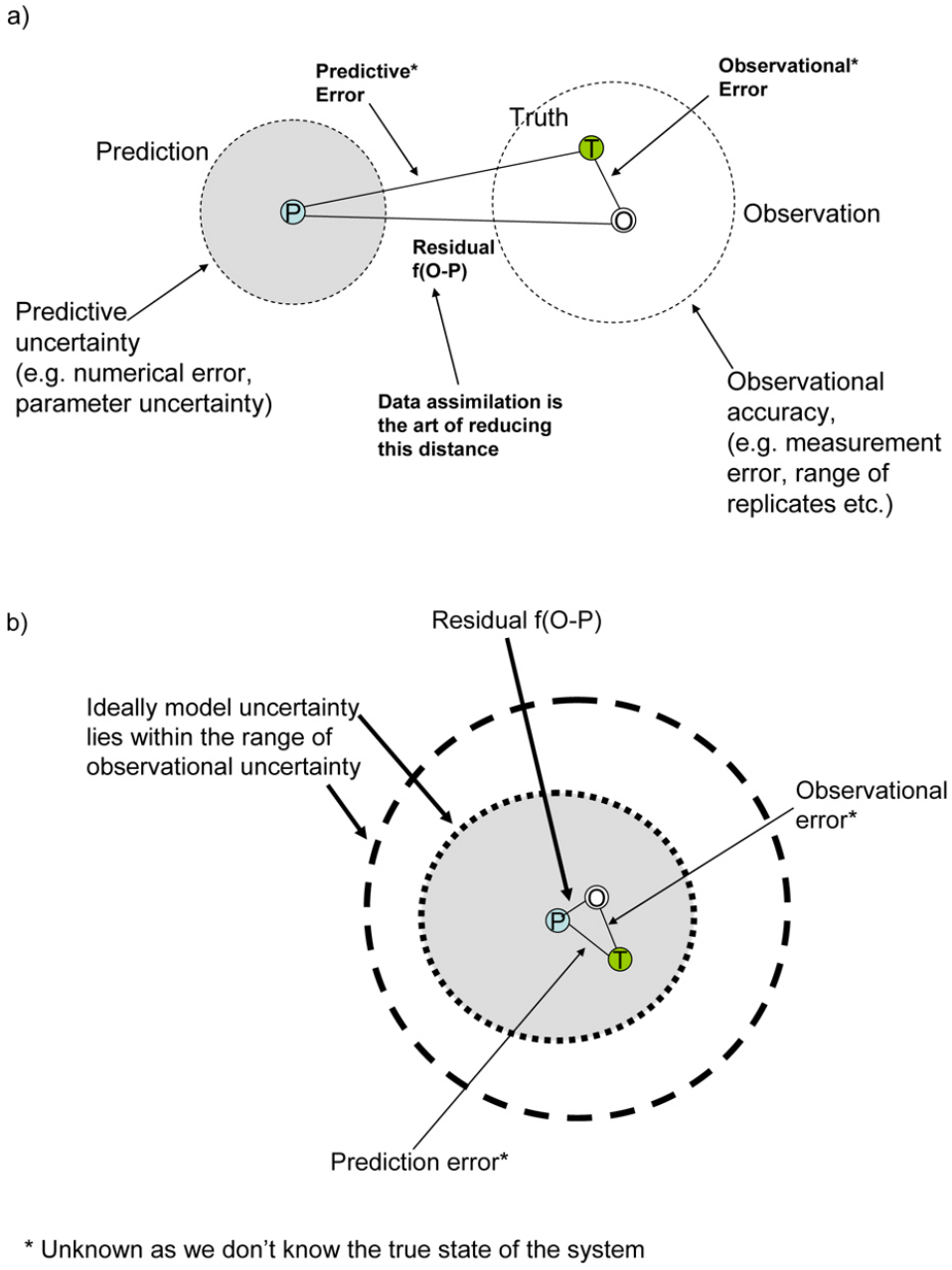

Figure 2.7: *Both measurements and model outputs are affected by uncertainty (a). Measurement uncertainty is, additional to the errors of the device, affected by environmental variability. Model uncertainties come from numerical errors as well as uncertainties in model parameters. Ideally, the model uncertainty lies within measurement uncertainty (b). Figure taken from Stow et al. (2009).*

2.4.3 Sensitivity analysis

In a sensitivity analysis, the uncertainty of a model is apportioned to the different uncertainty sources (*Saltelli et al.*, 2004) (Fig. 2.9). A related practice is uncertainty analysis (Sect. 2.4.4). Ideally, uncertainty and global sensitivity analyses accounting for interactions between parameters should be run in tandem, with uncertainty analysis preceding (*Saltelli et al.*, 2008). In practice, local sensitivity analyses on individual parameters are often performed previous to the uncertainty analysis to determine the most influential parameters and to reduce the parameter space. In this thesis, mainly local sensitivities are quantified to select the important model parameters. Local sensitivity measures the effect of a parameter θ_j by varying it and keeping all other parameters fixed at their baseline value Θ_0. Local sensitivity analyses are often done graphically or by calculating the partial derivative $s_{i,j}(\Theta)$:

$$s_{i,j}(\Theta) = \frac{\partial Y_i(\Theta)}{\partial \theta_j}|_{j=j_0}.$$

In order to compare the sensitivity $s_{i,j}(\Theta)$ of different parameters, the measure $s_{i,j}(\Theta)$ must be normalized with the range of plausible values of the parameter θ_j (*Reichert*, 2009). Local sensitivity measures are computationally cheap since two model simulations per parameter are sufficient, and are hence often used to preselect important parameters. On the other hand, local sensitivity analyses do not account for non-linearity and non-additivity in model formulations and do not take parameter interactions into account. Further, the results depend directly on the baseline value in the parameter space. In this thesis, local sensitivity analyses on individual parameters are performed for parameter selection.

The advantages and disadvantages of a global sensitivity analysis are reverse. The inputs are varied all together within their uncertainty range. Global sensitivity analysis can either be evaluated by using scatter plots or by calculating the fraction of the variance apportioned from one input to the whole model output variance (*Saltelli et al.*, 1999, *Sobol*, 2001, *Saltelli et al.*, 2008):

$$v_{i,j} = \frac{\mathrm{Var}(\mathrm{E}[Y_i(\Theta)|\theta_j])}{\mathrm{Var}(Y_i(\Theta))},$$

where Var is the variance and E is the expected value of a random variable. Variance based sensitivities can be estimated by decomposing the total variance of the model output, based on the independence assumption (*Sobol*, 1993). A common method is the Fourier Analysis Sensitivity Test (FAST). It was first introduced by *Cukier et al.* (1977) and improved by *Saltelli et al.* (2000) and is based on the spectral analysis of the outputs of model simulations performed with inputs sampled at different frequencies. The main

disadvantage of global sensitivity analyses is the high computational effort. To analyze the influence of all parameters and interactions results in a calculation of $2^n - 1$ integrals for a total number of n parameters (*Saltelli et al.*, 2008). Hence, global sensitivity analyses often only comprise first- and second-order sensitivities, which do not sum up to 100% of the total output uncertainty of the model.

2.4.4 Uncertainty analysis

Models support decision making on the local, regional, national and global scale. Since the consequences of many decisions are great (also financially), such decisions must be based on reliable statements that include the inherent degree of confidence. Uncertainty analysis aims at quantifying the total model output uncertainty arising from model input uncertainties, estimated parameters, the modeler's perception, structural model errors, etc. (*Beck*, 1987, *Gupta et al.*, 2005). It supports judging the reliability and quality of results and prognoses of a model (*Hebeler*, 2008). Model uncertainty is defined as (*AIAA*, 1998):

> a potential deficiency in any phase or activity of the modeling process that is due to the lack of knowledge,

i.e., physical properties or processes that are not known to the modeler. Sources of model uncertainties are classified in two groups (*Oberkampf and Trucano*, 2002): *aleatory* and *epistemic* uncertainties. The first includes parameters having values of a certain range that vary randomly in space and time, whereas epistemic uncertainties come from parameters that could theoretically be determined precisely. Model error is defined as (*AIAA*, 1998):

> a recognizable deficiency in any phase or activity of modeling and simulation that is not due to lack of knowledge,

and includes errors from physical approximations of processes, rounding or numerical discretization errors. In this thesis, the influence of diverse sources of errors and uncertainties on modeled mean annual ground temperature are studied.

Model output uncertainties arise from *parametric* and *input* (boundary or initial conditions) uncertainties, *structural* and *perceptual* model errors (*Butts et al.*, 2004, *Gupta et al.*, 2005, *Wagener and Gupta*, 2005) or numerical errors (Fig. 2.8 and 2.9). Model inputs are often time series derived from meteorological stations or from global or regional climate models. Model inputs are affected by measurement uncertainty, environmental

variability or, if coming from a GCM or RCM, model output uncertainty. Model parameters consist of physical properties or of empirically estimated parameters. A physical property can often not be measured due to high costs or impracticability issues and must therefore be estimated. Structural model errors arise from different descriptions, selection and coupling of the involved processes, differing numerical discretization, the spatial variability of the study area and its representation in the model, scaling and representation of sub-grid processes, lumping (e.g., *Fiddes and Gruber*, 2012), chosen parameterizations or diverging classifications of ground types or the geology, among others for example (c.f. *Butts et al.*, 2004). Errors in the mathematical implementation of numerical solutions and the discretization used in the numerical equations lead to errors in the model outputs. Structural and perceptual model differences are often examined in model inter-comparison projects, as, for example, the Snow Models Inter-comparison Project (SnowMIP) (*Etchevers et al.*, 2002), the European Ice Sheet Modeling INiTiative (EISMINT) (*Huybrechts and Payne*, 1996, *Payne et al.*, 2000), the distributed model intercomparison project (DMIP) for river forecasting (*Smith et al.*, 2004) or studies of the modeled shortwave radiation (*Gueymard*, 2003a,b, *Badescu et al.*, 2012). In climate modeling, ensemble GCMs are applied to provide different scenarios of future climates (e.g., *IPCC*, 2007).

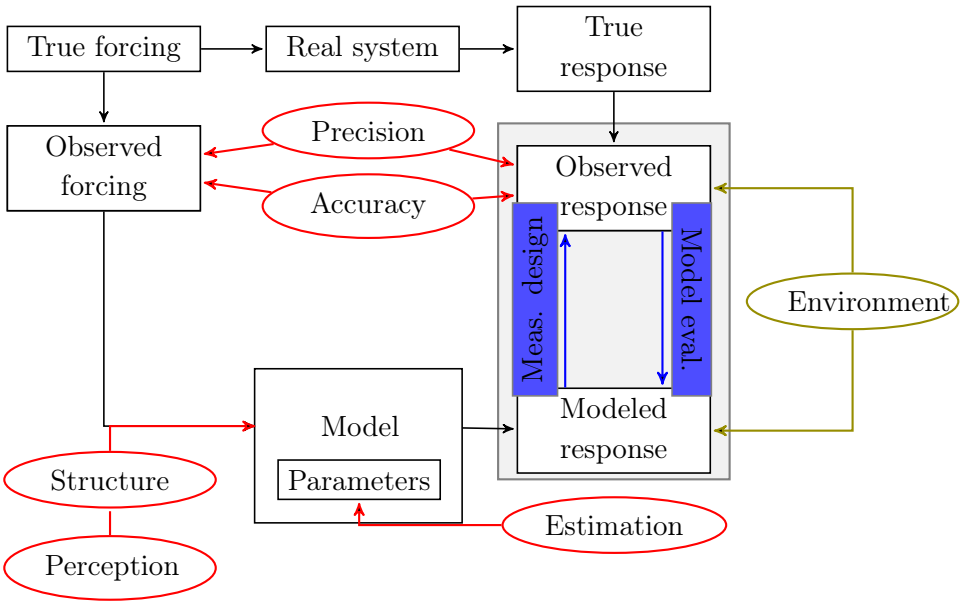

Figure 2.8: *Model uncertainties and errors have diverse sources, such as unknown parameters, uncertainties in input data, numerical errors, perceptual errors, etc. Observations of the modeled response can be used for model validation. Input and validation measurements, as well as modeled outputs, are influenced by the environmental variability encountered in the modeling domain (e.g., Fig. 2.4). Figure adapted from Gupta et al. (2005), Wagener and Gupta (2005).*

Quantification of model uncertainties due to input and parametric uncertainties is often done with Monte Carlo (MC) methods. MC methods are commonly applied in fields like atmospheric and land-surface research (*Pan et al.*, 1997, *Franks and Beven*, 1997, *Sathya et al.*, 2000, *Hanna et al.*, 2001, 2007, *Moore and Londergan*, 2001), hydrology (*Kuczera and Parent*, 1998, *Kavetski et al.*, 2003, *Vrugt et al.*, 2003), climate change (*New and Hulme*, 2000, *Tomassini et al.*, 2007, *Park*, 2008), metrology (*Allard and Fischer*, 2009), geographic information science (*Davis and Keller*, 1997, *Hebeler and Purves*, 2008), and the cryosphere (*Machguth et al.*, 2008, *Hebeler et al.*, 2008). To run a MC simulation, input data and parameters are sampled according to their (prior) distribution $\mathrm{p}(\Theta)$. The prior distribution is determined based on available measurements, literature values or expert knowledge. One model simulation is run per parameter sample. The output of a MC simulation is a frequency distribution representing the model output uncertainty (Fig. 2.9). Spatial auto-correlation of parameters (e.g., *Goodchild*, 1986) should be taken into account when using spatially-distributed models. In this study, the model experiments consist of individual point simulations within an artificial setting of locations, and hence spatial auto-correlation is not taken into account.

MC methods are applicable to any type of input data and parameters. They are easy to implement and capable of treating models characterized by any degree of complexity. The computational resources required to run an MC simulation, however, increase with increasing model complexity and an increasing number of model parameters. In this study, MC is applied to quantify the uncertainty due to parametric uncertainties of different models related to mountain permafrost. A focus is put on the environmental variability of the model evaluation measures. Since mountain permafrost reacts sensitively, highly non-linear and non-additive to changes in the environment, it is a suitable field to study the influence of environmental variability on model evaluation measures.

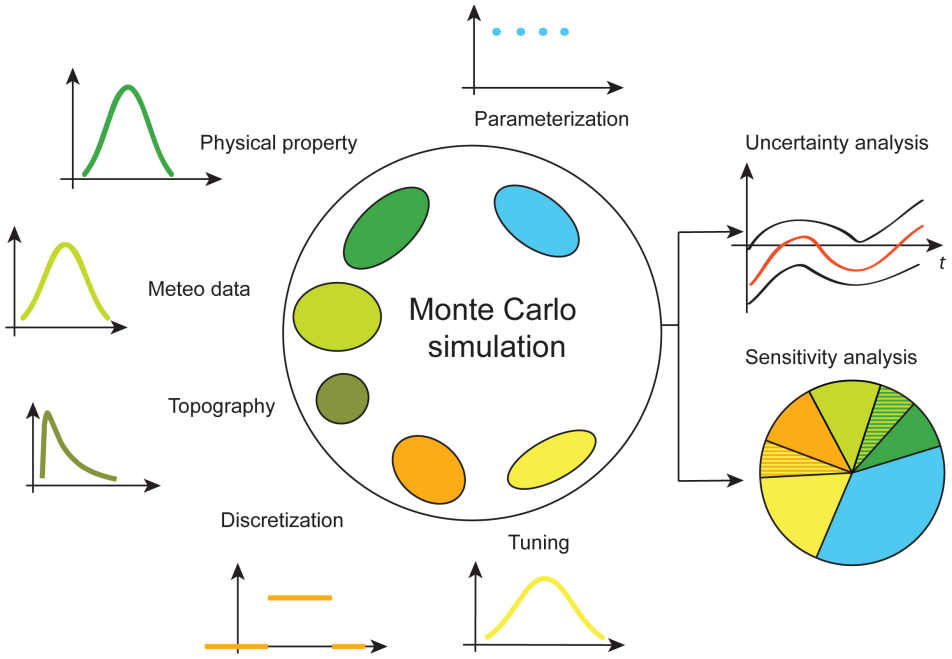

Figure 2.9: *Unknown parameters, errors in input data, model structures and differing parameterizations, numerical discretization and environmental attributes introduce uncertainty and errors in environmental models. Inter-comparison of models, as well as uncertainty analyses performed for individual models, allow to quantify the degree of confidence that can be attributed to a modeled quantity. In a sensitivity analyses, the total model output uncertainty is apportioned to the different error and uncertainty sources. Adapted from Saltelli et al. (2008).*

2.4.5 Calibration

Model calibration aims at increasing the accuracy of a model, and is often performed in a first step before a model is used for application driven purposes such as avalanche warning (e.g., *Bartelt and Lehning*, 2002). Empirical models for example are fitted to observations using methods such as linear, robust and non-linear regression analyses used to determine optimal parameter values and their uncertainty ranges. Therefore, the observed output $Y_{obs}(\Theta)$ can be partitioned into a deterministic part $Y_{det}(\Theta)$ from the model and a random error Z:

$$Y_{obs}(\Theta) = Y_{det}(\Theta) + Z, \tag{2.11}$$

where Z is assumed to be independent and normally distributed with zero mean. Before application, the assumption of independent and normally distributed errors should be verified, and, if necessary, adjusted by transformation of the variable (*Stahel*, 2008).

Model parameters are not regarded as random values in frequentist statistics, making the interpretation of, for example, confidence intervals rather unintuitive. By contrast, fixed but unknown parameters are treated as random in Bayesian statistics. Bayesian statistics is often applied to calibrate physically-based models (e.g., *Kennedy and O'Hagan*, 2001, *Renard et al.*, 2006, *Kavetski et al.*, 2006, *Reichert*, 2009). The prior belief of a parameter distribution $\mathrm{p}(\Theta)$ is combined with the likelihood function $\mathrm{L}(Y;\Theta)$ of the model parameters given the measurements. Thereby, the posterior distribution $\mathrm{p}(\Theta|Y)$ of the model parameters can be determined (e.g., *Gelman et al.*, 2004). The method is based on the Theorem of Bayes:

$$\mathrm{p}(\Theta|Y) = \frac{\mathrm{L}(Y;\Theta)\mathrm{p}(\Theta)}{\int_{\Theta} \mathrm{L}(Y;\Theta)\mathrm{p}(\Theta)\partial\Theta}. \tag{2.12}$$

i.e., the posterior distribution of the parameters is proportional to the likelihood times the prior distribution. Similar to frequentist inference, this method is based on the assumption that the model errors are identically and independently distributed. Variable transformation like auto-regression (*Burg*, 1968, *Brockwell and Davis*, 1991, 1996) or Box-Cox transformations (*Box and Cox*, 1964) are often applied to better meet this assumption.

Since Eq. 2.12 can mostly not be solved analytically, diverse algorithms have been developed to estimate the parameter posterior distribution (*Metropolis et al.*, 1953, *Hastings*, 1970, *Smith and Roberts*, 1993), commonly known under Markov Chain Monte Carlo (MCMC) algorithms. MCMC methods comprise the difficulty of determining if the equilibrium state is reached and are computer intense.

Another method often applied in hydrology is the generalized likelihood uncertainty estimation (GLUE) (*Beven and Binley*, 1992). It is also based on the Bayes Theorem, but instead of a proper likelihood function, a measure of model behavior is implemented. Analyses and calculations are easier, but the method looses its statistical interpretation, for which it has been criticized (e.g., *Mantovan and Todini*, 2006). In mountain permafrost research, model sensitivity and uncertainty analyses are relatively seldom carried out. Methods like MC uncertainty and local sensitivity analyses have therefore great potential to improve model formulations and deepen our understanding. Other studies like MCMC or model inter-comparisons were not undertaken in this thesis due to time constraints, but are discussed as a possible follow-up presented in the outlook.

Essence: A variety of model evaluation methods exist and have been broadly applied in environmental modeling, mainly so in the fields of hydrology, climatology and weather forecasting. Methods such as Monte Carlo analysis or global sensitivity testing to quantify model uncertainties and sensitivities, as well as Bayesian and pseudo Bayesian calibration, are widely known and applied. These methods serve the purpose of determining whether a model is able to represent a quantity with sufficient accuracy and precision and support decision makers by quantifying the degree of confidence that can be attributed to the model outputs. Model evaluation supports detection of model failures to improve the model formulations and deepen current knowledge. Acquisition of input and validation data is based on the observational system model resulting from current understanding of system functioning, requiring representative and informative measurements.

Needs: Mountain permafrost research has evolved very quickly, possibly due to its rapidly increasing discussion in public in relation with climate change and hazard potential. Mountain permafrost studies include measuring, as well as development and application of empirical and physically-based models. A variety of permafrost models exist, but a culture of model validation as found in hydrology has not yet been established. Model evaluation should be performed more commonly in mountain permafrost research. Quantification of sensitivities of physically-based mountain permafrost models would allow to learn more about parameter interactions, and to investigate the sensitivity of frozen ground to different processes. Uncertainty studies are needed to quantify the degree of confidence that can be attributed to the modeled permafrost conditions.

3

Methods: Measurements, models and analyses

This research project aims at quantifying the influence of environmental variability on measurement variability and model uncertainty in mountain permafrost. A measurement campaign on ground surface temperatures was conducted, and diverse modeling studies were performed. The uncertainties of the measurements and the models are quantified. A special focus is put on the variation of these uncertainties within the environmental setting consisting of diverse topographic factors and ground types. In this chapter, the measurement campaign and the model experiments are presented.

3.1 Spatially-distributed ground surface temperatures

The measurement campaign conducted for Publications I (*Gubler et al.*, 2011) and II (*Schmid et al.*, 2012) are presented in this section. Spatially-distributed ground surface temperature (GST) measurements were collected over three years. GST is an important variable in permafrost research that is extremely variable in time and space in mountain regions. It determines the ground thermal regime and provides insights into the temporal evolution of the active layer in permafrost. GST is a cost-effective measure suitable to investigate the spatial distribution of mountain permafrost and is therefore

a useful quantity for model validation. The aim of the measurement campaign is to provide a dataset suitable to quantify GST and derived variables at the coarse and the fine scale. The study region is an area of 16 km^2 around Corvatsch, Upper Engadine, Switzerland (Fig. 3.1). Since access to the study area is facilitated by a cable car, the region around Corvatsch mountain has been a place for numerous mountain permafrost studies (*Hoelzle et al.*, 2002) (see also Fig. 2.5).

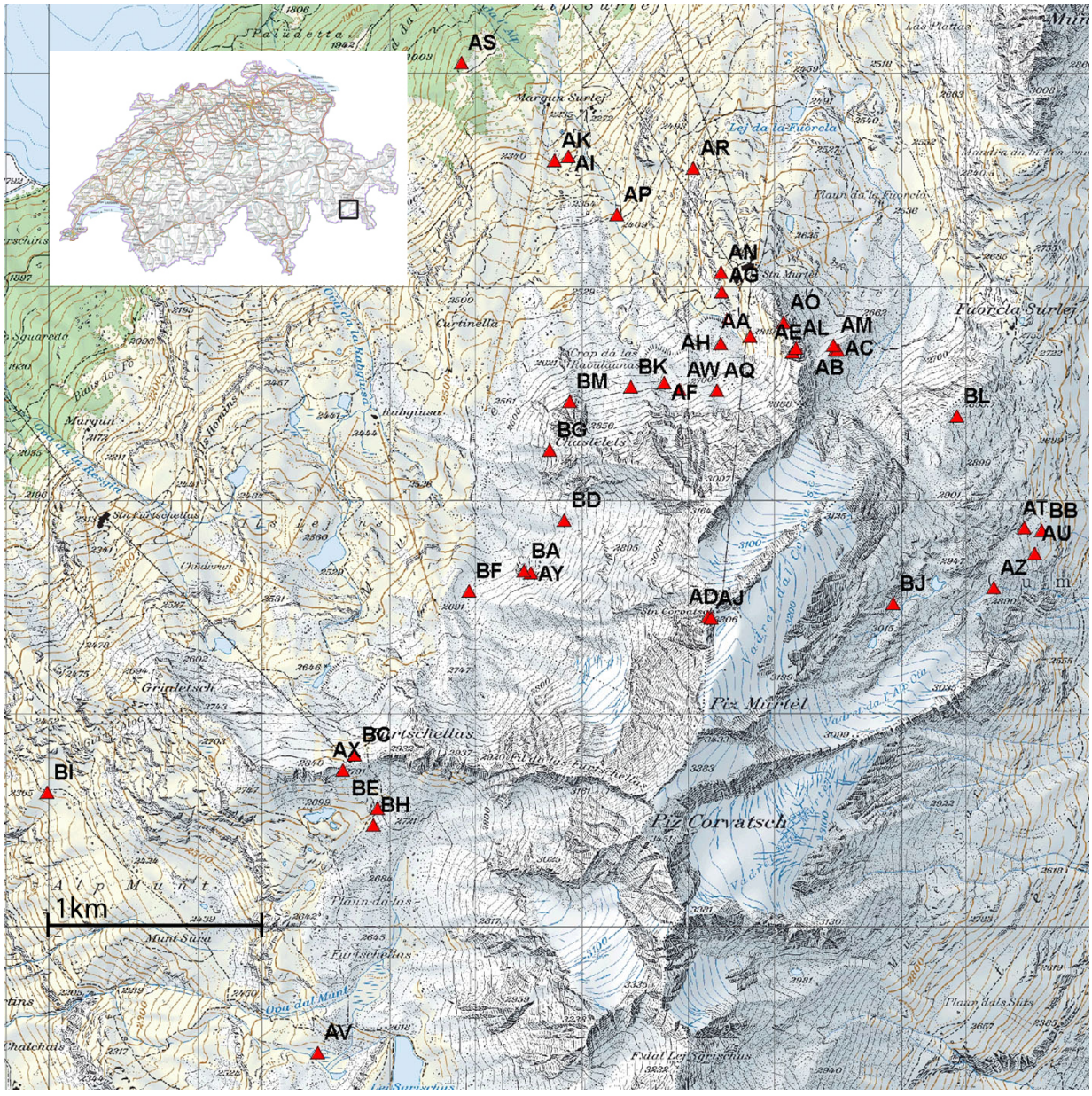

Figure 3.1: *Placement of GST measurements around Corvatsch, Switzerland, at the coarse scale.*

3.1.1 Measurement design

390 miniature temperature loggers called iButtons (`www.maxim.com`) were distributed at 39 locations, so-called footprints, to study GST variability at the coarse scale. At that scale, GST differences are mainly influenced by solar radiation, air temperature and snow distribution. The footprints were selected to represent the topographic variables elevation, slope and aspect, and both wind-exposed as well as snow accumulation areas are represented in the dataset. Different ground cover types (GCT), such as grass slopes (GCT 1), blocky fields (as typically encountered on rock glaciers, GCT 3) or fine grained material (GCT2), are represented. GCT 4 represents footprints consisting partly of bedrock. A special focus is put at one elevational band at 2600 to 2900 m to study the influence of the variables other than elevation. Further, some footprints are located along an elevational gradient from 2100 to 3300 m (Table 3.1) to quantify the GST lapse rate.

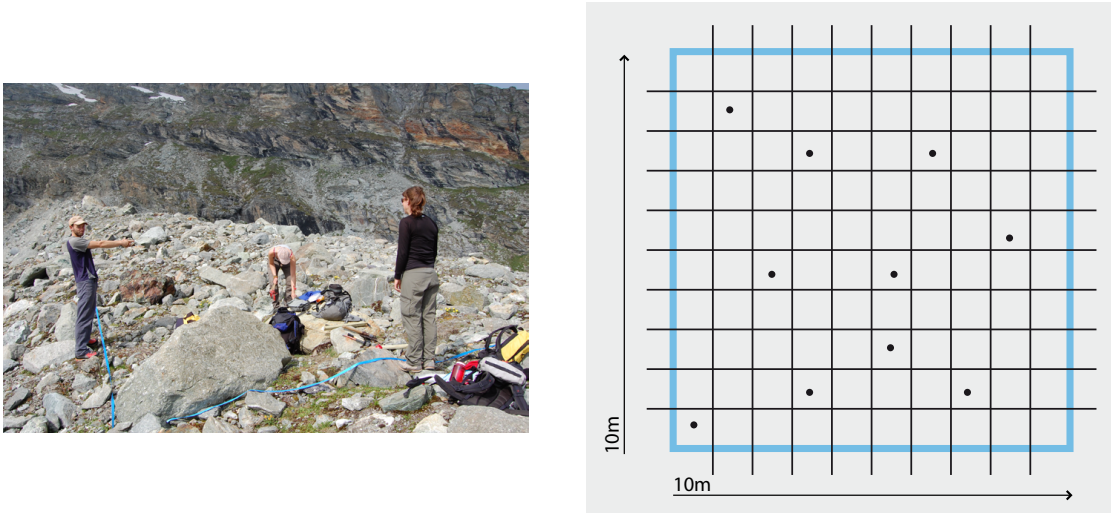

Figure 3.2: *Random distribution of the iButtons within the 10×10* m^2 *footprints. A grid of one hundred square meters was defined at each location (right). Ten iButtons were uniformly distributed based on random samples from the discrete uniform distribution* $\mathcal{U}(1, 100)$*. The random samples were obtained with R.*

Within each 10 m×10 m footprint, ten iButtons (Fig. 3.2) were randomly distributed to quantify the fine scale GST variability. Ten out of the one hundred square meters were uniformly sampled, and the iButtons were distributed according to the random num-

bers. That sampling allowed quantification of GST variability due to heterogeneous ground cover, local shading, variability in ground moisture or snow thickness. Measurement uncertainty due to environmental variability is thereby quantified at the fine scale. The iButtons were used since they are cost-effective and have proven useful in permafrost research (e.g. *Lewkowicz*, 2008, *Ramos et al.*, 2009). The iButton DS1922L measures temperature at a resolution of 0.0625°C with an accuracy of 0.5°C for temperatures between -40 and 80°C. In this campaign, temperatures are recorded at a temporal resolution of 3 hours. The temporal resolution allows for a continuous operation of 512 days, restricted by the storage space of the iButtons. Daily temperature fluctuation is represented in the time series. The loggers were buried in the ground at approximately 5 to 10 cm depth to protect them from direct solar radiation and to filter the highest frequency variations. In block fields, the loggers are placed between the boulders (e.g., *Raymond*, 2001). To avoid damage from infiltrating water (e.g. *Lewkowicz*, 2008), each iButton was sealed in a 140μm thick laminate pouch.

3.1.2 Derivatives

Based on the GST measurements, four permafrost relevant variables could be identified: the mean annual ground surface temperature (MAGST), the beginning and end (MD) of an insulating snow cover and the day when the snow pack becomes isothermal (RD). MAGST is derived from the GST measurements by calculating the yearly mean temperature, starting at the 20 of August 2010. The presence of an insulating snow cover can be determined based on the absolute temperature measurements (i.e. if GST is smaller than zero degrees Celsius (*Gadek and Leszkiewicz*, 2010)) or on daily temperature variance (e.g. *Danby and Hik*, 2007, *Schmidt et al.*, 2009). The algorithm published in Publication II (*Schmid et al.*, 2012) is based on GST variance. In a first place, a snow-cover reliability index MDr is defined:

$$\mathrm{MDr} = 0.2 - \sigma_{GST_{Jan-Mar}}. \tag{3.1}$$

MD is only determined for locations with $\mathrm{MDr} > 0$ to ensure sufficient insulation from the snow. The variance threshold T_{var} differentiates between GST above ($T_{var} = 0.1°\mathrm{C}$) or below ($T_{var} = 0.3°\mathrm{C}$) the freezing point. If the maximal daily GST exceeds 3°C, the day is assumed snow-free.

Footprint	x-coord	y-coord	Elev.	Slope	Aspect	GCT
AA	783292	144769	2694	38	251	1
AB	783691	144709	2745	16	96	2
AC	783701	144704	2743	31	112	2
AD	783092	143454	3303	29	263	4
AE	783490	144696	2826	29	290	1
AF	782888	144552	2689	23	9	4
AG	783159	144979	2664	48	243	4
AH	783151	144735	2663	9	318	3
AI	782437	145612	2307	18	330	1
AJ	783108	143449	3302	27	113	4
AL1	783506	144714	2824	14	347	1
AL2	783506	144714	2824	25	60	1
AM	783682	144727	2738	30	333	2
AN	783155	145070	2673	25	252	1
AO1	783446	144834	2811	36	64	4
AO2	783446	144834	2811	18	238	4
AP	782667	145339	2405	15	335	1
AQ	783135	144517	2729	29	12	3
AR	783026	145559	2528	28	288	2
AS	781936	146051	2100	35	315	1
AT	784575	143872	2790	36	100	1
AU	784625	143751	2773	33	88	3
AV	781263	141412	2538	0	212	1
AW	782960	144519	2700	19	333	3
AX	781380	142736	2810	23	135	1
AY	782264	143661	2687	9	328	2
AZ	784433	143592	2876	7	61	1
BA	782231	143669	2697	27	111	1
BB	784659	143858	2763	14	103	1
BC	781437	142806	2783	41	357	2
BD	782420	143906	2705	27	247	2
BE	781543	142558	2710	29	167	1
BF	781972	143576	2645	5	31	1
BG	782351	144237	2715	43	246	1
BH	781525	142480	2693	6	243	3
BI	779993	142631	2362	24	192	1
BJ	783961	143517	2997	36	90	2
BK	782731	144532	2691	31	355	2
BL	783962	143526	2875	19	35	3
BM	782444	144464	2715	44	314	4

Table 3.1: *Meta data of the GST measurement locations. Coordinates are given in the Swiss coordinate system* CH1903*. Elevation, slope and aspect are derived from a DEM of* $25\ \mathrm{m}$ *resolution. Slope and aspect are given in degrees. The aspect is counted from the north clockwise. GCT stands for ground cover type and classifies the footprints into four groups. Note that both footprints AL and AO are separated into two groups.*

The basal ripening date, i.e. the day when the snow pack becomes isothermal, is characterized by the beginning of a zero curtain period resulting in constant GST of $0°\mathrm{C}$ during a period of several days. In the measured time series, zero curtain periods are characterized by periods of constant temperatures c, where $c \in [-\delta, \delta]$, and δ is close to zero. Periods of constant temperatures c can be used to post calibrate temperature measurements by adding c. RD is only determined if the ground clearly freezes during winter time. The algorithms have been tested based on synthetic data and proved reliable (*Schmid et al.*, 2012).

3.1.3 Spatial analysis

Multiple linear regression is applied to quantify the influence of the environmental variables elevation, slope, aspect and GCT on MAGST, MD and RD at the coarse scale. Aspect was primarily sine and cosine transformed to ensure continuity. Starting with a model including each explanatory variable, a step-wise addition of quadratic and interaction terms together with an iterative model reduction was performed using the Akaike-Information-Criteria (*Akaike*, 1973). Geostatistical tools like semi-variograms (*Diggle and Ribeiro*, 2006) are used to detect spatial auto-correlations between the footprints. Fine scale variability is analyzed based on graphical methods such as box plots. The variability of the measurements is quantified by determining the range respectively the standard deviation between each footprint. A detailed description of the statistical analyses are found in Publication I (*Gubler et al.*, 2011). All analyses are performed in R (*R Development Core Team*, 2011).

3.2 Energy- and mass-balance modeling

In Publication IV (*Gubler et al.*, 2013), the sensitivities and the uncertainties of a mountain permafrost model are quantified. A focus is on the influence of environmental variability on model evaluation. The model GEOtop, originally a hydrological model, incorporates many of the processes relevant to model mountain permafrost. Downward longwave (LDR) and shortwave (SDR) radiation are two major inputs in the energy balance, and therefore important in any physically-based cryosphere model. Therefore, diverse LDR parameterizations were calibrated and validated (Publication III (*Gubler et al.*, 2012)), and the model uncertainties of parameterized clear-sky SDR and all-sky LDR were quantified. The results from these studies were implemented in GEOtop.

3.2.1 The energy-balance and heat-transfer model GEOtop

GEOtop is a coupled energy and water balance model (*Rigon et al.*, 2006) integrating temporal snow evolution, snow melt run-off and exchange of energy with the atmosphere and the ground (*Endrizzi*, 2007). The model integrates freezing and thawing processes in saturated and unsaturated ground (*Dall'Amico*, 2010) solving the Richards equation and calculates the heat conduction in the ground. Freezing and thawing processes are important in the active layer in permafrost regions. GEOtop integrates the characteristics of both land surface models and forecasting models (*Endrizzi*, 2007) and has therefore a broad range of applications. GEOtop was developed in the last 15 years and runs on a digital elevation model including lateral fluxes, or at the point scale. Model code is implemented in the programming language C. While detailed multi-layer snow models like SNTHERM (*Jordan*, 1991), SNOWPACK (*Bartelt and Lehning*, 2002) or CROCUS (*Brun et al.*, 1989, 1992) simulate the time evolution of the snow microstructure (e.g., *Vionnet et al.*, 2012), GEOtop models snow densification, liquid water percolation and refreezing, as well as snow temperature. Its special focus, however, lies on the heat conduction into the ground including freezing and thawing of water. It is therefore a promising tool to model ground temperatures in permafrost regions. Whether a more detailed snow module, such as integrated in the snow models as mentioned above, would for instance improve the ability of GEOtop to reproduce ground temperatures would have to be determined in a model inter-comparison project.

The great amount of processes implemented in GEOtop makes the distinction of errors difficult due to individual processes and feedback mechanisms. Therefore, we decided to study the parameterizations of two important energy fluxes, i.e., the downward short- and longwave radiation, separately. The approach is described in the next section.

3.2.2 Parameterized shortwave and longwave downward radiation

Solar radiation I_o at the top of the atmosphere is determined based on a geometrical approach (*Corripio*, 2002). Clear-sky direct SDR on a horizontal ground surface is:

$$SDR_{dir,cl} = 0.9751 I_0 \tau_r \tau_w \tau_o \tau_a \tau_g, \tag{3.2}$$

where the transmittance coefficients τ_i are Rayleigh scattering, water vapor, ozone, aerosols and the uniformly mixed gases O_2 and CO_2 modeled according to *Iqbal* (1983, Model C) (refer to Publication III for details). Solar radiation is scattered by aerosols and water vapor, reflected at surrounding terrain and back-forth reflected between the Earth and the atmosphere, determining the diffuse radiation. Global radiation is the sum of

the diffuse and the direct SDR. In modeling practice, and if measurements of global radiation are available, the cloud transmissivity τ_c can be determined as the fraction of observed (^{o}) and measured (^{m}) clear-sky SDR (e.g. *Greuell et al.*, 1997):

$$\tau_c = \frac{SDR^o}{SDR^m_{cl}}, \tag{3.3}$$

where $0 \leq \tau_c \leq 1$. Cloud transmissivity predominantly determines LDR and is hence an important input variable, but only rarely available (*Sicart et al.*, 2006). Clear-sky LDR is estimated based on the Stefan-Boltzmann law:

$$LDR_{cl} = \epsilon_{cl}\sigma T^4, \tag{3.4}$$

where $\sigma = 5.67 \cdot 10^{-8}\ \mathrm{Wm^{-2}K^{-4}}$ is the Stefan-Boltzmann constant, and $\epsilon_{cl} = \epsilon_{cl}(T, e)$ is the emissivity of the atmosphere. Diverse parameterizations exist to model the atmospheric emissivity for clear- and all-sky conditions (e.g. *Ångström*, 1915, *Brunt*, 1932, *Brutsaert*, 1975, *Satterlund*, 1979, *Pirazzini et al.*, 2000). The parameterizations are summarized in Table 3 of Publication III. The *Konzelmann et al.* (1994) parameterization is:

$$\epsilon_{cl} = 0.23 + x_1(p_v/T)^{1/x_2}, \tag{3.5}$$

and is studied more in detail since it has often been used in studies of the alpine cryosphere (e.g. *Greuell et al.*, 1997, *Klok and Oerlemans*, 2002, *Mittaz et al.*, 2002, *Machguth et al.*, 2008). Here, p_v denotes the water vapor pressure [hPa]. Originally, this parameterization was developed at the ETH camp on the Greenland ice sheet with $x_1 = 0.433$ and $x_2 = 8$. The all-sky LDR is estimated as:

$$LDR_{all} = (\epsilon_{cl}\tau_c^{p_1} + \epsilon_{oc}(1 - \tau_c^{p_2}))\sigma_{SB}T^4, \tag{3.6}$$

where ϵ_{oc} is the emissivity in overcast situations and p_1 and p_2 are empirical parameters. This parameterization was modified from studies by *Pirazzini et al.* (2000) to avoid additional uncertainties coming from conversion of τ_c to cloud cover (e.g. *Greuell et al.*, 1997, *Crawford and Duchon*, 1998, *Sicart et al.*, 2006). Cloud transmissivity τ_c (Eq. 3.3) can only be determined during day-time. To estimate the all-sky LDR, τ_c must be interpolated during the night (e.g., *Lhomme et al.*, 2007). Different interpolations are evaluated to increase the accuracy of LDR in impact models.

3.2.3 Modeling experiments

3.2.3.1 GEOtop sensitivities and uncertainties

As mentioned before, the high environmental variability typically encountered in the Alps requires systematic model evaluation. Therefore, GEOtop was evaluated at locations covering the whole range of environmental variability typically found in Alpine

regions: elevations from 500 to 4000 m, all aspects in steps of 45 degrees and slopes from zero to thirty degrees. Six different ground types, i.e. clay, sand, silt, peat, gravel and rock were studied. The ground types are characterized by their hydraulic properties (e.g., Eq. 2.7) such as the hydraulic conductivity K_h, the porosity θ_s and the van Genuchten parameters α_{vG} and n_{vG} (Table 3.2). In total, a number of 1328 points were simulated in the synthetic environment, consisting of a combination of each of the mentioned topographic attributes and ground types.

GEOtop runs with meteorological data such as air temperature, relative humidity, global radiation, wind direction and velocity, and precipitation. The data was obtained from the station by MeteoSwiss at Corvatsch at 3315 m. Measurements from 1995 to 2011 are used as model inputs at an hourly resolution. The ground temperatures are spun-up according to an algorithm developed and tested by S. Gruber.

The sensitivity study comprises a variety of numerical parameters determining the numerical stability, as well as discretization parameters of the snow pack and the ground column. Further, the influence of different model specific parameters such as differing LDR parameterizations and physical properties, such as the ground conductivity, albedo, and the emissivity, were analyzed. In total, the sensitivity of 52 parameters was quantified (Table 3.3). The parameter ranges were selected according to literature values and expert opinion (e.g., *Gubler et al.*, 2013). The parametric uncertainty of the mean annual ground temperature at different depths (MAGT) modeled with GEOtop was quantified based on a Monte Carlo (MC) approach. Therefore, a probability density function (PDF) was assigned to each of the previously selected physical parameters according to literature values, expert knowledge or available measurement series (Table 3.3). In a MC study, model simulations are performed with parameters sampled randomly from their prior PDFs. The parametric model uncertainty is quantified as the spread of the simulated model outputs using statistical parameters, such as standard deviation or the range between the 2.5 and 97.5% percentiles. Previously, a local sensitivity analysis on all parameters was performed. The sensitivity analysis informed to preliminarily reduce the parameter space.

Parameter	Symbol	Unit	Clay	Silt	Sand	Peat	Gravel	Rock
Residual water content	θ_r		0.072	0.057	0.055	0.2	0.055	0.002
Saturated water content	θ_s		0.475	0.487	0.374	0.85	0.374	0.05
van Genuchten α	α_{vG}	mm^{-1}	0.001	0.001	0.003	0.03	0.1	0.001
van Genuchten n	n_{vG}		1.4	1.6	3.2	1.8	2	1.2
Hydraulic conductivity	K_h	$\mathrm{mm\ s}^{-1}$	0.0019	0.0051	0.0825	0.3	10	0.000001
Thermal conductivity	K_T	$\mathrm{W\ m}^{-1}\ \mathrm{K}^{-1}$	2.5	-	-	-	-	-
Thermal capacity	C	$\mathrm{J\ m}^{-3}\ \mathrm{K}^{-1}$	$2.25{\cdot}10^6$	-	-	-	-	-

Table 3.2: *Hydraulic and thermal properties of the different ground types. The hydraulic parameters are assumed to change by ±20% for θ_s, ±10% for θ_r, ±50% for n_{vG} and ±25% for α_{vG} in the sensitivity analysis. The hydraulic conductivity K_h is multiplied by a factor f_{K_h} ranging from 0.01 to 100. The thermal conductivity changes by 50%, and the heat capacity by 20%. In the sensitivity analysis, the values are modified by the respective factors presented in Table 3.3.*

	Symbol	Unit	Sensitivity			Uncertainty		
			Base	Min	Max	Distr.	Par_1	Par_2
Numerical parameter								
Thickness of first ground layer	dz_{min}	mm	20	5	640			
Growth rate ground depth	b		0.5	0	1			
Maximal ground depth	z_{max}	m	10	1.25	20			
Number of top snow layers	n_t		4	1	10			
Number of bottom snow layers	n_b		2	1	10			
Number of snow layers in middle	n_m		4	1	64			
Maximal SWE	swe_m	mm	10	1.25	40			
Time discretization	dt	$3600 \cdot \mathrm{s}$	1	0.125	4			
Richard's tolerance	tol_r	mm	10^{-4}	10^{-8}	10^{-4}			
Heat equation tolerance	tol_h	$\mathrm{J\,m^{-2}}$	10^{-4}	10^{-8}	10^{-4}			
Model specific parameter								
Minimal wind velocity	V_{min}	$\mathrm{m\,s^{-1}}$	0.5	0.01	1.28			
Minimal relative humidity	RH_{min}	%	10	1	10			
LDR calibration	$LW_{in,K}$							
Monin-Obukhov param.	MO		1	1	4			
Water balance	WB		1	0	1			
Physical parameter								
Initial ground temperature	T_i	°C	1	-1	1			
Depth above which water drains laterally	z_f	m	10	0.01	10	Unif	0	10
Extinction parameter snow albedo	c_α	mm	10	0	200	Log-N	1.71	1.09
Ground roughness	r_g	mm	10	0.01	100	Log-N	1.96	0.83
Dry ground albedo	$\alpha_{g,dry}$		0.2	0.1	0.4	Norm	0.25	0.05
Divisor wet ground albedo	$f_{\alpha_{g,wet}}$		1	1	2.5	Norm	1.75	0.25
Ground emissivity	ϵ_g		0.96	0.81	0.99	Norm	0.93	0.02

Continued on next page

Table 3.3 – continued from previous page

	Symbol	Unit	Sensitivity			Uncertainty		
			Base	Min	Max	Distr.	Par_1	Par_2
Ground heat flux	Q_g	$\mathrm{W\,m^{-2}}$	0.05	-0.1	0.1			
Snow roughness	r_s	mm	0.1	0.01	10	Log-N	-2.64	0.83
Fresh snow albedo (vis)	$\alpha_{s,vis}$		0.96	0.8	0.96	Norm	0.93	0.02
Fresh snow albedo (nir)	$\alpha_{s,NIR}$		0.65	0.6	0.7	Norm	0.65	0.02
Snow emissivity	ϵ_s		0.98	0.96	0.99			
Snow viscosity	v_s	$\mathrm{Ns\,m^{-2}}$	10^6	10^6	$8 \cdot 10^6$	Norm	$4 \cdot 10^6$	$2 \cdot 10^6$
Ground-snow roughness threshold	$c_{s,r}$	mm	1	0.5	1			
Irreducible water saturation snow	$s_{w,irr}$		0.02	0.005	0.08	Log-N	-4.02	0.47
Snow density cutoff	$d_{s,cut}$	$\mathrm{kg\,m^{-3}}$	100	75	175	Log-N	4.58	0.2
Dry snow deformation rate	$df_{s,dry}$	%	1	0.75	1.25			
Wet snow deformation rate	$df_{s,wet}$	%	1.5	1.25	2.5			
Temperature threshold rain	$T_{r,0}$	°C	3	0	4	Norm	2	0.5
Temperature threshold snow	$T_{s,0}$	°C	-1	-3	0	Norm	-1.75	0.5
Ozone	O_3	DU	314	238	390			
Ångström α	α		1.38	0.46	2.30			
Ångström β	β		0.039	0.010	0.139	Log-N	-3.73	0.99
Albedo to determine SDR	α_c		0	0	1			
Residual water content (F)	$f_{\theta_{res}}$		1	0.8	1.2			
Saturated water content (F)	$f_{\theta_{sat}}$		1	0.9	1.1	Norm	1	0.05
van Genuchten parameter α (F)	$f_{\alpha_{vG}}$		1	0.75	1.25			
van Genuchten parameter n (F)	$f_{n_{vG}}$		1	0.5	1.5	Norm	1	0.25
Hydraulic conductivity (F)	f_{K_h}		1	0.01	100	Norm	0	1
Thermal Capacity (F)	f_C		1	0.8	1.2			
Thermal Conductivity (F)	f_{K_T}		1	0.5	1.5	Norm	1	0.25

Continued on next page

Table 3.3 – continued from previous page

	Symbol	Unit	Sensitivity			Uncertainty		
			Base	Min	Max	Distr.	Par_1	Par_2
Input parameter								
Temperature lapse rate	Γ_T	$^\circ\text{C}\,\text{km}^{-1}$	6.5	5.5	7.5			
Dew temperature lapse rate	Γ_{DT}	$^\circ\text{C}\,\text{km}^{-1}$	2.5	1.5	3.5			
Precipitation lapse rate	Γ_P	km^{-1}	0.2	-0.1	0.3			
Correction factor for precip.	c_p		2	1.6	2.4			
Sensor height wind velocity	h_w	m	2	0.5	16	Log-N	0.66	0.25
Sensor height temperature	h_T	m	2	0.5	16	Log-N	0.66	0.25

Table 3.3: *Parameters that were analyzed in the sensitivity study. The minimum and the maximum indicate the range in which the parameters are sampled, while the base indicates the standard choice used in the local sensitivity studies. The right part denotes the parameter distributions that were used in the uncertainty study.*

3.2.3.2 Evaluation of shortwave and longwave downward radiation

The study on SDR and LDR was performed at six locations in Switzerland. At these locations, stations of both the Swiss Meteorological network (SwissMetNet) and the Alpine Surface Radiation Budget network (ASRB) (*Philipona et al.*, 1996) exist. The SwissMetNet measurements were used as input data (air temperature, relative humidity and global SDR), and the ASRB measurements were used for validation and calibration (global SDR and LDR). All measurements were provided by MeteoSwiss. The study locations are Locarno-Monti, Cimetta, Davos, Weissfluhjoch, Payerne and Jungfraujoch (Fig. 3.3). The stations are located at elevations ranging from 200 to 3400 m. The study represents the main elevations encountered in Switzerland.

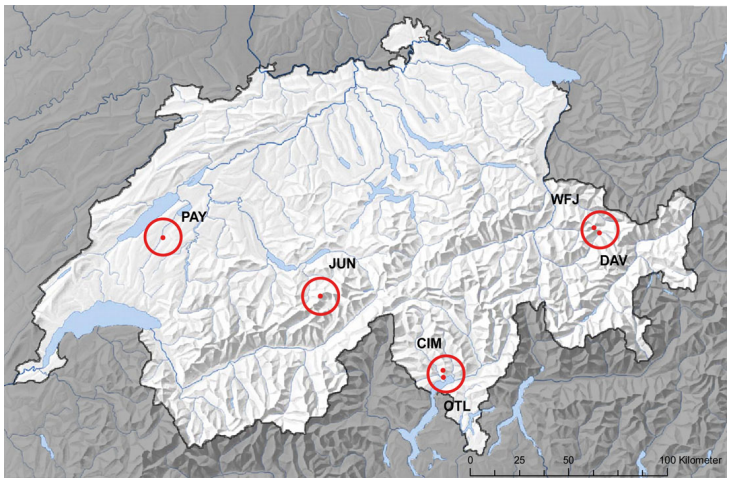

Figure 3.3: *The SDR and LDR parameterizations were evaluated at six locations. At each location, a station of both the SwissMetNet and ASRB networks exist (Source: MeteoSwiss). The stations are located at elevations ranging from 200 to 3300 m asl.*

The analyses were performed with hourly measurements from 1998 to 2008. The parameters of the LDR parameterization, i.e. x_1 and x_2 (Eq. 3.5) and p_1, p_2 and ϵ_{oc} (Eq. 3.6), were calibrated using non-linear least squares analysis (*Bates and Watts*, 1988, *Bates and Chambers*, 1992). The SDR parameterization (*Iqbal*, 1983, Model C) and the LDR parameterizations were validated using the MBD, RMSD and R^2 as model performance measures (Sect. 2.4.2). Parametric uncertainties of the clear-sky SDR and all-sky LDR parameterizations were quantified using MC. Prior distributions of the atmospheric parameters (ozone, precipitable water, aerosols) were assigned either based on individual time series obtained in Switzerland, such the ozone measurements in Arolla, through parameterization (e.g. *Prata*, 1996) or from literature values (Table 3.4). Measurement

uncertainty of the input variables air temperature, relative humidity and air pressure were obtained from MeteoSwiss (Courtesy of R. Philipona).

	Measurement	Distribution	μ	σ	Unit
Input	Air temperature	Norm (E)	0	0.2	K
	Relative humidity	Norm (E)	0	5	%
	Air pressure	Norm (E)	0	0.2	hPa
Parameter	Ozone column	Log-N	314	38	DU
	Ångström exponent	Norm	1.38	0.46	
	Ångström turbidity	Log-N	0.039	0.05	
	PrecWatConstant	Log-N	47	0.38	g K cm^{-2} hPa^{-1}
	Ground Albedo	Log-N			
	Cloud transmissivity	Norm (E)	0	0.08	

Table 3.4: *Input, model parameters and validation data with uncertainty distributions. Note that the distribution of the input data concern the error of the measurement (denoted with E), whereas the distribution in the parameters concerns the parameter value itself. Since ground albedo varies temporally and spatially, its distribution is estimated for each station and each month separately (e.g., Publication III).*

4

Results: Measurement variability and model uncertainties

The results of this thesis are published in the four papers presented in Part II of this thesis. The GST time series are analyzed, and the influence of environmental variability on the mean annual ground surface temperature (MAGST), the melt-out day of snow (MD) and the ripening date of snow (RD) is quantified at the coarse and the fine scale (Publications I and II). The uncertainties in parameterized downward clear-sky shortwave and all-sky longwave radiation are quantified, and the LDR parameterizations are calibrated to atmospheric conditions in Switzerland (Publication III). Sensitivities and uncertainties of the hydrological model GEOtop are systematically quantified at locations covering the environmental variability typically found in high mountain areas as the Swiss Alps (Publication IV).

4.1 Measurement variability related to topography and scale

The presented results are based on the findings in Publications I (*Gubler et al.*, 2011) and II (*Schmid et al.*, 2012).

4.1.1 General description

Some of the GST time series show a typical behavior as presented by *Hoelzle et al.* (2003) (e.g. Fig. 4.1, Footprint BC). Temperatures in summer are highly correlated to air temperature showing large daily fluctuations. With the first snow fall, the variations are dampened and reach their equilibrium in March and April. Clear zero curtain periods indicate the beginning of the melt phase, reaching their end when the snow has completely melted. At other locations, snow-free and snow-covered seasons cannot be distinguished (Fig. 4.1, left plots). These footprints are located at wind exposed locations where snow does not accumulate. There, GSTs follow air temperatures closely during the whole year. The smaller temperature fluctuations and the lower temperatures at west exposed in comparison to east exposed sites could be attributed to the formation of convective clouds in the afternoon (Fig. 4.1, left plots). At south east exposed slopes, snow melt-out occurs one month earlier than at nearby, northern exposed slopes (Fig. 4.1, middle plots). Steeper slopes of around 30 to 40 degrees in general have earlier melt out than flat snow-accumulation areas (Fig. 4.1, right plots). The following sections present the results from Publications I and II for coarse and fine scale variability of the MAGST, MD and RD. The analyses are performed on the basis of the three-year measurement series. They might slightly differ from the published results, which only include one (*Gubler et al.*, 2011) respectively two (*Schmid et al.*, 2012) years of continuous measurements.

Three-yearly GST time series for two footprints AA and AH are presented in Fig. 4.2. AA is a west exposed grass slope that does not freeze in winter. The footprint AH is located beside the meteorological station at Murtèl rock glacier. The horizontal distance of AA and AH is approximately 50 m (Fig. 3.1). GST at AH are much colder in winter due to ventilation of cold air in the blocks. At some locations, GST in winter stays close to zero degree Celsius indicating warm temperatures in the subsurface, whereas the negative GST at other locations may be an indication of permafrost (Fig. 4.1). The aim of the study was to quantify measurement variability at two scales that are used in high-resolution mountain permafrost modeling (fine-scale) or regional climate modeling (coarse scale). That will be discussed in the following sections.

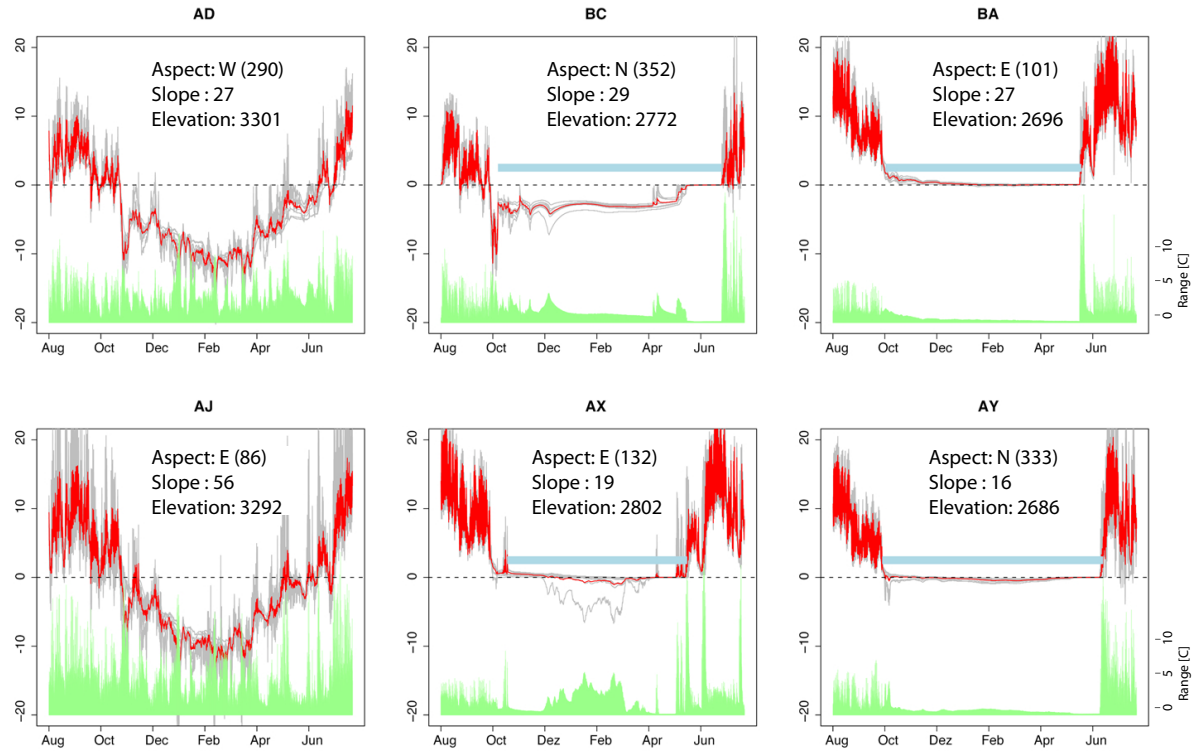

Figure 4.1: *Ground surface temperature series at six footprints for the year 2009/2010. The gray lines show the measurements of all ten iButtons, and the red line indicates the mean temperature at the footprint. The green series indicates the range of the individual measurements. At mountain ridges, snow is typically blown away and hence ground temperatures follow air temperature during the whole year (left figures). Snow accumulation can be observed in a dampening of the daily temperature fluctuation in the beginning of the winter (middle and right figures). Zero curtain perdiods in spring indicate the melt onset (Footprint BC). Snow melt-out is one month earlier at south-east exposed slopes (AX and BA) than at north exposed slopes (BC and AY). At BC, winter ground temperatures are clearly below zero degree Celsius, which is a possible indicator for permafrost.*

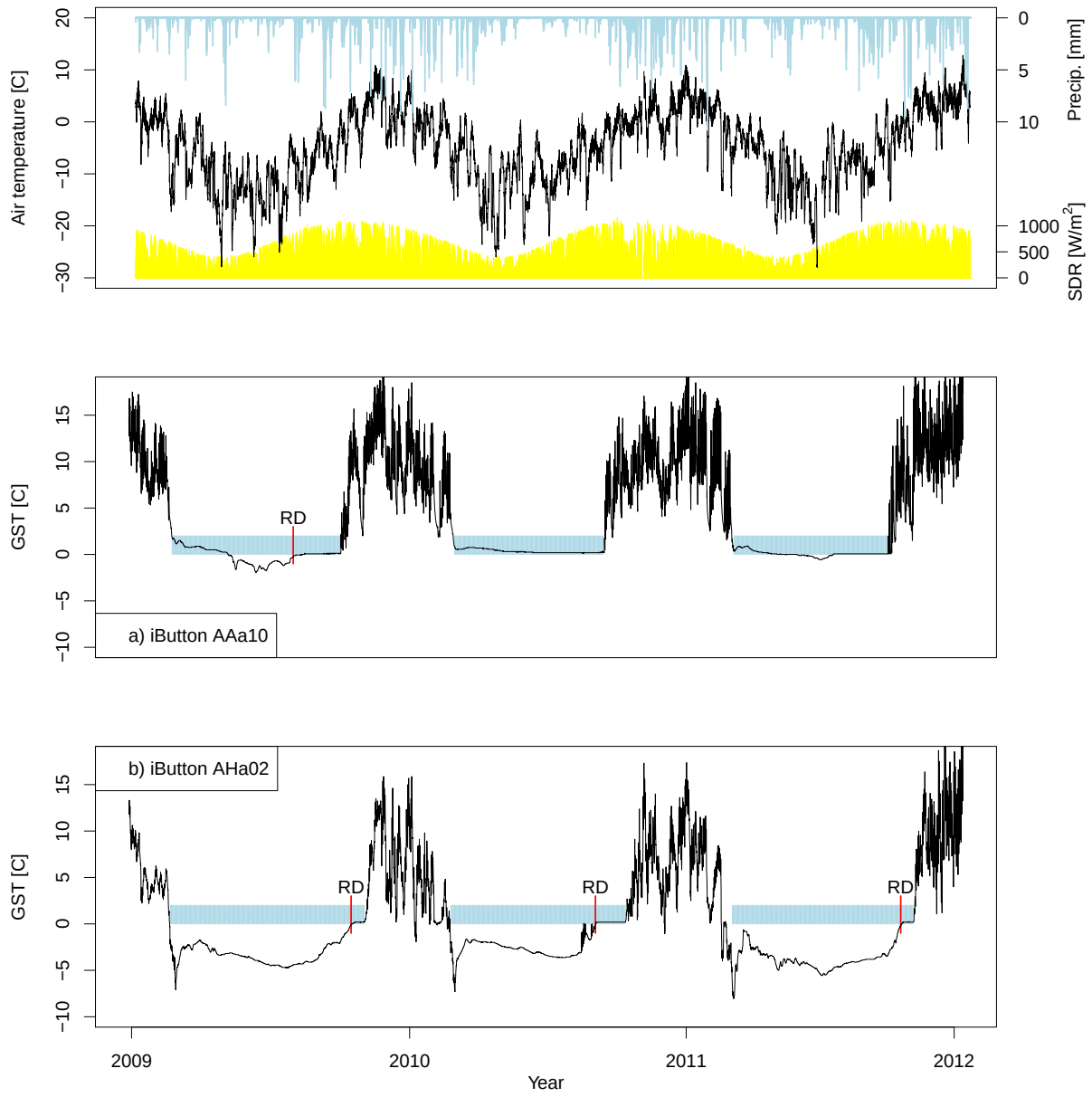

Figure 4.2: *Three year time series at footprints AA and AH. The footprint AA is 38 degrees steep, west exposed grass slope lying close to the Murtèl rock glacier, and AH is positioned on the rock glacier. Especially winter temperatures are clearly higher in AA than at AH. In 2011 and 2012, ground does not freeze at that AA, whereas on the rock glacier, temperatures decrease to -5°C. The top figure shows air temperature, precipitation and global SDR measured at the Corvatsch station, 3315 m asl.*

4.1.2 Coarse scale variability

In Table 4.1, observed MAGST, MD and RD of all footprints is presented. MAGST is estimated as the mean value of the GST measurements starting at the 20 of August each year. Thereby, three complete years of measurements were ensured. MAGST values for 2010 differ slightly from the values published in *Gubler et al.* (2011) due to the different start times.

At the coarse scale, MAGST varies approximately 9°C due to the elevational differences of 1300 m covered in the measurement campaign (Fig. 4.3). Differences in aspect, slope and ground cover type (GCT) explain approximately 6°C of the variation. The multiple linear model that quantifies the effect of the explanatory variables elevation, slope, aspect, and GCT on the mean annual ground surface temperature μ_k is:

$$\begin{aligned}\mu_{\mathrm{k}} =& 15.83 - 0.0050 \cdot \mathrm{Elevation}_k + 0.31 \cdot \sin(\mathrm{Aspect}_k) \\ & - 0.42 \cdot \cos(\mathrm{Aspect}_k) + 0.01 \cdot \mathrm{Slope}_k - 0.057 \cdot (\mathrm{Slope}_{\mathrm{k}} : \cos(\mathrm{Aspect}_{\mathrm{k}})) \\ & + 0.07 \cdot \mathrm{dGCT}_{k,2} - 1.61 \cdot \mathrm{dGCT}_{k,3} - 2.2 \cdot \mathrm{dGCT}_{k,4} \\ & + 0.17 \cdot \mathrm{dYear}_{k,2011} + 0.01 \cdot \mathrm{dYear}_{k,2012} + \varepsilon_k \,.\end{aligned} \tag{4.1}$$

The adjusted R^2 of the model is 0.91. Model assumptions of normally distributed errors were checked by visual inspection of residual plots provided by the linear regression function in R. A semi-variogram of the model residuals showed that the residuals are not spatially auto-correlated. MAGST changes with a lapse rate of $-5°\mathrm{C\,km^{-1}}$, a value close to temperature lapse rate of $-6.5°\mathrm{C\,km^{-1}}$. It is comparable to MAGST lapse rates found in the literature such as the $-5.7°\mathrm{C\,km^{-1}}$ in southern Norway (*Ødegård et al.*, 1992) or $-4°\mathrm{C\,km^{-1}}$ in the Czech republic (*Šafanda*, 1999). The difference between steep north and steep south facing slopes (40 degrees) is greater than 5°C, while for shallow slopes it is approximately 2°C. Differences in steep north-south exposed slopes result in MAGST changes similar to differences of 1000 m vertical (e.g. *Gruber et al.*, 2004b), and are in direct relation with the amount of received solar radiation. Blocky surfaces cool the ground by almost 2°C (Fig. 4.2). That effect can be attributed to processes such as ventilation of cold air, or to the low thermal conductivity of blocky fields (c.f. *Gruber and Hoelzle*, 2008), among others. Convective clouds, for example, may cool the ground by approximately half a degree at west exposed slopes in comparison to east exposed slopes. In the regression model 4.1, the inter-annual variability does not significantly apportion to MAGST variability. Nevertheless, the yearly values are listed to obtain an idea of the magnitude of inter-annual MAGST variability due to changing snow conditions. At individual footprints, the inter-annual variability is up to 1°C (for example, footprint BC for the years 2010 and 2012). Since the time series is not long enough, the influence of snow duration on MAGST could not be quantified.

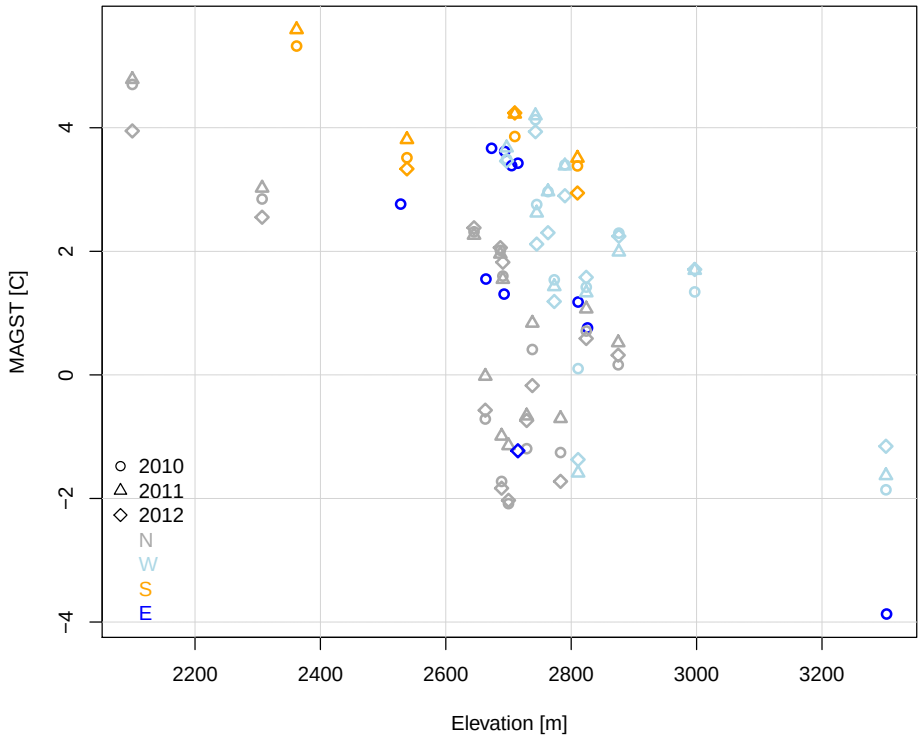

Figure 4.3: *At the coarse scale, MAGST varies approximately 9°C due elevational differences of 1300 m. At one elevation band at 2700 m asl., MAGST variability due to solar radiation and ground cover type is 6°C. This is comparable to MAGST variability due to distances of 1 km vertical (c.f. Gruber et al., 2004b).*

In a next step, melt-out day (MD) variability was quantified. Since GCT 4 consists mainly of ridges and other locations where an isolating snow cover could not be distinguished (e.g. Fig. 4.1, left plots), these footprints were excluded from the analysis. The linear model quantifying the influence of the topographic variables on MD of snow at the coarse scale is:

$$\begin{aligned} \mathrm{MD_k} =& 14 + 0.064 \cdot \mathrm{Elevation}_k \\ &+ 3 \cdot \cos(\mathrm{Aspect}_k) - \mathrm{Slope}_k \\ &+ 1.21 \cdot (\mathrm{Slope_k} : \cos(\mathrm{Aspect_k})) \\ &- 17 \cdot \mathrm{dYear}_{k,2011} - 10 \cdot \mathrm{dYear}_{k,2012} + \varepsilon_k \,, \end{aligned} \tag{4.2}$$

with an adjusted R^2 of 0.71. MD is delayed by approximately two months for an elevational distance of one kilometer. One and a half month difference is observed for

north-south differences at 30 degrees steep slopes, whereas in more shallow areas the MD only changes by two to three weeks. GCT 1 to 3 do not significantly influence MD. The inter-annual variability of MD is significant in the model, resulting in 17 days earlier melt-out in the year 2011 and 10 days in 2012, in comparison with the reference year 2010. The differences in the median MD are not as pronounced: it occurred at the 14th of June in 2010, the 2nd of June in 2011, and the 16th of June in 2012. In 2012, the spread of the MD is large, which explains the difference between the mean and the median. The beginning of an insulating snow cover was detected between the 17th and 19th of October for all three years. Since the average onset of the snow differs only by two days in the three years, the total snow duration is mainly determined by the melt-out day.

The model for the ripening date (RD) is:

$$\begin{aligned} \mathrm{RD_k} = &- 105 + 0.089 \cdot \mathrm{Elevation}_k - 7.17 \cdot \sin(\mathrm{Aspect}_k) \\ &+ 6.9 \cdot \cos(\mathrm{Aspect}_k) - 0.76 \cdot \mathrm{Slope}_k \\ &+ 0.99 \cdot (\mathrm{Slope_k} : \cos(\mathrm{Aspect_k})) \\ &- 9 \cdot \mathrm{dGCT}_{k,2} + 6 \cdot \mathrm{dGCT}_{k,3} \\ &- 19 \cdot \mathrm{dYear}_{k,2011} - 6 \cdot \mathrm{dYear}_{k,2012} + \varepsilon_k \end{aligned} \tag{4.3}$$

The adjusted R^2 is of the RD model is 0.69. Similar to the MD, the inter-annual variability in RD is significant. The start of snow melt in 2011 is almost three weeks earlier than in 2010, and one week earlier in 2012. As for MD, the footprints along GCT 4 were excluded from the analysis. In contrast, GCT 2 and 3 show significantly different RDs, being nine days earlier in fine grained ground and 6 days later in blocky surfaces compared to grass slopes. Higher elevations delay the beginning of the melting. East-west differences are attributed to more than two weeks, similar to north-south differences. However, the results of this analysis should be treated with care since the RD could only be detected at few locations (*Schmid et al.*, 2012).

The three variables MAGST, MD and RD are only moderately inter-correlated at the coarse scale (*Schmid et al.*, 2012). The measurements therefore provide a sound, complementary basis to validate spatially-distributed mountain permafrost model. The quantitative results of the Models 4.1, 4.2 and 4.3 agree well with the current understanding of the underlying processes. The presented dataset is the first that allows to quantify these effects based on a sufficient number of representative measurements at the coarse scale. The ten-fold replication of the measurements could further be used to quantify the confidence of the statistical parameters due to fine-scale environmental variability.

	MAGST [°C]			MD [Month-Day]			RD [Month-Day]		
Footprint	2010	2011	2012	2010	2011	2012	2010	2011	2012
AA	3.62	4.42	4.35	05-27	04-07	04-21	03-24		04-05
AB	2.76	2.62	2.12	06-26	06-03	06-23	04-25	04-11	05-01
AC	4.13	4.2	3.94	04-25	04-09	04-01	03-20	03-24	03-16
AD	-3.87	-3.52	-3.24	06-09	06-01	05-24			
AE	0.76	1.14	0.38	06-13	06-02	06-17	04-30	04-21	06-02
AF	-1.72	-0.99	-1.83	06-30	06-09	06-20	06-07	05-19	05-26
AG	1.55		2.73	03-30		03-01	03-22		05-01
AH	-0.71	-0.02	-0.57	06-27	06-06	06-18	06-06	04-27	05-30
AI	2.85	3.02	2.55	06-13	06-06	06-17		04-11	05-01
AJ	-1.86	-1.63	-1.16	04-25	04-07	05-12	06-06	04-08	05-26
AL1	0.71	1.07	0.59	07-04	06-21	06-23	06-08	05-08	05-26
AL2	1.42	1.33	1.58	07-14	07-07	07-01	06-10	05-11	05-31
AM	0.41	0.84	-0.17	06-28	06-25	06-23	05-25	05-10	05-13
AN	3.1	3.09	2.89	06-14	05-31	06-16			06-10
AO1	-1.53	-1.59	-1.37	06-05	05-07	05-19	06-05	05-20	05-13
AO2	1.18	1.01	0.69	05-28	04-21	05-27	05-24	04-02	05-19
AQ	-1.19	-0.66	-0.74	07-02	06-25	06-30	05-27	05-14	05-24
AR	2.76	2.6	2.05	06-14	06-01	06-14		04-18	04-30
AS	4.7	4.78	3.95	05-11	04-11	05-14			02-26
AT	3.4	3.38	2.9	06-14	05-22	06-22			03-16
AU	1.54	1.43	1.19	06-11	05-24	06-07	04-25	04-04	06-10
AV	3.52	3.81	3.33	06-14	05-24	06-15			03-05
AW	-2.08	-1.14	-2.03	07-30	07-02	07-28	06-07	05-15	05-26
AX	3.38	3.51	2.94	06-05	04-24	05-26	05-02	03-29	
AY	2.02	1.96	2.06	07-03	06-23	06-28	05-20	04-20	05-13
AZ	2.29	1.99	2.24	07-08	07-01	07-05			
BA	3.49	3.68	3.46	06-07	05-12	05-28			03-29
BB	2.97	2.97	2.3	06-12	05-21	06-12			04-29
BC	-1.26	-0.71	-1.72	07-20	07-17	06-27	06-04	05-19	06-08
BD	3.39	3.54	3.89	06-09	05-17	03-30	03-24	03-18	03-02
BE	3.86	4.22	4.24	04-28	04-08	05-16			
BF	2.32	2.26	2.38	06-30	06-16	06-25			04-10
BG	3.43	3.91	3.76	04-26	04-08	03-29	04-14	03-10	04-02
BH	1.31	1.3	1.09	06-29	06-07	06-20	05-30	04-23	06-03
BI	5.32	5.59		05-24	04-22				
BJ	1.34	1.69	1.71	07-02	06-25	06-16	04-25	03-31	03-30
BK	1.6	1.55	1.82	06-14	06-20	06-01	04-28	04-29	
BL	0.16	0.52	0.32	07-17	07-12	07-05	06-05	05-09	05-24
BM	-1.55	-1.14	-1.23	06-15	06-04	06-15	06-04	05-13	05-23

Table 4.1: *Derivatives of the iButton measurements around Corvatsch, Switzerland, for the three study years. MAGST is estimated as the mean of each year, starting at the 20 of August of each year. MD and RD are estimated based on algorithms developed by Schmid et al. (2012).*

4.1.3 Fine scale variability

Maximal MAGST differences of 2.5°C in 2010 and up to 3°C in 2012 were recorded at various footprints located on ridges, but also in relatively homogeneous terrain (see Publication I, Figure 4). The variability can be attributed to fine-scale variability of ground cover, ground moisture or local shading from large boulders (GCT 3) or from trees (e.g. footprint AS). The fine-scale variability increases with increasing GCT and is larger at steep slopes (*Gubler et al.*, 2011). The latter can be attributed to the greater variability of the snow conditions in steep slopes. Diverse footprints of GCT 1 and 2 show a maximal variability of 1°C possibly due to moisture and the high fine scale variability of the snow conditions. The intra-footprint variability does not change significantly in the three study years. The average standard deviation of MAGST is between 0.3 and 0.35°C, and the average range is approximately 1°C for the three years.

GCT 4 footprints were excluded from intra-footprint MD estimation. The average intra footprint variability in MD is slightly more than one week with a maximum of three to four weeks at single footprints (Fig. 4.4). The mean intra-footprint MD variability (expressed as the standard deviation) is a factor of 3 greater at south-exposed slopes than at north-exposed slopes. In addition to the turbulent heat fluxes and the longwave radiation, the direct radiation plays an important role determining snow melt at south-exposed slopes. The greater MD variability at south-exposed slopes indicate that fine-scale variability increases with number of influencing processes. Similarly as MD, RD variability ranges from few days to several weeks.

As has become clear, measurement uncertainty is large in regions of high environmental variability as encountered in mountains. Measurement variability is non-negligible even at small scales. Within the grid cell of a typical DEM of 10 m resolution, a quantity like MAGST, MD or RD may vary significantly. That variability adds to measurement uncertainty and may even account for the largest part of it (c.f. *Ramsey and Ellison*, 2007). These results clearly indicate the importance of replicated long-term measurements when used for decision making or model validation. The random measurement replication proved useful to quantify environmental variability. This is supported by the findings of *López-Moreno et al.* (2011) for snow height, showing that five replications were sufficient to determine snow height with an accuracy of 10% at the fine scale, and 8–10 replications reduced the measurement error due to spatial variability to less than 5%.

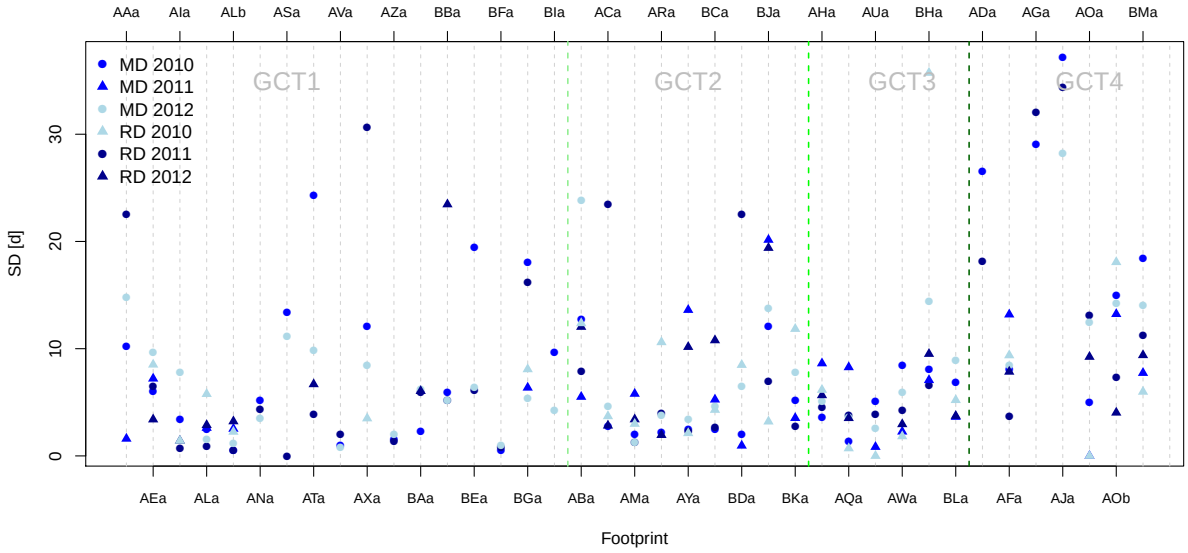

Figure 4.4: *Variability of MD and RD at the fine scale. The melt-out day varies up to three weeks within distances of less than 14 m. The average MD variance is one week. Similarly, the start of the melting period (RD) varies up to three weeks at individual footprints.*

4.2 Model evaluation in heterogeneous environments

The results presented here are based on the findings in Publications III (*Gubler et al.*, 2012) and IV (*Gubler et al.*, 2013).

4.2.1 Parameterized shortwave and longwave downward radiation

4.2.1.1 Calibration

A variety of clear-sky LDR parameterizations exist in the literature (e.g. *Ångström*, 1915, *Brunt*, 1932, *Swinbank*, 1963, *Brutsaert*, 1975, *Konzelmann et al.*, 1994, *Dilley and O'Brien*, 1997). In total, eleven parameterizations were studied and calibrated. The calibrated *Konzelmann et al.* (1994) parameterization is:

$$\epsilon_{cl} = 0.23 + 0.43(\frac{p_v}{T})^{0.175}. \tag{4.4}$$

The all-sky parameterization adapted from *Pirazzini et al.* (2000) resulted in:

$$LDR_{all} = (\epsilon_{cl}\tau_c^{3.77} + 0.968(1 - \tau_c^{2.97})) \cdot \sigma_{SB}T^4. \tag{4.5}$$

The calibrated parameter values for the other LDR parameterization can be found in Tables 4 (clear-sky) and 5 (all-sky) in Publication III. The most accurate results for the interpolation of cloud transmissivity during the night are obtained by averaging the four hours preceding sunset and the four hours after sunrise, and by linearly interpolating between the two averages.

The increased accuracy underlines the importance of calibrating to local conditions when applying parameterizations from the literature. After calibration, almost all parameterizations reproduce measurements equally well (Fig. 4.5). Hence, if measurements for calibration are available, the choice of the individual parameterization is insignificant. Otherwise, a parameterization developed or calibrated for similar atmospheric conditions should provide more accurate LDR estimates.

4.2.1.2 Validation

The *Iqbal* (1983) model fulfills the quality criteria by *Badescu et al.* (2012) for global SDR with $-5\% \leq MBD \leq 5\%$ and $RMSD \leq 15\%$, and for diffuse radiation with $-10\% \leq MBD \leq 10\%$ and $RMSD \leq 30\%$ if measurements of the atmospheric variables ozone, precipitable water and the Ångström parameters are available. If the parameters are set to fixed values, the errors in diffuse radiation rise considerably (Fig. 4.6).

Since diffuse SDR accounts only for a small part of global SDR, the modeled global SDR fulfills the *Badescu et al.* (2012) criteria also with fixed parameter values $\beta = 0.039$, $\alpha = 1.38$ and $o = 0.314$ mm and parameterized precipitable water (*Prata*, 1996). The adequate performance, simple implementation and the few required input data indicate that the *Iqbal* (1983, Model C) is suitable to be used in impact models. Errors in the LDR parameterizations are, after calibration, in the range found in other publications (e.g. *Konzelmann et al.*, 1994, *Wang and Liang*, 2009). As mentioned before, the most important step when using LDR parameterizations in impact models is calibration to local conditions.

4.2.1.3 Uncertainty and sensitivity

The SDR sensitivities were studied for a constant path length of two, the path length of the mean zenith angle of 60 degrees at Jungfraujoch. The most influencing parameter for clear-sky SDR is the atmospheric turbidity coefficient β (*Ångström*, 1929, 1930) resulting in changes of approximately 6 to -20% for direct, -30 to 80% for diffuse and 4 to -10% for global clear-sky SDR for $0 < \beta \leq 0.14$ (*Gubler et al.*, 2012, Figure 5). Estimated precipitable water (*Prata*, 1996) and the Ångström wavelength exponent α influence global clear-sky SDR by $\pm 4\%$. Ozone has only a minor impact on modeled

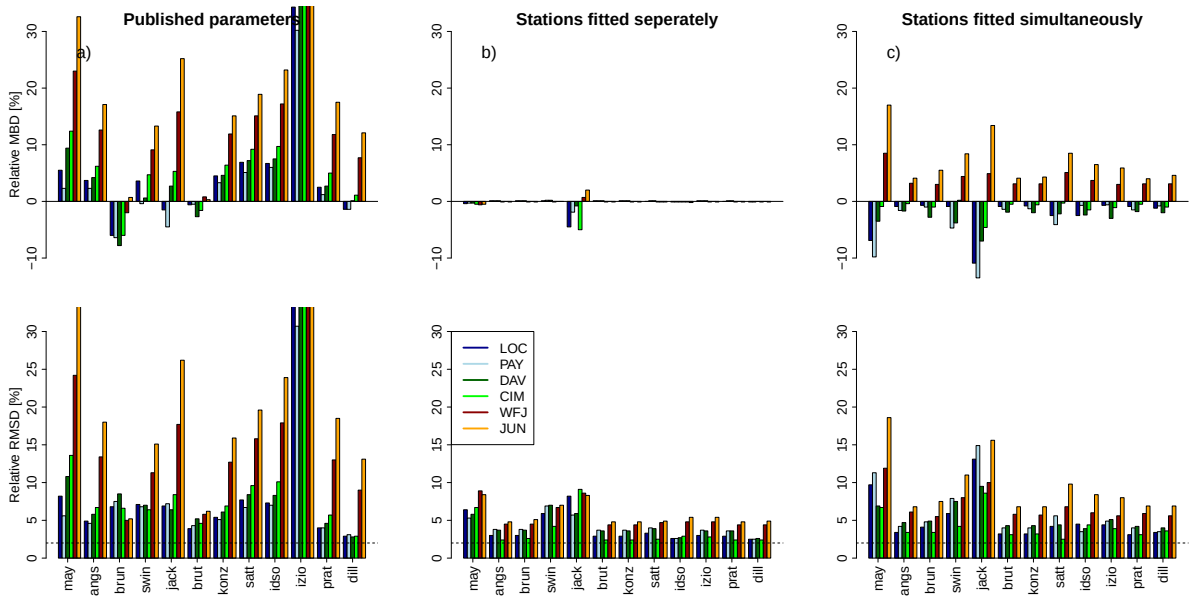

Figure 4.5: *Validation of the published (left) and the calibrated (middle and right) LDR parameterizations in Switzerland. Best performance is obtained by fitting the parameterization to each location separately (middle). To obtain one optimal parameter value for Switzerland, the parameterizations were fitted to all stations simultaneously (right). The errors of all parameterizations are reduced considerably, indicating the impact of calibration to local conditions.*

SDR. The diffuse radiation is sensitive to ground albedo. Since the diffuse radiation only accounts for a small part of global SDR, this sensitivity is not as pronounced in global radiation. An increase or decrease in modeled direct SDR due to a change in one of the atmospheric parameters goes along with a decrease or increase in modeled diffuse SDR. The sensitivity of global SDR is therefore smaller than one would expect from studying direct SDR alone (e.g. *Gueymard*, 2003b) since a higher value of the Ångström turbidity coefficient β results in a reduction of the direct SDR and an increase of diffuse SDR. Finally, the effect of the terms are compensated in the sum. The total output uncertainties of modeled clear-sky global SDR (*Iqbal*, 1983, Model C) is 3 to 6%. Clear-sky direct SDR uncertainty is approximately 10%, and the diffuse SDR has an uncertainty of 30%. The smaller uncertainty in global SDR results from compensating effects of direct and diffuse SDR.

All-sky LDR is mostly influenced by the amount of clouds in the sky (e.g. *Sicart et al.*, 2006), which was estimated using measured and modeled global SDR (Eq. 3.3). The uncertainty in modeled cloud transmissivity is 0.08 for $\tau_c \in [0, 1]$. If τ_c is close to one, the uncertainty produces differences of up to 10% in modeled all-sky LDR (*Gubler et al.*, 2012, Fig. 10). The sensitivity decreases for overcast situations. Measurement error of

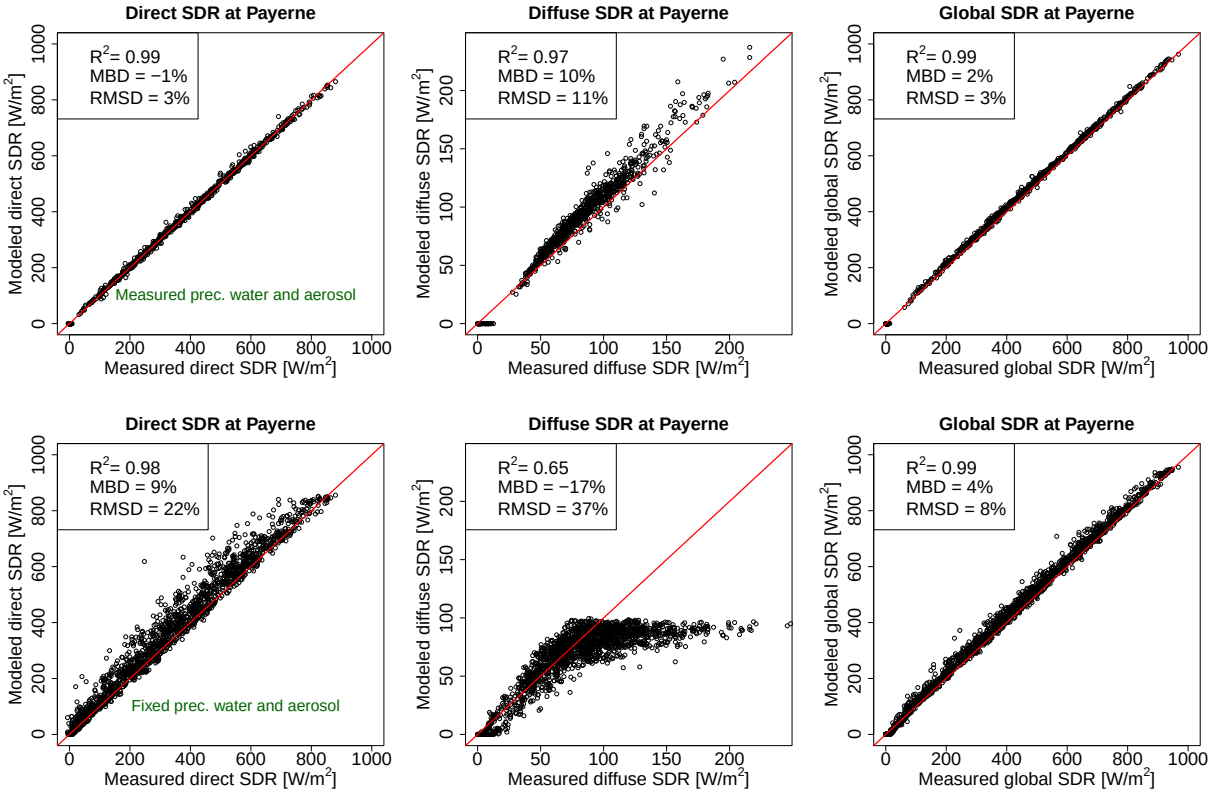

Figure 4.6: *Validation of clear-sky direct, diffuse and global SDR (Iqbal, 1983, Model C) at Payerne. The upper plots indicate the errors if measurements of the atmospheric variables ozone, precipitable water and the Ångström turbidity coefficients are available. If no such measurements are available (as is often the case), the errors in diffuse SDR increase considerably (lower figure, middle). Since diffuse accounts only for a small part of global SDR, the accuracy of global radiation is acceptable (e.g., Gueymard and Myers, 2008, Badescu et al., 2012).*

the relative humidity result in differences of up to 3%. The total LDR uncertainty is less than 6% for LDR greater than 100 $\mathrm{W/m^2}$ and 3% for LDR greater than 300 $\mathrm{W/m^2}$.

4.2.1.4 Implementation in GEOtop

The findings presented above were implemented in the model GEOtop. Clear-sky global SDR in GEOtop is simulated based on *Iqbal* (1983, Model C), and the calibrated *Konzelmann et al.* (1994) parameterization is implemented. This allows to determine the precision and the accuracy of the modeled downward radiative fluxes in GEOtop, and ensures that they are optimized for studies in Switzerland. The quantified uncertainties of the *Iqbal* (1983, Model C) and the *Konzelmann et al.* (1994) can be used directly when

studying the total output uncertainty of the model GEOtop, or any other model that incorporates these parameterizations.

4.2.2 GEOtop evaluation considering environmental variability

4.2.2.1 Preliminary analysis

A preliminary analysis based on the melt-out day (MD) of snow allowed to determine the most sensitive parameters for MD in GEOtop, namely the selection of the LDR parameterization, the snow correction factor c_{snow}, and the temperature and precipitation lapse rates (Γ_T and Γ_P). The findings of Publication III (Sect. 4.2.1) allow to reduce the sensitivity due to the selection of the LDR parameterization. The values of the three other parameters were optimized by performing a global sensitivity analysis validated with MD derived from the iButton measurements (Sect. 3.1) (*Schmid et al.*, 2012). Compensating effects of the parameters lead to several equally well behaving parameter sets, supporting the equifinality thesis (e.g., *Beven and Freer*, 2000). The two parameters c_{snow} and Γ_P both influence the amount of precipitation and thereby snow accumulation. Based on the iButton measurements, this effect cannot be separated from redistribution of snow to lower elevation sites by wind or avalanches. For the following analyses, the most physically based parameter, i.e. Γ_T, was set to its standard value of $6.5^{\circ}\mathrm{C\,km^{-1}}$, resulting in an optimal snow correction factor of 2 and a precipitation lapse rate of $0.2\ \mathrm{km^{-1}}$.

4.2.2.2 Sensitivities

The sensitivities differ considerably within the topographic setting (Fig. 4.7) and among the different ground types (Fig. 4.9). The temperature lapse rate Γ_T translates directly into MAGT. Uncertainties in Γ_T introduce great uncertainties at locations of large elevational distance to the meteorological station. The sensitivity to dry ground albedo increases with increasing amount of solar radiation received at a location, e.g., south exposed inclined slopes are more sensitive to the ground albedo than north facing slopes. Low elevation sites are more sensitive to ground albedo α_g since snow duration is shorter. The sensitivity to ground roughness, the height at which wind velocity is measured, and the dew temperature lapse rate increase for decreasing elevations, and thus underline increased importance of the turbulent fluxes in the energy balance for greater air temperatures (e.g. *Etchevers et al.*, 2004) and for less solar radiation.

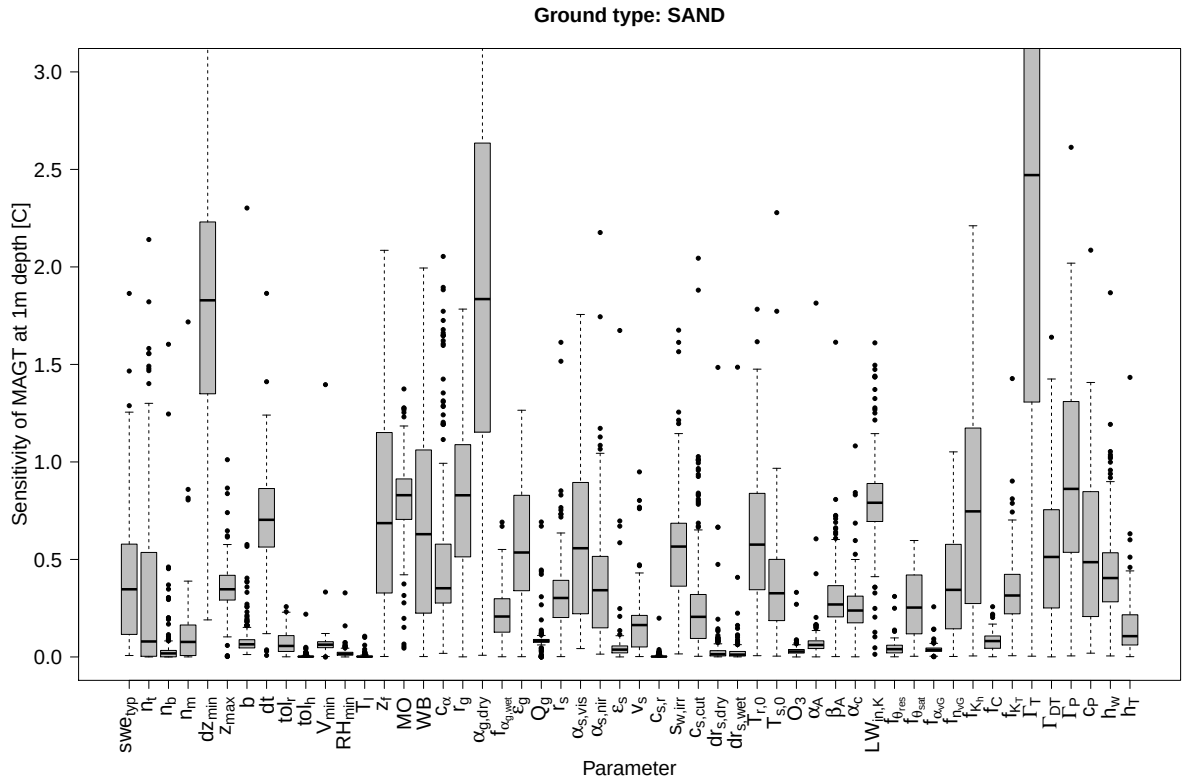

Figure 4.7: *Variability of model sensitivities at different locations within an synthetic mountain environment. The presented ground type is sand. The sensitivity to dry ground albedo $\alpha_{g,dry}$, for example, varies from zero to more than 3°C in the setting. In general, the sensitivities of important parameters vary considerably along the topographic variables.*

The error in MAGT due to the increasing thickness of the uppermost ground layer dz_{min} increases linearly for ground type sand, peat and gravel, while for clay, silt and rock, the increased sensitivity starts at $dz_{min} \geq 40$ mm. The median error to dz_{min} is relatively small up to 20 to 40 mm (Fig. 4.8, bottom right figure) under all environmental conditions studied here. The maximal error from dz_{min} is greatest for peat, gravel and rock (Fig. 4.9), resulting in changes of almost 4°C for rock. The maximal ground thickness z_{max} and the ground exponent b are insensitive for all ground types and topographic settings. The time step for which the numerical equations are solved results in maximal MAGT errors of 0.9 to 1.3°C. The minimal sensitivity to the time step is approximately 0.2°C. The sensitivity to the time step is negligible up to 15 minute time resolution and increases linearly with increasing time discretization (Fig. 4.8, top left figure). If computation time is no issue, the heat conduction and the Richard's equation should be solved at maximally half an hour resolution, whereas an hourly resolution leads to average

errors of 0.2°C. The sensitivity to dt increases linearly with increasing dt, with changes of 0.8°C for a resolution of four hours in average. The number of top layers in the snow module should be at least two, and the maximal snow water equivalent swe_{typ} of the top and bottom snow layers should not exceed 10 mm to ensure stable ground temperatures. Some individual locations react non-linearly to changes in the snow discretization parameters. However, we were not able to find the reason of the non-linear response for these individual points. All discretization parameters converge to stable solutions with average errors between 0.001 and 0.06 between the finest resolutions. The initial ground temperature is insensitive under all environmental conditions, which indicates that the ground initialization by S. Gruber is reliable.

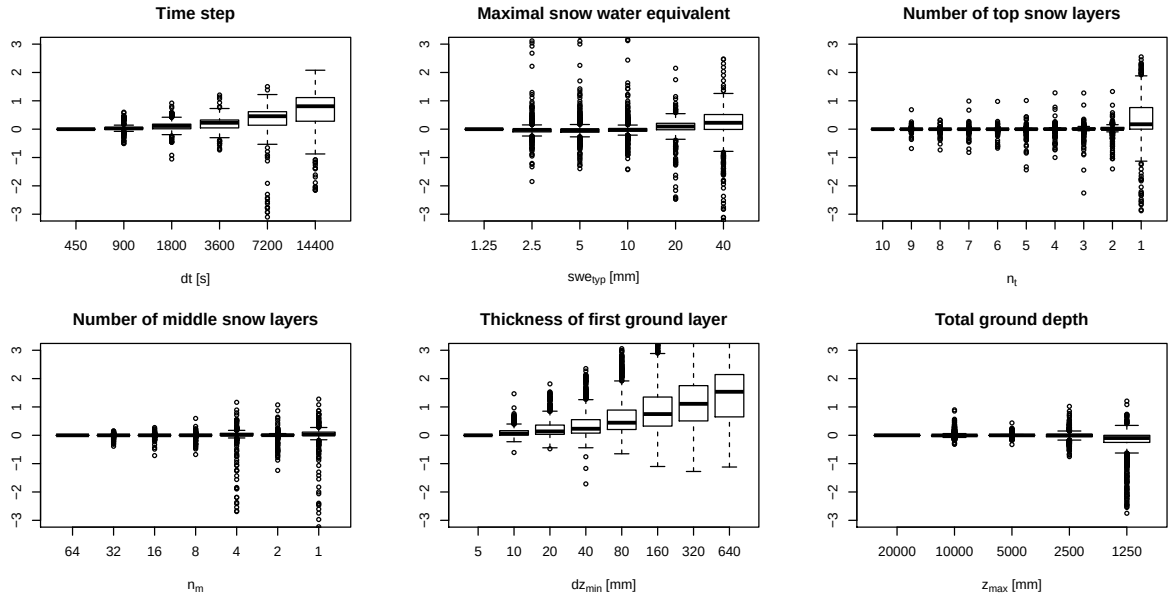

Figure 4.8: *MAGT (1 m) errors due to six discretization parameters: dt (top left), swe_{typ} (top middle), n_t (top right), n_m (bottom left), dz_{min} (bottom middle) and z_{max} (bottom right). The errors were normalized with MAGT modeled at the finest resolution of each parameter. The sensitivities are summarized as boxplots for all topographic properties and the six ground types.*

Changes in the dry ground albedo ($0.1 \leq \alpha_G \leq 0.4$) result in maximal differences of up to 2.5 to 4°C at inclined south exposed slopes. The sensitivity is increased for sandy ground, in gravel and for rock (Fig. 4.9). The albedo of fresh snow results in MAGT differences of more than 1°C, as well as the albedo extinction parameter c_α determining the linear interpolation between snow and ground albedo during snow melt. The sensitivity of the MAGT on the different ground and snow albedo values support the importance of the solar radiation in the energy balance at the Earth's surface. Calibra-

tion of the *Konzelmann et al.* (1994) LDR parameterization (*Gubler et al.*, 2012) results in GT differences of 0.5 to 1.2°C, which underlines the impact of calibration when using parameterizations in impact models. Other parameters influencing the turbulent fluxes have sensitivities of 0.5 to more than 1°C (e.g. the snow and ground roughness, the height of the station at which the wind velocity is measured, as well as the Monin Obhukov parameterization and the dew temperature lapse rate). The sensitivities of some parameters influencing the water content in the ground vary substantially for the different ground types (Fig. 4.9). For example, the depth above which all liquid water in the ground drains (ranging from few centimeters to ten meters in the modeling experiment) influences GTs by more than 2°C in gravel, whereas for rock the parameter is insensitive. The maximal sensitivity on the van Genuchten parameter n varies from 0.2 (rock) to more than 1°C (peat). The hydraulic conductivity is sensitive in sandy ground (1.8°C) and insensitive in rock (less than 0.2°C).

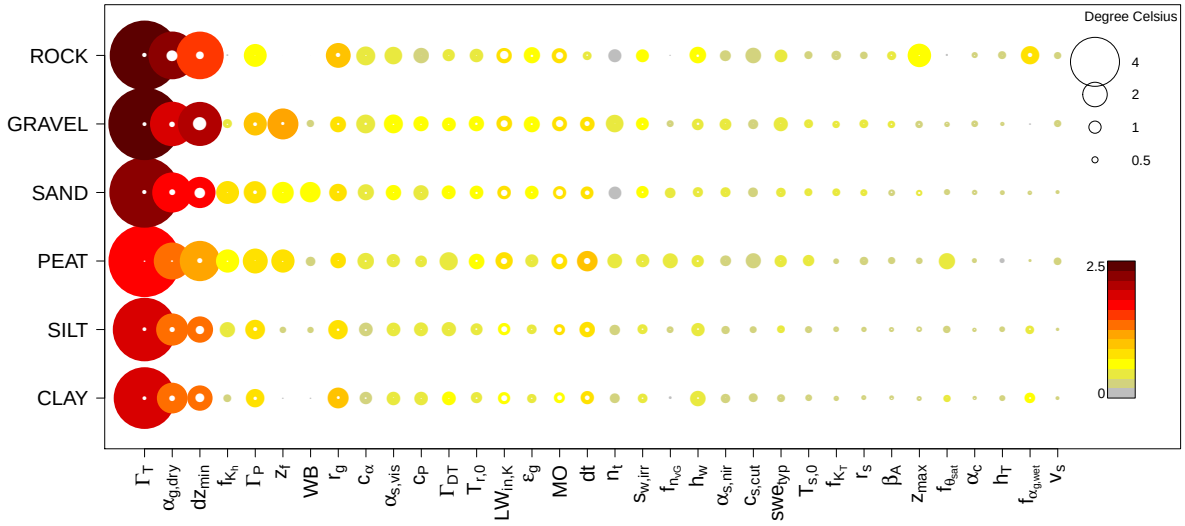

Figure 4.9: *Variability of model sensitivities for the different ground types. The 95%-percentile of the sensitivities along all topographic factors is depicted as the filled circles, the median sensitivity as the color of the circles, and the 5%-percentile is depicted as the white circle. Only the sensitive parameters, i.e., the parameters that influence MAGT by more than 0.5°C, are represented.*

It was shown that the sensitivity on individual parameters varies considerably at different topographic locations and for different ground types in the model GEOtop. The setting allowed to determine the differing influence of individual processes on GTs, and

to analyze the behavior of GEOtop more deeply. GEOtop behavior could be compared with our understanding of system functioning under differing environmental conditions. In conclusion, model evaluation performed at single points does not represent all the important model features. Model sensitivities estimated at a location cannot be simply extrapolated to other locations. These results suggest that the evaluation of spatially-distributed environmental models requires representative test environments as well as distributed validation data.

4.2.2.3 Uncertainties

Two arguments support the parameter selection for the uncertainty analysis: quantification of uncertainty is a) restricted to physical parameters and b) include only parameters that influence ground temperature for more than 0.5°C at least for one ground type (Fig. 4.9). All other parameters are kept fixed at their baseline value. The remaining parameters are sampled randomly according to their prior distribution (Table 3.3).

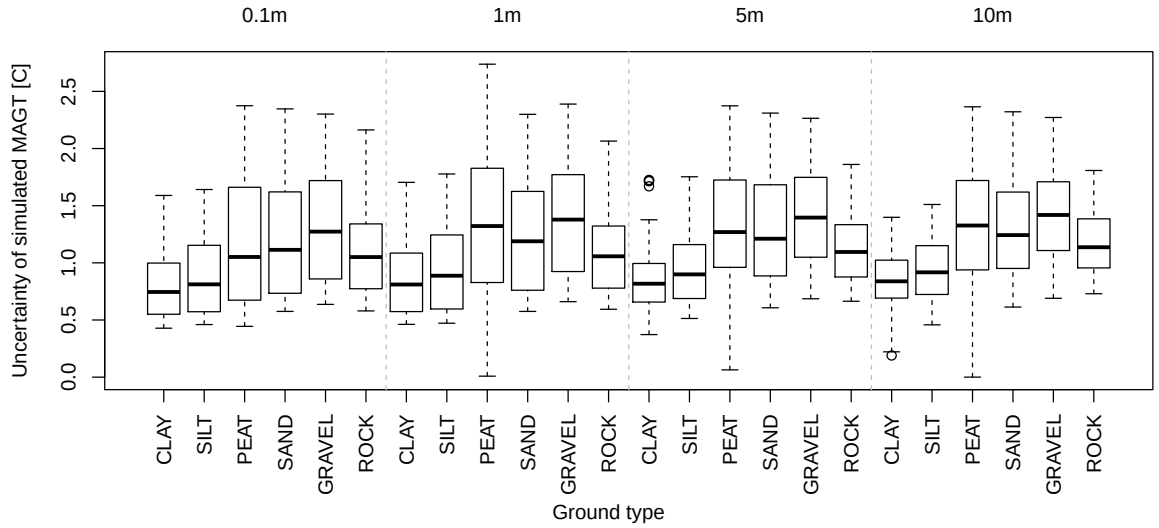

Figure 4.10: *Boxplots of parametric model uncertainty summarized for all topographic locations. The parametric model uncertainty is expressed as the length of the 95% uncertainty interval. The individual boxplots represent the different ground types and the depth in the ground column.*

MAGT uncertainty expressed as the length of the 95% uncertainty interval goes from 0.4 to 1.5°C for clay and silt, and is increased up to 2.4°C for ground types rock, sand, peat, and gravel (Fig. 4.10). The increased uncertainties in sand, peat, and gravel are

due to the sensitivity of these soil types to their hydraulic properties like the porosity of the soil or the hydraulic conductivity. The parametric model uncertainty decreases for increasing elevation for all ground types, which can be attributed to the increased sensitivity to parameters influencing the energy balance at low elevation sites, i.e. the sensitivity to ground albedo or roughness. The median uncertainty is 0.7°C for ground types which are only marginally influenced by the uncertainties in the hydraulic properties. The median uncertainty is 1°C for sand, rock, and peat, and 1.2°C for gravel. Model uncertainties are approximately constant in the ground profile.

Model uncertainty at the surface is comparable to the variability of ground surface temperatures measured within 10 m×10 m cells, ranging from approximately 0.25 at homogeneous grass sites to 2.5°C in block fields, expressed as the total range (*Gubler et al.*, 2011). One can observe that the fine-scale environmental variability is similar to the parametric uncertainty quantified for MAGT modeled at 10 cm depth. Ground temperatures at greater depths integrate over larger surface areas (*Gold and Lachenbruch*, 1973), and are hence expected to be less variable than at the surface. However, integration over large areas is not represented by GEOtop since the heat conduction is solved in one dimension.

In summary, the uncertainties of MAGT modeled at 10 cm depth are comparable to the variability encountered in nature. In a next step of the model evaluation process, GEOtop should be calibrated with spatially-distributed measurements, such as the iButton measurements presented in Sect. 4.1, and validated with independent measurements. Systematic calibration and validation of GEOtop should be a follow-up step for future research.

5
Discussion of results

This chapter summarizes the research that was conducted to investigate the combined effectiveness of measurements and models in quantifying transient and spatially heterogeneous environmental phenomena in mountain regions. Key contributions made to the field of permafrost research, such as the design of a measurement campaign providing data suitable to study measurement variability at the coarse and the fine scale, as well as the set-up of systematic modeling experiments, are discussed. The insights gained are shared, and discussed in relation to previous research. The high environmental variability encountered in Alpine regions calls for spatially-distributed measurements to quantify measurement variability and to provide a sound basis for mountain permafrost model validation. In hydrological research, where model evaluation has a long tradition, recent publications underline the importance of considering measurement representativeness and informativeness when data is used as model drivers or for validation. The importance of the design of appropriate measurement campaigns is also emphasized (*Gupta et al.*, 2008). This discussion aims to convince the reader of the potential of combining knowledge gained from measurements, models, and model uncertainties to modify the design and increase the value of future measurement campaigns in mountain permafrost research.

5.1 Contributions

The following contributions are provided in this thesis.

Random measurement distribution at the fine scale. Every footprint consists of a 10 m×10 m square representing the resolution of a DEM typically used in Alpine permafrost research. A set of ten numbers sampled from the discrete uniform distribution $\mathcal{U}(1, 100)$ was assigned to each footprint. To avoid biased logger placement, ten iButtons were placed according to the random samples within the one hundred square meters. This setting allows to quantify the stochastic variability of the measured quantities within each 10 m×10 m square. The mean value attributed to its confidence level can be determined for each footprint. These results should be used in model validation to quantify both the mean and the spread of the measured and modeled outputs at the respective scale.

Spatially-distributed measurements at the coarse scale. Empirical coarse scale permafrost modeling requires appropriate sampling design (*Brenning et al.*, 2005). We designed a campaign measuring permafrost relevant variables at 39 footprints covering the topographic variables elevation, slope, aspect, as well as different ground cover types and landforms, such as ridges and depressions. An elevational transect from 2100 to 3300 m consisting of footprints of similar aspect and slope, together with an elevational band in which different aspects, slopes and ground cover types are represented, allowed quantification of the influence of the topographic factors on the measured quantities at the coarse scale. The sample size, as well as the representativeness of the samples, is sufficient for statistical quantification of influencing processes.

Permafrost variables derived from ground surface temperatures (GST). GST is an important quantity in permafrost research since it determines the thermal state of the ground. If sampled at a sufficient resolution, the GST measurements allow quantifying different permafrost relevant variables such as the mean annual ground surface temperature (MAGST), the melt-out day of snow (MD), and the ripening date of the snow (RD). Within this work, an algorithm was developed to determine the presence of an insulating snow cover from GST measurements. The algorithm was tested based on synthetic data and proved reliable. The quantities MAGST, MD, and RD show little inter-correlation at the coarse scale and are therefore suitable measures to validate distributed mountain permafrost models.

Model development. The short- and longwave downward radiation (SDR and LDR)

are important inputs in any cryosphere model since they determine the radiation balance at the Earth's surface. Different SDR and LDR parameterizations were validated and calibrated to high quality measurements in Switzerland. The results implemented in the physically-based model GEOtop ensure better performance (higher precision and accuracy) of the modeled downward radiative fluxes. Validation was performed at six locations covering elevations from 200 to 3300 m meters, thereby ensuring the quality of the parameterization for the whole range of elevations encountered in Switzerland. Cloud cover is estimated based on global SDR and can therefore only be determined during daytime. Different cloud cover interpolation techniques during the night were evaluated.

However, there are many other processes that are important when modeling mountain permafrost or snow that were not studied independently in this thesis. Snow or ground roughness strongly influence the turbulent fluxes and ground albedo determines the amount of solar radiation reflected back to the sky. Mountain permafrost, and in general cryosphere, models would greatly benefit from validating these and other processes individually. Further, spatially-distributed measurement of the down- and upward radiative fluxes at the scale of a mountain would allow parameterization of the topographic influence on the individual components of the energy balance.

Quantification of input uncertainties. Model output uncertainty depends considerably on the assumptions made about the uncertainty of input variables and model parameters. Uncertainties of measured variables can be obtained from the manufacturer. Here, we quantified the uncertainty of parameterized downward clear-sky SDR and all-sky LDR based on uncertainties in atmospheric parameters and cloud transmissivity. The results can be used when determining the total output uncertainty of an environmental model that simulates the energy balance at the Earth's surface.

Systematic analysis of model sensitivities and uncertainties. The high environmental variability encountered in mountain regions requires a special design for model evaluation. The analysis of model sensitivities and uncertainties can be performed independently from ground truth measurements. Sensitivity and uncertainty analyses were performed covering elevations from 500 to 4000 m, all aspects in steps of 45 degrees, and different slopes. The six ground cover types clay, silt, sand, peat, gravel, and rock characterized by their hydraulic properties were analyzed. The analyses were performed for each combination of topographic factors and ground types, resulting in a total of 1200 simulation points. This allowed us to analyze the variability of model sensitivity and uncertainty in mountain regions, and to determine the relevance of individual processes under different environmental conditions.

Systematic model validation. At the coarse scale, the GST measurements are representative, and cover different topographic attributes and ground types that typically influence mountain permafrost distribution. The dataset is sufficient to systematically study the main features and errors of mountain permafrost models. The random replication at the fine scale ensures measurement quality by providing a degree of uncertainty attributed to the measurements. As a conclusion, the dataset gathered to evaluate the physically-based mountain permafrost model GEOtop fulfills the requirements by *Gupta et al.* (2008) for representative, informative, and high quality measurements of sufficient sampling size. A detailed validation of GST modeled by GEOtop could be a follow-up step for further research.

5.2 Insights

Fine-scale measurement variability. In general, it is known that measurement uncertainty is highly influenced by environmental variability (*Ramsey and Ellison*, 2007). The processes influencing snow accumulation and ablation vary at the plot scale in both Arctic and Alpine regions (e.g., *Weir*, 1979, *Pomeroy et al.*, 2004, *Essery and Pomeroy*, 2004a,b, *Clark et al.*, 2011), related to wind redistribution and terrain curvature (*Trujillo et al.*, 2007, *Grünewald et al.*, 2010, *López-Moreno et al.*, 2011), variability in precipitation recently measured at 100 m resolution using Light Detection And Ranging (LIDAR) methods (*Scipion et al.*, 2012), as well as the variability of the energy fluxes (*Essery and Etchevers*, 2004), for example due to local shading of solar radiation (e.g., *Corripio*, 2002). In this study, we observed average melt-out day (MD) differences of one week with individual footprints showing MD differences of more than three weeks at the fine scale. Snow duration, as well as properties like ground moisture or local shading, influence ground surface temperatures, and results in a variability of up to 2.5 to 3°C in MAGST within the 10 m×10 m squares. However, the large variability at the surface is integrated at greater depths (*Gold and Lachenbruch*, 1973), and hence the variability is certainly smaller deeper below the surface. Similar to MD, the ripening date of snow (RD) is highly variable at the fine scale. The results presented here allow quantification of the uncertainty of measurements at different locations at the fine scale. This uncertainty should be accounted for if measurements are used for decision making or model validation. In particular, these observations should be used when validating the model GEOtop.

Coarse-scale measurement variability. The representativeness of a measurement should be ensured if used to validate spatially-distributed models, because otherwise poor modeling results may be obtained at locations not used in the calibration procedure (e.g.

Refsgaard, 1997). A literature review shows that many GST or BTS measurements have been sampled worldwide (*Haeberli*, 1973, *Ishikiwa and Hirakawa*, 2000, *Heggem et al.*, 2006, *Etzelmüller et al.*, 2007, *Isaksen et al.*, 2002, *Gruber and Hoelzle*, 2001). Sampling strategies often include either elevational gradients (e.g. *Ødegård et al.*, 1992, *Farbrot et al.*, 2011), different ground or vegetation covers (e.g. *Hoelzle et al.*, 2003, *Etzelmüller et al.*, 2006, *Heggem et al.*, 2006) or topographic variables (*Gruber et al.*, 2003, in rock faces). The GST dataset presented in this thesis consisting of 39 locations covering the topographic variability and different ground cover types at the coarse scale is novel, and contributes to the general demand by *Gupta et al.* (2008) for representative measurements for model validation.

High variability of ground temperature has been observed earlier at the coarse scale (*Hoelzle et al.*, 2003, *Ødegård et al.*, 2008, *Isaksen et al.*, 2011, *Schneider et al.*, 2012) and was attributed to snow distribution and surface characteristics (*Gruber et al.*, 2004a, *Hanson and Hoelzle*, 2005). Similarly, the MD and RD variability was reported to be large (*Hoelzle et al.*, 2003), as well as processes influencing snow accumulation influenced by the variability in the precipitation patterns (*Scipion et al.*, 2012), and snow redistribution. Based on the dataset presented in this thesis, the influence of elevation, slope, aspect and ground cover type could be quantified statistically, which supports findings from previous research concerning lapse rates ($-5°\mathrm{C\,km^{-1}}$), north-south differences ($-4°\mathrm{C}$ for 40 degree steep slopes, and $1°\mathrm{C}$ at shallow slopes) and influence of ground cover (thermal offset of -2°C in block fields) on GTs (*Powell et al.*, 1988, *Šafanda*, 1999, *Rolland*, 2002, *Gruber et al.*, 2004b, *Gruber and Hoelzle*, 2008, *Nötzli and Gruber*, 2009). The difference in MD is approximately 1.5 month for 30 degree steep north respectively south exposed slopes, and two months per 1000 m elevational distance. Similarly, the beginning of the melt phase (RD) is highly variable at the coarse scale. The influence of the explanatory variables on RD (Eq. 4.3) should however be treated with care, since RD could be determined at selected locations only (*Schmid et al.*, 2012).

Inter-annual measurement variability. Within different years, MAGST can vary by several degrees Celsius. A warm summer as observed in 2003 for example raised MAGST by almost $2°\mathrm{C}$ (*PERMOS*, 2010). The average inter-annual variability observed around Corvatsch is $0.15°\mathrm{C}$, whereas the inter-annual variability at individual footprints goes up to $1°\mathrm{C}$. The GST variability is attributed to differing snow conditions (e.g. *Hoelzle et al.*, 2003). MD differs by approximately three weeks between 2010 and 2011, and slightly less between 2010 and 2012. Other factors like the day of the first snow fall and snow thickness influence the inter-annual variability of MAGST (e.g. *Hoelzle et al.*, 2003, *Brenning et al.*, 2005). The date of the first snow fall did not vary significantly in the three study years. The time series is not long enough to quantify the influence of snow duration on MAGST.

Validation of the parameterized downward radiative fluxes. In accordance with *Badescu et al.* (2012), we found that the *Iqbal* (1983, Model C) is suitable to model global SDR. It fulfills the quality criteria by *Badescu et al.* (2012) with a MBD of less than 5% and RMSE at most 12% for the measurements in Switzerland. If measurements of the atmospheric variables turbidity and precipitable water are not available, models such as ASHRAE2005 or King should be applied to simulate diffuse SDR (*Badescu et al.*, 2012). The MBD of the clear-sky and all-sky LDR parameterization is less than $\pm$10%, and the RMSD is smaller than 15%. The errors for LDR lie in the range of other studies (e.g., *Konzelmann et al.*, 1994, *Pirazzini et al.*, 2000, *Etchevers et al.*, 2004, *Wang and Liang*, 2009, *Flerchinger et al.*, 2009). These results indicate that the parameterizations are suitable to be used in impact modeling studies in Switzerland. The parameters of the calibrated LDR parameterizations are published in Publication III and can be used by other modelers. During night time, the linear interpolation of the cloud transmissivity gave best results if taking an average of the four hours preceding, and the four hours following the night for interpolation.

Uncertainties and sensitivities of parameterized clear-sky shortwave (SDR) and all-sky longwave downward radiation (LDR). Clear-sky direct SDR is most sensitive to aerosols and precipitable water (e.g. *Gueymard*, 2003b, *Schillings*, 2004). The insights on the uncertainty and sensitivity gained from studying direct SDR (as often done in the literature (e.g. *Gueymard*, 2003b, *Schillings*, 2004)) cannot be extrapolated to global SDR. The total uncertainty in modeled global SDR for example is 3–6%, much less than the uncertainty of the direct SDR (10 to 20%). This difference can be attributed to the opposite effect of the atmospheric parameters on direct and diffuse radiation that eliminate in the sum. The most sensitive parameter for the diffuse radiation is the ground albedo α_g resulting in changes of more than $\pm 20\%$. Global SDR is not sensitive to the ground albedo since the diffuse accounts only for approximately one tenth of the global SDR.

All-sky LDR is primarily determined by the clouds in the sky (e.g. *Sicart et al.*, 2006). We found that the sensitivity on cloud cover is greater if the sky is almost cloud-free (roughly 10%). In overcast situations, the same uncertainty plays only a minor role of approximately 1 to 2%. Accurate estimation of cloud coverage is hence more important for almost clear-sky days. The total uncertainty in modeled all-sky LDR is roughly 3 to 6%.

GEOtop sensitivities and uncertainties. The amount of net shortwave radiation influences GTs considerably during daytime. It is influenced by ground and snow albedo, which constitute the most sensitive physical parameters in GEOtop. The importance of ground albedo was detected in other permafrost modeling studies (e.g., *Hoelzle*, 1996, *Ling and Zhang*, 2004, *Gruber*, 2005) and within the SnowMIP project for snow albedo (*Etchevers et al.*, 2004). Calibration of the longwave parameterization resulted in simi-

lar GT changes, such as the fresh snow albedo, and the ground emissivity (1°C). High wind speeds and high temperatures increase the influence of the turbulent fluxes on the energy balance of the snow (*Etchevers et al.*, 2004, *Essery and Etchevers*, 2004). Parameters determining the turbulent fluxes at the Earth-atmosphere or snow-atmosphere interface, such as roughness length or wind are important, resulting in GT differences of approximately 1°C. These sensitivities are increased at low elevation sites, illustrating the influence of higher air temperatures on the turbulent fluxes (e.g. *Etchevers et al.*, 2004). Physically-based models that consider the energy balance only indirectly use n-factors (e.g. *Anisimov and Nelson*, 1996, *Smith and Riseborough*, 2002, *Juliussen and Humlum*, 2007, *Etzelmüller et al.*, 2011, *Hipp et al.*, 2012) and therefore contain a potential source of uncertainty that should be handled appropriately.

Great variability of the sensitivity was observed for some of the parameters determining the hydraulic properties of the ground. While rock is quite insensitive to changes in the hydraulic properties, modeled GTs in gravel react quite sensitively to changes in the van Genuchten parameter n_{vG}, the hydraulic conductivity, or the depth at which water drains laterally. The variability of the parameter sensitivity for the ground types and within the topographic setting is large, which may be a reason for the different ranking of sensitivities found in the literature (e.g., *Jhorar et al.*, 2002, *Mertens et al.*, 2005, *Pollaco and Mohanty*, 2012).

We found that the time step for which the numerical equations of a physically-based mountain permafrost model are solved should not exceed one hour. The thickness of the first ground layer of 20 mm results in errors of 0.1°C and the errors increase linearly with increasing ground layer thickness. These findings agree with the findings by *Romanovsky et al.* (1997) performed on different physical permafrost models.

Systematic model evaluation. We have provided a first framework of a systematic model evaluation covering different environmental aspects of the modeling domain in mountain permafrost research. We have shown that model features such as sensitivities and uncertainties can vary considerably within the selected modeling domain, and that individual parameter sensitivities cannot be detected by analyzing a model at a single location only. Even though systematic model analysis calls for high computational effort, we think that it is indispensable for model development, especially to use models operationally. The approach presented in this thesis has the potential to detect model deficiencies more systematically and to give greater confidence in model outputs within the whole application domain. Additionally, we have presented a dataset that fulfills the requirements by *Gupta et al.* (2008) for representative, informative, and high quality data that can be used for mountain permafrost model validation.

Individual parameters such as the ground albedo are very important when modeling mountain permafrost (e.g. *Hoelzle*, 1996, *Gruber*, 2005) at all topographic locations and

ground types. Hence, spatially-distributed albedo measurements could improve the reliability of spatially-distributed mountain permafrost models, but are nowadays not available at the required resolution (e.g., 10 to 25 m), since the scale of measurements obtained from remote sensing methods (e.g. MODIS (`http://modis.gsfc.nasa.gov/`)) is too coarse for the fine scale. The sensitivity of other parameters like the hydraulic properties of ground depends highly on the ground type. In that case, determining the ground properties more accurately is only important in sand, gravel, or peat lands, whereas the water balance in rock can be neglected. The systematic design presented allows us to quantify the value of an accurate model parameter. Locations and times when the model is most uncertain can be determined to inform about potential locations to gather model validation data.

6
Conclusions and outlook

The variability of mean annual ground surface temperature (MAGST) measurements taken within a typical grid cell of a digital elevation model is considerable, ranging up to 3°C within 10 m×10 m. We conclude that this fine scale variability should not be neglected when measurements are used for model validation or for decision making. At the coarse scale, the variability of MAGST is determined by topography and ground cover type. Model evaluation measures such as model sensitivities or uncertainties vary strongly under different environmental conditions. To make general statements about the model behavior, the evaluation should represent the main environmental features influencing the modeled outputs. This underlines the importance of spatially-distributed measurements sampled at appropriate scales to validate models.

In summary, environmental variability plays a vital role in determining both the variability of measured quantities, as well as model outputs and evaluation measures. To provide more detail, the objectives defined in the introduction of this thesis are briefly revisited.

6.1 Revisiting the objectives

1. Design a measurement campaign providing data that:

   (a) allows quantification of measurement variability in mountain regions, and

   (b) provides a basis for systematic mountain permafrost model validation.

   A field campaign with 390 tiny loggers was conducted to measure GST spatially-distributed around Corvatsch mountain. The iButtons were distributed at 39 footprints. Measurement replication allowed quantification of the stochastic variability of the three derived mean annual ground surface temperature (MAGST), the melt-out day of snow (MD), and the ripening date of the snow (RD) at the fine scale (Obj. 1a). The three variables are suitable to validate spatially-distributed mountain permafrost models since they determine the thermal state of the subsurface and are relatively simple to obtain. The measurement design developed in this thesis forms a basis for systematic model validation by representing the main topographic and environmental attributes determining permafrost distribution in mountain regions (Obj. 1b).

2. Validate parameterized meteorological input data and quantify the uncertainties of the parameterizations.

   In contrast to variables such as air temperature, relative humidity, or global shortwave radiation, measurements of the downward longwave radiation (LDR) are scarce. LDR is a relevant meteorological input in mountain permafrost models determining an important input in the the energy balance at the Earth's and snow surface. It has a major influence at night time when no radiation from the sun is received. LDR is often parameterized, and, in contrast to the other meteorological variables, its uncertainty can only be determined based on modeling experiments. To ensure appropriate model behavior, all parameterizations were validated and calibrated to measurements from six locations in Switzerland covering different elevations. The uncertainty of parameterized all-sky LDR is quantified by propagating the uncertainties in modeled SDR through estimated cloud transmissivity.

3. Evaluate a physically-based permafrost model and quantify the influence of environmental variability on model evaluation.

   GEOtop, originally a hydrological model, incorporates many environmental processes relevant for mountain permafrost and is flexible to model ground temperatures for differing environmental conditions. A lack of validation, however, impedes operational use of GEOtop to provide scenarios of future, past or current

environments. In this thesis, the uncertainties and the sensitivities of the model GEOtop are quantified. A framework for systematic model evaluation was developed. It provides a basis to study model behavior within the whole application domain, and allows us to compare model outputs at diverse locations to our expectations about system functioning. The systematic model evaluation provides a sound basis to study the interactions and feedback between different processes.

4. Optimize the efficiency and the effectiveness of jointly used measurements and models.

   The observational system model (*Gupta et al.*, 2008) guides the design of measurement campaigns performed to drive and validate models. It is based on the conceptual and perceptual understanding of system functioning. The insights gained from these studies on measurement variability and model uncertainty can be used to reflect the current observational system model by determining the importance of parameters as well as quantifying where and when our knowledge described in mathematical formulae is most uncertain.

6.2 Outlook

We presented a study directing at the importance of evaluating mountain permafrost models covering the range of environmental variability. This certainly also holds when modeling other environmental phenomena such as snow cover or ground moisture. In general, we suggest evaluation of models along all environmental variables such as topography, land surface and subsurface characteristics, and vegetation that influence the model outputs. Mountain permafrost is a phenomenon that is highly variable and that reacts sensitively to environmental changes. The main outlook of this thesis is to enhance consistent evaluation of mountain permafrost models within the research community to increase the general use of models and to support comparability of model results. Further, the four following problems could be addressed in future research.

GEOtop calibration and validation. Before ground temperatures modeled with GEOtop can be used for decision making or to study permafrost related processes such as creeping of rock glaciers, the model should be calibrated and validated. These spatially-distributed ground surface temperature measurements gathered around Corvatsch could be used for calibration and validation under different environmental conditions.

Measurement campaign. Based on the model evaluation study, a strategy for an improved measurement campaign should be discussed. That includes collection of validation data where the model is most uncertain and measurements of variables that

considerably influence modeled GTs such as moisture or snow. Based on the GST measurements, processes influencing snow melt such as total precipitation and melting could not be separated. To analyze complex phenomena like mountain permafrost, the reliability of individual processes should be determined independently, if possible. Spatially-distributed high-resolution snow height measurements would be useful to differentiate between melting processes, snow accumulation and densification processes, as well as spatially-distributed measurements of the radiative fluxes. Separation of processes such as snow modeling would allow us to compare the snow module in GEOtop and its sensitivities to the results of the SnowMIP project (*Etchevers et al.*, 2002, 2004), for example. Further, sampling of spatially-distributed measurements such as the ground albedo would improve physically-based permafrost models.

Spatial uncertainty model. High resolution modeling of large areas like the Alps is still restricted by computational resources. Many methods to distribute model outputs spatially (such as TopoSub (*Fiddes and Gruber*, 2012)) have been developed in recent years. The quantification of model uncertainties even at few points is computationally intense. The development of similar tools to spatially interpolate uncertainties would have the potential to support the applicability of models by providing outputs in addition with uncertainty ranges for the whole modeling domain. Instead of the systematic approach as presented in this thesis, a random selection of the locations and conditions at which the model is run might be preferred.

Model inter-comparison. In this study, the sensitivities and uncertainties of a physically-based mountain permafrost model were quantified. A next step would be to compare the outputs of these uncertainties, as well as the validation results to other mountain permafrost models to determine the usefulness of individual models and rank their ability to reproduce permafrost conditions in relation to their complexity. Only the joint use of different models and model evaluation outputs can thoroughly improve knowledge and provide tools to simulate permafrost reasonably well.

References

AIAA (1998), *Guide for the verification and validation of computational fluid dynamics simulations*, American Institute of Aeronautics and Astronautics.

Akaike, H. (1973), A new look at the statistical model identification, *IEEE Trans. Autom. Control*, *19*, 716.723.

Allard, A., and N. Fischer (2009), *Sensitivity analysis in metrology: study and comparison on different indices for measurement uncertainty*, chap. 1, pp. 1–6, World Scientific Publishing Company.

Allen, J. (2009), *D2.7 User guide and report outlining validation methodology*, Deliverable in project Marine Ecosystem Evolution in a Changing Environment (MEECE).

Anderson, J. L. (2001), An ensemble adjustment Kalman filter for data assimilation, *Monthly Weather Review*, *129*, 2884–2903.

Anderson, M. G., and P. D. Bates (Eds.) (2001), *Model validation: perspectives in hydrological science*, Wiley.

Ångström, A. (1915), *A study of the radiation of the atmosphere*, vol. 65, 1-159 pp., Smithsonian Miscellaneous Collection.

Ångström, A. (1929), On the atmospheric transmission of sun radiation and on dust in the air, *Geografiska Annaler*, *11*, 156–166.

Ångström, A. (1930), On the atmospheric transmission of sun radiation., *Geografiska Annaler*, *12*, 130–159.

Anisimov, O. A., and F. E. Nelson (1996), Permafrost distribution in the northern hemisphere under scenarios of climatic change, *Global and Planetary Change*, *14*, 59–72.

Arenson, L. U., M. Hoelzle, and S. M. Springman (2002), Borehole deformation measurements and internal structure of some rock glaciers in Switzerland, *Permafrost and Periglacial Processes*, *13*, 117–135.

Badescu, V., C. Gueymard, S. Cheval, C. Oprea, M. Baciu, A. Dumitrescu, F. Iacobescu, I. Milos, and C. Rada (2012), Computing global and diffuse solar hourly irradiation on clear sky. Review and testing of 54 models, *Renewable and Sustainable Energy Reviews*,

16, 1636–1656.

Barsch, D. (1971), Rockglacier and ice-core moraines, *Geografiska Annaler*, *53*, 203–206.

Bartelt, P., and M. Lehning (2002), A physical SNOWPACK model for the Swiss avalanche warning: Part I: numerical model, *Cold Regions Science and Technology*, *35*, 123–145.

Bates, D. M., and J. M. Chambers (1992), *Nonlinear models*, chap. 10, Wadsworth and Brooks/Cole.

Bates, D. M., and D. G. Watts (1988), *Nonlinear regression analysis and its applications*, Wiley.

Beck, M. B. (1987), Water quality modeling: A review of the analysis of uncertainty, *Water Resources Research*, *23*, 1393–1442.

Bernhard, L., F. Sutter, W. Haeberli, and F. Keller (1998), Processes of snow/permafrost-interactions at a high-mountain site, Murtèl Corvatsch, Eastern Swiss Alps, in *Proceedings of the Seventh International Conference on Permafrost*, pp. 35–41.

Bertoldi, G., R. Rigon, and T. M. Over (2006), Impact of watershed geomorphic characteristics on the energy and water budgets, *Journal of Hydrometeorology*, *7*, 389–403.

Beven, K. (1993), Prophecy, reality and uncertainty in distributed hydrological modelling, *Advances in water resources*, *16*, 41–51.

Beven, K., and A. Binley (1992), The future of distributed models: model calibration and uncertainty prediction, *Hydrological Processes*, *6*, 279–298.

Beven, K., and J. Freer (2000), Equifinality, data assimilation, and uncertainty estimation in mechanistic modelling of complex environmental systems using the GLUE methodology, *Journal of Hydrology*, *249*, 11–29.

Boeckli, L., A. Brenning, S. Gruber, and J. Noetzli (2012a), A statistical approach to modelling permafrost distribution in the European Alps or similar mountain ranges, *The Cryosphere*, *6*, 125–140, doi: 10.5194/tcd-5-1419-2011.

Boeckli, L., A. Brenning, S. Gruber, and J. Noetzli (2012b), Permafrost distribution in the European Alps: calculation and evaluation of an index map and summary statistics, *The Cryosphere*, *6*, 807–820.

Bolch, T., and S. Marchenko (2006), Significance of glaciers, rockglacier and ice-rich permafrost in the Northern Tien Shan as water towers under climate change conditions, in *Assessment of Snow, Glacier and Water Resources in Asia in Almaty, Kazakhstan*.

Bommer, C., M. Phillips, and L. U. Arenson (2010), Practical recommendations for planning, constructing and maintaining infrastructure in mountain permafrost, *Permafrost and Periglacial Processes*, *21*, 97–104.

Box, G. E. P., and D. R. Cox (1964), An analysis of transformations, *Journal of the Royal Statistical Society. Series B (Methodological)*, *26*, 221–252.

Braithwaite, R. J. (2008), Temperature and precipitation climate at the equilibrium-line altitude of glaciers expressed by the degree-day factor for melting snow, *Journal of Glaciology*, *54*, 437–444.

Braithwaite, R. J., and Y. Zhang (2000), Sensitivity of mass balance of five Swiss glaciers to temperature changes assessed by tuning a degree-day model, *Journal of Glaciology*, *46*, 7–14.

Brenning, A., S. Gruber, and M. Hoelzle (2005), Sampling and statistical analyses of BTS measurements, *Permafrost and Periglacial Processes*, *16*, 383–393.

Brockwell, P. J., and R. A. Davis (1991), *Time series and forecasting methods*, Springer, New York.

Brockwell, P. J., and R. A. Davis (1996), *Introduction to Time Series and Forecasting*, Springer, New York.

Brown, J., O. J. Ferrians, J. A. Heginbottom, and E. S. Melnikov (1997), *Circum-arctic map of permafrost and ground-ice conditions*, U. S. Geological Survey for the International Permafrost Association.

Brown, R. J. E., and T. L. Péwé (1973), Distribution of permafrost in North America and its relationship to the environment, a review 1963-1973, in *Proceedings of the 2nd International Conference on Permafrost, Yakutsk, USSR*, pp. 71–100.

Brun, E., E. Martin, V. Simon, C. Gendre, and C. Coléou (1989), An energy and mass model of snow cover suitable for operational avalanche forecasting, *Journal of Glaciology*, *35*, 333–342.

Brun, E., P. David, M. Sudul, and B. G. (1992), A numerical model to simulate snow-cover stratigraphy for operational avalanche forecasting, *Journal of Glaciology*, *38*, 13–22.

Brunt, D. (1932), Notes on radiation in the atmosphere, *Quartely Journal of the Royal Meteorological Society*, *58*, 389–420.

Brutsaert, W. (1975), On a derivable formula for long-wave radiation from clear skies, *Water Resources Research*, *11*, 742–744.

Burg, J. P. (1968), *A new analysis technique for time series data*, Modern Spectrum Analysis, IEEE Press, New York.

Burn, C. R., and C. A. S. Smith (1987), Observations of the "thermal offset" in near-surface mean annual ground temperatures at several sites near Mayo, Yukon Territory, Canada, *Arctic*, *41*, 99–104.

Butts, M. B., J. T. Payne, M. Kristensen, and H. Madsen (2004), An evaluation of the impact of model structure on hydrological modelling uncertainty for streamflow simulation, *Journal of Hydrology*, *298*, 242–266.

Carslaw, H. S., and J. C. Jaeger (1959), *Conduction of Heat in Solids*, Oxford University Press.

Clark, M. P., J. Hendrikx, A. G. Slater, D. Kavetski, N. J. Anderson, B .and Cullen, T. Kerr, E. Örn Hreinsson, and R. A. Woods (2011), Representing spatial variability of snow water equivalent in hydrologic and land-surface models: A review, *Water Resources Research*, *47*, doi: 10.1029/2011WR010745.

Corripio, J. G. (2002), Vectorial algebra algorithms for calculating terrain parameters from DEMs and solar radiation modelling in mountainous terrain, *Geographical Information Science*, *17*, 1–23.

Crawford, T. M., and C. E. Duchon (1998), An improved parameterization for estimating effective atmospheric emissivity for use in calculating daytime downwelling longwave radiation, *Journal of Applied Meteorology*, *38*, 474–480.

Cukier, R. I., H. B. Levine, and K. E. Shuler (1977), Nonlinear sensitivity analysis of multiparameter model systems, *The Journal of Physical Chemistry*, *81*, 2365–2366.

Dall'Amico, M. (2010), Coupled water and heat transfer in permafrost modeling, Ph.D. thesis, Institute of Civil and Environmental Engineering, Universita degli Studi di Trento, Trento.

Danby, R. K., and D. S. Hik (2007), Responses of white spruce (Picea Glauca) to experimental warming at a subarctic alpine treeline, *Global Change Biology*, *13*, 437–451.

Davis, T. J., and C. P. Keller (1997), Modelling uncertainty in natural resource analysis using fuzzy sets and Monte Carlo simulation: slope stability prediction, *Geographical Information Science*, *11*, 409–434.

de Vries, D. A. (1963), *Physics of plant environment*, chap. Thermal properties of soils, pp. 210–235, North-Holland Publishing Co., Amsterdam.

Delaloye, R., E. Reynard, C. Lambien, L. Marescot, and R. Monnet (2008), Thermal anomaly in a cold scree slope (Creux du Van, Switzerland), in *Proceedings of the 8th International Conference on Permafrost, Zurich, Switzerland*.

Diggle, P. J., and P. J. Ribeiro (2006), *Model-based geostatistics*, Springer Series in Statistics.

Dilley, A. C., and D. M. O'Brien (1997), Estimating downward clear sky long-wave irradiance at the surface from screen temperature and precipitable water, *Q. J. R. Meteorological Society*, *124a*, 1391–1401.

Dorren, L. K. A. (2003), A review of rockfall mechanics and modelling approaches, *Progress in Physical Geography*, *27*, 69–87.

Dorren, L. K. A. (2012), *Rockyfor3D (v4.1) - Transparent description of the complete 3D rockfall model*, ecorisq paper ed.

Endrizzi, S. (2007), Snow cover modelling at local and distributed scale over complex terrain, Ph.D. thesis, Institute of Civil and Environmental Engineering, Universita degli Studi di Trento, Trento.

Essery, R., and P. Etchevers (2004), Parameter sensitivity in simulation of snowmelt, *Journal of geophysical research*, *109*.

Essery, R., and J. W. Pomeroy (2004a), Spatial variability of alpine snowfall and snow accumulation from radar and lidar data, *Journal of Hydrometeorology*, *5*, 735–744.

Essery, R., and J. W. Pomeroy (2004b), Implications of spatial distributions of snow mass and melt rate for snow-cover depletion: theoretical considerations, *Annals of Glaciology*, *38*, 261–265.

Etchevers, P., E. Martin, R. Brown, C. Fierz, Y. Lejeune, E. Bazile, A. Boone, Y. J. Dai, R. Essery, A. Fernandez, Y. Gusev, R. Jordan, V. koren, E. Kowalczyk, R. D. Pyles, A. Schlosser, A. B. Shmakin, T. G. Smirnova, U. Strasser, D. Verseghy, T. Yamazaki, and Z. L. Yang (2002), SnowMIP, an intercomparison of snow models: first results, in *International Snow Science Workshop*.

Etchevers, P., E. Martin, R. Brown, C. Fierz, Y. Lejeune, E. Bazile, A. Boone, Y. J. Dai, R. Essery, A. Fernandez, Y. Gusev, R. Jordan, V. Koren, E. Kowalczyk, N. O. Nasonova, R. D. Pyles, A. Schlosser, A. B. Shmakin, T. Smirnova, U. Strasser, D. Verseghy, T. Yamazaki, and Z. L. Yang (2004), Validation of the energy budget of an alpine snowpack simulated by several snow models (SnowMIP project), *Annals of Glaciology*, *38*, 150–158.

Etzelmüller, B., M. Hoelzle, E. S. F. Heggem, K. Isaksen, C. Stocker-Mittaz, R. S. Ødegård, W. Haeberli, and J. L. Sollid (2001a), Mapping and modelling the occurrence and distribution of mountain permafrost, *Norsk Geografisk Tidsskrift*, *55(4)*, 186–194.

Etzelmüller, B., R. S. Ødegård, I. Berthling, and J. L. Sollid (2001b), Terrain parameters and remote sensing in the analysis of permafrost distribution and periglacial processes: principles and examples from southern Norway, *Permafrost and Periglacial Processes*, *12*, 79–92.

Etzelmüller, B., E. S. F. Heggem, N. Sharkhuu, R. Frauenfelder, A. Kääb, and C. E. Goulden (2006), Mountain permafrost distribution modelling using a multi-criteria approach in the Hövsgöl area, northern Mongolia, *Permafrost and Periglacial Processes*, *17*, 91–104, doi: 10.1002/ppp.554.

Etzelmüller, B., H. Farbrot, A. Gudmundsson, O. Humlum, O. E. Tveito, and H. Björnsson (2007), The regional distribution of mountain permafrost in Iceland, *Permafrost and Periglacial Processes*, *18*, 185–199.

Etzelmüller, B., T. V. Schuler, H. H. Christiansen, H. Farbrot, and R. Benestad (2011), Modeling the temperature evolution of Svalbard permafrost during the 20th and 21st century, *The Cryosphere*, *5*, 67–79.

Evensen, G. (1994), Sequential data assimilation with a nonlinear quasigeostrophic model using Monte Carlo methods to forecast error statistics, *Journal of Geophysical Research*, *99*, 10,143–10,162.

Farbrot, H., T. Hipp, B. Etzelmüller, K. Isaksen, R. S. Ødegård, T. V. Schuler, and O. Humlum (2011), Air and ground temperature variations observed along elevation and continentality gradients in Southern Norway, *Permafrost and Periglacial Processes*, *22*, 343–360, doi: 10.1002/ppp.733.

Fiddes, J., and S. Gruber (2012), TopoSUB: a tool for efficient large area numerical modelling in complex topography at sub-grid scales, *Geoscientific Model Development*, *5*, 1245–1257.

Fischer, L. (2009), Slope instabilities on perennially frozen and glacierised rock walls: Multi-scale observations, analyses and modelling, Ph.D. thesis, Department of Geography, University of Zurich, Switzerland.

Flerchinger, G. N., W. Xiao, D. Marks, T. J. Sauer, and Q. Yu (2009), Comparison of algorithms for incoming atmospheric long-wave radiation, *Water Resources Research*, *45*, W03,423, doi: 10.1029/2008WR007394.

Franks, S. W., and K. Beven (1997), Bayesian estimation of uncertainty in land surface-atmosphere flux predictions, *Journal of Geophysical Research*, *102*, doi: 10.1029/97JD02011.

Fuchs, M., G. S. Campbell, and R. I. Papendick (1978), An analysis of sensible and latent heat flow in a partially frozen unsaturated soil, *Soil Science Society of America Journal*, *42*, 379–385.

Funk, M., and M. Hoelzle (1992), A model of potential direct solar radiation for investigating occurrences of mountain permafrost, *Permafrost and Periglacial Processes*, *3*, 139–142.

Gadek, B., and J. Leszkiewicz (2010), Influence of snow cover on ground surface temperature in the zone of sporadic permafrost, Tatra mountains, Poland and Slovakia, *Cold Regions Science and Technology*, *60*, 205–211.

Gavrilowa, M. K. (1988), Permafrost-climatic characteristics of different classes, in *Proceedings of the 5th International Conference on Permafrost, Trondheim*, pp. 78–106.

Gelman, A., J. Carlin, H. Stern, and D. B. Rubin (2004), *Bayesian data analysis*, Chapman and Hall/ CRC.

Gold, L. W., and A. H. Lachenbruch (1973), Thermal conditions in permafrost - a review of North American literature, in *Proceedings of the 2nd International Conference on Permafrost, Yakutsk, USSR*, pp. 3–25.

Goodchild, M. F. (1986), *Spatial autocorrelation*, University of Western Ontario.

Greuell, W., W. H. Knap, and P. C. Smeets (1997), Elevational changes in meteorological variables along a midlatitude glacier during summer, *Journal of Geophysical Research*, *102*, 941–954.

Gruber, S. (2005), Mountain permafrost: Transient spatial modelling, model verification and the use of remote sensing, Ph.D. thesis, University of Zurich.

Gruber, S., and W. Haeberli (2007), Permafrost in steep bedrock slopes and its temperature-related destabilization following climate change, *Journal of Geophysical Research*, *112*.

Gruber, S., and W. Haeberli (2009), *Permafrost Soils*, chap. Mountain permafrost, pp. 33–44, Springer.

Gruber, S., and M. Hoelzle (2001), Statistical modelling of mountain permafrost distribution: Local calibration and incorporation of remotely sensed data, *Permafrost and Periglacial Processes*, *12*, 69–77, doi: 10.1002/ppp374.

Gruber, S., and M. Hoelzle (2008), The cooling effect of coarse blocks revisited: a modeling study of a purely conductive mechanism, in *9th International Conference on Permafrost*.

Gruber, S., M. Peter, M. Hoelzle, I. Woodhatch, and W. Haeberli (2003), Surface temperatures in steep alpine rock faces - a strategy for regional-scale measurement and modelling, in *Proceedings of the 8th International Conference on Permafrost*.

Gruber, S., M. Hoelzle, and W. Haeberli (2004a), Permafrost thaw and destabilization of alpine rock walls in the hot summer of 2003, *Geophysical Research Letters*, *31*.

Gruber, S., M. Hoelzle, and W. Haeberli (2004b), Rock-wall temperatures in the alps: Modelling their topographic distribution and regional differences, *Permafrost and Periglacial Processes*, *15*, 299–307, doi: 10.1002/ppp.501.

Gruber, S., L. King, T. Kohl, T. Herz, W. Haeberli, and M. Hoelzle (2004c), Interpretation of geothermal profiles perturbed by topography: the alpine permafrost boreholes at Stockhorn plateau, Switzerland, *Permafrost and Periglacial Processes*, *15*, 349–357.

Grünewald, T., M. Schirmer, R. Mott, and M. Lehning (2010), Spatial and temporal variability of snow depth and ablation rates in a small mountain catchment, *The Cryosphere*, *4*, 215–225.

Gubler, S., J. Fiddes, M. Keller, and S. Gruber (2011), Scale-dependent measurement and analysis of ground surface temperature variability in alpine terrain, *The Cryosphere*, *5*,

431–443, doi: 10.5194/tc-5-431-2011.

Gubler, S., S. Gruber, and R. S. Purves (2012), Uncertainties of parameterized surface downward clear-sky shortwave and all-sky longwave radiation, *Atmospheric Chemistry and Physics*, *12*, 5077–5098, doi: 10.5194/acp-12-5077-2012.

Gubler, S., S. Endrizzi, S. Gruber, and R. S. Purves (2013), Sensitivities and uncertainties of modeled ground temperatures in mountain environments, *Geoscientific Model Development*, *6*, 1319–1336, doi: 10.5194/gmd-6-1319-2013.

Gueymard, C. (2003a), Direct solar transmittance and irradiance predictions with broadband models. Part I: detailed theoretical performance assessment, *Solar Energy*, *74*, 355–379.

Gueymard, C., and D. R. Myers (2008), *Validation and ranking methodologies for solar radiation models*, chap. 20, pp. 479–509, Springer.

Gueymard, C. A. (2003b), Direct solar transmittance and irradiance predictions with broadband models. Part II: validation with high-quality measurements, *Solar Energy*, *74*, 381–395.

Gueymard, C. A. (2012), Clear-sky irradiance predictions for solar resource mapping and large-scale applications: Improved validation methodology and detailed performance analysis of 18 broadband radiative models, *Solar Energy*, *86*, 2145–2169.

Gupta, H. V., K. Beven, and T. Wagener (2005), *Model calibration and uncertainty estimation*, John Wiley & Sons.

Gupta, H. V., T. Wagener, and Y. Liu (2008), Reconciling theory with observations: elements of a diagnostic approach to model evaluation, *Hydrological Processes*, *22*, 3802–3813.

Haeberli, W. (1973), Die Basis-Temperatur der winterlichen Schneedecke als möglicher Indikator für die Verbreitung von Permafrost in den Alpen, *Zeitschrift für Gletscherkunde und Glaziologie*, *9*, 221–227.

Haeberli, W. (1975), Untersuchung zur Verbreitung von Permafrost zwischen Flüelapass und Piz Grialetsch (Graubünden), Ph.D. thesis, Universitiy of Basel.

Haeberli, W. (1985), Creep of mountain permafrost: internal structure and flow of alpine rock glaciers, *Mitteilungen der Versuchsanstalt für Wasserbau, Hydrologie und Glaziologie der ETH Zürich*, *77*, 142pp.

Haeberli, W. (1992), Construction, environmental problems and natural hazards in periglacial mountain belts, *Permafrost and Periglacial Processes*, *3*, 111–124.

Haeberli, W., J. Huder, H. R. Keusen, J. Pika, and H. Röthlisberger (1988), Core drilling through rock glacier-permafrost, in *Proceedings of the 5th International Conference on Permafrost*, pp. 937–942.

Haeberli, W., M. Wegmann, and D. Vonder Mühll (1997), Slope stability problems related to glacier shrinkage and permafrost degradation in the alps, *Eclogae Geologicae Helvetiae*, *90*, 407–414.

Haeberli, W., B. Hallet, L. U. Arenson, R. Elocin, O. Humlum, A. Kääb, V. Kaufmann, B. Ladanyi, N. Matsuoka, S. M. Springman, and D. Vonder Mühll (2006), Permafrost creep and rock glacier dynamics, *Permafrost and Periglacial Processes*, *17*, 189–214.

Haeberli, W., J. Noetzli, L. U. Arenson, R. Delaloye, I. Gärtner-Roer, S. Gruber, K. Isaksen, C. Kneisel, M. Krautblatter, and M. Phillips (2010), Mountain permafrost: development and challenges of a young research field, *Journal of Glaciology*, *56*, 1043–1058.

Hand, D. J. (1997), *Construction and assessment of classification rules*, Wiley Series in Probability & Statistics.

Hanna, S. R., Z. Lu, H. C. Frey, N. Wheeler, J. Vukovich, S. Arunachalam, M. Fernau, and D. A. Hansen (2001), Uncertainties in predicted ozone concentrations due to input uncertainties for the UAM-V photochemical grid model applied to the July 1995 OTAG domain, *Atmospheric Environment*, *35*, 891–903.

Hanna, S. R., R. Paine, D. Heinold, E. Kintigh, and D. Baker (2007), Uncertainties in air toxics calculated by the dispersion models AERMOD and ISCST3 in the Houston Ship Channel Area, *Journal of Applied Meteorology and Climatology*, *46*, 1372–1382.

Hanson, S., and M. Hoelzle (2005), Installation of a shallow borehole network and monitoring of the ground thermal regime of a high alpine discontinuous permafrost environment, Eastern Swiss Alps, *Norsk Geografisk Tidsskrift*, *59*, 84–93.

Harris, C., W. Haeberli, D. Vonder Mühll, and L. King (2001a), Permafrost monitoring in the high mountains of Europe: the PACE project in its global context, *Permafrost and Periglacial Processes*, *12*, 3–11.

Harris, R. N., M. C. R. Davies, and B. Etzelmüller (2001b), The assessment of potential geotechnical hazards associated with mountain permafrost in a warming global climate, *Permafrost and Periglacial Processes*, *12*, 145–156.

Hasler, A., S. Gruber, M. Font, and A. Dubois (2011a), Advective heat transport in frozen rock clefts: conceptual model, laboratory experiments and numerical simulation, *Permafrost and Periglacial Processes*, *22*, 378–389.

Hasler, A., S. Gruber, and W. Haeberli (2011b), Temperature variability and offset in steep alpine rock and ice faces, *The Cryosphere*, *5*, 977–988, in prep.

Hastings, W. K. (1970), Monte Carlo sampling methods using Markov Chains and their applications, *Biometrika*, *57*, 97–109.

Hauck, C., K. Isaksen, D. Vonder Mühll, and J. L. Sollid (2004), Geophysical surveys designed to delineate the altitudinal limit of mountain permafrost: an example from

Jotunheimen, Norway, *Permafrost and Periglacial Processes*, *15*, 191–205.

Hebeler, F. (2008), Modelling topographic uncertainty: Impacts on large scale environmental modelling, Ph.D. thesis, University of Zurich, Department of Geography, Switzerland.

Hebeler, F., and R. S. Purves (2008), *Modeling DEM data uncertainties for Monte Carlo simulations of ice sheet models*, pp. 175–196, CRC Press.

Hebeler, F., R. S. Purves, and S. R. Jamieson (2008), The impact of parametric uncertainty and topographic error in ice sheet modelling, *Journal of Glaciology*, *45*, 899–919.

Heggem, E. S. F., B. Etzelmüller, S. Anarmaa, N. Sharkhuu, C. E. Goulden, and B. Nandinsetseg (2006), Spatial distribution of ground surface temperatures and active layer depths in the Hövsgöl area, northern Mongolia, *Permafrost and Periglacial Processes*, *17*, 357–369, doi: 10.1002/ppp.568.

Heginbottom, J. A., J. Brown, E. S. Melnikov, and O. J. Ferrians (1993), Circum-arctic map of permafrost and ground ice conditions, in *Proceedings of the 6th International Conference on Permafrost, Guangzhou, China*, pp. 1132–1136.

Hilbich, C., C. Hauck, M. Hoelzle, M. Scherler, L. Schudel, I. Völksch, D. Vonder Mühll, and R. Mäusbacher (2008), Monitoring mountain permafrost evolution using electrical resistivity topography: A 7-year study of seasonal, annual, and long-term variations at Schilthorn, Swiss Alps, *Journal of Geophysical Research*, *113*, 13pp.

Hilbich, C., L. Marescot, C. Hauck, M. H. Loke, and R. Mäusbacher (2009), Applicability of electrical resistivity tomography monitoring to coarse blocky and ice-rich permafrost landforms, *Permafrost and Periglacial Processes*, *20*, 269–284, doi: 10.1002/ppp.652.

Hipp, T., B. Etzelmüller, H. Farbrot, and T. V. Schuler (2012), Modelling borehole temperatures in Southern Norway - insights into permafrost dynamics during the 20th and 21st century, *The Cryosphere*, *6*, 553–571, doi: 10.5194/tc-6-553-2012.

Hock, R. (2003), Temperature index melt modelling in mountain areas, *Journal of Hydrology*, *282*, 104–115.

Hoelzle, M. (1992), Permafrost occurrence from BTS measurements and climatic parameters in the Eastern Swiss Alps, *Permafrost and Periglacial Processes*, *3*, 143–147.

Hoelzle, M. (1994), Permafrost und Gletscher in Oberengadin. Grundlagen und Anwendungsbeispiele für automatisierte Schätzverfahren, Ph.D. thesis, ETH Zürich.

Hoelzle, M. (1996), Mapping and modelling of mountain permafrost distribution in the Alps, *Norsk Geografisk Tidsskrift*, *50*, Ho11–15.

Hoelzle, M., W. Haeberli, and F. Keller (1993), Application of BTS-measurements for modelling permafrost distribution in the Swiss Alps, in *Proceedings of the 6th Inter-*

national Conference on Permafrost, South China University Technology Press, Beijing, pp. 272–277.

Hoelzle, M., M. Wegmann, and B. Krummenacher (1999), Miniature temperature dataloggers for mapping and monitoring of permafrost in high mountain areas: First experience from the Swiss Alps, *Permafrost and Periglacial Processes*, *10*, 113–124.

Hoelzle, M., C. Mittaz, B. Etzelmüller, and W. Haeberli (2001), Surface energy fluxes and distribution models of permafrost in European mountain areas: an overview of current developments, *Permafrost and Periglacial Processes*, *12*, 53–68.

Hoelzle, M., D. Vonder Mühll, and W. Haeberli (2002), Thirty years of permafrost research in the Corvatsch-Furtschellas area, Eastern Swiss Alps: a review, *Norsk Geografisk Tidsskrift*, *56*, 137–145.

Hoelzle, M., W. Haeberli, and C. Mittaz (2003), Miniature ground temperature data logger measurements $2000-2002$ in the Murtèl-Corvatsch area, Eastern Swiss alps, in *8th International Conference on Permafrost, Proceedings*, edited by M. Phillips, S. Springman, and L. Arenson, pp. 419–424, Swets & Zeitlinger: Lisse, Zürich.

Huggel, C., J. Caplan-Auerbach, C. F. Waythomas, and R. L. Wessels (2007), Monitoring and modeling ice-rock avalanches from ice-capped volcanoes: a case study of frequent large avalanches on Iliamna Volcano, Alaska, *Journal of Volcanology and Geothermal Research*, *168*, 114–136.

Huybrechts, P., and T. Payne (1996), The EISMINT benchmarks for testing ice-sheet models, *Annals of Glaciology*, *23*.

Ingersoll, L. R., O. J. Zobel, and A. C. Ingersoll (1948), *Heat conduction with engineering, geological and other applications*, McGraw-Hill Book Company, First Edition.

IPCC (2007), Climate change 2007: Synthesis report, *Tech. rep.*, Intergovernmental Panel on Climate Change.

Iqbal, M. (1983), *An introduction to solar radiation*, Academic Press, Toronto.

Isaksen, K., C. Hauck, E. Gudevang, and R. S. Ødegård (2002), Mountain permafrost distribution in Dovrefjell and Jotunheimen, southern Norway, based on BTS measurements and 2D tomography data., *Norsk Geografisk Tidsskrift*, *56*, 122–136.

Isaksen, K., R. S. Ødegård, B. Etzelmüller, C. Hilbich, C. Hauck, H. Farbrot, T. Eiken, H. O. Hygen, and T. Hipp (2011), Degrading mountain permafrost in Southern Norway: Spatial and temporal variability of mean ground temperatures, 1999-2009, *Permafrost and Periglacial Processes*, *22*, 361–377, doi: $10.1002/\mathrm{ppp}.728$.

Ishikawa, M. (2003), Thermal regime at the snow-ground interface and their implications for permafrost investigation, *Geomorphology*, *52*, 105–120.

Ishikiwa, M., and K. Hirakawa (2000), Mountain permafrost distribution based on BTS measurements and DC resistivity soundings in the Daisetsu mountains, Hokkaido, Japan, *Permafrost and Periglacial Processes*, *11*, 109–123.

Ives, J. D., and M. J. Bovis (1978), Natural hazards maps for land-use planning, San Juan Mountains, Colorado, USA, *Arctic and Alpine Research*, *10 (2)*, 185–212.

JCGM (2008), *Evaluation of measurement data - Guide to the expression of uncertainty in measurement*, Joint Committee for Guides in Metrology.

Jhorar, R. K., W. G. M. Bastiaanssen, R. A. Feddes, and J. C. Van Dam (2002), Inversely estimating soil hydraulic functions using evapotranspiration fluxes, *Journal of Hydrology*, *258*, 198–213.

Jordan, R. (1991), A one-dimensional temperature model for a snow cover: Technical documentation for SNTHERM, *Tech. rep.*, Cold Regions Research and Engineering Lab Hanover, New Hampshire.

Juliussen, H., and O. Humlum (2007), Towards a TTOP ground temperature model for mountainous terrain in central-eastern norway, *Permafrost and Periglacial Processes*, *18*, 161–184.

Kavetski, D., S. W. Franks, and G. Kuczera (2003), Confronting input uncertainty in environmental modeling, *Water Science and Applications Series*, *6*, 49–68.

Kavetski, D., G. Kuczera, and S. W. Franks (2006), Bayesian analysis of input uncertainty in hydrological modeling: 1. theory, *Water Resources Research*, *42*.

Keller, F. (1992), Automated mapping of mountain permafrost using the program PERMAKART within the geographical information system arc/info, *Permafrost and Periglacial Processes*, *3*, 133–138.

Keller, F., and H. U. Gubler (1993), Interaction between snow cover and high mountain permafrost at Murtèl Corvatsch, Swiss Alps, in *The Sixth International Conference on Permafrost, Beijing*, pp. 332–337.

Keller, F., R. Frauenfelder, J.-M. Gardaz, M. Hoelzle, C. Kneisel, R. Lugon, M. Phillips, E. Reynard, and L. Wenker (1998), Permafrost map of Switzerland, in *Permafrost- Seventh International Conference (Proceedings), Yellowknife, Canada*.

Kennedy, M. C., and A. O'Hagan (2001), Bayesian calibration of computer models, *Journal of the royal statistical society*, *63*, 425–464.

Keusen, H. R., and W. Haeberli (1983), Site investigation and foundation design aspects of cable car construction in Alpine permafrost at Chli Matterhorn, Wallis, Swiss Alps, pp. 601–605.

Kirchner, J. W., R. P. Hooper, C. Kendall, C. Neal, and G. Leavesley (1996), Testing and validating environmental models, *The Science of the Total Environment*, *183*, 33–47.

Klok, E. J., and J. Oerlemans (2002), Model study of the energy and mass balance of the Morteratschgletscher, Switzerland, *Journal of Glaciology*, *48*, 505–518.

Konzelmann, T., R. S. W. van de Wal, W. Greuell, R. Bintanja, E. A. C. Henneken, and A. Abe-Ouchi (1994), Parameterization of global and longwave incoming radiation for the Greenland ice sheet, *Global and Planetary Change*, *9*, 143–164.

Koopmans, R. W. R., and R. D. Miller (1966), Soil freezing and soil water characteristic curves, *Soil Science Society of America Journal*, *30*, 680–685.

Koster, E. A., M. E. Nieuwenhujzen, and A. S. Judge (1994), *Permafrost and climatic change: an annotated bibliography*, World Data Center for Glaciology (Snow and Ice).

Kuczera, G., and E. Parent (1998), Monte Carlo assessment of parameter uncertainty in conceptual catchment models: the Metropolis algorithm, *Journal of Hydrology*, *211*, 69–85.

Kwong, T. T. J., and T. Y. Gan (1994), Northward migration of permafrost along the Mackenzie Highway and climatic warming, *Climatic Change*, *26*, 399–419.

Lachenbruch, A. H., and B. V. Marhsall (1986), Changing climate: geothermal evidence from permafrost in the Alaskan Arctic, *Science*, *234*, 689–696.

Legates, D. R., and G. J. J. McCabe (1999), Evaluating the use of "goodness-of-fit" measures in hydrologic and hydroclimatic model validation, *Water resources research*, *35*, 233–241.

Lehning, M., P. Bartelt, B. Brown, and C. Fierz (2002a), A physical SNOWPACK model for the Swiss avalanche warning Part III: meteorological forcing, thin layer formation and evaluation, *Cold Regions Science and Technology*, *35*, 169–184.

Lehning, M., P. Bartelt, B. L. Brown, C. Fierz, and P. Satyawali (2002b), A physical SNOWPACK model for the Swiss Avalanche Warning Services: Part II: Snow microstructure, *Cold Regions Science and Technology*, *35*, 147–176.

Lewkowicz, A. G. (2008), Evaluation of miniature temperature-loggers to monitor snowpack evolution at mountain permafrost sites, northwestern Canada, *Permafrost and Periglacial Processes*, *19*, 323–331.

Lewkowicz, A. G., and M. Ednie (2004), Probability mapping of mountain permafrost using the BTS method, Wolf Creek, Yukon Territory, Canada, *Permafrost and Periglacial Processes*, *15*, 67–80.

Lhomme, J. P., J. J. Vacher, and A. Rocheteau (2007), Estimating downward long-wave radiation on the Andean Altiplano, *Agricultural and Forest Meteorology*, *145*, 139–148.

Ling, F., and T. Zhang (2004), A numerical model for surface energy balance and thermal regime of the active layer and permafrost containing unfrozen water, *Cold Regions Science and Technology*, *38*, 1–15.

López-Moreno, J. I., S. R. Fassnacht, S. Beguería, and J. B. P. Latron (2011), Variability of snow depth at the plot scale: implications for mean depth estimation and sampling strategies, *The Cryosphere*, *5*, 617–629.

Luethi, M., and M. Funk (2001), Modelling heat flow in a cold, high-altitude glacier: interpretation of measurements from Colle Gnifetti, Swiss Alps, *Journal of Glaciology*, *47*, 314–324.

Luetschg, M. (2004), A model and field analysis of the interaction between snow cover and alpine permafrost, Ph.D. thesis, Department of Geography, University of Zurich, Switzerland.

Luetschg, M., and W. Haeberli (2005), Permafrost evolution in the Swiss Alps in a changing climate and the role of the snow cover, *Norsk Geografisk Tidsskrift*, *59*, 78–83.

Luetschg, M., M. Lehning, and W. Haeberli (2008), A sensitivity study of factors influencing warm/thin permafrost in the Swiss Alps, *Journal of Glaciology*, *54*, 696–704.

Lunardini, V. J. (1981), *Heat transfer in cold climates*, Van Nostrand Reinhold Co.

Machguth, H., R. S. Purves, J. Oerlemans, M. Hoelzle, and F. Paul (2008), Exploring uncertainty in glacier mass balance modelling with Monte Carlo simulation, *The Cryosphere*, *2*, 191–204.

Mantovan, P., and E. Todini (2006), Hydrological forecasting uncertainty assessment: Incoherence of the GLUE methodology, *Journal of Hydrology*, *330*, 368–381.

Mayer, D. G., and D. G. Butler (1993), Statistical validation, *Ecological Modelling*, *68*, 21–32.

Mertens, J., H. Madsen, M. Kristensen, D. Jaques, and J. Feyen (2005), Sensitivity of soil parameters in unsaturated zone modeling and the relation between effective, laboratory and in situ measurements, *Hydrological Processes*, *19*, 1611–1633.

Metropolis, N., A. Rosenbluth, M. Rosenbluth, A. Teller, and E. Teller (1953), Equation of state calculations by fast computing machines, *Journal of Chemical Physics*, *21*, 1087–1092.

Mittaz, C., M. Imhof, M. Hoelzle, and W. Haeberli (2002), Snowmelt evolution mapping using an energy balance approach over an Alpine terrain, *Arctic, Antarctic, and Alpine Research*, *34*, 274–281.

Monte, L., L. Håkanson, U. Bergström, J. Brittain, and R. Heling (1996), Uncertainty analysis and validation of environmental models: the empirically based uncertainty analysis, *Ecological Modelling*, *91*, 139–152.

Moore, G. E., and R. J. Londergan (2001), Sampled Monte Carlo uncertainty analysis for photochemical grid models, *Atmospheric Environment*, *35*, 4863–4876.

Moradkhani, H., K. L. Hsu, H. V. Gupta, and S. Sorooshian (2005), Uncertainty assessment of hydrologic model states ans parameters: Sequential data assimilation using the particle filter, *Water Resources Research*, *41*, doi: 10.1029/2004WR003604.

Moretti, L., A. Mangeney, Y. Capdeville, S. Stutzmann, C. Huggel, D. Schneider, and F. Bouchut (2012), Numerical modeling of the Mount Steller landslide flow history and of the generated long period seismic waves, *Geophysical Research Letters*, *39*, 7 pp., doi: 10.1029/2012GL052511.

Muller, S. W. (1947), *Permafrost or permanently frozen ground and related engineering problems*, U. S. Geological Survey.

Nash, J. E., and J. Sutcliffe (1970), River flow forecasting through conceptual models: Part 1 - a discussion of principles, *Journal of Hydrology*, *10*, 282– 290.

Nelson, F. E., and O. A. Anisimov (1993), Permafrost zonation in Russia under anthropogenic climatic change, *Permafrost and Periglacial Processes*, *4*, 137–148.

New, M., and M. Hulme (2000), Representing uncertainty in climate change scenarios: a Monte-Carlo approach, *Integrated Assessment*, *1*, 203–213.

Nötzli, J. (2008), Modeling transient three-dimensional temperature fields in mountain permafrost, Ph.D. thesis, University of Zurich.

Nötzli, J., and S. Gruber (2009), Transient thermal effects in Alpine permafrost, *The Cryosphere*, *3*, 85–99.

Nötzli, J., C. Huggel, M. Hoelzle, and W. Haeberli (2006), GIS-based modelling of rock-ice avalanches from Alpine permafrost areas, *Computational Geosciences*, *10*, 161–178, doi: 10.1007/s10596-005-9017-z.

Nötzli, J., S. Gruber, T. Kohl, N. Salzmann, and W. Haeberli (2007), Three-dimensional distribution and evolution of permafrost temperatures in idealized high-mountain topography, *Journal of Geophysical Research*, *112*.

Oberkampf, W. L., and T. G. Trucano (2002), Verification and validation in computional fluid dynamics, *Tech. rep.*, Sandia National Laboratories.

Ødegård, R. S., J. L. Sollid, and O. Liestol (1992), Ground temperature measurements in mountain permafrost, Jotunheimen, southern Norway, *Permafrost and Periglacial Processes*, *3*, 231–234.

Ødegård, R. S., M. Hoelzle, K. V. Johansen, and J. L. Sollid (1996), Permafrost mapping and prospecting in southern Norway, *Norsk Geografisk Tidsskrift*, *50*, 41–54.

Ødegård, R. S., K. Isaksen, T. Eiken, and J. L. Sollid (2008), MAGST in mountain permafrost, Dovrefjell, southern Norway, in *Proceedings of the 9th International Conference on Permafrost, Fairbanks, Alaska*.

Ohmura, A. (1982), Climate and energy balance on the Arctic tundra, *Journal of Climatology*, *2*, 65–84.

Osterkamp, T. E., and V. E. Romanovsky (1999), Evidence for warming and thawing of discontinuous permafrost in Alaska, *Permafrost and Periglacial Processes*, *10*, 17–37.

Pan, W., M. A. Tatang, G. J. McRae, and R. G. Prinn (1997), Uncertainty analysis of direct radiative forcing by anthropogenic sulfate aerosols, *Journal of geophysical research*, *102*, 21,915–21,924.

Park, J. (2008), Assessing climate change under uncertainty: A Monte Carlo approach, Master's thesis, Nicholas School of the Environment and Earth Sciences of Duke University.

Payne, A. J., P. Huybrechts, A. Abe-Ouchi, R. Calov, J. Fastook, R. Greve, S. Marshall, I. Marsiat, C. Ritz, L. Tarasov, and M. P. A. Thomassen (2000), Results from the EISMINT model intercomparison: the effects of thermomechanical coupling, *Journal of Glaciology*, *46*, 227–238.

Pellicciotti, F., B. Brock, U. Strasser, P. Burlando, M. Funk, and J. G. Corripio (2005), An enhanced temperature-index glacier melt model including the shortwave radiation balance: development and testing for Haut Glacier d'Arolla, Switzerland, *Journal of Glaciology*, *51*, 573–587.

PERMOS (2007), Permafrost in Switzerland, 2002/2003 and 2003/2004, in *Glaciological Report (Permafrost) No. 4/5 of the Cryospheric Commission of the Swiss Academy of Sciences*, edited by D. Vonder Mühll, J. Nötzli, I. Roer, K. Makowski, and R. Delaloye.

PERMOS (2009), Permafrost in Switzerland 2004/2005 and 2005/2006, in *Glaciological Report (Permafrost) No. 6/7 of the Cryospheric Commission of the Swiss Academy of Sciences*, edited by J. Nötzli and D. Vonder Mühll.

PERMOS (2010), Permafrost in Switzerland 2006/2007 and 2007/2008, in *Glaciological Report (Permafrost) No. 8/9 of the Cryospheric Commission of the Swiss Academy of Sciences*, edited by J. Nötzli and D. Vonder Mühll.

Philipona, R., C. Marty, C. Fröhlich, and A. Heimo (1996), Measurements of the longwave radiation budget in the alps, in *IRS 96: Current Problems in Atmospheric Radiation*, edited by W. L. Smith and K. Stamnes, pp. 786–789, A. Deepak Publishing, Hampton, Virginia.

Phillips, M. (2000), Influences of snow supporting structures on the thermal regime of the ground in alpine permafrost terrain, *Tech. rep.*, Swiss Federal Institute for Snow and Avalanche Research Davos.

Pilkey, O. H., and L. Pilkey-Jarvis (2007), *Useless Arithmetic: Why Environmental Scientists Can't Predict the Future*, Columbia University Press.

Pirazzini, R., M. Nardino, A. Orsini, F. Calzolari, T. Georgiadis, and V. Levizzani (2000), Parameterization of the downward longwave radiation from clear and cloudy skies at Ny Ålesund (Svalbard), in *IRS 2000: Current Problems in Atmospheric Radiation*, edited by W. L. Smith and Y. A. Timofeyev, pp. 559–562, A. Deepak Publishing, Hampton, Virginia.

Pollaco, J. A. P., and B. P. Mohanty (2012), Uncertainties of water fluxes in soil-vegetation-atmosphere transfer models: Inverting surface soil moisture and evapotranspiration retrieved from remote sensing, *Vadose Zone Journal*.

Pomeroy, J. W., R. Essery, and B. Toth (2004), Implications of spatial distributions of snow mass and melt rate for snow-cover depletion: observations in a subarctic mountain catchment, *Annals of Glaciology*, *38*, 195–201.

Powell, W. G., D. S. Chapman, N. Balling, and A. E. Beck (1988), *Handbook of terrestrial heat-flow density determination: with guidelines and recommendations of the International Heat Flow Commission*, chap. Continental heat-flow density, pp. 167–222, Kluwer Academic Publishing.

Prata, A. J. (1996), A new long-wave formula for estimating downward clearsky radiation at the surface, *Q. J. R. Meteorological Society*, *122*, 1127–1151.

R Development Core Team (2011), *R: A language and environment for statistical computing*, R Foundation for Statistical Computing, ISBN 3-900051-07-0.

Ramos, M., A. Hasler, G. Vieira, C. Hauck, and S. Gruber (2009), Drilling and installation of boreholes for permafrost thermal monitoring on Livingston Island in the maritime Antarctic, *Permafrost and Periglacial Processes*, *20*, 57–64.

Ramsey, M. H., and S. L. R. Ellison (2007), *Measurement uncertainty arising from sampling: A guide to methods and approaches*, Eurachem, EUROLAB, CITAC, Nordtest and the RSC Analytical Methods Committee.

Rango, A., and J. Martinec (1995), Revisiting the degree-day method for snowmelt computations, *Journal of American Water Resources Association*, *31*, 657–669, doi: 10.1111/j.1752-1688.1995.tb03392.x.

Raymond, M. (2001), Analysis of near-surface temperatures in high mountain permafrost environment. study at the Murtèl-Corvatsch, Swiss Alps, Master's thesis, ETH Zürich.

Reckhow, K. H., J. T. Clements, and R. C. Dodd (1990), Statistical evaluation of mechanistic water-quality models, *Journal of Environmental Engineering*, *116*, 250–268.

Refsgaard, J. C. (1997), Parameterisation, calibration and validation of distributed hydrological models, *Journal of Hydrology*, *198*, 69–97.

Reichert, P. (2009), *Environmental Systems Analysis*, Department of Systems Analysis, Integrated Assessment, and Modelling: EAWAG.

Renard, B., V. Garreta, and M. Lang (2006), An application of Bayesian analysis and Markov Chain Monte Carlo methods to the estimation of a regional trend in annual maxima, *Water Resources Research*, *42*.

Rigon, R., G. Bertoldi, and T. M. Over (2006), GEOtop: A distributed hydrological model with coupled water and energy budget, *Journal of Hydrometeorology*, *7*, 371–388.

Riseborough, D., N. I. Shiklomanov, B. Etzelmüller, S. Gruber, and S. Marchenko (2008), Recent advances in permafrost modelling, *Permafrost and Periglacial Processes*, *19*, 137–156.

Roer, I., and M. Nyenhuis (2007), Rockglacier activity studies on a regional scale: comparison of geomorphological mapping and photogrammetric monitoring, *Earth Surface Processes and Landforms*, *32*, 1747–1758.

Roer, I., A. Kääb, and R. Dikau (2005), Rockglacier kinematics derived from small-scale aerial photography and digital airborne imagery, *Zeitschrift für Geomorphologie*, *49*, 73–87.

Rolland, C. (2002), Spatial and seasonal variations of air temperature lapse rates in alpine regions, *Journal of Climate*, *16*, 1032–1046.

Romanovsky, V. E., T. E. Osterkamp, and N. S. Duxbury (1997), An evaluation of three numerical models used in simulations of the active layer and permafrost temperature regimes, *Cold Regions Science and Technology*, *26*, 195–203.

Romanovsky, V. E., S. L. Smith, H. H. Christiansen, N. I. Shiklomanov, D. S. Drozdov, N. G. Oberman, A. L. Kholodov, and S. S. Marchenko (2011), Arctic report card: Permafrost, *Tech. rep.*, National Oceanic and Atmospheric Administration, United States Department of Commerce.

Rykiel, J. E. J. (1996), Testing ecological models: the meaning of validation, *Ecol. Model.*, *90*, 299–244.

Saltelli, A., S. Tarantola, and K. P.-S. Chan (1999), A quantitative model-independent method for global sensitivity analysis of model output, *Technometrics*, *41*(1), 39–56, doi: http://sensitivity-analysis.jrc.ec.europa.eu/tutorial/Technometrics99.pdf.

Saltelli, A., K. Chan, and E. M. Scott (2000), *Sensitivity analysis*.

Saltelli, A., S. Tarantola, and F. Campolongo (2004), *Sensitivity analyses in practice*, doi: 10.1002/0470870958.

Saltelli, A., M. Ratto, T. Andres, F. Campolongo, J. Cariboni, D. Gatelli, M. Saisana, and S. Tarantola (2008), *Global sensitivity analysis. The Primer*, John Wiley & Sons.

Sathya, V., A. G. Russel, S. Perego, M. Maignan, M. Junier, and A. Clappier (2000), *Uncertainties in photochemical grid modeling of ozone: The impact of uncertainties in meteorological inputs*, Kluwer Academic Publishers.

Satterlund, D. R. (1979), An improved equation for estimating longwave radiation from the atmosphere, *Water Resources Research*, *15*, 1649–1650.

Schillings, C. (2004), Bestimmung langjähriger stündlicher Zeitreihen und räumlich hochaufgelöster Karten der Direkt-Normal-Strahlung auf der Basis von Meteosat-Daten und Atmosphärenparametern für die Nutzung in konzentrierenden Solarkraftwerken, Ph.D. thesis, Philipps-Universität Marburg.

Schmid, M.-O., S. Gubler, J. Fiddes, and S. Gruber (2012), Inferring snowpack ripening and melt-out from distributed measurements of near-surface ground temperatures, *The Cryosphere*, *6*, 1127–1139, doi: 10.5194/tc-6-1127-2012.

Schmidt, S., B. Weber, and M. Winiger (2009), Analyses of seasonal snow disappearance in an alpine valley from micro- to meso-scale (Loetschental, Switzerland), *Hydrological Processes*, *23*, 1041–1051.

Schneider, D. (2011), On characteristics and flow dynamics of large rapid mass movements in glacial environments, Ph.D. thesis, University of Zurich, Department of Geography, Switzerland.

Schneider, S., M. Hoelzle, and C. Hauck (2012), Influence of surface and subsurface heterogeneity on observed borehole temperatures at a mountain permafrost site in the Upper Engadine, Swiss Alps, *The Cryosphere*, *6*, 517–531, doi: 10.5194/tc-6-517-2012.

Schoeneich, P. (2011), Guide lines for monitoring: Ground surface temperature, *Tech. rep.*, Longterm Permafrost Monitoring Network - PermaNET.

Scipion, D. E., R. Mott, M. Lehning, and A. Berne (2012), Spatial variability of alpine snowfall and snow accumulation from radar and lidar data.

Sicart, J. E., J. W. Pomeroy, R. L. H. Essery, and D. Bewley (2006), Incoming longwave radiation to melting snow: observations, sensitivity and estimation in northern environments, *Hydrological Processes*, *20*, 3697–3708.

Smith, A. F. M., and G. O. Roberts (1993), Bayesian computation via the Gibbs Samples and related Markov Chain Monte Carlo methods, *Journal of the Royal Statistical Society, Series B*, *55*, 3–23.

Smith, E. P., and K. A. Rose (1995), Model goodness-of-fit analysis using regression and related techniques, *Ecological Modelling*, *77*, 49–64.

Smith, M. B., D.-J. Seo, V. I. Koren, S. M. Reed, Z. Zhan, Q. Duan, F. Moreda, and S. Cong (2004), The distributed model intercomparison project (DMIP): motivation and experiment design, *Journal of Hydrology*, *298*, 4–26, doi: 10.1016/j.jhydrol.2004.03.040.

Smith, M. W. (1975), Microclimatic influences on ground temperatures and permafrost distribution, mackenzie delta, *Canadian Journal of Earth Science*, *12*, 1421–1438.

Smith, M. W., and D. Riseborough (2002), Climate and the limits of permafrost: A zonal analysis, *Permafrost and Periglacial Processes*, *13*, 1–15.

Sobol, I. (2001), Global sensitivity indices for nonlinear mathematical models and their Monte Carlo estimates, *Mathematics and Computers in Simulation*, *55*, 271–280.

Sobol, I. M. (1993), Sensitivity analysis for non-linear mathematical model, *Mathematical Modelling Computation Experiments*, *1*, 407–414.

Sommerfeld, R. A., R. C. Musselman, G. L. Wooldridge, and M. A. Conrad (1991), The performance of a simple degree-day estimate of snow accumulation to an alpine watershed, in *Snow, Hydrology and Forests in High Alpine Areas, Proceedings of the Vienna Symposium*.

Stahel, W. (2008), *Lineare Regression*, ETH Zürich.

Stocker-Mittaz, C., M. Hoelzle, and W. Haeberli (2002), Modelling alpine permafrost distribution based on energy-balance data: a first step, *Permafrost and Periglacial Processes*, *13*, 271–282.

Stow, C., J. Jollif, S. C. McGillicuddy D. J. Jr, Doney, A. J. I., M. A. M. Friedrichs, K. A. Rose, and P. Wallhead (2009), Skill assessment for coupled biological/physical models of marine systems, *Journal of Marine Systems*, *76*, 4–15.

Stow, C. A., C. Roessler, M. E. Borsuk, J. D. Bowen, and K. H. Reckhow (2003), A comparison of estuarine water quality models for TMDL development in the Neuse river estuary, *Journal of Water Resources Planning and Managment*, *129*, 307–314.

Swinbank, W. C. (1963), Long-wave radiation from clear skies, *Q. J. R. Meteorological Sociecty*, *89*, 330–348.

Tomassini, L., P. Reichert, R. Knutti, T. F. Stocker, and M. E. Borsuk (2007), Robust Bayesian uncertainty analysis of climate system properties using Markov Chain Monte Carlo, *Journal of Climate*, *20*, 1239–1254.

Trujillo, E., J. A. Ramírez, and K. J. Elder (2007), Topographic, meteorologic, and canopy controls on the scaling characteristics of the spatial distribution of snow depth fields, *Water Resources Research*, *43*, doi: 10D1029/2006WR005317.

Tsuang, B.-J. (2005), Ground heat flux determination according to land skin temperature observations from in situ stations and satellites, *American Meteorological Society*, pp. 371–390.

van Genuchten, M. T. (1980), A closed-form equation for predicting the hydraulic conductivity of unsaturated soils, *Soil Science Society of America Journal*, *44*, 892–898.

Vionnet, V., E. Brun, S. Morin, A. Boone, S. Faroux, P. Le Moigne, E. Martin, and J.-M. Willemet (2012), The detailed snowpack scheme Crocus and its implementation in SURFEX v7.2, *Geoscientific Model Development*, *5*, 773–791, doi: 10.5194/gmd-5-773-2012.

Vonder Mühll, D., and W. Haeberli (1990), Thermal characteristics of the permafrost within an active rock glacier (Murtèl/Corvatsch, Grisons, Swiss Alps), *Journal of Glaciology*, *36*, 151–158.

Vonder Mühll, D., T. Stucki, and W. Haeberli (1998), Borehole-temperatures in alpine permafrost: a ten year series, in *7th International Conference on Permafrost (Yellowknife)*, Collection Nordicana 57, pp. 1089–1095, Centre d'etudes nordiques, Universite Laval, Quebec.

Vonder Mühll, D., C. Hauck, H. Gubler, R. McDonald, and N. Russill (2001), New geophysical methods of investigating the nature and distribution of mountain permafrost with special reference to radiometry techniques, *Permafrost and Periglacial Processes*, *12*, 27–38, doi: 10.1002/ppp.382.

Vrugt, J. A., H. V. Gupta, W. Bouten, and S. Sorooshian (2003), A shuffled complex evolution Metropolis algorithm for optimization and uncertainty assessment of hydrologic model parameters, *Water Resources Research*, *39*, doi: 10.1029/2002WR001642.

Šafanda, J. (1999), Ground surface temperature as a function of the slope angle, *Tectonophysics*, *360*, 367–375.

Wagener, T., and H. V. Gupta (2005), Model identification for hydrological forecasting under uncertainty, *Stochastic Environmental Res Risk Assessment*, *19*, 378–387.

Wagner, S. (1992), Creep of alpine permafrost, investigated on the Murtèl rock glacier, *Permafrost and Periglacial Processes*, *3*, 157–162.

Wainwright, J., and M. Mulligan (2004), *Environmental modelling: Finding simplicity in complexity*, Chichester, West Sussex, England: Wiley.

Wang, K., and S. Liang (2009), Global atmospheric downward longwave radiation over land surface under all-sky conditions from 1973 to 2008, *Journal of Geophysical Research*, *1114*, D19,101, doi: 10.1029/2009JD011800.

Washburn, A. L. (1979), *Geocryology - A survey of periglacial processes and environments*, 406p. pp., Edward Arnold Ltd., London.

Wegmann, M., and H. R. Keusen (1998), Recent geophysical investigations at a high alpine permafrost construction site in Switzerland, in *7th International Conference on Permafrost (Yellowknife)*, Collection Nordicana 57, pp. 1119–1123, Centre d'etudes nordiques, Universite Laval, Quebec.

Weir, P. L. (1979), Topographic influences on snow accumulation at Mount Hutt, Master's thesis, University of Canterbury, Christchurch, New Zealand.

Wettlaufer, J. S., and M. G. Worster (2006), Premelting dynamics, *Annual Review of Fluid Mechanics*, *38*, 427–452.

Williams, P., and M. Smith (1989), *The ground thermal regime*, chap. 4, pp. 83–121, Cambridge University Press.

Woo, M.-K., A. G. Lewkowicz, and W. R. Rouse (1992), Response of the Canadian permafrost environment to climatic change, *Physical geography*, *13*, 287–317.

Woo, M.-K., D. L. Kane, S. K. Carey, and D. Yang (2008), Progress in permafrost hydrology in the new millennium, *Permafrost and Periglacial Processes*, *19*, 237–254.

Young, P. C. (2002), Advances in real-time flood forecasting, *Philosophical Transactions of the Royal Society*, *360*, 1433–1450.

Young, P. C. (2003), Top-down and data-based machanistic modelling of rainfall-flow dynamics at the catchment scale, *Hydrological Processes*, *17*, 2195–2217.

Zhang, T., R. G. Barry, and W. Haeberli (2001), Numerical simulations of the influence of the seasonal snow cover on the occurrence of permafrost at high latitudes, *Norsk Geografisk Tidsskrift*, *55*, 261–266.

Zhang, Y., W. Chen, and J. Cihlar (2003), A process-based model for quantifying the impact of climate change on permafrost thermal regimes, *Journal of Geophysical Research*, *108*, doi: 10.1029/2002JD003354.

Part II

Publications

Publication I

Gubler, S., J. Fiddes, M. Keller, and S. Gruber (2011), Scale-dependent measurement and analysis of ground surface temperature variability in alpine terrain, *The Cryosphere*, *5*, 431–443, doi: 10.5194/tc-5-431-2011

Contributions:

- Measurement design with J. Fiddes and S. Gruber
- R-code used for statistical data analyses
- Interpretation and visualization of results

The Cryosphere, 5, 431–443, 2011
www.the-cryosphere.net/5/431/2011/
doi:10.5194/tc-5-431-2011

The Cryosphere

Scale-dependent measurement and analysis of ground surface temperature variability in alpine terrain

S. Gubler[1], J. Fiddes[1], M. Keller[2], and S. Gruber[1]

[1]Department of Geography, University of Zurich, Switzerland
[2]Computer Engineering and Networks Laboratory, ETH Zurich, Switzerland

Received: 23 December 2010 – Published in The Cryosphere Discuss.: 25 January 2011
Revised: 3 May 2011 – Accepted: 17 May 2011 – Published: 25 May 2011

Abstract. Measurements of environmental variables are often used to validate and calibrate physically-based models. Depending on their application, the models are used at different scales, ranging from few meters to tens of kilometers. Environmental variables can vary strongly within the grid cells of these models. Validating a model with a single measurement is therefore delicate and susceptible to induce bias in further model applications.

To address the question of uncertainty associated with scale in permafrost models, we present data of 390 spatially-distributed ground surface temperature measurements recorded in terrain of high topographic variability in the Swiss Alps. We illustrate a way to program, deploy and refind a large number of measurement devices efficiently, and present a strategy to reduce data loss reported in earlier studies. Data after the first year of deployment is presented.

The measurements represent the variability of ground surface temperatures at two different scales ranging from few meters to some kilometers. On the coarser scale, the dependence of mean annual ground surface temperature on elevation, slope, aspect and ground cover type is modelled with a multiple linear regression model. Sampled mean annual ground surface temperatures vary from $-4\,^{\circ}\mathrm{C}$ to $5\,^{\circ}\mathrm{C}$ within an area of approximately $16\,\mathrm{km}^2$ subject to elevational differences of approximately 1000 m. The measurements also indicate that mean annual ground surface temperatures vary up to $6\,^{\circ}\mathrm{C}$ (i.e., from $-2\,^{\circ}\mathrm{C}$ to $4\,^{\circ}\mathrm{C}$) even within an elevational band of 300 m. Furthermore, fine-scale variations can be high (up to $2.5\,^{\circ}\mathrm{C}$) at distances of less than 14 m in homogeneous terrain. The effect of this high variability of an environmental variable on model validation and applications in alpine regions is discussed.

Correspondence to: S. Gubler
stefanie.gubler@geo.uzh.ch

1 Introduction

The combination of environmental monitoring and modeling plays an important role when investigating current and future climate and their control of diverse phenomena of the cryosphere. Measurements are widely used for model validation and calibration. However, the problem of comparing model simulations made at one scale to measurements taken at another scale has no simple solution. The relevance of this issue increases when modeling phenomena such as snow cover or permafrost in highly variable terrain such as the Swiss Alps, since variations occur at smaller scales than in more homogeneous terrain. The difficulties that arise from scaling issues can be large: in contrast to measurements, spatially-distributed models are often grid-based and represent areas of several square meters to square kilometers. Since the physical processes that influence the pattern of variation of a phenomena operate and interact at different spatial scales, spatial variation can simultaneously occur on scales of different orders of magnitude (Oliver and Webster, 1986). Therefore, the extrapolation of results (including calibrated model outputs) based on point measurements requires caution, especially in highly variable terrain (Nelson et al., 1998). A specific statement concerning this issue was made by Gupta et al. (2005):

> A less obvious source of error is when the variable predicted by a model is not the same quantity as that measured (even though they might be referred to by the same name) because of scale effects, nonlinearities or measurement technique problems.

Due to the lack of spatially-distributed measurements, the influence of the scaling problem on model validation has barely been investigated earlier.

The study of permafrost in mountain regions has become important in view of ongoing climate change (Harris et al., 2009; Gruber and Haeberli, 2007). Alpine environments are

characterized by variable topography, influencing slope, aspect, elevation, ground properties, snow distribution and the energy fluxes at the Earth's surface. Ground surface temperatures thus vary over short distances and permafrost, while integrating over larger surface areas in depth, is strongly affected by this topographic variability. Diverse permafrost studies have been performed in alpine regions in the last decades; ranging from long-term monitoring projects such as Permafrost Monitoring Switzerland (PERMOS: www.permos.ch), over measurement campaigns of bottom temperature of snow (BTS) (Haeberli, 1973; Hoelzle et al., 2003) and ground surface temperatures (GST) (Gruber et al., 2004a; Hoelzle and Gruber, 2008) to statistical and physically based modeling (Haeberli, 1975; Stocker-Mittaz et al., 2002; Gruber, 2005; Nötzli et al., 2007). While measuring ground temperatures (GT) is costly, GST and BTS measurements usually require much less resources. Distributed measurement of GST and BTS at fine scales is therefore feasible, however measurements at the surface are strongly affected by topographic and ground cover variations. Since GST is strongly coupled to air temperature, it depends, in a first approximation, on altitude. However, GST is also strongly influenced by topography through snow redistribution, exposition to the sun, shading from surrounding terrain and ground properties. Snow cover exerts an important influence on the ground thermal regime based on differing processes (Keller and Gubler, 1993; Zhang, 2005; Luetschg et al., 2008). On gently inclined Alpine slopes, snow cover mostly causes a net increase of mean annual ground surface temperatures (MAGST) due to its insulating effect during winter, but the timing and thickness of first snow cover, mean snow cover thickness as well as the timing of melt-out strongly control the local magnitude of this effect and are subject to strong inter-annual variation (Hoelzle et al., 2003; Brenning et al., 2005). Near-surface material can also affect GST and induce a large lateral variability of GST over just tens of meters. Especially for large block material, a lowering of MAGST has been observed and can be attributed to the circulation of cold air during winter (Haeberli, 1973; Harris, 1996; Juliussen and Humlum, 2008; Gorbunov et al., 2004) as well as purely conductive effects that do not require ventilation (Gruber and Hoelzle, 2008). Furthermore, the exposition to solar radiation has a strong effect on the energy budget at a specific point. The amount of radiation received at a point depends on slope angle, the exposure to the sun and shading from surrounding terrain. The difference in GST between two sides of an east-west oriented ridge can be more than 5 °C (Gruber et al., 2004b; PERMOS, 2010).

The following questions are addressed in this paper:

– How can we efficiently obtain a spatially-distributed and dense set of measurements, that represent the diverse sources of variability that operate on different spatial and temporal scales?

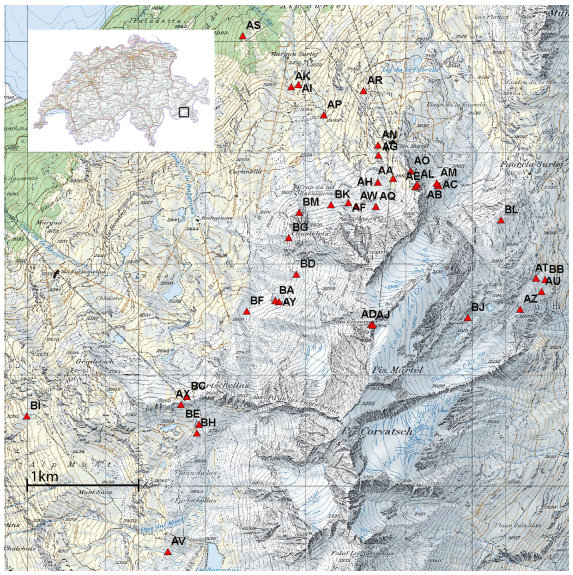

Fig. 1. Locations of the 39 footprints at Corvatsch study site. Reproduced by permission of swisstopo (BA110077).

– How do topographic parameters and ground cover types influence MAGST in an area of several square kilometers?

– What is the variation of ground surface temperatures within a 10 m × 10 m field?

– What uncertainty is associated with scaling between point measurements and gridded models?

2 Instruments and methods

2.1 Study site

The study site of Corvatsch lies in the eastern part of the Swiss Alps (46.42° N/9.82° E, Fig. 1). Several rock glaciers and some small glaciers exist around Piz Corvatsch, and the area has a long tradition of cryosphere research (Hoelzle et al., 2002). A cable car facilitates the access to the area. Elevation ranges from approximately 1900 m to 3300 m a.s.l. Precipitation reaches mean values of 800 mm in the valley floors and 1000 mm to 2000 mm in the valley side belts (Schwarb et al., 2000). The zero degree isotherm of the mean annual air temperature (MAAT) is at 2200 m a.s.l. Meteorological data are measured by MeteoSwiss at Piz Corvatsch (3315 m a.s.l.) in the center of the study area.

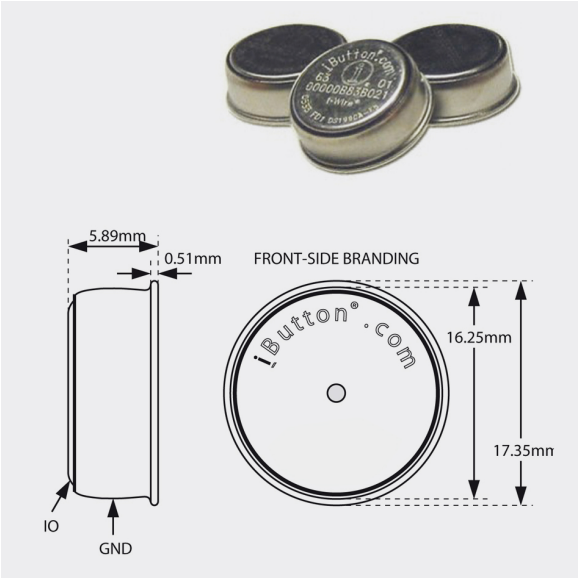

Fig. 2. The iButton® DS1922L that was used for temperature measurements.

2.2 Instruments

The iButton® DS1922L (Fig. 2) is a coin-sized, commercial device that integrates a micro-controller, 8 kB storage, a real-time clock, a temperature sensor, and a battery in a single package. The iButton measures temperatures from −40 °C to 85 °C with ±0.5 °C accuracy from −10 °C to 65 °C. At that resolution, it can store 4096 readings in memory.
Lewkowicz (2008) states that about 13 % of the iButtons that were deployed to monitor the snow-pack in Northern Canada failed, most probably due to water entry. To avoid this, iButtons were waterproofed by sealing them in pouches of 40 mm × 100 mm in the present study. The material is a 140 µm thick laminate (oriented polyamide, polyethylene and aluminium) designed to withstand long periods of wetness as well as intense solar radiation without significant deterioration. Since the iButtons are buried into the ground, the pouches have no influence on the measured GST. Using a portable impulse tong sealer (polystar 300 A) operated with 12 V batteries, these pouches can be re-sealed in the field after cutting the seal and reading out the iButton data.
A campaign with hundreds of devices (almost 400 in this study) asks for as much automation as possible, and generates a large amount of data that must be handled properly. For this, the iAssist management tool (Keller et al., 2010) was developed to deploy, localize and maintain the iButton data loggers. A relational database is used to store measurements and meta data, i.e., GPS coordinates and pictures.

2.3 Experiment design

The amount of samples required to adequately resolve the spatial patterns of the phenomena of interest increases with their heterogeneity (cf., Nelson et al., 1998). In order to resolve the spatial patterns and the variability of GST around Corvatsch, 39 locations, so-called footprints, were selected such that most of the topographic variability within this area of approximately 16 km^2 is represented (Fig. 1). On the one hand, the focus in footprint selection lay on the influence of the topographic variables elevation, slope and aspect, and additionally ground cover types and terrain curvature. On the other hand, the replication of GST measurements within each 10 m × 10 m footprint reflects the variability in GST at a fine scale. Each footprint is chosen to be as homogeneous as possible with respect to aspect, slope and surface cover.
To represent GST variability due to slope, aspect and ground material, one main elevational band was selected for intense instrumentation. It ranges from 2600 m to 2900 m a.s.l. Some footprints lie outside this band and reflect the dependence of GST on elevation. The footprints cover all aspects, steep and gentle slopes and different ground cover types such as meadow, fine material and large blocks (Table 1). Aspect, slope, elevation and terrain curvature were estimated from a digital elevation model (DEM) of 25 m resolution.
Note that slopes larger than 50° are not sampled in this study. The ground cover type (GCT) is differentiated in four groups: GCT1 represents near-surface material with a high amount of fine, and often also organic material. GCT3 stands for entirely block-covered areas, GCT2 lies in between. GCT4 consists of all footprints that do not fit into GCT1 to GCT3, i.e. indicating either meadows covered with small to medium size blocks, or ridges consisting of rock and large boulders.
Shading from surrounding terrain plays a major role in determining the amount of solar radiation reaching the ground. At each footprint, the local horizon was recorded using a digital camera (Nikon Coolpix 990) with a fish eye converter (Nikon FC-E8) (Gruber et al., 2003). These pictures permit to determine the sky view factor at each footprint. Snow depth and snow water equivalent were measured three times during winter, in January, mid March and end of April 2010. Due to avalanche danger, snow data only exists for some footprints.

2.4 Logger placement

In order to record near-surface temperatures and avoid heating by direct solar radiation, the iButtons were buried approximately 5 cm into the ground or placed between and underneath boulders. GST is measured every 3 h at 0.0625 °C resolution, enabling operation for 512 days. The data recording always started at midnight. Within each 10 m × 10 m footprint, we randomly distributed ten iButtons (Fig. 3). The one hundred square meters were numbered, and a uniform sample of size 10 was generated with R (R Development Core Team, 2011), determining the ten squares to place the

Table 1. Meta data of footprints. B_k denotes the number of valid iButton measurements at footprint k. MAGST of footprint k is denoted by μ_k (Eq. 1) and the variability of MAGST is ξ_k (Eq. 2). Coordinates are given in the Swiss coordinate system CH1903. Elevation, slope and aspect are derived from a DEM with 25 m resolution. Slope is given in degrees, as well as aspect counting from the north clockwise. GCT stands for ground cover type and classifies the footprints into four groups: group one is fine material often including organic material, group three is very coarse material such as the large boulders on the rock glaciers, and group two lies in between. Group four contains all footprints consisting of heterogeneous ground cover, partially including bedrock. Note that both footprints AL and AO are separated into two groups. Within AL, half of the iButtons lie in slightly concave terrain (AL2), the rest in convex terrain (AL1) on a ridge. Due to this difference which influences snow accumulation, AL1 and AL2 are treated as two different footprints. Similarly within AO: the ten iButtons are located on both sides of a steep N–S ridge, i.e., five iButtons are north-east exposed (AO1), five are south-west exposed (AO2).

Footprint	x-coord	y-coord	B_k	Elev.	Slope	Aspect	GCT	μ_k	ξ_k
AA	783292	144769	10	2694	38	251	1	3.82	0.59
AB	783691	144709	10	2745	16	96	2	2.96	1.33
AC	783701	144704	10	2743	31	112	2	4.34	1.15
AD	783092	143454	10	3303	29	263	4	−3.65	1.69
AE	783490	144696	10	2826	29	290	1	0.89	1.88
AF	782888	144552	10	2689	23	9	4	−1.62	2.12
AG	783159	144979	9	2664	48	243	4	2.29	2.52
AH	783151	144735	10	2663	9	318	3	−0.55	1.10
AI	782437	145612	7	2307	18	330	1	3.17	0.36
AJ	783108	143449	10	3302	27	113	4	−1.56	2.22
AL1	783506	144714	5	2824	14	347	1	1.00	0.22
AL2	783506	144714	5	2824	25	60	1	1.53	0.16
AM	783682	144727	10	2738	30	333	2	0.52	0.87
AN	783155	145070	9	2673	25	252	1	3.24	0.27
AO1	783446	144834	5	2811	36	64	4	−1.43	1.72
AO2	783446	144834	5	2811	18	238	4	1.41	0.60
AP	782667	145339	5	2405	15	335	1	2.56	0.45
AQ	783135	144517	10	2729	29	12	3	−1.04	1.06
AR	783026	145559	7	2528	28	288	2	2.91	0.25
AS	781936	146051	8	2100	35	315	1	4.89	1.09
AT	784575	143872	10	2790	36	100	1	3.52	1.00
AU	784625	143751	10	2773	33	88	3	1.67	0.55
AV	781263	141412	10	2538	0	212	1	3.59	0.16
AW	782960	144519	9	2700	19	333	3	−2.01	0.63
AX	781380	142736	10	2810	23	135	1	3.55	1.03
AY	782264	143661	10	2687	9	328	2	2.12	0.8
AZ	784433	143592	10	2876	7	61	1	2.41	0.28
BA	782231	143669	10	2697	27	111	1	3.60	0.44
BB	784659	143858	10	2763	14	103	1	3.06	0.45
BC	781437	142806	8	2783	41	357	2	−1.24	1.00
BD	782420	143906	10	2705	27	247	2	3.56	0.81
BE	781543	142558	9	2710	29	167	1	3.98	0.73
BF	781972	143576	10	2645	5	31	1	2.43	0.65
BG	782351	144237	10	2715	43	246	1	3.56	2.14
BH	781525	142480	10	2693	6	243	3	1.42	2.47
BI	779993	142631	4	2362	24	192	1	5.42	0.36
BJ	783961	143517	10	2997	36	90	2	1.46	1.24
BK	782731	144532	9	2691	31	355	2	1.69	0.46
BL	783962	143526	10	2875	19	35	3	0.21	1.01
BM	782444	144464	10	2715	44	314	4	−1.49	2.26

iButtons. This random placement reduces systematic bias in the measurements due to subjectivity.

Each iButton was fixed to a yellow string to facilitate refinding. To prevent iButtons from falling down steep slopes, loggers were attached to large, stable boulders. At each footprint, a wooden stick was stamped into the ground, marking one vertex of the 10 m × 10 m square. Two blue ropes were then attached to the stick identifying the local grid.

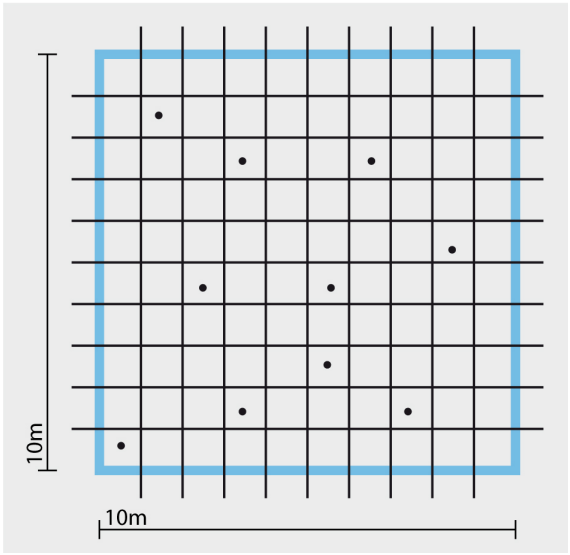

Fig. 3. Ten iButtons were randomly distributed in each 10 m × 10 m footprint. One vertex of the square was marked with a stick. Two ropes representing two orthogonal edges were attached to the stick. The blue ropes served as rulers. The local grid and the sampled numbers were manually recorded.

The iButtons were distributed in two field campaigns. Therefore, the two groups AA to AS (17 July 2009 to 16 July 2010, period 1) and AT to BM (14 August 2009 to 13 August 2010, period 2) cover slightly different time periods.

2.5 Data analysis

The main focus of the data analysis is the variability of MAGST at the two scales investigated. At the coarse scale (16 km^2), we analyse the variability (the so-called inter-footprint variability) of the mean MAGST μ_k, which at footprint k is defined as the mean of the mean of each time series within that footprint, i.e.:

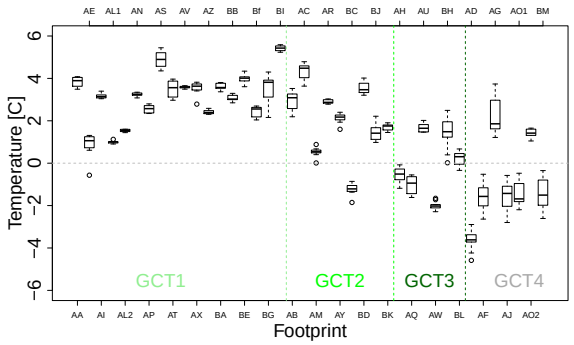

Fig. 4. Boxplots of MAGST of all iButtons at the footprints. The footprints are ordered according to the ground cover types, the vertical dashed lines separate the four GCT groups from each other.

$$\mu_k := \frac{1}{B_k} \sum_{i=1}^{B_k} \mu_{k,i}. \quad (1)$$

Here, B_k is the number of iButtons at footprint k, and $\mu_{k,i}$ denotes MAGST of iButton i at footprint k. The distribution of the $\mu_{k,i}$ for all footprints is presented in Fig. 4. The intra-footprint variability ξ_k of MAGST at footprint k, which is used to study the variability at the fine scale (100m^2), is defined as the range of the MAGST of all iButtons within that footprint:

$$\xi_k := \max_{i=1,\cdots,B_k} (\mu_{k,i}) - \min_{i=1,\cdots,B_k} (\mu_{k,i}). \quad (2)$$

To quantify the influence of the topographic variables on μ_k and ξ_k, a multiple linear regression analysis is performed.

3 Results

3.1 General description

In Fig. 5, ground surface temperatures of four different footprints are presented. GST vary strongly between different footprints, depending on elevation, exposition to the sun and conditions of snow. The two footprints on the top station of Corvatsch, AD and AJ, are highly correlated to air temperature, even in winter (Fig. 5). They are wind-exposed and thick snow is unlikely to accumulate. AJ, which is oriented to the east, shows bigger daily temperature amplitudes and is two degrees warmer than AD, which is west-exposed. Since clouds often develop in the afternoon, the west exposed footprint AD receives less direct solar radiation.
The footprints BC and AX are snow-covered during winter. Daily temperature variations cease in the beginning of October, when the first large snow fall event of winter 2009/2010 occurred. At BC, a steep north-oriented slope, temperature damping by snow is observed some weeks later than at AX.

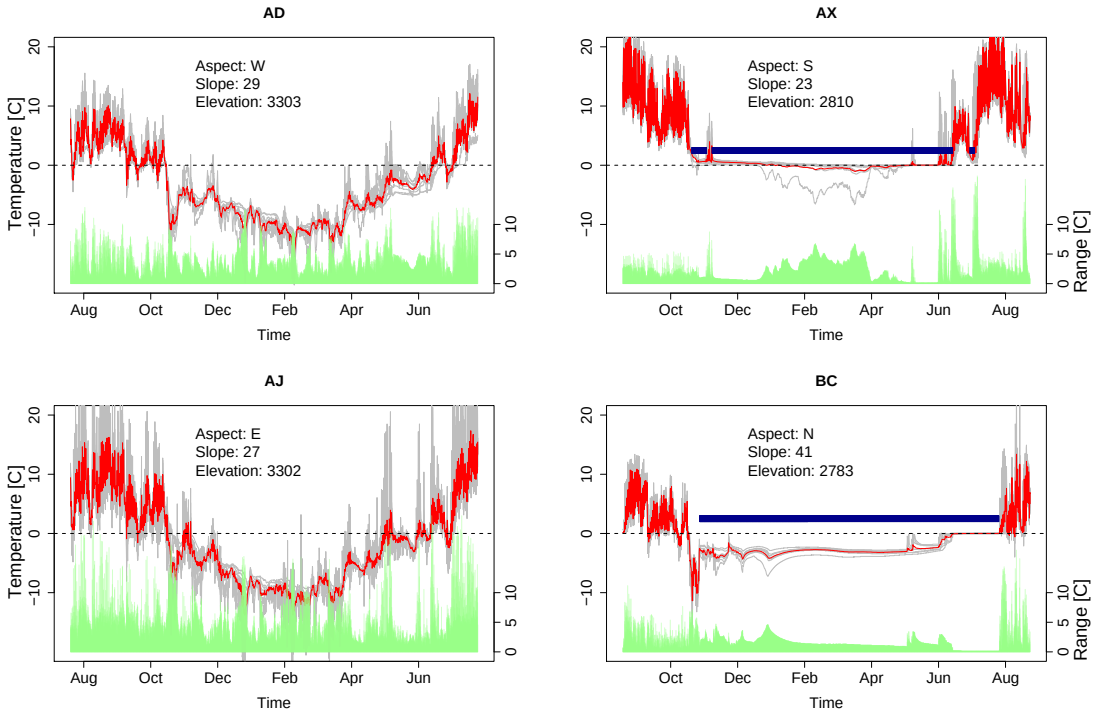

Fig. 5. GST of footprints AD, AJ, AX and BC. The grey lines in the background plot a maximum of ten iButtons located at the footprints. The red line indicates the mean GST at each time step. At the bottom of each plot, the range of all iButtons is plotted, indicating the temperature variability within each footprint. Snow cover is indicated in blue and was estimated manually based on daily temperature variations (Danby and Hik, 2007). Zero curtains can be identified at the end of the snow periods at AX and BC.

In late spring, the snow cover at BC lasts much longer. Since the slope is north exposed, it receives limited solar radiation, and therefore snow melting occurs much slower than at the nearby, south-oriented slope AX. The difference in MAGST between AX and BC is more than 4 °C. At AX, GST in summer is much higher than at BC, and thus the combined effect of warming due to solar radiation at AX and cooling due to long lasting snow in late spring at BC are responsible for this large difference. The snow depths measurements confirm that at both BC and AX a homogeneous snow cover isolated the ground from the cold winter air temperatures, in comparison to AJ and AD, where only small snow patches of several centimeter depths were observed.

Similar effects can be observed at diverse other footprints, for example at BA and AY. They lie close together (i.e., less than 30 m distance), however AY is in a zone with high snow accumulation. Melting takes more time, and snow cover in AY lasts approximately one month longer than at BA, resulting in a 1.5 °C lower MAGST (Table 1).

3.2 Data quality

The techniques developed to protect, manage, distribute and refind many data loggers have proven to be effective. In order to refind the buttons, mainly the yellow strings and the local grids were of great help, resulting in the recovery of 367 out of 390 iButtons after the first year.

Every retrieved iButton recorded valid data, indicating the importance of the pouches used when compared to 13 % loss reported previously (Lewkowicz, 2008). However, some iButtons reappeared on the surface (i.e., the measurements are disturbed by the direct solar radiation) and were excluded from the analysis. In total, 93 % of the iButtons recorded data that could be used for the analysis.

A zero curtain, i.e., the effect of latent heat due to freezing or thawing, results in stable temperatures near 0 °C over extended time periods. Zero curtains were detected at several footprints (for example at the end of the snow season in both AX and BC, Fig. 5) and serve, in this study, to analyse the accuracy of the measurement devices. The zero curtains at each individual iButton were detected in a first step by using a threshold of the temperature deviation from zero degrees. Varying the threshold from 0.0625 °C to 0.25 °C in steps of

0.0625 °C indicated that variations of zero curtain periods within even very homogeneous footprints are large for the smallest threshold. When choosing a threshold of 0.125 °C, detected zero curtain periods become homogeneous. Choosing the larger two thresholds does not have a big influence on the detected zero curtain periods. This vicarious calibration indicates that the iButtons measure temperatures at an accuracy of ±0.125 °C (i.e. two digital numbers) near zero degrees.

3.3 Inter-footprint variability

Measured MAGST varies from −3.65 °C to 5.42 °C around Corvatsch (Table 1). This variation can, to a large degree, be explained with the topographic variability. In order to quantify the influence of the topographic variables, a multiple linear regression model was fitted to the data using ordinary least squares. The full model contained the explanatory variables elevation, slope, aspect, ground cover type, sky view factor and curvature. An iterative, step-wise model reduction according to the Akaike-Information-Criteria (Akaike, 1973) combined with the addition of higher polynomials and interaction terms led to the model shown in Eq. (3). Note that sine and cosine of the aspect are taken to ensure continuity. Since aspect is recorded from the north clockwise, cosine represents the dependence on north-south differences, and west-east differences are represented by the sine.

$$\begin{aligned}\mu_k = {} & 17.63 - 0.0056 \cdot \mathrm{Elevation}_k \\ & - 0.48 \cdot \cos(\mathrm{Aspect}_k) \\ & + 0.42 \cdot \sin(\mathrm{Aspect}_k) \\ & + 0.0056 \cdot \mathrm{Slope}_k \\ & + 0.22 \cdot \mathrm{dGCT}_{k,2} \\ & - 1.66 \cdot \mathrm{dGCT}_{k,3} \\ & - 2.2 \cdot \mathrm{dGCT}_{k,4} \\ & - 0.057 \cdot (\mathrm{Slope_k} : \cos(\mathrm{Aspect_k})) \\ & + \varepsilon_k \,.\end{aligned} \tag{3}$$

MAGST plotted against elevation is shown in Fig. 6. Additionally, the fitted values of Model (3) are plotted. The model explains 93 % of the MAGST variability (Fig. 7), the adjusted R^2 equals 91 % and the model is highly significant ($p < 10^{-14}$, where p is the p-value). The model coefficients and their interpretation are explained in Sect. 4.1 in more detail. Note that GCT is a categorical variable and is therefore represented through the dummy variable dGCT (i.e., $\mathrm{dGCT}_{k,2} = 1$ if and only if footprint k is of ground cover type 2, else $\mathrm{dGCT}_{k,2} = 0$). Consequently, the different ground cover types influence the intercept of the linear regression. The random variables ε_k are independent and normally distributed with zero mean and constant variance. Residual analysis did not show any strong deviations from this model assumptions. The spatial autocorrelation was studied by estimating the semivariogram of the residuals, showing that the residuals are spatially not autocorrelated. This supports the statement by Nelson et al. (1998), who concluded that the variability due to the high variations in topography at small to medium distances dominates over spatial structures. The confidence interval of a coefficient contains all values that would not be rejected by the t-test at a previously specified significance level, i.e., it indicates the uncertainty associated with the coefficient. The 95 % confidence intervals of Model (3) are presented in Table 2. Some confidence intervals are rather large, since the data sample is relatively small (forty values fitted to four explanatory variables). Model uncertainty is smallest at the data center. All variables except for three differ significantly from zero. The exceptions are dGCT_2 which, as part of a dummy variable, is not separable from the highly significant dGCT_3, and cos(Aspect) and Slope, which are kept in the model since their interaction is significant.

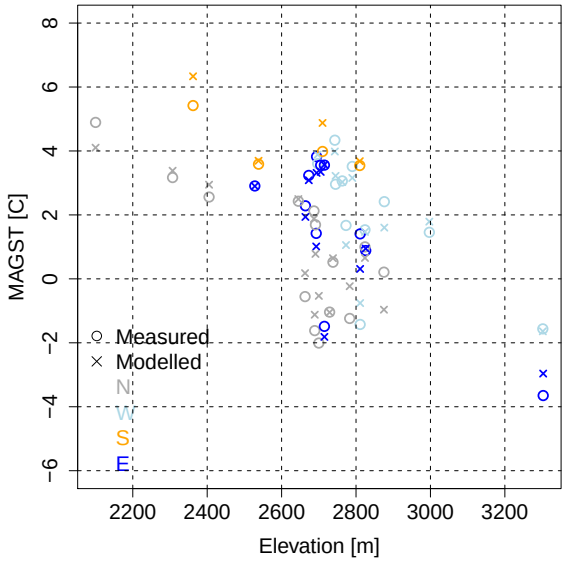

Fig. 6. MAGST of all footprints plotted against elevation. Colors identify the different aspects. Measured MAGST are indicated with a circle, the crosses denote the fitted values from the linear model shown in Eq. (3).

10-fold cross-validation has been performed to estimate the model behaviour. Thereby, one of ten randomly selected subsets serves as validation data, and the remaining nine as training data. The residuals at each point in the validation data are estimated, and the procedure is repeated until each subset exactly once served as validation data. The mean of the residuals of the 39 footprints resulted in −0.03 °C with standard deviation 0.78 °C. The root mean squared error was 0.77 °C.

Further, the influence of the difference in summer temperatures of the two time periods 1 and 2 on the results of the regression analysis was analysed. MAAT differs by

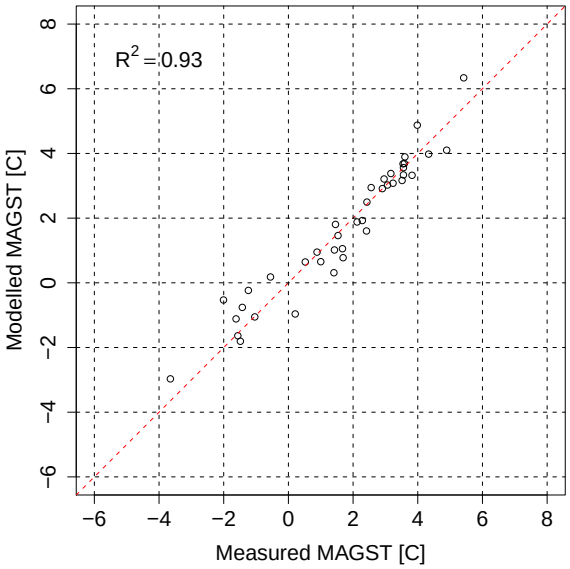

Fig. 7. Scatterplot of measured and modelled MAGST of Model (3). The dashed red line indicates the diagonal $y = x$. The model explains 93 % of the variability of measured MAGST.

Table 2. 95 % confidence intervals of the inter-footprint analysis coefficients (Model (3)).

Coefficient	2.5 %	97.5 %
Intercept	14.24	21.04
Elevation	−0.0068	−0.0043
cos(Aspect)	−1.23	0.27
sin(Aspect)	0.11	0.72
Slope	−0.01	0.03
$dGCT_2$	−0.38	0.82
$dGCT_3$	−2.34	−0.98
$dGCT_4$	−2.94	−1.47
Slope:cos(Aspect)	−0.086	−0.027

approximately 0.16 °C between the two periods. To analyse the influence of this difference in MAAT, Model (3) was fitted to the mean of the GST measurements of the overlapping time period (14 August 2009 to 16 July 2010) instead of the μ_k. The only difference observed between the two analyses is a negative shift of the intercept of approximately 0.8 °C, resulting from the absent summer temperatures between the 17 July and the 13 August of the respective years. This indicates that air temperature has an effect on absolute, but not on relative MAGST, and that sign and order of magnitude of the influence of the topographic variables on MAGST are representative for that year.

Table 3. 95 % confidence intervals of the intra-footprint analysis coefficients (Model (4)).

Coefficient	2.5 %	97.5 %
Intercept	−1.7	−8.56
$Slope^2$	0.0004	0.001
$dGCT_2$	0.093	1.88
$dGCT_3$	0.83	2.49
$dGCT_4$	0.47	2.3
$Slope^2$:$dGCT_2$	−0.0018	$7.86 \cdot 10^{-5}$
$Slope^2$:$dGCT_3$	−0.003	$-4.77 \cdot 10^{-4}$
$Slope^2$:$dGCT_4$	−0.001	$2.38 \cdot 10^{-4}$

3.4 Intra-footprint variability

Variability in MAGST varies strongly between the different footprints. It ranges from 0.16 °C at the very homogeneous footprint AV to almost 2.5 °C at BH (Table 1). Variation is generally larger for coarser ground material and more heterogeneous ground cover (Fig. 4). Similarly as before, we modelled the dependence of the variation on the topographic variables. The final model is:

$$\begin{aligned}\log(\xi_k) = &- 1.28 + 0.0009 \cdot \mathrm{Slope}_k^2 \\ &+ 0.98 \cdot \mathrm{dGCT}_{k,2} \\ &+ 1.66 \cdot \mathrm{dGCT}_{k,3} \\ &+ 1.38 \cdot \mathrm{dGCT}_{k,4} \\ &- 0.0009 \cdot (\mathrm{Slope}_k^2 : \mathrm{dGCT}_{k,2}) \\ &- 0.0018 \cdot (\mathrm{Slope}_k^2 : \mathrm{dGCT}_{k,3}) \\ &- 0.0006 \cdot (\mathrm{Slope}_k^2 : \mathrm{dGCT}_{k,4}) \\ &+ \varepsilon_k \,. \end{aligned} \quad (4)$$

Again, model assumptions are not violated and the residuals are spatially not autocorrelated. The model explains 58 % of the total variability in the range, the adjusted R^2 equals 49 %. The model is significant ($p < 10^{-4}$). The confidence intervals of the linear model are shown in Table 3.

4 Discussion

4.1 Inter-footprint variability

While our measurements have a high reliability due to their spatial density, their temporal support of only one full year needs to be kept in mind. As previous studies have demonstrated, considerable inter-annual variability of ground temperatures (Isaksen et al., 2002; Hoelzle et al., 2003; Gruber et al., 2004a; Brenning et al., 2005; Etzelmüller et al., 2007; Hipp et al., 2011) depending especially on snow conditions, absolute values need to be interpreted with caution.

4.1.1 Elevation and temperature lapse rate

MAGST decreases with a lapse rate of $-5.6\,^{\circ}\mathrm{C\,km^{-1}}$. While this overall value lies within the range of MAAT lapse rates reported for the Alps by Rolland (2002) and MAGST lapse rates of $-4\,^{\circ}\mathrm{C\,km^{-1}}$ to $-7\,^{\circ}\mathrm{C\,km^{-1}}$ found in the literature (Powell et al., 1988; Šafanda, 1999), it should not indicate that ground temperature gradients are exclusively tied to those of the air. The complex coupling between atmosphere and subsurface can results in markedly differing lapse rates depending on ground type, topography and snow cover.

4.1.2 Aspect, slope and incoming solar radiation

Exposition to the sun has a large influence, resulting in a difference of 1 °C between north and south facing slopes, if the slopes are rather gentle. Steep slopes however show a much larger variations between north and south, resulting in differences of 2 °C for 10 ° steep slopes, and up to 5 °C for 40 ° steep slopes, which can be seen in the interaction term Slope : cos(Aspect) in Eq. 3. This clearly shows the influence of the incoming solar radiation on GSTs, since northern exposed, steep slopes receive almost no direct solar radiation (especially in winter time), in contrast to more gentle slopes. South-exposed slopes show an opposite behaviour: depending on the angle of the incoming solar radiation (and thus the season), steeper slopes receive more radiation and accumulate less snow than gentle slopes, resulting in faster snow melting and thus warming of the ground in spring. This increased difference in MAGST for north-south variations for steep slopes is in accordance with the findings for steep rock (cf., Gruber et al., 2004b; PERMOS, 2010). East exposed slopes are approximately 0.8 °C warmer than west exposed slopes, which can possibly be attributed to the formation of convective clouds during afternoons. Since the interaction of slope and the sine of aspect is not significant, the coefficient of the sine is interpreted as a mean difference between all west- and east-exposed slopes.

4.1.3 Slope and snow

The re-distribution of snow by avalanches, which results in higher snow depths at the rather gentle slopes, would result in a cooling of gentle slopes in late spring, as it is suggested by the model for south-facing slopes (a 40 ° steep slope is predicted to be around around 2 °C warmer than a 10 ° slope on a south face). At north-exposed slopes, the contrast is predicted (the steeper slope is around 1.5 °C colder than the gentle slope). This may be mainly explained with solar radiation (see above). However, the interactions between snow cover and ground surface temperatures are complex. A thick snow cover in early winter insulates the ground from cold air temperatures. On the other hand, a thin snow cover can cool the ground during winter due to the high albedo of snow. Through modeling experiments, Bartlett et al. (2004) have shown that especially the timing and the duration of the snow cover have a large, non-linear influence on MAGST, and that snow cover can produce both a cooling and a warming of the GST in respect to the air temperature.
Wind plays an important role determining snow depths and snow water equivalent (Föhn and Meister, 1983). The influence of wind on the snow distribution is strongly determined by terrain parameters, such as slope, aspect and curvature. However, since curvature does not significantly determine MAGST in Model (3), and since the influence of slope and aspect are already discussed above, the influence of wind on MAGST is not discussed separately.

4.1.4 Ground cover type

The influence of near-surface material on MAGST detected in this study (around 1.6 °C smaller in large blocks than at meadow sites) is supported by the findings of Hoelzle et al. (2003) and Gruber and Hoelzle (2008) for the Alps. Higher differences of around 4 °C to 7 °C of MAGST between blocky material and finer-grained soils were found by Harris (1996) and Harris et al. (1998) in Kunlun Shan, China, and the Rocky mountains, Canada. This effect can be attributed to various processes (Gruber and Hoelzle, 2008), such as the ventilation of cold air below the snow cover on block fields or contrasts in thermal conductivity. Furthermore, moisture and water content encountered in the upper layer of the ground play a crucial role for GSTs. Temperatures in moisture-rich ground drop less quickly due to the energy release during the phase change from water to ice. On the other hand, a lot of energy is needed in spring time to melt ice contained in the ground. In contrast to the negative coefficient of dGCT3, the coefficient for dGCT2 is positive. Since this coefficient is not significantly different from zero on one hand, and its value is small, this is not further interpreted. Similarly, we do not treat the coefficient of dGCT4, since GCT4 consists of all ground cover types that could not be classified properly into the three classes.

4.2 Intra-footprint variability

The variability of MAGST was defined as the range of the MAGST at one footprint. We found that MAGST can vary from 0.2 °C up to 2.5 °C within $100\,\mathrm{m^2}$. The variability is larger at footprints with large boulders and in steep terrain (Model (4)). These fine-scale variations can be attributed to differing ground properties, water availability, heterogeneous snow cover, solar radiation and local shading of small to medium boulders, etc. However, the variability is small in homogeneous grass sites. Within large blocks, logger placement probably also has an effect on intra-footprint variability due to the difficulty of defining the surface. Snow distribution affects MAGST variability strongly, and is likely to be more variable at steep slopes and in rough terrain. Model (4) indicates that especially in blocky material and

in steep slopes, a measurement might not represent its surrounding convincingly, and that the replication of a measurement would yield important additional information.

This result and the outcomes of Sect. 4.1 support the importance of the statement made by Gupta et al. (2005). When modeling permafrost conditions and comparing the outputs to a (point) measurement, we should keep in mind that the measurement only to a certain degree represents its surroundings. This not only applies for GSTs, but also at greater depths: even though temperatures integrate over larger surface areas and are thus not that susceptible to changes at the surface, ground temperatures might still vary considerably within some meters of distance. The uncertainty in measurements due to fine-scale variations can influence the outputs of permafrost models of any order of complexity; such as statistical models which are often based on and fitted to BTS or GST measurements (Haeberli, 1973; Keller, 1992; Boeckli et al., 2011) on one hand, and also more physically-based models used to estimate ground temperatures, active layer thicknesses and permafrost evolution (Zhang et al., 2003; Gruber et al., 2004a; Heggem et al., 2006; Nötzli et al., 2007; Farbrot et al., 2007; Etzelmüller et al., 2011; Hipp et al., 2011), which are often fitted to measurements of a few boreholes and extrapolated in space and time.

4.3 Findings in relation to previous works

Many studies addressing GST, GT and BTS variability due to solar radiation, snow cover, humidity, vegetation, etc. have been performed at diverse locations all over the world (Ishikiwa and Hirakawa, 2000; Heggem et al., 2006; Bonnaventure and Lewkowicz, 2008), and recently, even below the tree line (Lewkowicz and Bonnaventure, 2011). In this section, the findings discussed in Sect. 4.1 are related to similar studies concerning GST and BTS measurements.

As we have seen, measured MAGST varies up to 9 °C in an area of approximately 16 km^2. However, elevation only explains 33 % of the variability in MAGST. We can observe in Fig. 6 that MAGST varies more than 6 °C within one elevational band (2600 m to 2900 m). A similar pattern has been found by Etzelmüller et al. (2007, Fig. 4a) in Iceland, where MAGST varies around 6 °C within 800 m a.s.l. to 1000 m a.s.l. Since these measurements cover three years, this variability was mainly attributed to differing snow cover. However, the scatter within one year can also be attributed to the topographic variability, supporting the findings made in this study. In contrast to the small correlation with elevation found in this study and by Gruber and Hoelzle (2001), where elevation explained 31 % of the variability of BTS measurements performed in the upper Matter Valley, Switzerland, Isaksen et al. (2002) analysed hundreds of BTS measurements in Southern Norway and found a high correlation of 91 %. The high correlation by Isaksen et al. (2002) was attained through a grouping of the BTS measurements following Hoelzle (1992), in contrast to the correlations of around 60 % reached before the grouping. The relationship to aspect or potential incoming solar radiation was estimated to be very low (Isaksen et al., 2002), the analysis is however reported to be not representative due to missing measurements towards south and west exposed slopes. Further, Hauck et al. (2004) estimated high correlations of MAGST with elevation (more than 90 %), but attribute this to the fact that the measurements are placed along an altitudinal transect, but do not differ much in aspect or slope.

In the context of previous works, the findings presented in this study demonstrate:

a. The importance of the systematic approach when distributing the measurement devices to capture the influence of the topographic variables. The coefficients estimated by the multiple regression Model 3 are reasonable, the model captures the influence of the topography quite well. For further analyses, the approach could even be expanded by for example integrating more samples of GCT3.

b. Simple regression analyses are not able to capture the influence of diverse predictors on a predictand, in contrast to multiple regression. In this study, correlation of MAGST with the cosine of the aspect reaches only 24 %, and correlations with the sine are even less than 1 %. Concluding that the topographic variables do not satisfyingly describe MAGST would be easy, since correlations to elevation (33 %) and slope (less than 1 %) are also small. Multiple linear regression allowed to include the dummy variable GCT, and further accounts for interactions and non-linearities, resulting in a robust model enabling new insight.

5 Conclusions

The use of iButtons to intensively measure spatially-distributed GST was successful and pouches have shown to be very important. iButtons measure temperature with an accuracy of ± 0.125 °C. The experiment design was useful to both investigate the dependence of MAGST on topography, and to study fine scale variability of MAGST.

The use of multiple linear regression has shown that MAGST variability can be explained with the topographic variables elevation, slope, aspect and ground cover type. The model shows that MAGST are 1.6 °C to 2.2 °C higher in soil than within coarse blocks. South-exposed slopes are in general warmer than north facing slopes, however the difference changes with slope angle. East-exposed slopes are around 0.8°C warmer than west-exposed slopes. The terrain curvature and the sky view factor have no significant influence on MAGST in this model. Over the whole study area, measured MAGST variations go up to 9 °C.

MAGST vary also at very fine scales: even in homogeneous areas, variations amount to more than 2.5 °C at distances of

less than ≈14 m at steep slopes or in terrain of large blocks. This is one fourth of the variation encountered over the whole study area, and is similar to the modelled north-south differences of 15 ° slopes.

This study indicates that validation and calibration of grid-based models using measurements has to be performed with caution. The question of representativeness of a measurement location for its surroundings is often unclear. Since environmental variables vary strongly at even very fine scales, model validation and calibration with measurements of these variables can strongly be biased. Repeated measuring at different scales allows to estimate the natural variability of a variable, and thereby to improve model validation.

6 Data availability

The measurements, the meta data and the source code of the presented statistical analyses are published as supplementary material. The data is ordered according to the footprint names (i.e., all measurements taken at footprint AA are found in the file data_AA.csv). Each file contains the temperature measurements of all iButtons that were placed within that footprint together with the time stamps. The file Footprint_Metadata.csv contains the meta data shown in Table 1 plus sky view factor and different curvature indices. Additionally, a horizon file of each footprint is given (called hor_AA.txt for footprint AA). The second column in the horizon file indicates the elevation of the surrounding terrain above the horizon in direction of the azimuth given in the first column. The file src_ibutton.r contains the R-code. The two files meta.csv and meta_coord.csv are used as input to the code.

Supplementary material related to this article is available online at: http://www.the-cryosphere.net/5/431/2011/ tc-5-431-2011-supplement.zip.

Acknowledgements. The authors are grateful for the support given by the Corvatschbahnen, the developers of iAssist Guido Hungerbühler, Oliver Knecht and Suhel Sheikh, as well as Vanessa Wirz, Marlene Scheel, Christina Lauper and Marc-Olivier Schmid and everybody else who helped to distribute and refind the iButtons. The constructive comments given by the two referees B. Etzelmüller and I. Berthling are greatly acknowledged. This project was funded by the Swiss National Science Foundation (SNSF) via the NCCR MICS project PermaSense and the project CRYOSUB (Mountain Cryosphere Subgrid Parameterization and Computation, 200021_121868). All statistical analyses were performed with R (www.cran.r-project.org).

Edited by: T. Zhang

References

Akaike, H.: A new look at the statistical model identification, IEEE Trans. Autom. Control, 19, 716–723, 1973.

Bartlett, M. G., Chapman, D. S., and Harris, R. N.: Snow and the ground temperature record of climate change, J. Geophys. Res., 109, F04008, doi:10.1029/2004JF000224, 2004.

Boeckli, L., Brenning, A., Gruber, S., and Noetzli, J.: A statistical permafrost distribution model for the European Alps, The Cryosphere Discuss., 5, 1419–1459, doi:10.5194/tcd-5-1419-2011, 2011.

Bonnaventure, P. B. and Lewkowicz, A. G.: Mountain permafrost probability mapping using the BTS method in two climatically dissimilar locations, northwest Canada, Can. J. Earth Sci., 45, 443–455, 2008.

Brenning, A., Gruber, S., and Hoelzle, M.: Sampling and statistical analyses of BTS measurements, Permafrost Periglac., 16, 383–393, 2005.

Danby, R. K. and Hik, D. S.: Responses of white spruce (Picea Glauca) to experimental warming at a subarctic alpine treeline, Global Change Biol., 13, 437–451, 2007.

Etzelmüller, B., Farbrot, H., Gudmundsson, A., Humlum, O., Tveito, O. E., and Björnsson, H.: The regional distribution of mountain permafrost in Iceland, Permafrost Periglac., 18, 185–199, 2007.

Etzelmüller, B., Schuler, T. V., Isaksen, K., Christiansen, H. H., Farbrot, H., and Benestad, R.: Modeling the temperature evolution of Svalbard permafrost during the 20th and 21st century, The Cryosphere, 5, 67–79, doi:10.5194/tc-5-67-2011, 2011.

Föhn, P. and Meister, R.: Distribution of snow drifts on ridge slope: measurements and theoretical approximations, Ann. Glaciol., 4, 52–57, 1983.

Farbrot, H., Etzelmüller, B., Schuler, T. V., Gudmundsson, A., Eiken, T., Humlum, O., and Björnsson, H.: Thermal characteristics and impact of climate change on mountain permafrost in Iceland, J. Geophys. Res., 112, F03S90, doi:10.1029/2006JF000541, 2007.

Gorbunov, A. P., Marchenko, S. S., and Seversky, E. V.: The thermal environment of blocky materials in the mountains of Central Asia, Permafrost Periglac., 15, 95–98, 2004.

Gruber, S.: Mountain permafrost: Transient spatial modelling, model verification and the use of remote sensing, Ph.D. thesis, University of Zurich, 2005.

Gruber, S. and Haeberli, W.: Permafrost in steep bedrock slopes and its temperature-related destabilization following climate change, J. Geophys. Res., 112, F02S18, doi:10.1029/2006JF000547, 2007.

Gruber, S. and Hoelzle, M.: Statistical Modelling of Mountain Permafrost Distribution: Local Calibration and Incorporation of Remotely Sensed Data, Permafrost Periglac., 12, 69–77, doi:10.1002/ppp 374, 2001.

Gruber, S. and Hoelzle, M.: The cooling effect of coarse blocks revisited: a modeling study of a purely conductive mechanism, in: 9th International Conference on Permafrost, 2008.

Gruber, S., Peter, M., Hoelzle, M., Woodhatch, I., and Haeberli, W.: Surface Temperatures in steep alpine rock faces – a strategy for regional-scale measurement and modelling, in: Proceedings of the 8th International Conference on Permafrost, 2003.

Gruber, S., Hoelzle, M., and Haeberli, W.: Permafrost thaw and destabilization of Alpine rock walls in the hot summer of 2003,

Geophys. Res. Lett., 31, L13504, doi:10.1029/2004GL020051, 2004a.

Gruber, S., King, L., Kohl, T., Herz, T., Haeberli, W., and Hoelzle, M.: Interpretation of Geothermal Profiles Perturbed by topography: the alpine permafrost boreholes at Stockhorn plateau, Switzerland, Permafrost Periglac., 15, 349–357, 2004b.

Grünewald, T., Schirmer, M., Mott, R., and Lehning, M.: Spatial and temporal variability of snow depth and ablation rates in a small mountain catchment, The Cryosphere, 4, 215–225, doi:10.5194/tc-4-215-2010, 2010.

Gupta, H. V., Beven, K., and Wagener, T.: Model calibration and uncertainty estimation, 2005.

Haeberli, W.: Die Basis-Temperatur der winterlichen Schneedecke als möglicher Indikator für die Verbreitung von Permafrost in den Alpen, Zeitschrift für Gletscherkunde und Glaziologie, 9, 221–227, 1973.

Haeberli, W.: Untersuchung zur Verbreitung von Permafrost zwischen Flüelapass und Piz Grialetsch (Graubünden), Ph.D. thesis, Universitiy of Basel, 1975.

Harris, S. A.: Lower mean annual ground temperature beneath a block stream in the Kunlun Pass, Qinghai Province, China, 1996.

Harris, S. A., Cheng, G., Zhao, X., and Yongqin, D.: Nature and Dynamics of an Active Block Stream, Kunlun Pass, Qinghai Province, People's Republic of China, Geogr. Ann. A, 80, 123–133, 1998.

Harris, C., Arenson, L. U., Christiansen, H. H., Etzelmüller, B., Frauenfelder, R., Gruber, S., Haeberli, W., Hauck, C., Hölzle, M., Humlum, O., Isaksen, K., Kääb, A., Kern-Lötschg, M. A., Lehning, M., Matsuoka, N., Murton, J. B., Nötzli, J., Phillips, M., Ross, N., Seppälä, M., Springman, S. M., and Vonder Mühll, D.: Permafrost and climate in Europe: Monitoring and modelling thermal, geomorphological and geotechnical responses, Earth-Sci. Rev., 92, 117–171, doi:10.1016/j.earscirev.2008.12.002, 2009.

Hauck, C., Isaksen, K., Vonder Mühll, D., and Sollid, J. L.: Geophysical Surveys Designed to Delineate the Altitudinal Limit of Mountain Permafrost: an Example from Jotunheimen, Norway, Permafrost Periglac., 15, 191–205, 2004.

Heggem, E. S. F., Etzelmüller, B., Anarmaa, S., Sharkhuu, N., Goulden, C. E., and Nandinsetseg, B.: Spatial distribution of ground surface temperatures and active layer depths in the Hövsgöl area, northern Mongolia, Permafrost Periglac., 17, 357–369, doi:10.1002/ppp.568, 2006.

Hipp, T., Etzelmüller, B., Farbrot, H., and Schuler, T. V.: Modelling the temperature evolution of permafrost and seasonal frost in southern Norway during the 20th and 21st century, The Cryosphere Discuss., 5, 811–854, doi:10.5194/tcd-5-811-2011, 2011.

Hoelzle, M.: Permafrost occurrence from BTS measurements and climatic parameters in the Eastern Swiss Alps, Permafrost Periglac., 3, 143–147, 1992.

Hoelzle, M. and Gruber, S.: Borehole and ground surface temperatures and their relationship to meteorological conditions in the Swiss alps, in: 9th International Conference on Permafrost, 2008.

Hoelzle, M., Vonder Mühll, D., and Haeberli, W.: Thirty years of permafrost research in the Corvatsch-Furtschellas area, Eastern Swiss Alps: a review, Norsk Geogr. Tidsskr., 56, 137–145, 2002.

Hoelzle, M., Haeberli, W., and Mittaz, C.: Miniature ground temperature data logger measurements 2000–2002 in the Murtèl-Corvatsch area, Eastern Swiss alps, in: 8th International Conference on Permafrost, Proceedings, edited by: Phillips, M., Springman, S., and Arenson, L., 419–424, Swets & Zeitlinger: Lisse, Zürich, 2003.

Isaksen, K., Hauck, C., Gudevang, E., and Oedegaard, R. S.: Mountain permafrost distribution in Dovrefjell and Jotunheimen, southern Norway, based on BTS measurements and 2D tomography data, Norsk Geogr. Tidsskr., 56, 122–136, 2002.

Ishikiwa, M. and Hirakawa, K.: Mountain permafrost distribution based on BTS measurements and DC resistivity soundings in the Daisetsu Mountains, Hokkaido, Japan, Permafrost Periglac., 11, 109–123, 2000.

Juliussen, H. and Humlum, O.: Thermal regime of openwork block fields on the mountains Elaahogna and Solen, central-eastern Norway, Permafrost Periglac., 19, 1–18, doi:10.1002/ppp.607, 2008.

Keller, F.: Automated mapping of mountain permafrost using the program PERMAKART within the Geographical Information System ARC/INFO, Permafrost Periglac., 3, 133–138, 1992.

Keller, F. and Gubler, H. U.: Interaction between snow cover and high mountain permafrost, Murtèl-Corvatsch, Swiss Alps, in: Proceedings VI. International Conference on Permafrost, Beijing, South China University of Technology Press., 1993.

Keller, M., Hungerbühler, G., Knecht, O., Skeikh, S., Beutel, J., Gubler, S., Fiddes, J., and Gruber, S.: iAssist: Rapid Deployment and Maintenance of Tiny Sensing Systems, 2010.

Lewkowicz, A. G.: Evaluation of Miniature Temperature-loggers to Monitor Snowpack Evolution at Mountain Permafrost Sites, Northwestern Canada, Permafrost Periglac., 19, 323–331, 2008.

Lewkowicz, A. G. and Bonnaventure, P. B.: Equivalent Elevation: A New Method to Incorporate Variable Surface Lapse Rates into Mountain Permafrost Modelling, Permafrost Periglac., 22, doi:10.1002/ppp.720, 2011.

Luetschg, M., Lehning, M., and Haeberli, W.: A sensitivity study of factors influencing warm/thin permafrost in the Swiss Alps, J. Glaciol., 54, 696–704, 2008.

Nelson, F. E., Hinkel, K. M., Shiklomanov, N. I., Mueller, G. R., Miller, L. L., and Walker, D. A.: Active-layes thickness in north central Alaska: Systematic sampling, scale, and spatial autocorrelation, J. Geophys. Res., 103, 28963–28973, 1998.

Nötzli, J., Gruber, S., Kohl, T., Salzmann, N., and Haeberli, W.: Three-dimensional distribution and evolution of permafrost temperatures in idealized high-mountain topography, J. Geophys. Res., 112, F02S13, doi:10.1029/2006JF000545, 2007.

Oliver, M. A. and Webster, M.: Combining Nested and Linear Sampling for Determining the Scale and Form of Spatial Variation of Regionalized Variables, Geogr. Anal., 18, 227–242, 1986.

PERMOS: Permafrost in Switzerland 2006/2007, in: Glaciological Report (Permafrost) No. 8/9 of the Cryospheric Commission of the Swiss Academy of Sciences, edited by: Nötzli, J. and Vonder Mühll, D., 2010.

Powell, W. G., Chapman, D. S., Balling, N., and Beck, A. E.: Handbook of terrestrial heat-flow density determination: with guidelines and recommendations of the International Heat Flow Commission, chap. Continental heat-flow density, 167–222, Kluwer Academic Publishing, 1988.

R Development Core Team: R: A language and environment for statistical computing, R Foundation for Statistical Computing,

ISBN 3-900051-07-0, 2011.

Rolland, C.: Spatial and seasonal variations of air temperature lapse rates in alpine regions, J. Climate, 16, 1032–1046, 2002.

Schwarb, M., Frei, C., Schär, C., and Daly, C.: Mean annual precipitation throughout the European Alps 1971–1990, 2000.

Stocker-Mittaz, C., Hoelzle, M., and Haeberli, W.: Modelling alpine permafrost distribution based on energy-balance data: a first step, Permafrost Periglac., 13, 271–282, 2002.

Šafanda, J.: Ground surface temperature as a function of the slope angle, Tectonophysics, 360, 367–375, 1999.

Zhang, T.: Influence of the seasonal snow cover in the ground thermal regime: An overview, Rev. Geophys., 43, doi:10.1029/2004RG000157, 2005.

Zhang, Y., Chen, W., and Cihlar, J.: A process-based model for quantifying the impact of climate change on permafrost thermal regimes, J. Geophys. Res., 108, doi:10.1029/2002JD003354, 2003.

Publication II

Schmid, M.-O., S. Gubler, J. Fiddes, and S. Gruber (2012), Inferring snowpack ripening and melt-out from distributed measurements of near-surface ground temperatures, *The Cryosphere*, *6*, 1127–1139, doi: 10.5194/tc-6-1127-2012

Contributions:

- Supervision of master thesis that forms the basis of the publication with J. Fiddes and S. Gruber
- Support in developing R-code for data analyses
- Manuscript review

The Cryosphere, 6, 1127–1139, 2012
www.the-cryosphere.net/6/1127/2012/
doi:10.5194/tc-6-1127-2012

The Cryosphere

Inferring snowpack ripening and melt-out from distributed measurements of near-surface ground temperatures

M.-O. Schmid, S. Gubler, J. Fiddes, and S. Gruber

Department of Geography, University of Zürich, Switzerland

Correspondence to: M.-O. Schmid (marc-olivier.schmid@geo.uzh.ch)

Received: 13 January 2012 – Published in The Cryosphere Discuss.: 10 February 2012
Revised: 25 August 2012 – Accepted: 10 September 2012 – Published: 15 October 2012

Abstract. Seasonal snow cover and its melt regime are heterogeneous both in time and space. Describing and modelling this variability is important because it affects diverse phenomena such as runoff, ground temperatures or slope movements. This study presents the derivation of melting characteristics based on spatial clusters of ground surface temperature (GST) measurements. Results are based on data from Switzerland where ground surface temperatures were measured with miniature loggers (iButtons) at 40 locations referred to as footprints. At each footprint, up to ten iButtons have been distributed randomly over an area of 10 m × 10 m, placed a few cm below the ground surface. Footprints span elevations of 2100–3300 m a.s.l. and slope angles of 0–55°, as well as diverse slope expositions and types of surface cover and ground material. Based on two years of temperature data, the basal ripening date and the melt-out date are determined for each iButton, aggregated to the footprint level and further analysed. The melt-out date could be derived for nearly all iButtons; the ripening date could be extracted for only approximately half of them because its detection based on GST requires ground freezing below the snowpack. The variability within a footprint is often considerable and one to three weeks difference between melting or ripening of the points in one footprint is not uncommon. The correlation of mean annual ground surface temperatures, ripening date and melt-out date is moderate, suggesting that these metrics are useful for model evaluation.

1 Introduction

Seasonal snowmelt is important for mountain hydrology and water supply to lowlands (Viviroli and Weingartner, 2004); it can contribute to the triggering of landslides and debris flows (Iverson et al., 1997; Wirz et al., 2011) and it is linked to many other physical and ecological processes and phenomena. Depending on environmental conditions, two distinct points in time can be recognized that help to quantify the temporal patterns of snowmelt. The melt-out date (MD) describes the time when the snow cover is depleted and no further release of meltwater occurs, allowing the ground surface to warm above 0 °C. The basal-ripening date (RD) describes the time when a frozen ground surface is warmed to 0 °C by melt-water percolation or by strong rain-on-snow events (cf. Westermann et al., 2011). RD can only be detected in situations having negative temperatures at the snow-ground interface. In this paper, we use near-surface ground temperature, measured at depths of a few centimetres, as a proxy of ground surface temperature (GST).

MD can be investigated using optical space-borne (Bitner et al., 2002; Li and Wang, 2011; Parajka and Blöschl, 2008) or ground-based (Schmidt et al., 2009) remote sensing. Furthermore, attempts have been made to detect RD with optical space-borne remote sensing (Foster et al., 2011; Lampkin and Yool, 2004). On the ground, measurements are feasible by means of miniature temperature loggers (Etzelmüller et al., 2007; Gadek and Leszkiewicz, 2010; Hoelzle et al., 1999, 2003), hand tests (Techel and Pielmeier, 2011) or as part of more comprehensive measurement stations (Lehning et al., 1999). First studies using GST to monitor snow cover evolution were carried out in North America (Lundquist and Lott, 2008; Tyler et al., 2008). Patterns of snowpack evolution and melting are usually heterogeneous both in time and space, especially in mountain regions. This is because topography influences snow redistribution by wind and avalanches, surface micrometeorology and also the

distribution of ground material. Grid-based snow cover distribution models are often used to estimate snow cover evolution (e.g. Bartelt and Lehning, 2002; Blöschl et al., 1991a, b; Lehning et al., 2002a, b; Luce et al., 1998) or ground temperatures (Dall'Amico et al., 2011; Luetschg and Haeberli, 2005). Scales of gridded applications range from grid sizes of few meters (e.g. Groot Zwaaftink et al., 2011; Marsh et al., 2012) to tens or hundreds of kilometers in climate models (e.g. Best et al., 2011; Essery and Clark, 2003; Tribbeck et al., 2004). Often, the interaction with vegetation (e.g. Endrizzi and Marsh, 2010; Rutter et al., 2009) and processes of snow redistribution (e.g. Groot Zwaaftink et al., 2011; Pomeroy et al., 1997) are simulated as well. While Anderton et al. (2002) show that the micro-scale spatial variability of the snow cover needs to be taken into account to model snowmelt at larger scales, most data products for the evaluation of models are based on satellite data with rather coarse resolution (Brown, 2000; Dyer and Mote, 2006; Gutzler and Rosen, 1992; Scherrer, 2006). In contrast to this, the role of topography and fine-scale variability of snow cover evolution is investigated in a number of local studies by, e.g. Jost et al. (2007), López-Moreno et al. (2011), Grünewald et al. (2010), and Schmidt et al. (2009).

In the validation of grid-based models, point measurements are often implicitly assumed to adequately represent the area around them that constitutes a model cell. Variation at distances smaller than the grid used, however, can confound such studies by hiding the larger-scale landscape signal under investigation. This is especially true when small numbers of single-point measurements distributed over a landscape are used, which is a typical situation due to the high cost of site access in many cases. Gubler et al. (2011) showed that even within a distance of less than 15 m, mean annual ground surface temperatures (MAGST) can exhibit a range of more than 2 °C. Based on the same measurements but with a duration of two years, we investigate the potential of GST to provide reliable, inexpensive and distributed information about MD and RD. Specifically, we investigate (a) how to derive MD and RD in diverse topographic situations, and (b) how fine-scale variability affects the relationship between point measurements and grid-based representations with the aim to inform studies that validate grid-based models based on few point measurements.

2 Data

2.1 Research area and meteorological conditions during the measurement period

This study is based on the dataset described by Gubler et al. (2011) for which two measurement years are now available. The study area is situated around Piz Corvatsch, a mountain in the Eastern Swiss Alps, close to St. Moritz. The 0 °C isotherm of the mean annual air temperature (MAAT) is situated at an altitude of about 2200 m a.s.l. The investigation area extends above 3000 m a.s.l. and is partially subject to permafrost conditions. The western and northern flanks of Piz Corvatsch feature large debris slopes and several rock glaciers, whereas further south in the Furtschellas area, inactive and relict rock glaciers are present. Figure 1 shows a map of the measuring locations.

Air temperature from which the MAAT is derived is measured by MeteoSwiss at Piz Corvatsch in the research area and at the nearby weather stations Passo del Bernina and Samedan. The 2011 period (20 August 2010 to 19 August 2011) was between 0.2 °C and 0.47 °C warmer than the 2010 period (20 August 2009 to 19 August 2010). Both were warmer than the normal period 1961–1990. The snow cover development at nearby stations during both winters was relatively similar to the long-term average. Snow heights in winter 2009/2010 were slightly above average and in 2010/2011 slightly below average. MD at Passo del Bernina and Samedan was earlier in 2011 than in 2010 (Fig. 3). Both periods had strong snowfall outside the winter season: significant events occurred in mid June and early October 2010 (Pielmeier, 2011; Stucki, 2010).

2.2 Measurement design

Miniature temperature loggers iButton® DS1922L with a resolution of 0.0625 °C were programmed to record GST every three hours, allowing for more than one year of autonomous operation with the memory available. The accuracy is stated to be ±0.5 °C by the manufacturer and has been determined to be ±0.125 °C near 0 °C by Gubler et al. (2011). In July and August 2009, 390 iButtons were distributed within 40 so-called footprints. These span diverse topographic situations with elevations of 2100–3300 m a.s.l., slope aspects north, south, east, and west, slope angles of 0–55° and various ground cover types (GCT). Each footprint consists of up to ten iButtons randomly placed within 10 m × 10 m in order to capture small-scale variability. The devices were generally buried a few cm below the ground surface at locations with no fine-grained material (i.e. exposed bedrock), placed in voids in the ground. Programming and read-out were facilitated by the software iAssist (Keller et al., 2010). A digital elevation model with a resolution of 10 m (SwissPhoto) was used to derive elevation, slope angle and slope exposition of all footprints. The GCT classification defined by Schmid (2011) and Gubler et al. (2011) was used: GCT1 is fine-grained, sometimes partly organic material; GCT3 consists of large boulders (e.g. on rock glaciers); and GCT2 is an intermediate type between the two. GCT4 is characterized by strongly heterogeneous and steep footprints partially composed of bedrock.

In July and August 2010, 368 of 390 iButtons were retrieved and contained GST measurements for one year. In August 2011, 357 iButtons were recovered and 355 contained complete GST time-series. The one-year periods used

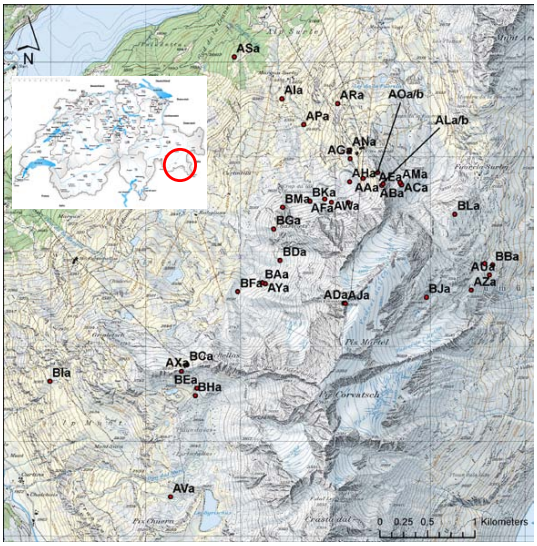

Fig. 1. Research area around Piz Corvatsch (south-eastern Switzerland) with locations of all footprints.

for analysis range from 20 August to 19 August and are here referred to as 2010 and 2011, indicating the year of data read-out. iButtons found on the surface during read-out were excluded from subsequent analysis because exposure to solar radiation may have affected their temperature. This resulted in 92 % (first year) and 89 % (second year) of valid time series. Data gaps during read-out have a maximum length of one day and are filled by linear interpolation between adjacent measurements. The analyses shown here are based on 343 iButtons from the 2010 period, 348 iButtons from 2011 and 338 iButtons with valid data spanning both years. The snow cover was measured at most sites during three campaigns in January, March and April in 2010 (Gubler et al., 2011; Schmid, 2011). At each measured footprint, ten snow-height measurements and one SWE measurement were made (Table 1). At all sites, a snow-free period occurs in late summer and autumn.

3 Methods

3.1 Melt-out date

Due to its low thermal conductivity, snow insulates the ground from the cold atmosphere during winter (Goodrich, 1982) and in several studies this effect is used to detect a snow cover based on GST time series. Based on the daily variance of GST, Danby and Hik (2007) considered a threshold of 1 °C (4 h sampling rate), and Schmidt et al. (2009) one of 0.09 °C (1 h sampling rate) to indicate snow-covered ground. Gadek and Leszkiewicz (2010) estimated the presence of a snow cover simply based on days with GST ≤ 0 °C. All three approaches are based on rather small range of environmental conditions and, when applied to the large dataset of this study yield only partially satisfying results. The following observations are made based on visually inspecting time series of GST and their daily variance: (a) most locations clearly show the presence of an insulating snow cover during winter, few locations clearly show the absence of it, and some appear to lie in between. (b) The beginning of a snow cover, which at the time may be thin and provide little insulation, is more difficult to detect than the date of its melt-out (MD). (c) Detection of MD based on daily variance alone is unreliable and leads to spurious snow-free periods during winter. Furthermore, snow-cover days are overestimated at locations with a generally low daily GST variance when using fixed thresholds. (d) Detection of MD based on temperature alone is unreliable because low-elevation sites can maintain positive temperatures a few centimeters below the ground surface for prolonged periods when a thick snow cover is present.

As the detection of MD requires an insulating snow cover, we define a snow-cover reliability index (MDr) based on the mean daily standard deviation of GST during January, February and March:

Table 1. Snow measurements from winter 2009/10, all values are in mm. Snow heights are based on 10 randomly chosen measurement points. SWE was measured in the centre of each footprint and adapted accordingly to the mean height.

Foot-	30.01.–02.02.2010		12.–14.03.2010		23.–25.4.2010	
print	height	SWE	height	SWE	height	SWE
AA	600	160	620	214	NA	NA
AD	135	50	225	60	142	45
AE	1210	508	NA	NA	NA	NA
AF	1406	NA	NA	NA	NA	NA
AH	1350	466	1560	531	NA	NA
AI	NA	NA	1490	NA	1160	431
AJ	790	NA	460	172	NA	NA
AK	1460	435	NA	NA	NA	NA
AL	1833	627	NA	NA	NA	NA
AN	1395	457	1660	564	2050	741
AP	1320	453	1590	607	1685	528
AQ	1067	276	2080	592	NA	NA
AR	1450	549	1240	488	1810	711
AS	1460	373	1560	535	1190	394
AT	1580	463	520	182	NA	NA
AU	1005	283	NA	NA	NA	NA
AW	1600	500	1580	564	NA	NA
AY	1610	541	1830	614	NA	NA
AZ	1705	537	1920	714	1915	720
BA	1210	332	870	249	NA	NA
BC	1855	594	1800	617	2500	1210
BD	1200	315	1540	607	NA	NA
BE	905	266	1240	448	718	335
BH	1145	415	1870	788	2009	798
BJ	1320	386	1943	695	1820	663

$$\mathrm{MDr} = 0.2 - \sigma\,(\mathrm{GST}_{\mathrm{Jan–Mar}})\,. \quad (1)$$

This threshold of 0.2 has been determined subjectively, based on visual interpretation of GST and its daily variance during winter. The sensitivity to the chosen threshold is relatively low, with a change of the sample size selected being smaller than 10 % when changing the threshold by 50 % (Fig. 2). If MDr is greater than zero, we assume that the insulation effect of the snow cover is sufficient to allow the reliable derivation of MD. For iButtons with MDr > 0, days with a snow cover were detected based on the daily standard deviation. If the daily mean GST is positive, we chose a threshold of 0.1 °C, and if the daily mean GST is negative, we chose a threshold of 0.3 °C. Two different thresholds are necessary because, for days with negative GST, mostly the thermal insulation of the snow cover affects the standard deviation. Positive GST, however, can only occur under a partly wet snow cover where temperature fluctuations are additionally damped by phase change. Spurious gaps were closed for days with GST ≤ 0.5 °C. Days with a maximum GST > 3 °C are considered snow-free based on observations at the lowest site (2100 m a.s.l.). MD is defined as the end date of the snow cover period with the longest duration. It is aggregated to the footprint level as a mean value. Where MD could not be detected for all iButtons in a footprint, it was calculated if at least five values were available.

3.2 Basal ripening date

In many places, temperatures below 0 °C seasonally prevail in the snowpack and the ground below (Gubler et al., 2011). Liquid water originating from surface melting or rain infiltrates and warms deeper layers through the release of latent heat during freezing (Westermann et al., 2011). Once the meltwater reaches the ground surface and warms it to 0 °C, the snowpack above is mostly isothermal at a temperature of 0 °C, with the exception of refreezing near the surface during clear nights or cold periods. This point in time, the ripening date (RD), is detected as the beginning of the zero curtain period (defined here as the duration of the zero curtain effect, which is the effect of latent heat in maintaining temperatures near 0 °C over extended periods in freezing or thawing soils, e.g. Outcalt et al., 1990) in spring and marks the beginning of meltwater runoff or percolation into the ground (Taras et al., 2002; Tyler et al., 2008). The development of preferential flow paths in snow (Williams et al., 2010) increases the lateral variability between cold and isothermal portions of the snowpack and ground below and, as a consequence, also the lateral variability of RD. Commonly, no cooling below 0 °C takes place at the ground surface after the RD; sometimes however, cold conditions can cause a complete refreezing of the melting snowpack and interrupt the zero curtain period in shallow ground levels below.

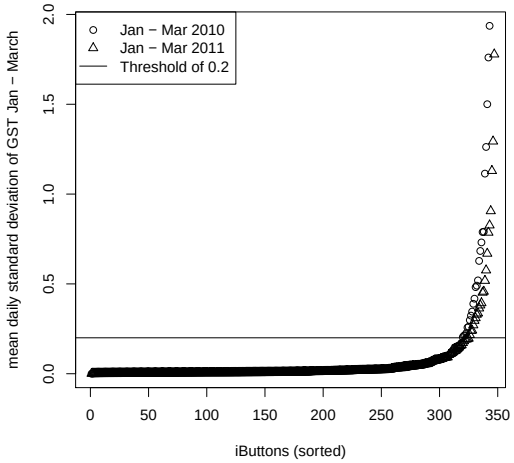

Fig. 2. Mean daily standard deviation of GST from January to March. The horizontal line indicates the threshold of 0.2. The obvious knee in the curve represents the separation between an insulating- and a non-insulating snow cover with one threshold. The sensitivity to the chosen threshold is relatively low, as shown by a change in the applied threshold of 50 % causes a change in the selected sample size of less than 10 %.

RD can only be determined together with MD for locations where the ground surface is frozen underneath the snowpack. This is expressed in the RD reliability index:

$$\mathrm{RDr} = \begin{cases} -50 - \mathrm{FDD} & \text{if } \mathrm{MDr} > 0 \\ 0 & \text{if } \mathrm{MDr} \le 0 \end{cases}, \quad (2)$$

where FDD is the sum of negative daily mean GST during the snow-cover period with the longest duration. Only for RDr > 0 is RD derived. This is because zero curtain periods during freezing can only be distinguished from those during thawing if the ground can clearly be detected as frozen in between. At many low-elevation footprints, iButtons did not record negative temperatures, making it impossible to detect the start of an isothermal snowpack.

Based on the calibration reported by Gubler et al. (2011), days with GST between −0.25 °C and 0.25 °C were defined as a zero curtain period. RD was then detected as the beginning of zero-curtain days after the longest period having a daily mean GST smaller than −0.25 °C. RD is aggregated to the footprint level as a mean value. Where RD could not be detected for all iButtons in a footprint, it was calculated if at least five values were available.

3.3 Mean annual ground surface temperature

Mean annual ground surface temperature (MAGST) is a useful measure characterising the ground thermal regime of a location. It was calculated as the mean of all measurements per iButton. Due to the fact that at all footprints at least five

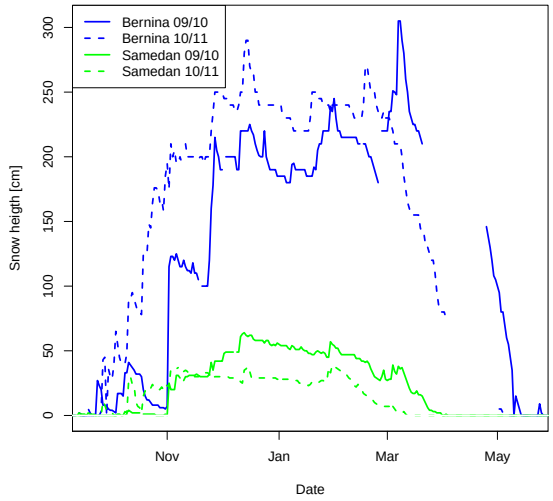

Fig. 3. Snow height at Passo del Bernina and Samedan during the winters 2009/10 and 2010/11 (source: MeteoSwiss).

measurement series were recorded, the MAGST could be aggregated to the footprint level at all locations.

3.4 Algorithm testing with modelled data

We tested our algorithm based on simulations for which MD can be determined independently of GST. We performed numerical experiments with the open-source and physically-based numerical model GEOtop that accounts for heat and water transfer in soil, including effects of phase change and partial saturation (Dall'Amico et al., 2011). GEOtop contains a multi-layer snowpack that accommodates compaction as well as water percolation and refreezing. The influence of topography on micro-climatology is parameterized, allowing for the solution of the surface energy balance for differing topographic situations, based on one driving climate time series (Endrizzi and Marsh, 2010). A distributed version of GEOtop exists but in this study, a one-dimensional mode was employed. In these experiments, the lower boundary condition was given by a zero heat and mass flux. Lateral drainage was parameterized by a free surface that can be placed at arbitrary distance below the surface. Snow was discretized into ten layers, which are finer near the interfaces with the atmosphere and the soil than in the middle of the snowpack. The thickness of the 14 soil layers was parameterized by where n is the layer number from the surface downwards, $a = 1.5$ governs the thickening of layers with depth and $z_{\min} = 20$ mm is the thickness of the top layer. The depth of the deepest node is 8.8 m. The system was initialized with a starting temperature of $-1\,^{\circ}$C and spun up from August 1986 to April 2005. Output was then generated for the period May 2005 to October 2011 with an interval of 3 h, corresponding to the iButton measurements. Model output consisted of mean ground temperatures at depths of 10, 50 and 100 mm as well as snow water equivalent (SWE). A large number of hypothetical points were simulated to test the robustness of the method. These were defined by elevation (2000 m, 2500 m, 3000 m, 3500 m), slope aspect (north, east, south, west), slope angle (0°, 20°, 40°), lateral drainage (free surface at 10 and 2000 mm depth), soil type (silt, sand, gravel, rock) and precipitation altered by a factor (0.5, 1, 2) to approximate high accumulation and low accumulation terrain facets.

The algorithm developed for the iButton dataset to detect MD was then driven with modelled ground temperatures and the results were compared to the MD based on the modelled SWE. Simulated points for which the minimum SWE during a year was larger than 0 were excluded.

This simulation-based approach is preferred over validation with field data because the scale difference between a ground temperature measurement and conventional snow height sensors is likely to challenge the interpretation of results. Usually installed at 4–7 m height, their opening angle of around 20° (e.g. SR50, Campbell Scientific) caused them to integrate over an area with an approximate diameter of 1.5–4 m, much larger than that measured by an iButton. A future option for validation is a high-resolution automatic camera pointed at one footprint containing several iButtons, but this has not been pursued in the current study.

4 Results

4.1 Algorithm testing

In Fig. 4, the difference between the MD based on GST and the MD based on the SWE is shown with simulated data from five years. The different boxes represent the modelled GST depths. The number of detected MD increases as the depth shifts from 10 mm to 50 mm to 100 m. The detected MD shifts slightly towards a later date with increasing depth. In general, detected MD from all depths fit very well with MD based on SWE with maximum differences of one day for 99 % of the simulated points at 10 mm; 97 % at 50 mm and 85 % at 100 mm depth.

4.2 General description

In Fig. 5, typical characteristics of the measured locations are exemplified: iButton ALa04 is located on a ridge composed of gravel. After the freezing of the ground in autumn, the GST is strongly damped with respect to the atmosphere during winter, indicating the presence of an insulating snow cover. In spring, a zero curtain period occurs. For this device it is possible to detect both the RD and the MD. iButton ASa10 is located in a forest glade at 2100 m a.s.l. The insulating snow cover prevents the ground from freezing, and therefore MD but not RD was detected. iButton AOa03 classified as GCT4 has a standard deviation of 0.19, which is the

Table 2. Standard deviations of the intra-footprint and inter-footprint scale.

Mean standard deviation	RD [days]		MD [days]		MAGST [C]	
	2010	2011	2010	2011	2010	2011
Intra-footprint	6	5	8	8	0.33	0.33
Inter-footprint	26	21	22	29	2.19	2.08

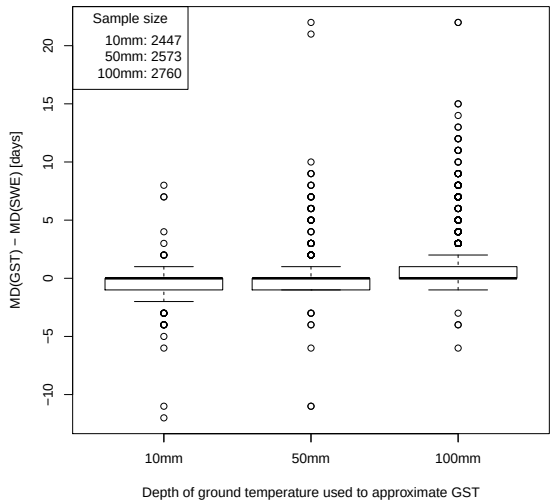

Fig. 4. MD based on SWE compared to MD based on GST from three different depths. Both SWE and GST were modelled with GEOtop. The length of the whiskers is 1.5 times the interquartile range.

highest value where we still predict an insulating snow cover. An overview with the number of valid iButtons per footprint and the number of detected MD and RD is in Table 3.

4.3 Intra-footprint variability

MD was detected in 2010 for 319 iButtons and in 2011 for 325. In both years, average values for footprint AGa and AOa were not calculated and in 2011 also AJa and AOb had to be excluded due to the absence of an insulating snow cover. The mean standard deviation of MD per footprint in both years is 8 days (Table 2). RD could be calculated only for approximately half the iButtons due to a lack of snow or ground freezing. Lack of snow was frequent on footprints of GCT 4 and lack of ground freezing mostly occurred at low-elevation sites. In 2010, RD could be calculated for 178 iButtons and aggregated for 20 footprints, and in 2011 for 167 iButtons or 16 footprints. A mean value per footprint over both years is calculated for 14 locations. The mean standard deviation of RD per footprint is 5 and 6 days. Table 2 shows the standard deviation to be expected within a radius of several meters, based on all footprints with at least

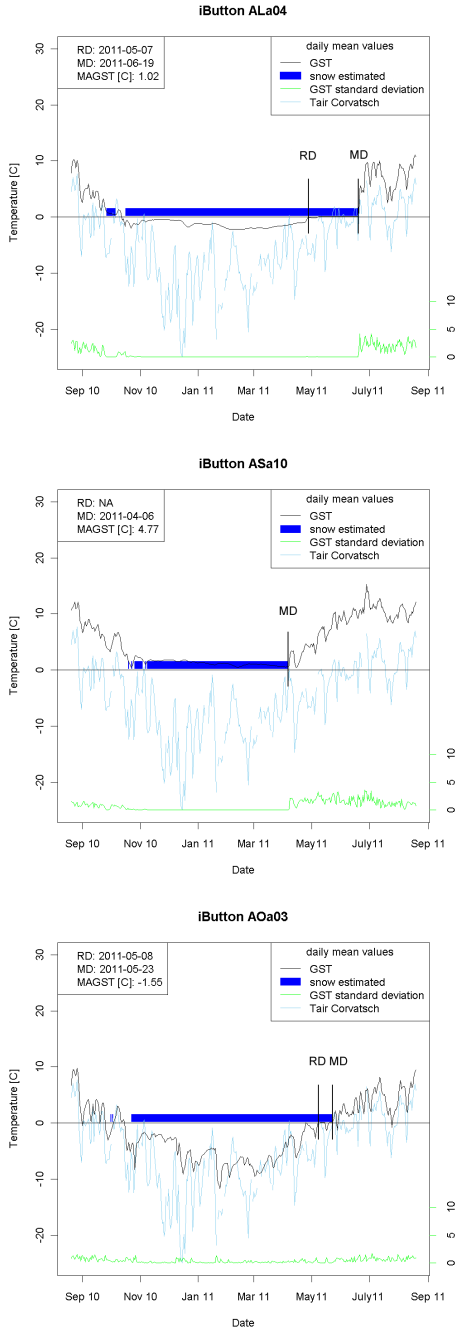

Fig. 5. Typical examples of temperature evolution. For all three iButtons an insulating snow cover is present. For ALa10, RD and MD are detected, whereas for ASa10, only MD can be detected. At AOa03, MD and RD were detected as well, but with a mean standard deviation of the GST (Jan–Mar) of 0.19, it is the location with the highest value where we still predict an insulation snow cover.

Table 3. List of footprints and the amount of GST, MD and RD values derived. The lack of an insulating snow cover resulted in iButtons where MD was not detected. The lack of a clearly frozen ground resulted in snow covered iButtons where RD was not detected, except for some locations with GCT4 where no zero curtain phase occurred (marked with *). Elevation, slope angle and slope exposition are based on a 10 m digital elevation model.

					2010			2011		
Footprint	Elevation	Slope	Aspect	GCT	GST	MD	RD	GST	MD	RD
AAa	2694	38	251	1	10	10	8	10	10	0
ABa	2745	16	96	2	10	10	3	10	10	5
ACa	2743	31	112	2	10	10	7	10	10	8
ADa	3303	29	263	4	10	5	5	10	8	7*
AEa	2826	29	290	1	10	9	9	10	10	10
AFa	2689	23	9	4	10	10	10	10	9	9
AGa	2664	48	243	4	10	2	2	10	3	3
AHa	2663	9	318	3	10	10	10	10	10	10
AIa	2307	18	330	1	4	4	0	6	6	2
AJa	3302	27	113	4	10	5	4*	10	4	2*
ALa	2824	14	347	1	4	4	4	4	4	4
ALb	2824	25	60	1	5	5	5	5	5	3
AMa	2738	30	333	2	10	10	10	10	10	10
ANa	2673	25	252	1	9	9	0	9	9	0
AOa	2811	36	64	4	5	2	2	5	1	1
AOb	2811	18	238	4	5	5	5	5	4	4
APa	2405	15	335	1	1	1	0	1	1	0
AQa	2729	29	12	3	10	10	10	10	10	10
ARa	2528	28	288	2	6	6	0	9	9	3
ASa	2100	35	315	1	6	6	0	7	7	0
ATa	2790	36	100	1	10	10	0	9	9	0
AUa	2773	33	88	3	10	10	10	10	10	10
AVa	2538	0	212	1	10	10	0	10	10	0
AWa	2700	19	333	3	9	9	9	11	11	11
AXa	2810	23	135	1	10	10	2	10	9	4
AYa	2687	9	328	2	9	9	2	10	10	2
AZa	2876	7	61	1	10	10	0	10	10	0
BAa	2697	27	111	1	10	10	0	10	10	0
BBa	2763	14	103	1	10	10	0	9	9	0
BCa	2783	41	357	2	8	8	8	10	10	10
BDa	2705	27	247	2	10	10	4	8	8	2
BEa	2710	29	167	1	9	9	0	9	9	0
BFa	2645	5	31	1	10	10	0	10	10	0
BGa	2715	43	246	1	10	10	6	10	10	4
BHa	2693	6	243	3	10	10	6	10	10	6
BIa	2362	24	192	1	4	4	0	3	3	0
BJa	2997	36	90	2	10	10	10	10	10	7
BKa	2691	31	355	2	9	9	9	10	10	4
BLa	2875	19	35	3	10	10	10	9	9	9
BMa	2715	44	314	4	10	8	8	9	8	7*
Total					343	319	178	348	325	167

5 detected RD, respectively MD. In some cases, small-scale variability can be much higher with a standard deviation of more than 20 days, as shown in Fig. 6 for all footprints. This demonstrates the importance of understanding the limitation of single point measurements for the evaluation of grid-based models.

With a linear regression model, no direct relationship with topography (elevation, slope, sine and cosine of the aspect) or ground cover type could be detected for this or for the difference of the standard deviation between the two years. This difference shows no correlation with the standard deviation. The weak relationship with site-specific factors implies, at least for the short period of observation reported here, that

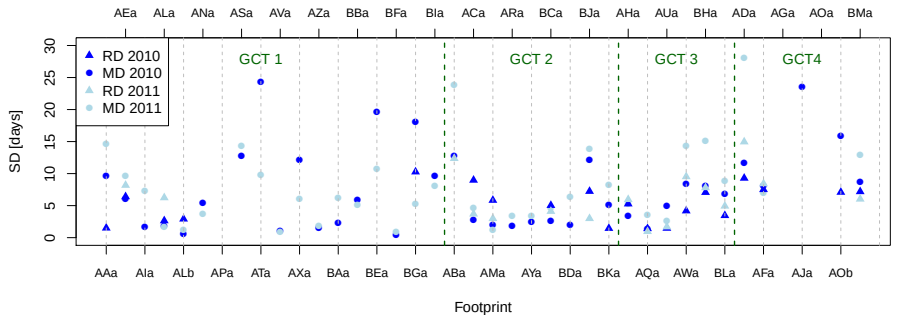

Fig. 6. Standard deviation (SD) for the RD and the MD per footprint for both measuring years. The locations are ordered by their ground cover type (GCT).

meteorological conditions and their influence on processes such as snow drift and deposition exert a dominating control on intra-footprint variability. As a consequence, it is difficult to predict how well one single time series of GST represents RD and MD for a small area surrounding it or a model grid cell in a validation exercise.

4.4 Inter-footprint variability

Mean MD varies from 25 April at ACa to 24 July at AWa in 2010 and from 9 April at ACa to 18 July at BCa in 2011. The mean MD is 15 June in 2010 and 31 May in 2011. RD varies from 23 March at AAa to 11 June at ADa in 2010 and from 22 March at ACa to 5 June at ADa in 2011. The mean RD is 14 May in 2010 and 30 April in 2011. Standard deviations for RD and MD are shown in Fig. 6. RD and MD are shifted towards an earlier date in 2011 with respect to 2010. In 2011, the average RD is 20 days earlier than in 2010 and the MD is on average 12 days earlier than in 2010, taking in account only footprints where RD, respectively MD, were detected for both years. The shift of MD is more pronounced at locations with an early MD, whereas at locations with a late MD, the difference between the two years is much smaller.

For 15 footprints, RD and MD could be detected in both years (Fig. 7). This makes it possible to calculate an average melting period, which lasts from the RD to the MD, for the footprint. At most footprints, GST constantly remains at 0 °C from RD to MD, but in few cases GST briefly drops below 0 °C. This can be explained by the reduced insulation of the ground from the atmosphere due to a reduction of snow height and increase in thermal conductivity because of melting. The length change of the melting period is less pronounced with an average melting period for those 15 locations of 37 days in the first year, and 45 days in the second year. No relationship between the melt length and the GCT is visible, even though this has to be interpreted with caution due to the very small sample size.

At the footprint level, the coefficients of determination for the periods 2010 and 2011 are 0.60 and 0.83 between

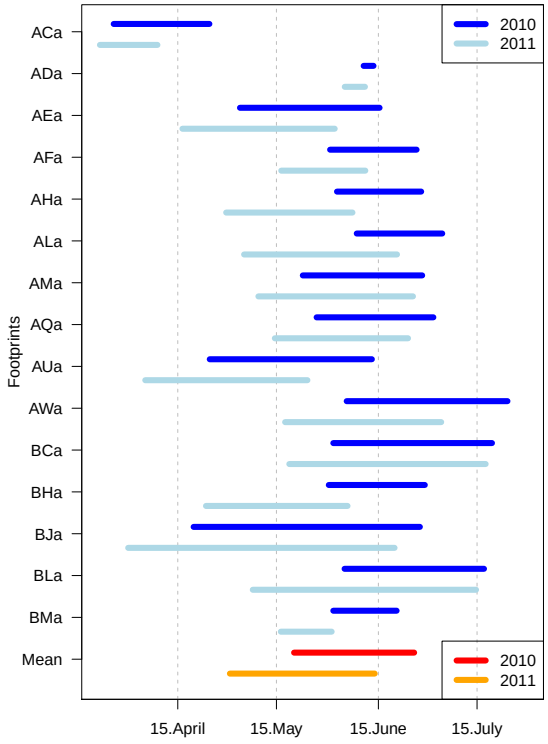

Fig. 7. Melting period defined as the time span between RD and MD for both years of analysis.

MAGST and RD, 0.28 in both years between MAGST and MD, and 0.55 and 0.38 between RD and MD. This suggests that these are useful and complementary metrics for model evaluation.

4.5 Inter-annual MAGST variations

The mean intra-footprint standard deviation of MAGST over all footprints is 0.33 °C in both years. The mean difference of

intra-footprint standard deviations between 2010 and 2011 is on average 0.1 °C, indicating control of meteorological conditions on this quantity.

At Piz Corvatsch, MAAT during the 2011 analysis period was 0.4 °C warmer than in 2010 and similar differences were recorded at the nearby stations Samedan and Passo del Bernina. By comparison, MAGST averaged over all footprints increased by 0.17 °C. This is, however, not a uniform response; the mean absolute difference of footprint-level MAGST is 0.27 °C, with 16 cooling and 25 warming footprints.

A comparison of daily mean GST for 2010 and 2011 shows much larger differences during summer than winter (Fig. 8). This can be explained by the effect of a snow cover that provides insulation between the ground and the atmosphere. Both the onset and the melt-out of the snow cover determine whether the seasonal snow cover has a warming or a cooling effect on MAGST (Zhang, 2005). In this study both situations were observed. An absolute quantification is not possible because air temperature has not been measured at any of the snow-covered locations. GST in winter in the second year are slightly warmer than in the first year, even though the snow coverage was thinner in the second winter (Pielmeier, 2011; Stucki, 2010). The difference of MAGST is also strongly influenced by air temperature during the snow-free period. For example, the cold July in 2011 led at all locations to significantly colder GST than in the previous year. Therefore, the average difference of MAGST from the two years is only 0.17 °C.

When looking at inter-annual GST differences and snow cover, a pattern exemplified by the three typical situations in Fig. 8 is visible: at footprints such as AGa or AOa with a low MDr indicative of a thin snow cover, large fluctuations and often slightly warmer temperatures during winter 2011 occurred. For footprints such as ANa or BAa with a high MDr, indicative of an insulating snow cover and a low RDr indicative of unfrozen ground, GST stayed close to 0 °C during winter. The earlier MD in 2011, however, caused earlier warming of the ground and a positive difference of GST between the two years in spring. In footprints such as AMa or AHa, with high values of MDr and RDr which are indicative of a well-developed snow cover and frozen ground below, a later onset of winter (Stucki, 2010) led to a stronger cooling of the ground and lower GST during winter in the 2010 period. These three classes fit into the classification done by Ishikawa (2003), except that classes 3 and 4 (no short-term GST fluctuation with gradually increasing or decreasing GST during winter time) are taken as one in this study. The strongly differing reactions of MAGST to the meteorological differences between 2010 and 2011 (some showing warming and some showing cooling), underscores the differences in transient response of frozen ground and permafrost conditions to be expected from climate change, even if the longer-term averaging will likely have a smoothing effect.

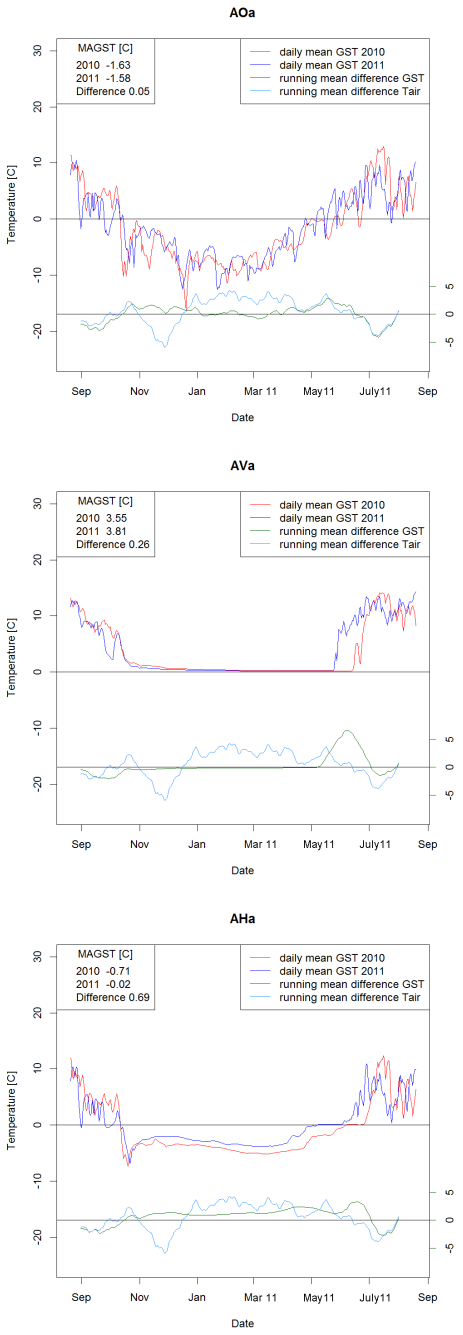

Fig. 8. Differences in the daily GST for footprints with no insulating snow cover (AOa), an insulating snow cover but no frozen ground (Ava), and an insulating snow cover with frozen ground (AHa). Based on air temperature measurements from Piz Corvatsch, the running mean of the difference between the air temperature of the two years is shown.

5 Discussion

The spatial resolution and replication of GST measurements in this study provides a sound basis for deriving RD, MD, and GST, as well as for investigating their spatio-temporal patterns. As measurements are from two years only, results regarding the inter-annual variability and to a lesser degree all absolute values, must be interpreted with caution since meteorological conditions, and especially snow cover, can vary strongly (cf. Brenning et al., 2005; Etzelmüller et al., 2007; Gruber, 2004; Hipp et al., 2011; Hoelzle et al., 2003; Isaksen et al., 2002). Detection of the onset of a snow cover based on GST is inherently uncertain but also of minor importance for model validation as it is much more homogeneous than MD. As MD coincides with rapidly increasing GST, it is also relatively straightforward to detect. MD was only calculated for locations with a comprehensive snow cover, identified based on a standard deviation based reliability index to avoid imprecision. As no suitable ground truth data for RD and MD exists, no direct validation can be performed. The shown methods are to be interpreted as tools for the repeatable extraction of information that could also be interpreted subjectively. In comparison to other published GST-based snow-detection algorithms (Danby and Hik, 2007; Gadek and Leszkiewicz, 2010; Schmidt et al., 2009; Schneider et al., 2012), the method proposed in this study has been tested in a far wider range of topographic situations. MD could be detected at nearly all locations, whereas RD was only detected at half of the locations. RD (the start of the zero curtain in spring) can be detected precisely based on GST where sufficient freezing occurs below the snowpack. While some uncertainties exist for locations with only slightly negative GST below the snowpack, the threshold of at least -50 FDDs (used in the reliability index RDr) effectively excludes these locations. The possible field of application for RD is more limited, as it only works for a subset of the places at which a snow cover is present. MD has a high correlation with maximum snow height (Anderton et al., 2004), warranting a comparison of this study with results concerning the SWE from Jost et al. (2007).

The average standard deviation of the intra-footprint variability for the RD and the MD is significant, with a length of around one week and a strong variation between footprints. The standard deviation could not be explained by topography or ground cover type, implying that at each new location, an intra-footprint variability much higher than the average can occur. The inter-footprint variability of RD and MD lies between three and four weeks. Absolute values have seen a strong shift between the two years, making both RD and MD earlier in 2011. The differences in the length of the melting period (MD–RD) between 2010 and 2011 are for nearly all footprints smaller than the absolute shift in days (Fig. 7).

The algorithm testing performed with GST and SWE modelled with GEOtop shows that the algorithm developed to detect the MD works on a wide range of topographic situations. The increasing number of locations where an insulating snow cover is detected the further in the depth GST is modelled shows the damping effect of the ground surface. For the same reason, the error of the MD based on GST develops towards a later MD with increasing depths.

6 Conclusions

Based on GST measurements, it is possible to derive MD for all locations with an insulating snow cover and RD if the ground below the snow cover freezes during parts of the winter. The methods described here have been tested in a wide range of topographic situations and provide reproducible results. Because MAGST, RD and MD are only moderately correlated, they are complimentary measures for model validation.

A large intra-footprint variability was observed for both RD and MD at many locations. This underscores the importance of using multiple measurement points to characterise one footprint. If validation of a grid-based model with single point measurements is undertaken, a difference of one to three weeks between RD or MD at the measured point and its immediate surroundings must be considered realistic in environments similar to that investigated here.

While based on the comparison of only two years, inter-annual variation of the GST-derived products provides interesting insight into the importance of snow cover in moderating ground thermal response to atmospheric forcing. The difference in MD between 2010 and 2011 is stronger for locations with an early MD than those with a late MD. This adds to earlier findings of a non-linear relationship between changing environmental conditions and snow cover (Beniston et al., 2003; Schöner et al., 2009). Furthermore, the response of MAGST to a 0.4 °C increase of MAAT from one year to the other was diverse and included both warming and cooling.

In view of the anticipated environmental changes in cold regions, a GST-based distributed monitoring can provide a cost-effective method for detecting change and for validating models. Due to the strong variability of GST over short distances, the method of sampling fine-scale variability at the footprint level is important for deriving reliable measurements for interpretation or further aggregation.

Supplementary material related to this article is available online at: http://www.the-cryosphere.net/6/1127/2012/tc-6-1127-2012-supplement.zip.

Acknowledgements. This study was funded through the nanotera.ch project X-Sense, the NCCR-MICS project Permasense and the SNF project CRYOSUB. The authors are grateful for the support given by the Corvatschbahnen and acknowledge the contribution of implementing the iAssist software for work-flow automation in the field by M. Keller, J. Beutel, G. Hungerbühler, O. Knecht and Suhel Sheikh of the ETH computer engineering department. As fieldwork was time consuming it would not have been possible without the support of many friends – thanks a lot!

Edited by: A. Nolin

References

Anderton, S., White, S., and Alvera, B.: Micro-scale spatial variability and the timing of snow melt runoff in a high mountain catchment, J. Hydrol., 268, 158–176, doi:10.1016/S0022-1694(02)00179-8, 2002.

Anderton, S. P., White, S. M., and Alvera, B.: Evaluation of spatial variability in snow water equivalent for a high mountain catchment, Hydrol. Process., 18, 435–453, doi:10.1002/hyp.1319, 2004.

Bartelt, P. and Lehning, M.: A physical SNOWPACK model for the Swiss avalanche warning Part I: numerical model, Cold Reg. Sci. Technol., 35, 123–145, doi:10.1016/S0165-232X(02)00074-5, 2002.

Beniston, M., Keller, F., and Goyette, S.: Snow pack in the Swiss Alps under changing climatic conditions: an empirical approach for climate impacts studies, Theor. Appl. Climatol., 74, 19–31, doi:10.1007/s00704-002-0709-1, 2003.

Best, M. J., Pryor, M., Clark, D. B., Rooney, G. G., Essery, R .L. H., Ménard, C. B., Edwards, J. M., Hendry, M. A., Porson, A., Gedney, N., Mercado, L. M., Sitch, S., Blyth, E., Boucher, O., Cox, P. M., Grimmond, C. S. B., and Harding, R. J.: The Joint UK Land Environment Simulator (JULES), model description – Part 1: Energy and water fluxes, Geosci. Model Dev., 4, 677–699, doi:10.5194/gmd-4-677-2011, 2011.

Bitner, D., Carroll, T., Cline, D., and Romanov, P.: An assessment of the differences between three satellite snow cover mapping techniques, Hydrol. Process., 16, 3723–3733, doi:10.1002/hyp.1231, 2002.

Blöschl, G., Gutknecht, D., and Kirnbauer, R.: Distributed snowmelt simulations in an Alpine catchment 2. Parameter study and model predictions, Water Resour. Res., 27, 3181–3188, doi:10.1029/91WR02251, 1991a.

Blöschl, G., Kirnbauer, R., and Gutknecht, D.: Distributed snowmelt simulations in an Alpine catchment 1. Model evaluation on the basis of snow cover patterns, Water Resour. Res., 27, 3171–3179, doi:10.1029/91WR02250, 1991b.

Brenning, A., Gruber, S., and Hoelzle, M.: Sampling and statistical analyses of BTS measurements, Permafrost Periglac., 16, 383–393, doi:10.1002/ppp.541, 2005.

Brown, R. D.: Northern Hemisphere snow cover variability and change, 1915–97, J. Climate, 13, 2339–2355, doi:10.1175/1520-0442(2000)013<2339:NHSCVA>2.0.CO;2, 2000.

Dall'Amico, M., Endrizzi, S., Gruber, S., and Rigon, R.: A robust and energy-conserving model of freezing variably-saturated soil, The Cryosphere, 5, 469–484, doi:10.5194/tc-5-469-2011, 2011.

Danby, R. K. and Hik, D. S.: Responses of white spruce (Picea glauca) to experimental warming at a subarctic alpine treeline, Glob. Change Biol., 13, 437–451, doi:10.1111/j.1365-2486.2006.01302.x, 2007.

Dyer, J. L. and Mote, T. L.: Spatial variability and trends in observed snow depth over North America, Geophys. Res. Lett., 33, doi:10.1029/2006GL027258, 2006.

Endrizzi, S. and Marsh, P.: Observations and modeling of turbulent fluxes during melt at the shrub-tundra transition zone 1: point scale variations, Hydrol. Res., 41, 471–490, 2010.

Essery, R. and Clark, D. B.: Developments in the MOSES 2 land-surface model for PILPS 2e, Global Planet. Change, 38, 161–164, doi:10.1016/S0921-8181(03)00026-2, 2003.

Etzelmüller, B., Farbrot, H., Guðmundsson, Á., Humlum, O., Tveito, O. E., and Björnsson, H.: The regional distribution of mountain permafrost in Iceland, Permafrost Periglac., 18, 185–199, doi:10.1002/ppp.583, 2007.

Foster, J. L., Hall, D. K., Eylander, J. B., Riggs, G. A., Nghiem, S. V., Tedesco, M., Kim, E., Montesano, P. M., Kelly, R. E. J., Casey, K. A., and Choudhury, B.: A blended global snow product using visible, passive microwave and scatterometer satellite data, Int. J. Remote Sens., 32, 1371–1395, doi:10.1080/01431160903548013, 2011.

Gadek, B. and Leszkiewicz, J.: Influence of snow cover on ground surface temperature in the zone of sporadic permafrost, Tatra Mountains, Poland and Slovakia, Cold Reg. Sci. Technol., 60, 205–211, 2010.

Goodrich, L. E.: The influence of snow cover on the ground thermal regime, Can. Geotech. J., 19, 421–432, 1982.

Groot Zwaaftink, C. D., Löwe, H., Mott, R., Bavay, M., and Lehning, M.: Drifting snow sublimation: A high-resolution 3-D model with temperature and moisture feedbacks, J. Geophys. Res., 116, D16107, doi:10.1029/2011JD015754, 2011.

Gruber, S.: Permafrost thaw and destabilization of Alpine rock walls in the hot summer of 2003, Geophys. Res. Lett., 31, L13504, doi:10.1029/2004GL020051, 2004.

Grünewald, T., Schirmer, M., Mott, R., and Lehning, M.: Spatial and temporal variability of snow depth and ablation rates in a small mountain catchment, The Cryosphere, 4, 215–225, doi:10.5194/tc-4-215-2010, 2010.

Gubler, S., Fiddes, J., Keller, M., and Gruber, S.: Scale-dependent measurement and analysis of ground surface temperature variability in alpine terrain, The Cryosphere, 5, 431–443, doi:10.5194/tc-5-431-2011, 2011.

Gutzler, D. S. and Rosen, R. D.: Interannual variability of wintertime snow cover across the Northern Hemisphere, J. Climate, 5, 1441–1447, doi:10.1175/1520-0442(1992)005<1441:IVOWSC>2.0.CO;2, 1992.

Hipp, T., Etzelmüller, B., Farbrot, H., and Schuler, T. V.: Modelling the temperature evolution of permafrost and seasonal frost in southern Norway during the 20th and 21st century, The Cryosphere Discuss., 5, 811–854, doi:10.5194/tcd-5-811-2011, 2011.

Hoelzle, M., Wegmann, M., and Krummenacher, B.: Miniature temperature dataloggers for mapping and monitoring of permafrost in high mountain areas: first experience from the Swiss Alps, Permafrost Periglac., 10, 113–124, doi:10.1002/(SICI)1099-1530(199904/06)10:2<113::AID-PPP317>3.0.CO;2-A, 1999.

Hoelzle, M., Haeberli, W., and Stocker-Mittaz, C.: Miniature ground temperature data logger measurements 2000–2002 in the Murtèl-Corvatsch area, Eastern Swiss Alps, in: Proceedings of the Eighth International Conference on Permafrost, 419–424, 2003.

Isaksen, K., Hauck, C., Gudevang, E., Ødegård, R. S., and Sollid, J. L.: Mountain permafrost distribution in Dovrefjell and Jotunheimen, southern Norway, based on BTS and DC resistivity tomography data, Norsk Geogr. Tidsskrift, 56, 122–136, doi:10.1080/00291950260056459, 2002.

Ishikawa, M.: Thermal regimes at the snow-ground interface and their implications for permafrost investigation, Geomorphology, 52, 105–120, doi:10.1016/S0169-555X(02)00251-9, 2003.

Iverson, R. M., Reid, M. E., and LaHusen, R. G.: Debris-flow mobilization from landslides, Annu. Rev. Earth Pl. Sc., 25, 85–138, doi:10.1146/annurev.earth.25.1.85, 1997.

Jost, G., Weiler, M., Gluns, D. R., and Alila, Y.: The influence of forest and topography on snow accumulation and melt at the watershed-scale, J. Hydrol., 347, 101–115, doi:10.1016/j.jhydrol.2007.09.006, 2007.

Keller, M., Hungerbühler, G., Knecht, O., Skeikh, S., Beutel, J., Gubler, S., Fiddes, J., and Gruber, S.: iAssist: Rapid Deployment and Maintenance of Tiny Sensing Systems, 2010.

Lampkin, D. J. and Yool, S. R.: Monitoring mountain snowpack evolution using near-surface optical and thermal properties, Hydrol. Process., 18, 3527–3542, doi:10.1002/hyp.5797, 2004.

Lehning, M., Bartelt, P., Brown, B., Russi, T., Stöckli, U., and Zimmerli, M.: Snowpack model calculations for avalanche warning based upon a new network of weather and snow stations, Cold Reg. Sci. Technol., 30, 145–157, doi:10.1016/S0165-232X(99)00022-1, 1999.

Lehning, M., Bartelt, P., Brown, B., and Fierz, C.: A physical SNOWPACK model for the Swiss avalanche warning Part III: meteorological forcing, thin layer formation and evaluation, Cold Reg. Sci. Technol., 35, 169–184, doi:10.1016/S0165-232X(02)00072-1, 2002a.

Lehning, M., Bartelt, P., Brown, B., Fierz, C., and Satyawali, P.: A physical SNOWPACK model for the Swiss avalanche warning Part II. Snow microstructure, Cold Reg. Sci. Technol., 35, 147–167, doi:10.1016/S0165-232X(02)00073-3, 2002b.

Li, H.-Y. and Wang, J.: Simulation of snow distribution and melt under cloudy conditions in an Alpine watershed, Hydrol. Earth Syst. Sci., 15, 2195–2203, doi:10.5194/hess-15-2195-2011, 2011.

López-Moreno, J. I., Fassnacht, S. R., Beguería, S., and Latron, J. B. P.: Variability of snow depth at the plot scale: implications for mean depth estimation and sampling strategies, The Cryosphere, 5, 617–629, doi:10.5194/tc-5-617-2011, 2011.

Luce, C. H., Tarboton, D. G., and Cooley, K. R.: The influence of the spatial distribution of snow on basin-averaged snowmelt, Hydrolog. Process., 12, 1671–1683, 1998.

Luetschg, M. and Haeberli, W.: Permafrost evolution in the Swiss Alps in a changing climate and the role of the snow cover, Norsk Geogr. Tidsskrift, 59, 78–83, doi:10.1080/00291950510020583, 2005.

Lundquist, J. D. and Lott, F.: Using inexpensive temperature sensors to monitor the duration and heterogeneity of snow-covered areas, Water Resour. Res., 44, W00D16, doi:10.1029/2008WR007035, 2008.

Marsh, C. B., Pomeroy, J. W., and Spiteri, R. J.: Implications of mountain shading on calculating energy for snowmelt using unstructured triangular meshes, Hydrol. Process., 26, 1767–1778, doi:10.1002/hyp.9329, 2012.

Outcalt, S. I., Nelson, F. E., and Hinkel, K. M.: The zero-curtain effect: Heat and mass transfer across an isothermal region in freezing soil, Water Resour. Res., 26, 1509, doi:10.1029/WR026i007p01509, 1990.

Parajka, J. and Blöschl, G.: The value of MODIS snow cover data in validating and calibrating conceptual hydrologic models, J. Hydrol., 358, 240–258, doi:10.1016/j.jhydrol.2008.06.006, 2008.

Pielmeier, C.: Wetter, Schneedecke und Lawinengefahr Hydrologisches Jahr 2010/11, WSL-Insitut für Schnee- und Lawinenforschung SLF, 2011.

Pomeroy, J. W., Marsh, P., and Gray, D. M.: Application of a distributed blowing snow model to the Arctic, Hydrol. Process., 11, 1451–1464, doi:10.1002/(SICI)1099-1085(199709)11:11<1451::AID-HYP449>3.0.CO;2-Q, 1997.

Rutter, N., Essery, R., Pomeroy, J., Altimir, N., Andreadis, K., Baker, I., Barr, A., Bartlett, P., Boone, A., Deng, H., Douville, H., et al.: Evaluation of forest snow processes models (SnowMIP2), J. Geophys. Res., 114, D06111, doi:10.1029/2008JD011063, 2009.

Scherrer, S. C.: Swiss Alpine snow pack variability: major patterns and links to local climate and large-scale flow, Clim. Res., 32, 187–199, 2006.

Schmid, M.-O.: Variability of ground surface temperatures and related processes in high Alpine regions, MSc., Universty of Zurich, 2011.

Schmidt, S., Weber, B., and Winiger, M.: Analyses of seasonal snow disappearance in an alpine valley from micro- to meso-scale (Loetschental, Switzerland), Hydrol. Process., 23, 1041–1051, doi:10.1002/hyp.7205, 2009.

Schneider, S., Hoelzle, M., and Hauck, C.: Influence of surface and subsurface heterogeneity on observed borehole temperatures at a mountain permafrost site in the Upper Engadine, Swiss Alps, The Cryosphere, 6, 517–531, doi:10.5194/tc-6-517-2012, 2012.

Schöner, W., Auer, I., and Böhm, R.: Long term trend of snow depth at Sonnblick (Austrian Alps) and its relation to climate change, Hydrol. Process., 23, 1052–1063, doi:10.1002/hyp.7209, 2009.

Stucki, T.: Wetter, Schneedecke und Lawinengefahr, Hydrologisches Jahr 2009/10, WSL-Insitut für Schnee- und Lawinenforschung SLF, 2010.

Taras, B., Sturm, M., and Liston, G. E.: Snow–Ground Interface Temperatures in the Kuparuk River Basin, Arctic Alaska: Measurements and Model, J. Hydrometeorol., 3, 377–394, doi:10.1175/1525-7541(2002)003<0377:SGITIT>2.0.CO;2, 2002.

Techel, F. and Pielmeier, C.: Point observations of liquid water content in wet snow – investigating methodical, spatial and temporal aspects, The Cryosphere, 5, 405–418, doi:10.5194/tc-5-405-2011, 2011.

Tribbeck, M. J., Gurney, R. J., Morris, E. M., and Pearson, D. W. C.: A new Snow-SVAT to simulate the accumulation and ablation of seasonal snow cover beneath a forest canopy, J. Glaciol., 50, 171–182, doi:10.3189/172756504781830187, 2004.

Tyler, S. W., Burak, S. A., McNamara, J. P., Lamontagne, A., Selker, J. S., and Dozier, J.: Spatially distributed temperatures at the base of two mountain snowpacks measured with fiber-optic sensors,

J. Glaciol., 54, 673–679, doi:10.3189/002214308786570827, 2008.

Viviroli, D. and Weingartner, R.: The hydrological significance of mountains: from regional to global scale, Hydrol. Earth Syst. Sci., 8, 1017–1030, doi:10.5194/hess-8-1017-2004, 2004.

Westermann, S., Boike, J., Langer, M., Schuler, T. V., and Etzelmüller, B.: Modeling the impact of wintertime rain events on the thermal regime of permafrost, The Cryosphere, 5, 945–959, doi:10.5194/tc-5-945-2011, 2011.

Williams, M. W., Erickson, T. A., and Petrzelka, J. L.: Visualizing meltwater flow through snow at the centimetre-to-metre scale using a snow guillotine, Hydrol. Process., 24, 2098–2110, doi:10.1002/hyp.7630, 2010.

Wirz, V., Schirmer, M., Gruber, S., and Lehning, M.: Spatio-temporal measurements and analysis of snow depth in a rock face, The Cryosphere, 5, 893–905, doi:10.5194/tc-5-893-2011, 2011.

Zhang, T.: Influence of the seasonal snow cover on the ground thermal regime: An overview, Rev. Geophys., 43, RG4002, doi:10.1029/2004RG000157, 2005.

Publication III

Gubler, S., S. Gruber, and R. S. Purves (2012), Uncertainties of parameterized surface downward clear-sky shortwave and all-sky longwave radiation, *Atmospheric Chemistry and Physics*, *12*, 5077–5098, doi: 10.5194/acp-12-5077-2012

Contributions:

- Design of modeling study
- R-code used for modeling and model evaluation
- Interpretation and visualization of results

Atmos. Chem. Phys., 12, 5077–5098, 2012
www.atmos-chem-phys.net/12/5077/2012/
doi:10.5194/acp-12-5077-2012

Atmospheric Chemistry and Physics

Uncertainties of parameterized surface downward clear-sky shortwave and all-sky longwave radiation.

S. Gubler, S. Gruber, and R. S. Purves

University of Zurich, Department of Geography, Zurich, Switzerland

Correspondence to: S. Gubler (stefanie.gubler@geo.uzh.ch)

Received: 17 September 2011 – Published in Atmos. Chem. Phys. Discuss.: 31 January 2012
Revised: 8 May 2012 – Accepted: 22 May 2012 – Published: 8 June 2012

Abstract. As many environmental models rely on simulating the energy balance at the Earth's surface based on parameterized radiative fluxes, knowledge of the inherent model uncertainties is important. In this study we evaluate one parameterization of clear-sky direct, diffuse and global shortwave downward radiation (SDR) and diverse parameterizations of clear-sky and all-sky longwave downward radiation (LDR). In a first step, SDR is estimated based on measured input variables and estimated atmospheric parameters for hourly time steps during the years 1996 to 2008. Model behaviour is validated using the high quality measurements of six Alpine Surface Radiation Budget (ASRB) stations in Switzerland covering different elevations, and measurements of the Swiss Alpine Climate Radiation Monitoring network (SACRaM) in Payerne. In a next step, twelve clear-sky LDR parameterizations are calibrated using the ASRB measurements. One of the best performing parameterizations is elected to estimate all-sky LDR, where cloud transmissivity is estimated using measured and modeled global SDR during daytime. In a last step, the performance of several interpolation methods is evaluated to determine the cloud transmissivity in the night.

We show that clear-sky direct, diffuse and global SDR is adequately represented by the model when using measurements of the atmospheric parameters precipitable water and aerosol content at Payerne. If the atmospheric parameters are estimated and used as a fix value, the relative mean bias deviance (MBD) and the relative root mean squared deviance (RMSD) of the clear-sky global SDR scatter between between −2 and 5 %, and 7 and 13 % within the six locations. The small errors in clear-sky global SDR can be attributed to compensating effects of modeled direct and diffuse SDR since an overestimation of aerosol content in the atmosphere results in underestimating the direct, but overestimating the diffuse SDR. Calibration of LDR parameterizations to local conditions reduces MBD and RMSD strongly compared to using the published values of the parameters, resulting in relative MBD and RMSD of less than 5 % respectively 10 % for the best parameterizations. The best results to estimate cloud transmissivity during nighttime were obtained by linearly interpolating the average of the cloud transmissivity of the four hours of the preceeding afternoon and the following morning.

Model uncertainty can be caused by different errors such as code implementation, errors in input data and in estimated parameters, etc. The influence of the latter (errors in input data and model parameter uncertainty) on model outputs is determined using Monte Carlo. Model uncertainty is provided as the relative standard deviation σ_{rel} of the simulated frequency distributions of the model outputs. An optimistic estimate of the relative uncertainty σ_{rel} resulted in 10 % for the clear-sky direct, 30 % for diffuse, 3 % for global SDR, and 3 % for the fitted all-sky LDR.

1 Introduction

Downward shortwave (SDR) and longwave radiation (LDR) strongly control the energy budget at the Earth's surface. They drive processes such as photosynthesis and evapotranspiration, and are therefore of great importance in a variety of areas such as hydrological, agricultural (Cooter and Dhakhwa, 1996), and energy technology studies (Schillings, 2004). Especially in view of climate change, the modeling of environmental processes is important in temporal and spatial estimation of changes and rates of change, and to improve

the knowledge about the complex interactions between the atmosphere, the Earth surface and subsurface. In mountain areas, changes in the energy budget can already be observed at small distances due to the strong topographic variability.

Modeling energy fluxes and their uncertainties at the land surface is a key step in many model applications. A wide variety of models estimating SDR or LDR have been proposed in the literature, ranging from complex physical models using radiative transfer schemes and integrating aerosol and gaseous profiles of the atmosphere (e.g. LOWTRAN or MODTRAN) to empirical models based on relations between meteorological variables. For many applications, sophisticated models such as MODTRAN are inappropriate due to their complexity, required input data and computational effort. This study is based on the clear-sky broadband radiation model by Iqbal (1983, based on Bird and Hulstrom, 1980, 1981) and empirical parameterizations for clear- and all-sky LDR found in the literature (e.g. Brutsaert, 1975; Konzelmann et al., 1994; Pirazzini et al., 2000). The performance of many of these parameterizations has extensively been evaluated (e.g. Gueymard, 1993, 2003a,b, 2011; Crawford and Duchon, 1998; Battles et al., 2000; Pirazzini et al., 2000; Nimielä et al., 2001a,b), but sensitivity or uncertainty studies are rare in the literature (e.g. Gueymard, 2003b; Schillings, 2004; Badescu et al., 2012). Thus we focus on evaluating the Iqbal (1983) clear-sky SDR model and fitting the LDR parameterization to six locations at different elevations in Switzerland, and estimating model sensitivities and uncertainties due to different error sources.

The Iqbal (1983) model has been chosen since it has shown to reproduce SDR reasonably well under different climatic settings (Gueymard, 1993; Battles et al., 2000; Gueymard, 2003b). Furthermore, it has been frequently used in impact model applications (e.g. Corripio, 2002; Gruber, 2005; Machguth et al., 2008; Helbig et al., 2009) as well as other studies aiming at an optimal use of solar power, for example (Schillings, 2004). The Iqbal (1983) model assumes a homogeneous atmosphere and uses an isotropic view factor approach. Due to these simplifications, input is limited to a few quantities such as screen-level temperature (i.e. the temperature at the height of the measurement device, here 2 m above the ground), relative humidity and atmospheric pressure, and model parameters consist of the amount of ozone, aerosols and water vapor in the overlying atmosphere, among others, to determine the transmission respectively scattering of the solar rays. Under clear skies and non-polluted conditions, transmittance from ozone, precipitable water, aerosols, mixed gases and the Rayleigh transmittance cause most atmospheric attenuation (Gueymard, 2003a). In the past, these parameters could "not be easily determined from normally available information" (Dozier, 1980). Nowadays, ozone, aerosol content and water vapor is measured and can be obtained from Aeronet or satellite data such as MODIS for many locations, the datasets however often have spatial or temporal gaps (Gueymard, 2003a). Using this data therefore requires temporal interpolation and spatial extrapolation causing errors that are propagated into model outputs (Gueymard, 2003b). Practical model applications incorporating parameterizations of the downward radiation as a driving factor of other environmental processes are usually restricted to few input quantities such as the variables recorded at ordinary weather stations. Such impact models often treat parameters such as ozone, aerosol content and water vapor as constants (Longman et al., 2012). On one hand, this approach reduces the time and data management effort of a model user, on the other hand it introduces a considerable source of uncertainty and error into the model (Gueymard, 2003b; Badescu et al., 2012).

This study investigates the uncertainty of the Iqbal (1983) model due to uncertainties in inputs and the above mentioned simplifications concerning the estimated atmospheric parameters. A Monte Carlo based uncertainty analysis is performed based on previously determined input error and parameter probability distributions. The latter are determined using high quality measurements and/or established parameterizations of the correspondent parameter, while the input measurements are obtained from MeteoSwiss. In a next step, some of the most commonly used clear-sky LDR parameterizations are fitted to local conditions in Switzerland, resulting in the identification of the most appropriate parameterizations. For one of these parameterizations, the total output uncertainty is assessed based on input and parameter uncertainty similarly as discussed above. Clouds are one of the main LDR forcings. Since cloud cover is only rarely measured and measurements are error-prone, it is common to estimate the cloud transmissivity as the ratio of the measured and modeled clear-sky global SDR during daytime. During the night, when this approach is not feasible, cloud transmissivity is interpolated. In a last step, we therefore examine different cloud transmissivity interpolations, and propagate inherent uncertainties into all-sky LDR model outputs.

Thus, the aims of the present study are:

- to evaluate the clear-sky SDR model by Iqbal (1983) at six sites in Switzerland;
- to calibrate diverse clear- and all-sky LDR models and to assess the best all-sky parameterizations for impact modeling studies in Switzerland;
- to study the output of different interpolation techniques of the cloud transmissivity during nighttime; and
- to estimate the total output uncertainty of the clear-sky SDR model by Iqbal (1983) and one of the all-sky LDR models due to uncertainties in input variables and parameters.

All these steps are necessary to estimate the all-sky LDR and its associated uncertainties during day- and nighttime. To reach these aims, we firstly introduce the data and the parameters necessary in the study. In Sect. 3, the methods to assess

Table 1. Meta data of the MeteoSwiss stations. At each place, one ANETZ and one ASRB station is located.

Location	Abbreviation	Lat (deg N)	Long (deg E)	Ele [m]
Locarno-Monti	OTL	46.1726	8.7874	367
Payerne	PAY	46.8116	6.9424	490
Davos	DAV	46.8130	9.8435	1590
Cimetta	CIM	46.2010	8.7908	1672
Weissfluhjoch	WFJ	46.8333	9.8064	2690
Jungfraujoch	JUN	46.5474	7.9853	3580

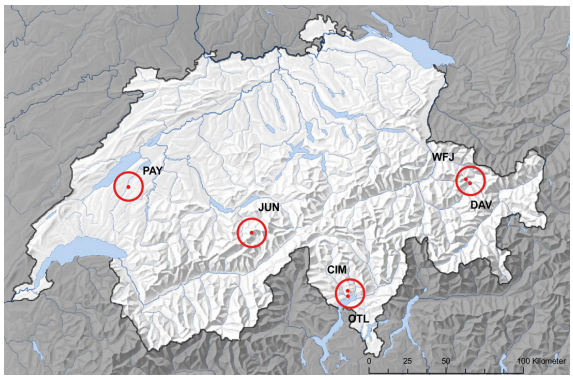

Fig. 1. Locations of the six MeteoSwiss stations in Switzerland (geodata © swisstopo). The coordinates of the locations are from MeteoSwiss (http://www.meteoswiss.admin.ch).

the sensitivity and the uncertainties in the clear-sky SDR and LDR model, and the validation and calibration methods are introduced. Then, the results are presented and discussed.

2 Data description

This modeling study is performed for six locations in Switzerland (Fig. 1, Table 1). The model is run with measurements from MeteoSwiss (Sect. 2.1) and estimated parameters (Sect. 2.2). The uncertainties in the input data and the parameters were assigned based on expert knowledge and literature, or were estimated based on representative measurements. Perceptual and structural model errors (cf., Beck, 1987; Beven, 1993; Kavetski et al., 2003; Gupta et al., 2005) are not investigated.

The data are structured as (a) input data, (b) physical and empirical model parameters and (c) validation data.

2.1 Input and validation data

The input data is obtained from the MeteoSwiss automatic meteorological network (ANETZ). The Alpine Surface Radiation Budget (ASRB, Philipona et al., 1996) network data serves for validation (SDR) and calibration (clear-sky and all-sky LDR). The number of study sites is restricted to the intersection of both networks. The study is performed with hourly data ranging from 1996 to 2008, resulting in 113 976 data points. Since synoptic cloud observations are rare (they exist only for 3 stations of this study) and error-prone, clear-sky hours are estimated according to the clear-sky index (CSI) introduced by Marty and Philipona (2000). The number of clear-sky hours varies between 25 000 and 38 000. The measurement errors are assumed to be normally distributed with zero mean. Standard deviations of the input and validation data (Table 2) were obtained from MeteoSwiss (courtesy of Rolf Philipona Philipona et al., 1995). All the measured data are denoted in equations with a superscript * (for example, T^* denotes measured air temperature).

2.2 Physical and empirical model parameters

2.2.1 SDR

The main focus of this study concerning modeled SDR lies on the estimation of the total output uncertainty of the Iqbal (1983) model due to the absorption, scattering and transmittance of the incoming solar radiation in the atmosphere, plus their reflection at the ground surface. Uncertainties in ozone column data, aerosol, precipitable water and in ground albedo are investigated and the probability density functions of each parameter are determined. Mean and standard deviation of the parameters are estimated using high quality measurements recorded in Switzerland, or using established parameterizations found in the literature. All uncertainty ranges are compared to estimates by Gueymard (2003b), and result to be representative. The uncertainty in Rayleigh and mixed gas transmittance is not investigated since it has limited influence on modeled SDR (Gueymard, 2003b).

Aerosol: Attenuation effects of scattering and absorption by aerosols were modeled according to Ångström (1929, 1930):

$$\tau_{\alpha\lambda} = \beta(\lambda/\lambda_0)^{-\alpha}, \quad (1)$$

where α is the wavelength exponent (also called Ångström exponent), β is the turbidity coefficient and $\lambda_0 = 1000\,\text{nm}$ for λ in nm. Aerosol optical depths (AOD) $\tau_{\alpha\lambda}$ data for diverse wavelengths λ are from aeronet.gsfc.nasa.gov. Level 2.0 AOD data for Davos for the years 2001 to 2010 were used in this study. The Ångström exponent α and the Ångström

Table 2. Input, model parameters and validation data with uncertainty distributions, mean μ and standard deviation σ. Note that the distribution for the ANETZ and ASRB measurements concern the error of the measurement (denoted with E), whereas the distribution in the parameters concerns the parameter value itself. Since ground albedo varies temporally and spatially, its distribution is estimated for each station and each month separately (Table B1).

	Measurement	Distribution	μ	σ	Unit	Symbol
Input	Air temperature	Normal (E)	0	0.2	K	T^*
	Relative humidity	Normal (E)	0	5	%	h_r^*
	Air pressure	Normal (E)	0	0.2	hPa	p^*
Parameter	Ozone column	Lognormal	314	38	DU	l
	Ångström exponent	Normal	1.38	0.46		α
	Ångström turbidity	Lognormal	0.039	0.05		β
	PrecWatConstant	Lognormal	47	0.38	g K cm^{-2} hPa^{-1}	a_w
	Ground Albedo	Lognormal				ρ_g
	Cloud transmissivity	Normal (E)	0	0.08		τ_c
Validation	Global SDR	Normal (E)	0	2 %	W m^{-2}	SDR^*_{glob}
	LDR	Normal (E)	0	2 %	W m^{-2}	LDR^*_{in}

turbidity coefficient β are determined from a linearised version of the Ångström's law in Eq. (1) (Gueymard, 2011):

$$\ln \tau_{\alpha\lambda} = \ln \beta - \alpha \ln(\lambda/\lambda_0). \quad (2)$$

To estimate α and β, we used $\tau_{\alpha\lambda}$ for wavelengths between 380 and 1020 nm. According to the resultant frequency distributions, α is assumed to be normally distributed with lower limit zero, and β is represented by a trimmed log-normal distribution with an upper limit equal to 0.5. The estimated mean value for α of 1.38 is close to the recommended value by Ångström (1930) $\alpha = 1.3$.

Water vapor: The effect of absorption due to water vapor contained in the atmosphere is estimated using the precipitable water w (Eq. A10). The precipitable water is the water contained in a column of unit cross section extending from the Earth's surface to the top of the atmosphere. Data of precipitable water is rarely available (Iqbal, 1983), and is thus often parameterized. Historical overviews of precipitable water parameterizations are given in Iqbal (1983) and Okulov et al. (2002). Here, the parameterization found in Reitan (1963); Leckner (1978) and Prata (1996) is used:

$$w = a_w \frac{h_r^* p_s}{T^*}, \quad (3)$$

where a_w is estimated (Eq. 4), h_r^* is the measured relative humidity in fractions of one, p_s is saturated water vapor pressure in hPa and T^* is screen-level temperature in K. The vapor pressure in saturated air is determined as a function of air temperature (Flatau et al., 1992). The parameter a_w [10g K hPa^{-1} cm^{-2}] is estimated as (Prata, 1996):

$$a_w = \frac{M_w}{R \cdot k \cdot \psi}, \quad (4)$$

where $M_w = 18.02\,\mathrm{g\,mol^{-1}}$ is the molecular weight of water vapor, $R = 8.314\,\mathrm{J\,K^{-1}\,mol^{-1}}$ is the universal gas constant and $\psi = 1.006$ is a constant. Further, $k = k_w + \frac{\gamma}{T^*}$, where $k_w = 0.44\,\mathrm{km^{-1}}$ is the inverse water vapor scale height (Reitan, 1963; Brutsaert, 1975) and γ is the lapse rate. The uncertainty of a_w is estimated by propagating the uncertainty inherent in the air temperature measurements and the lapse rate. The lapse rate is assumed to be normally distributed with mean equal to the standard value of $-6.5\,\mathrm{K\,km^{-1}}$ for the Alps and standard deviation of $1\,\mathrm{K\,km^{-1}}$, based on the investigations of Hebeler and Purves (2008). Following the investigations of Foster et al. (2006), a_w and w are assumed to be lognormally distributed. The uncertainty in a_w is around 1 %. By propagating the input measurement errors through Eq. 3, we observe an estimated uncertainty in precipitable water greater than 100 % (see Fig. 5), which is in accordance with Gueymard (2003b).

Ozone: MeteoSwiss provides accurate ozone column measurements in Arosa (Staehelin et al., 1998) on about two thirds of all days during the year. Ozone is assumed to be lognormally distributed. The estimated standard deviation of the ozone frequency distribution is around 12 % of the mean ozone, implying that the assumed uncertainty represents the ozone measurement uncertainty (5 to 30 %) as estimated by Gueymard (2003b) well.

Ground albedo: Ground albedo measurements for each of the study sites were obtained from the MODIS/Terra + Aqua BRDF and Calculated Albedo data set (ORNL DAAC, 2010). Ground albedo is assumed to be lognormally distributed (Oreopoulos and Davies, 1998; Mulrooney and Matney, 2007), with an upper cut-off at the maximum albedo. Due to the strong temporal and spatial variability of ground albedo, the measurements are separately examined for each study site and each month of the year (Table B1). Albedo is averaged over a square of 6.5 km by 6.5 km centered around each location.

Table 3. Parameterizations of clear-sky emissivity. p_v is the water vapor pressure [hPa], and T^* the measured temperature [K]. x_1, x_2 and x_3 denote the empirical parameters.

Publication	Abbr.	Eq.	ϵ_{cl}	x_1	x_2	x_3
Maykut and Church (1973)	may	18	x_1	0.7855		
Ångström (1915)	angs	8	$x_1 - x_2 \cdot 10^{-x_3 \cdot p_v}$	0.83	0.18	0.067
Brunt (1932)	brun	7	$x_1 + x_2 \cdot \sqrt{p_v}$	0.52	0.065	
Swinbank (1963)	swin	9	$x_1 \cdot T^{*2}$	9.365×10^{-6}		
Idso and Jackson (1969)	jack	10	$1 - x_1 \cdot \exp(-x_2 \cdot (273 - T^*)^2)$	0.261	7.77×10^{-4}	
Brutsaert (1975)	brut	12	$x_1 \cdot (\frac{p_v}{T^*})^{1/x_2}$	1.24	7	
Konzelmann et al. (1994)	konz	13	$0.23 + x_1 \cdot (\frac{100 p_v}{T^*})^{1/x_2}$	0.484	8	
Satterlund (1979)	satt	14	$x_1 \cdot (1 - \exp(-p_v^{\frac{T^*}{2016}}))$	1.08		
Idso (1981)	idso	11	$x_1 + x_2 \cdot p_v \cdot \exp(\frac{x_3}{T^*})$	0.7	5.95×10^{-5}	1500
Iziomon et al. (2003)	izio	16	$1 - x_1 \cdot \exp(-x_2 \cdot \frac{p_v}{T^*})$	0.43	11.5	
Prata (1996)	prat	15	$1 - (1 + 46.5 \cdot \frac{p_v}{T^*}) \cdot \exp(-(x_1 + x_2 \cdot 46.5 \cdot \frac{p_v}{T^*})^{x_3})$	1.2	3	0.5
Dilley and O'Brien (1997)	dill	17	$(x_1 + x_2 \cdot (\frac{T^*}{273.16})^6 + x_3 \cdot (\frac{46.5 \frac{p_v}{T^*}}{2.5})^{0.5})/(\sigma_{SB} T^{*4})$	59.38	113.7	96.96

2.2.2 LDR

The LDR parameterizations contain empirical parameters (Table 3) which originally were fitted to measurements at specific research sites (see Sect. 3.1.2 for details). In this study, we fit the selected parameterizations to the measurements at the six study sites in Switzerland, and identify reliable parameter values for the local conditions. The confindence intervals of the non-linear least-quares parameter estimation are used to quantify the uncertainty of the parameters. Clouds are a major forcing of LDR, and are estimated using measured and modeled global SDR. Uncertainties in modeled SDR thus are propagated to cloud transmissivity through Eq. (19). The standard deviation results in approximately 0.08 for modeled cloud transmissivity.

3 Methods

3.1 Model formulations

In this section, we give a brief overview of the model formulations and parameterizations used in the study.

3.1.1 Clear-sky SDR

In a first step, the clear-sky broadband global SDR is estimated (Iqbal, 1983, model C). For details the reader is asked to refer to Appendix A. The model estimates the direct SDR by calculating the radiation at the top of the atmosphere (Corripio, 2002), and the attenuation of the solar radiation by ozone, water vapor, aerosol and dry-air particles in the atmosphere. Then, the diffuse SDR due to Rayleigh-scattering, scattering by aerosols and the multiple reflection of the sun rays between the Earth's surface and the atmosphere is estimated. Direct and diffuse radiation sum up to the global SDR. Radiation due to scattering from surrounding terrain is included. However, it only accounts for a very small part of the total global SDR since the study locations are situated in locally flat terrain.

3.1.2 Clear-sky LDR

Clear-sky LDR is determined by the Stefan-Boltzmann law:

$$\mathrm{LDR_{cl}} = \epsilon_{atm} \cdot \sigma_{SB} \cdot T_{atm}^4, \quad (5)$$

where $\sigma_{SB} = 5.67 \times 10^{-8}\ \mathrm{W\,m^{-2}\,K^{-4}}$ denotes the Stefan-Boltzmann constant, ϵ_{atm} the bulk emissivity and T_{atm} the effective temperature of the overlying atmosphere. In practice, $\mathrm{LDR_{cl}}$ is estimated as:

$$\mathrm{LDR_{cl}} = \epsilon_{cl}(p_v, T^*) \cdot \sigma_{SB} \cdot T^{*4}, \quad (6)$$

where T^* denotes absolute air temperature (K) at the reference height of 2 m above the ground and ϵ_{cl} is the parameterized clear-sky emissivity. In the present study, twelve parameterizations (Table 3) are calibrated with measurements in Switzerland, and the most suitable ones are determined. The parameterizations are shortly presented in the following paragraph.

Estimating clear-sky emissivity based on water vapor pressure and temperature measurements has a long history. Brunt (1932) for example observed a linear relationship between ϵ_{cl} and $\sqrt{p_v}$. He showed that fitting a linear regression line:

$$\epsilon_{cl} = x_1 + x_2 \cdot \sqrt{p_v} \quad (7)$$

represented clear-sky emissivity better than the Ångström (1915) formula:

$$\epsilon_{\mathrm{cl}} = x_1 + x_2 \times 10^{-x_3 p_{\mathrm{v}}} \tag{8}$$

for measurements made in Uppsala (Asklöf, 1920). The parameter values for Brunt (1932) however vary significantly for different locations due to different rates of changes of air temperature and vapor pressure with elevation, but also due to differing methods estimating vapor pressure (Brunt, 1932). The parameters used here were estimated with monthly measurements from Benson, UK (Dines, 1921). Swinbank (1963) states that the relationship between ϵ_{cl} and p_{v} found by Ångström (1915) and Brunt (1932) basically arise from the relationship between humidity and temperature, and would only be appropriate for an atmosphere of constant grayness (e.g. Idso and Jackson, 1969). A better representation of $\mathrm{LDR_{cl}}$ was found using temperature alone (Swinbank, 1963):

$$\mathrm{LDR_{cl}} = x_1 \sigma_{SB} T^{*6}, \tag{9}$$

with $x_1 = 5.31 \times 10^{-13}$ in Australia, $x_1 = 5.21 \times 10^{-13}$ for the Benson measurements, and $\mathrm{LDR_{cl}}$ in $\mathrm{mWcm^{-2}}$. Idso and Jackson (1969) proposed the relation:

$$\epsilon_{\mathrm{cl}} = 1 - x_1 \exp(-x_2 (273 - T^*)^2), \tag{10}$$

assuming that just above 273 K clear-sky emissivity may be described as an exponential function of temperature, and that the variation in ϵ_{cl} is symmetrical around the freezing point. They proved their relationship with $x_1 = 0.261$ and $x_2 = 7.77 \times 10^{-4}$ to provide more reliable results than Ångström (1915); Brunt (1932) and Swinbank (1963), and tested the parameterization for measurements in Alaska, Arizona, Australia and the Indian Ocean. Some years later, Idso (1981) established a physically based formula using new measurements of the total LDR for all wavelengths and the portions contained within the 10.5- to 12.5 µm and the 8 to 14 µm bands, resulting in:

$$\epsilon_{\mathrm{cl}} = x_1 + x_2 p_{\mathrm{v}} \exp(x_3 / T^*) \tag{11}$$
$$x_1 = 0.7,\ x_2 = 5.95 \times 10^{-5},\ x_3 = 1500.$$

This is one of the first attempts to express the clear-sky effective emissivity in dependence of both temperature and water vapor. Earlier, Brutsaert (1975) suggested:

$$\epsilon_{\mathrm{cl}} = x_1 (\frac{p_{\mathrm{v}}}{T^*})^{1/x_2},\ x_1 = 1.24,\ x_2 = 7 \tag{12}$$

by integrating the Schwarzschild's radiative-transfer equation for simple atmospheric profiles. The formula can be reduced to $\epsilon_{\mathrm{cl}} = 0.553 p_{\mathrm{v}}^{1/7}$ for $T = 288$ K since it not very sensitive to changes in temperature (Brutsaert, 1975). To include the effect of greenhouse gases other than vapor pressure on LDR, Konzelmann et al. (1994) changed Brutsaert (1975) equation to:

$$\epsilon_{\mathrm{cl}} = 0.23 + x_1 (\frac{p_{\mathrm{v}}}{T^*})^{1/x_2}, \tag{13}$$

where $x_1 = 0.443$ and $x_2 = 8$ were optimal for measurements on the Greenland ice sheet. Note that p_{v} is in Pascal in the Konzelmann et al. (1994) publication. To be consistent, we use $\epsilon_{\mathrm{cl}} = 0.23 + x_1 (\frac{100 p_{\mathrm{v}}}{T^*})^{1/x_2}$ here. Another physically based equation taking into account both temperature and water vapor was proposed by Satterlund (1979) to ensure that ideal black body radiation is not exceeded by any extreme temperature or humidity value. Tested with measurements from Aase and Idso (1978) at Sidney, Montana, his formula resulted in:

$$\epsilon_{\mathrm{cl}} = x_1 \cdot (1 - \exp(-p_{\mathrm{v}}^{\frac{T^*}{2016}})),\ \text{where } x_1 = 1.08. \tag{14}$$

Prata (1996) found:

$$\epsilon_{\mathrm{cl}} = 1 - (1 + u) \exp(-(x_1 + x_2 u)^{x_3}), \tag{15}$$

with $u = 46.5 \frac{p_{\mathrm{v}}}{T^*}$ to represent the full long-wave spectrum such that $\epsilon_{\mathrm{cl}} \to 1 - \exp(-x_1^{x_3}) = \text{const}$ for $u \to 0$ and $\epsilon_{\mathrm{cl}} \to 1$ for $u \to \infty$. Prata (1996) estimated $x_1 = 1.2$, $x_2 = 3$ and $x_3 = 0.5$ for the measurements of Robinson (1947, 1950), the data that was also used by Brutsaert (1975). Iziomon et al. (2003) suggested another equation:

$$\epsilon_{\mathrm{cl}} = 1 - x_1 \exp(-x_2 \frac{p_{\mathrm{v}}}{T^*}),\ x_1 = 0.43 \text{ and } x_2 = 11.5 \tag{16}$$

which was fitted to measurements performed in Germany, whereas Dilley and O'Brien (1997) estimated $\mathrm{LDR_{cl}} = (1 - \exp(-1.66\tau))\sigma_{\mathrm{SB}} \cdot T^*$ where $\tau = 2.232 - 1.875(T/273.16) + 0.7356(w/2.5)^{1/2}$ is the grey-body optical thickness. His aim was to represent the main emission processes of the lower atmosphere, i.e. emission from water vapor and CO_2. Approximating the exponential by power series and neglecting all but the lowest order multinomials leads to:

$$\mathrm{LDR_{cl}} = x_1 + x_2 (T^*/273.16)^6 + x.3\sqrt{w/2.5}, \tag{17}$$
$$x_1 = 59.38,\ x_2 = 113.7,\ x_3 = 96.96.$$

The exponent of temperature is in accordance with the findings by Swinbank (1963). The simples equation assuming constant emissivity:

$$\epsilon_{\mathrm{cl}} = \text{const} \tag{18}$$

resulted convenient for Maykut and Church (1973) in Point Barrow, Alaska, and König-Langlo and Augstein (1994) for Arctic and Antarctic measurements.

3.1.3 Cloud transmissivity and cloud cover

The amount of clouds in the atmosphere determines the difference between clear-sky and all-sky LDR. Since cloud observations rarely exist, it is common to estimate the cloud

transmissivity τ_c as the ratio of the estimated clear-sky global SDR_{glob} and the measured global SDR^*_{glob} (e.g. Greuell et al., 1997):

$$\tau_c = \frac{SDR^*_{glob}}{SDR_{glob}}. \quad (19)$$

Note that $\tau_c < 1$ if the sky is overcast, and $\tau_c = 1$ denotes clear-sky conditions. Most parameterizations for all-sky LDR are based on the cloud-factor N, which is zero if the sky is completely clear, and one if the sky is cloud-covered. The linear relation between τ_c and N (Crawford and Duchon, 1998):

$$N = 1 - \tau_c \quad (20)$$

is used in this study. Different relationships involving a quadratic dependence of N and τ_c (Greuell et al., 1997) or even containing further parameters such as the relative humidity (Sicart et al., 2006) can be found in the literature.

3.1.4 All-sky LDR

Existing all-sky LDR parameterizations were summarized and tested for measurements recorded at Ny-Ålesund, Spitsbergen by Pirazzini et al. (2000) and result in the following two equations:

$$LDR_{all} = LDR_{cl} \cdot (1 + aN^{p_0}) \quad (21)$$

and

$$LDR_{all} = (\epsilon_{cl}(1 - N^{p_1}) + \epsilon_{oc}N^{p_2})\sigma_{SB}T^{*4}, \quad (22)$$

where ϵ_{cl} is the estimated clear-sky emissivity, a, p_0, p_1 and p_2 are parameters and ϵ_{oc} is the cloud emissivity. In this study, a slightly modified formula is further examined:

$$LDR_{all} = (\epsilon_{cl}\tau_c^{\tilde{p_1}} + \tilde{\epsilon}_{oc}(1 - \tau_c^{\tilde{p_2}}))\sigma_{SB}T^{*4}, \quad (23)$$

where the all-sky LDR is determined based on cloud transmissivity directly. This has the advantage of not having to choose a conversion from τ_c to N, but the disadvantage that a comparison with published values for the parameters $\tilde{p_1}$, $\tilde{p_2}$ and $\tilde{\epsilon}_{oc}$ is not possible.

3.1.5 Interpolation of cloud transmissivity during nighttime

The cloud transmissivity can, during daytime, be estimated according to Eq. 19. During the night, it is often determined by linearly interpolating between the last point in time at sunset, and the first point in time in the morning, or using a constant interpolation taking a mean cloud amount value from the preceding afternoon (Lhomme et al., 2007). These interpolated cloud transmissivity estimates are rarely validated due to the lack of available data. Here, we use different interpolation techniques, calculate the all-sky LDR during the night and evaluate the outputs with the ASRB measurements. The interpolation methods are:

1. linear interpolation between a mean value of x points in time (where each point in time represents an hourly value) before sunset and x points in time after sunrise,

2. constant interpolation of the mean value of x points in time before sunset,

3. constant interpolation of the mean value of x points in time after sunrise,

where $x = 1, 2, ..., 6$.

3.2 Model evaluation

The models are evaluated by a) investigating the model sensitivities to certain previously selected parameters, b) assessing the models' output uncertainty coming from uncertainty in input data and model parameters, c) comparing model outputs to measurements for validation, and d) calibrating diverse empirical and physical LDR parameterizations to conditions in Switzerland. To investigate a) and b), a probability density function (often called prior distribution, Table 2) is assigned to estimate the errors in the input variables and the parameters (Sect. 2.2). The errors in the parameters and input measurements are assumed to be independent. These distributions form the basis to analyze the local sensitivity of the model to each parameter (Sect. 3.2.1), and to perform a Monte Carlo based uncertainty analysis (Sect. 3.2.2). Using the mean parameter values and zero error for the input measurements, a simulation is run and the models are validated (Sect. 3.2.3). Calibration of the LDR parameterizations is performed based on non-linear least-squares estimation (Sect. 3.2.4).

3.2.1 Sensitivity analysis

SDR: Local relative sensitivities of direct, diffuse and global clear-sky SDR to ozone, precipitable water, the Ångström parameters and ground albedo are estimated. The sensitivities are estimated for constant path length $m_r = 2$, the path length estimated for a mean solar zenith angle of around 60 degrees at Jungfraujoch. Each model parameter θ_i is varied, unless the interval exceeds the physically possible values, within the interval $[\mu_i - 2\sigma_i, \mu_i + 2\sigma_i]$ while all other parameter $\theta_{j \neq i}$ are kept fixed at μ_j. Thereby, the influence of 97 % of the most plausible parameter values on SDR is investigated.

LDR: The sensitivity analysis focuses on the three main inputs determined in a preliminary analysis: cloud transmissivity, air temperature and relative humidity. LDR sensitivity is expressed as the *relative standard deviation* σ_{rel} of the output frequency distribution by varying the errors of each input variable according to its prior distribution, and keeping the others fixed. This is repeatedly done for different values of air temperature, relative humidity and cloud transmissivity to study the interactions between the three variables.

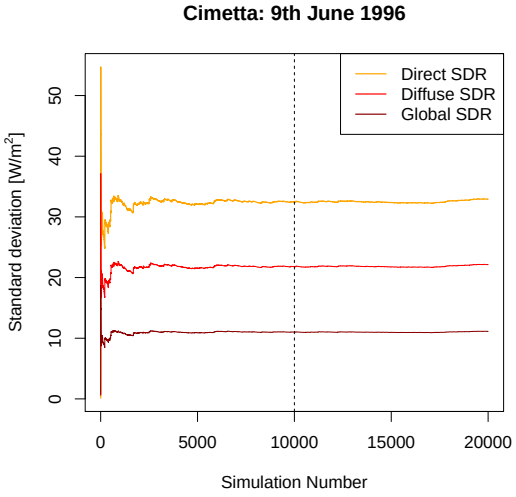

Fig. 2. Standard deviations of the model simulations at Cimetta. 10 000 model simulations result sufficient to reach stable standard deviations of the output frequency distribution.

3.2.2 Uncertainty assessment

Monte-Carlo based methods are widely used to derive the frequency density of the output of a model due to the simple implementation even for complex, non-linear models. 10 000 model simulations were sufficient to estimate total model output uncertainty (Fig. 2). The standard uncertainty of the model is defined as the standard deviation $\sigma_{t,\mathrm{abs}}$ of the model result at each time step (JCGM, 2008). The relative uncertainties are $\sigma_{t,\mathrm{rel}} := \sigma_{t,\mathrm{abs}}/\mu_t$. The 90 %-quantile and the median of the relative uncertainties for all time steps are estimated, and used as conservative respectively confidence estimates of the total output uncertainty. Further, a function $f(\mathrm{SDR}) = \sigma_{\mathrm{SDR,\,rel}}$ is fitted to the relative uncertainties using non-linear least-squares regression to derive the relative uncertainty in dependence of the modeled radiation.

3.2.3 Validation

Clear-sky global SDR and all-sky LDR are validated using the ASRB measurements (Sect. 2.1). The models are evaluated for a simulation which is performed with the measured input time series (assumed error-free) and the fixed parameter values μ (Table 2). According to Gueymard (2011), model performance is measured using the mean bias deviance (MBD) and the mean root squared deviance (RMSD) expressed in percent of the mean measured radiation. This naming is preferred over the often found mean bias error (ME) and root mean squared error (RMSE) to emphasize that a deviation between the model output and the measured value can come from both model error and measurement uncertainty (Gueymard, 2011). The MBD is a simple and very familiar measure that neglects the magnitude of the errors (i.e. positive errors can compensate for negative ones):

$$\mathrm{MBD} = \frac{1}{\overline{y^*}} \cdot \frac{\sum_{t=1}^{n} e_t}{n} \tag{24}$$

$$\mathrm{MBD} \in (-\infty, \infty),\ \mathrm{MBD}_{\mathrm{perf}} = 0,$$

where $e_t := y_t - y_t^*$ are the residuals of the models. Here, y_t denotes the modeled output variable, and y_t^* is the corresponding measured variable. The RMSD is:

$$\mathrm{RMSD} = \frac{1}{\overline{y^*}} \cdot \sqrt{\frac{1}{n}\sum_{t=1}^{n} e_t^2}, \tag{25}$$

$$\mathrm{RMSD} \in [0, \infty),\ \mathrm{RMSD}_{\mathrm{perf}} = 0.$$

It accounts for the average magnitude of the errors and puts weight on larger errors, but does not account for the direction of the errors. For clarity, both MBD and RMSD are expressed in percents throughout the manuscript. The correlation coefficient R measures the linear agreement between the modeled and the measured variable:

$$\mathrm{R} = \frac{\sum_{t=1}^{n}(y_t - \overline{y})(y_t^* - \overline{y^*})}{\sqrt{\sum_{t=1}^{n}(y_t - \overline{y})^2 (y_t^* - \overline{y^*})^2}} \tag{26}$$

$$\mathrm{R} \in [-1, 1],\ \mathrm{R}_{\mathrm{perf}} = 1,$$

The coefficient of determination R^2 indicates the amount of variation in one variable explained through the other.

3.2.4 LDR calibration using non-linear least-squares

Non-linear least-squares estimation (Bates and Watts, 1988; Bates and Chambers, 1992) is used to fit the clear-sky LDR parameterizations to observational data. In a first step, the clear-sky emissivity is estimated as:

$$\epsilon_{\mathrm{cl}} = \frac{\mathrm{LDR}_{\mathrm{in,cl}}^*}{\sigma_{\mathrm{SB}} T^{*4}}, \tag{27}$$

where both $\mathrm{LDR}_{\mathrm{in,cl}}^*$ and T^* are measurements of the ASRB stations. Then, the parameterizations presented in Table 3 are fitted to ϵ_{cl}. The start values for the non-linear estimation are the parameters presented in the respective publications. Thereby, optimal parameter values are obtained for each station. Furthermore, the parameterizations are fitted simultaneously to all stations, resulting in one single set of optimal parameters. Clear-sky situations are determined according to Marty and Philipona (2000); Dürr and Philipona (2004).

In a next step, the behaviour of the different parameterizations is evaluated according to three criteria: a) small MBD as an absolute value (Eq. 24), b) small RMSD (Eq. 25), and c) similarity in order of magnitude and sign of parameter estimates and published values. According to these criteria, the best parameterizations are identified.

4 Results

4.1 Clear-sky SDR

4.1.1 Validation

Modeled clear-sky global SDR is validated using the ASRB measurements. In general, a good linear agreement between model output and the measurements is observed (Fig. 3). The larger relative errors for low radiation can be attributed to the larger path length and thus higher influence of the estimated parameters ozone, precipitable water, aerosol content and ground albedo. Further, errors in cloud cover estimation by Marty and Philipona (2000); Dürr and Philipona (2004) might be responsible for some of the scatter observed at Jungfraujoch, for example (Fig. 3). To confirm the validity of the Iqbal-model for conditions in Switzerland, a model experiment was additionally performed using measurements of the atmospheric parameters (precipitable water, Ångström parameter α and β), and measured diffuse SDR in Payerne from the Swiss Alpine Climate Radiation Monitoring network (SACRaM) of MeteoSwiss. We see that the Iqbal (1983) model performs satisfactorily when using measured atmospheric parameters (Fig. 4, top). The scatter in diffuse SDR is normal for simple models such as the one by Iqbal (1983) (personal communication with C. Gueymard). Assuming that measurements of the atmospheric parameters do not exist, the diffuse SDR indicates large errors of $-17\,\%$ (MBD) and $37\,\%$ (RMSD) compared to $10\,\%$ (MBD) and $11\,\%$ (RMSD) when using the measurements (Fig. 4). Further, a limiting value of around $100\,\mathrm{W\,m^{-2}}$ in modeled diffuse SDR arises from an underestimation of the aerosol content. Global SDR however is modeled satisfyingly using constant values of the atmospheric parameters since the diffuse SDR only accounts for around one tenth of global SDR, and since errors due to "incorrect" aerosol content in direct and diffuse SDR are of opposite sign and compensate for each other (see Sect. 4.1.2).

To check for systematic errors, the residuals e_t were correlated with the input variables and the sun elevation. While for the input variables the correlations are low ($-0.2 < \mathrm{R} < 0.2$), errors slightly correlate with sun elevation (between 0 and 0.4 for direct, around -0.4 for diffuse and between -0.3 and 0.2 for global SDR). For direct SDR, the residuals scatter more (towards positive values) above the freezing point and for a relative humidity of around $60\,\%$, similarly the diffuse SDR (but in opposite direction). Due to compensating effects, this is not observed for global SDR. Since the correlations are not large, systematic errors are not further investigated.

One restriction already mentioned above must be kept in mind: clear-sky hours are based on the cloud estimation of Marty and Philipona (2000); Dürr and Philipona (2004) and thus error-prone. This might be a cause for some of the scatter in Fig. 3 at Jungfraujoch, for example. To analyze the effect of the clear-sky estimation, the validation measures were further estimated for clear-sky hours using synoptic cloud observations at the three stations Jungfraujoch, Payerne and Locarno-Monti. Since the overall picture of the model evaluation did not change the analysis strongly, the results of the clear-sky evaluation presented here are assumed to be reliable. A further indication of the validity of the approach is that the errors in the modeled clear-sky radiation do not correlate with the Dürr and Philipona (2004) cloud cover estimates.

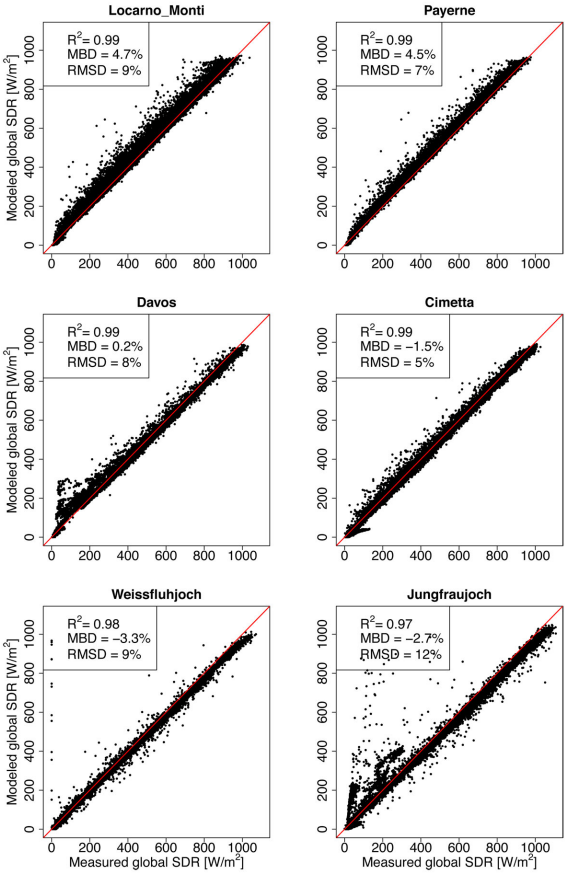

Fig. 3. Scatter plots of global modeled and measured SDR at all locations. The solid red line indicates the perfect fit.

4.1.2 Sensitivity of the clear-sky SDR

SDR is most sensitive to the atmospheric turbidity coefficient β (e.g. Gueymard, 2003b; Schillings, 2004, aerosol estimated from a visibility index), resulting in changes of -20 to $6\,\%$ for direct, -10 to $4\,\%$ global SDR, and of -30 to $80\,\%$ and more for diffuse SDR for $0 < \beta \leq 0.14$ for a mean path length of 2 (Fig. 5). The second most important parameter determining SDR is precipitable water, translating into an

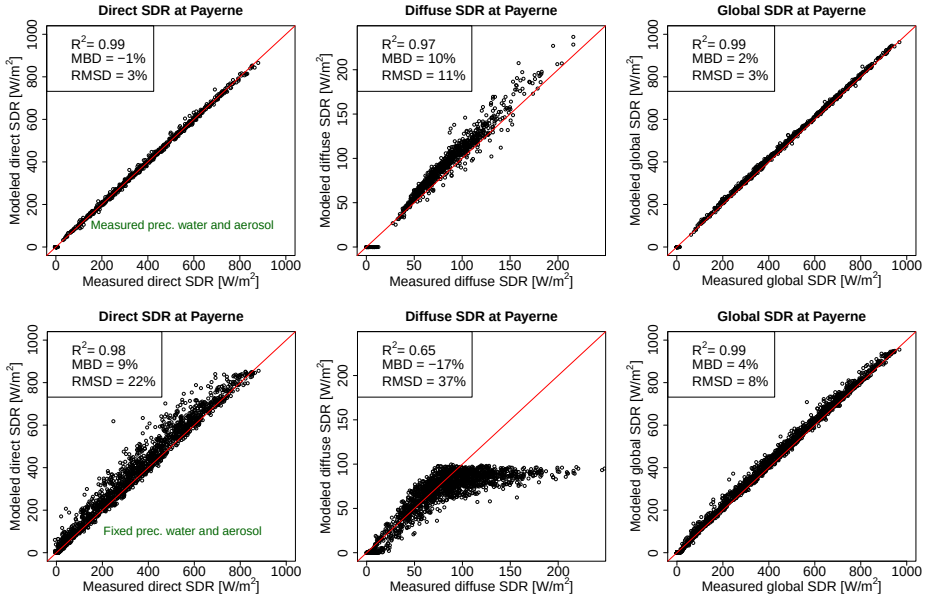

Fig. 4. Scatter plots of direct, diffuse and global SDR at Payerne. The top figures result from a model experiment when using measurements of the precipitable water and aerosol content. The lower figure show the model results when the atmospheric parameters have fixed values. The solid red line indicates the perfect fit.

uncertainty of around −4 to 10 % in direct and global SDR, whereas the Ångström coefficient α produces around −4 to 4 % uncertainty for direct, and a slightly smaller uncertainty for global SDR. Sensitivity to ozone is negligible for modeled SDR (less than 0.5 %). The ground albedo is an important parameter for diffuse SDR. It changes strongly within a year, having values of 0.1 for snow-free soils in summer, and more than 0.8 after fresh snow in winter. Clear-sky diffuse SDR changes by around ±20 % within this range of values. Since the diffuse SDR accounts only for a small part of the clear-sky global SDR, ground albedo does not play such an important role there (around ±2 %). The sensitivities in direct and diffuse SDR to aerosol content are opposite, i.e. an overestimation results in an underestimation of direct, but an overestimation of diffuse SDR. In the sum, these uncertainties compensate for each other and the relative error in global SDR is therefore smaller.

An additional uncertainty comes from estimating SDR at an hourly value for an instantaneous sun zenith angle. By calculating the solar zenith angle every 10 min and averaging the estimated SDR to hourly values, a mean deviance of less than 0.5 %, and a root mean squared deviance of 3 % was estimated for all direct, diffuse and global SDR.

4.1.3 Uncertainty of the clear-sky SDR

Uncertainty in direct SDR increases with decreasing elevation as there is a clear positive correlation of uncertainty with path length (Fig. 6), which can, to a smaller degree, also be observed for diffuse and global SDR. The 90 %-quantile of the absolute uncertainty for direct SDR goes from 43 W m^{-2} (JUN) to 55 W m^{-2} (OTL), and the median is around 38 W m^{-2}. Global SDR has the smallest absolute uncertainty of less than 20 W m^{-2}, resulting from the compensating effects of modeled direct and diffuse SDR with respect to aerosol content (see Sect. 4.1.2). The relative uncertainty for direct SDR approximates 5 % with increasing radiation. The median of direct SDR uncertainty does not exceed 10 % at all stations, however the 90 %-quantile of the relative uncertainties goes up to 20 %. For diffuse SDR, relative uncertainty goes from 25 % to 40 %, and the median scatters around 38 %. In contrast to direct and global SDR, the relative uncertainty increases with increasing diffuse SDR until around 60 W m^{-2}. For global SDR, the 90 %-quantiles of the relative uncertainty scatters around 6 % and goes down to 3 %. A conservative estimate (i.e. towards higher uncertainty) of the uncertainty in SDR is thus:

$$\mathrm{SDR}_i = \mathrm{SDR}_i^{\mathrm{est}} \cdot (1 + \varepsilon_{\mathrm{SDR}_i,\mathrm{rel}}), \qquad (28)$$

$$\varepsilon_{\mathrm{SDR}_i,\mathrm{rel}} \sim \mathcal{N}(0, \sigma^2_{\mathrm{SDR}_i,\mathrm{rel}}),$$

with

$$\sigma_{\mathrm{SDR}_i,\mathrm{rel}} = \begin{cases} 0.2, & \text{if } i = \text{direct}, \\ 0.4, & \text{if } i = \text{diffuse}, \\ 0.06, & \text{if } i = \text{global}, \end{cases} \qquad (29)$$

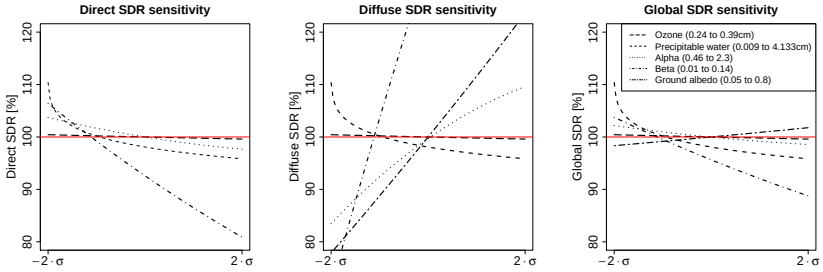

Fig. 5. Local sensitivities of clear-sky direct, diffuse and global SDR to ozone, precipitable water, the Ångström parameters α and β and ground albedo. The sensitivities are estimated for constant path length $m_r = 2$, the value for the mean solar zenith angle at Jungfraujoch. The range of the different parameters are given in the legend. The slope of the different curves reflect the relative sensitivity to each parameter. The mean downward radiation is indicated in red. The x-range is $\mu - 2\sigma$ to $\mu + 2\sigma$ avoiding parameter values without physical meaning (cf. Table 2).

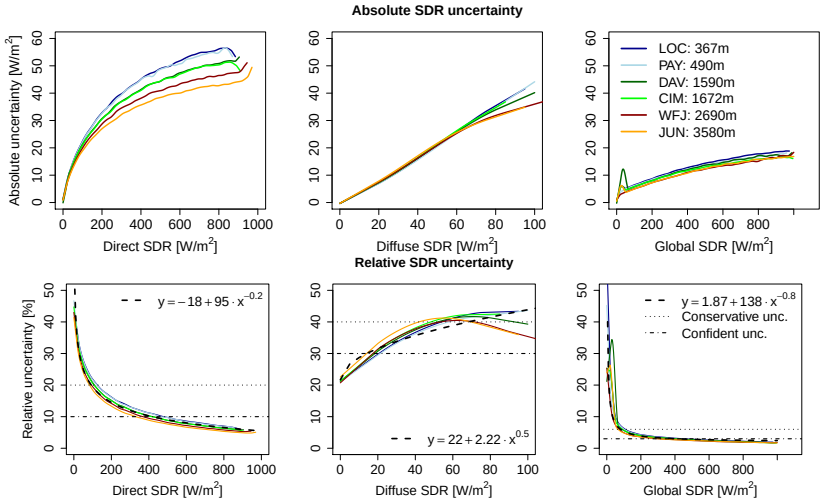

Fig. 6. Uncertainty expressed as smoothed mean lengths of the standard deviation of clear-sky direct, diffuse and global SDR, as a function of radiation [W m^{-2}]. The graphs were obtained by estimating the mean standard deviation of each 5 W m^{-2} radiation interval. Smoothing was performed using non-parametric regression. The dashed black line denotes the fit of the function $f(\mathrm{SDR}) = \sigma_{\mathrm{SDR,rel}}$, where $x := \mathrm{SDR}_i$ and $y := \sigma_{\mathrm{SDR}_i,\mathrm{rel}}$. The coefficients of the function $f(x) = y$ were obtained by non-linear least-squares regression.

while a more confident estimate results in:

$$\sigma_{\mathrm{SDR}_i,\mathrm{rel}} = \begin{cases} 0.1, & \text{if } i = \text{direct}, \\ 0.3, & \text{if } i = \text{diffuse}, \\ 0.03, & \text{if } i = \text{global}. \end{cases} \quad (30)$$

Further, a function $f(\mathrm{SDR}) = \sigma_{\mathrm{SDR,\,rel}}$ was fitted through the relative uncertainties for all three SDR types using non-linear least-squares estimation, resulting in:

$$\sigma_{\mathrm{SDR}_i,\mathrm{rel}} = \frac{1}{100} \begin{cases} -18 + \frac{95}{\mathrm{SDR}_i^{0.2}}, & \text{if } i = \text{direct}, \\ 22 + 2.22\sqrt{\mathrm{SDR}_i}, & \text{if } i = \text{diffuse}, \\ 1.87 + \frac{138}{\mathrm{SDR}_i^{0.8}}, & \text{if } i = \text{global} \end{cases} \quad (31)$$

where $\sigma_{\mathrm{SDR}_i,\mathrm{rel}}$ determines the standard deviation of the relative errors $\varepsilon_{\mathrm{SDR}_i,\mathrm{rel}}$ in modeled SDR. This function allows to determine the uncertainty in modeled clear-sky SDR more precisely for individual cases.

4.2 Clear- and all-sky LDR

4.2.1 Parameter estimation and validation of the clear-sky LDR

The non-linear least-squares fitting of the clear-sky LDR parameterizations (Table 3) to the six stations in Switzerland resulted in the parameter values presented in Table 4. For most parameterizations, a trend of the estimates is observed with elevation, indicating that a function depending on elevation

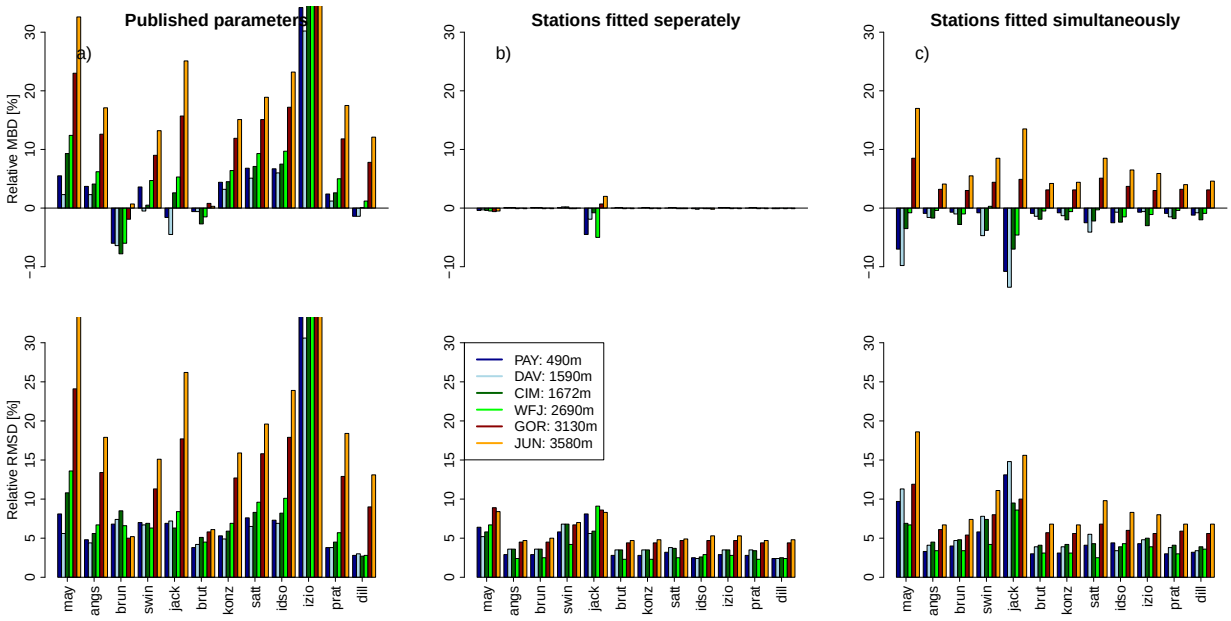

Fig. 7. MBD and RMSD for the LDR parameterizations using **(a)** the published parameter values, **(b)** the parameter values when fitting the parameterizations to each station separately and **(c)** when fitting all stations together simultaneously.

could result in an improvement of the parameterizations. For many applications, a modeler would apply the published parameterization as it is and use only one parameter value instead of modeling the elevation dependence of the parameter additionally. To get the best parameter estimate for all stations together, the parameterizations were also fitted to the measurements of all stations simultaneously (Table 4, second column). Except for Idso and Jackson (1969), all fitted parameters vary around the published values. The parameter in the exponential function of Idso and Jackson (1969) changes sign and thus appears to be not representative for high elevations such as JUN or WFJ. It is further less accurate than the other parameterizations together with the simple Maykut and Church (1973) parameterization (Fig. 7, middle and right). From the latter we conclude that clear-sky emissivity is not adequately represented by a constant value.

To compare the behaviour of the estimated parameters, the MBD and the RMSD of the clear-sky LDR of the published parameterizations were estimated in a first step (Fig. 7, left). The Brunt (1932); Brutsaert (1975) and Dilley and O'Brien (1997) have smallest MBD (-10 to 15 %) and RMSD (less than 10 % (except for Dilley and O'Brien (1997) at JUN and WFJ)). LDR is mostly overestimated by the models. In general (except for Brunt, 1932; Brutsaert, 1975), the lower elevation stations are better represented by the parameterizations. One possible reason is that most parameterizations were developed and fitted to measurements in lowland areas. Fitting the parameterizations to each location separately strongly improves model predictions leading to MBDs around zero and RMSDs of less than 10 % for all parameterizations (Fig. 7, middle). This can be expected since the parameterizations were trained and compared with and to the same data, i.e. validation was not performed on independent data. Measured air temperature and relative humidity used to *drive* the model are however *independent*; for fitting the ASRB and for validation the ANETZ measurements were used. When using the parameterizations with the simultaneously fitted parameter estimates (Fig. 7, right), the accuracy of the parameterization in comparison to the published values is also improved, and the uncertainty is reduced. Also in this experiment, training and validation data are not completely independent, the validation measurements in each case however consist only of one sixth of the training data. One can see that LDR at lower elevation stations is generally underestimated, and overestimated at the higher stations. The best performing parameterizations are Ångström (1915); Brunt (1932); Brutsaert (1975); Konzelmann et al. (1994) and Dilley and O'Brien (1997), having relative MBDs of less than 5 % and RMSDs of less than 10 %. We conclude that the behaviour of the parameterizations can be strongly improved by fitting them to local climatic conditions.

Since the performance of the best parameterizations is comparable, only one of the parameterizations was selected to study the all-sky situations. Konzelmann et al. (1994) was chosen because apparently the use of only two parameters is sufficient to model clear-sky emissivity in Switzerland. Further, the parameterization has earlier on been used in studies performed in Alpine regions (Greuell et al., 1997; Klok

Table 4. Values of the fitted parameters of the clear-sky LDR parameterizations to the six locations. The first column indicates the published parameter values and the second column indicates the estimated parameters when the stations are treated simultaneously.

	Pub	All	OTL	PAY	DAV	CIM	WFJ	JUN	
may_1	0.7855	0.69	0.74	0.77	0.72	0.70	0.63	0.59	
$angs_1$	0.83	0.79	0.83	0.86	0.80	0.77	0.72	0.65	
$angs_2$	0.18	0.26	0.21	0.19	0.17	0.19	0.20	0.18	
$angs_3$	0.067	0.10	0.05	0.03	0.06	0.09	0.14	0.31	
$brun_1$	0.52	0.53	0.60	0.64	0.60	0.58	0.51	0.48	
$brun_2$	0.065	0.073	0.049	0.042	0.050	0.055	0.075	0.084	
$swin_1$	9.365	8.97	9.05	9.43	9.34	8.94	8.58	8.27	$\times 10^{-6}$
$jack_1$	0.261	0.33	0.285	0.245	0.287	0.331	0.357	0.394	
$jack_2$	7.77	6.0	4.5	2.2	1.2	10.7	−4.5	−5.1	$\times 10^{-4}$
$brut_1$	1.24	1.12	1.05	1.03	1.00	1.00	1.00	0.96	
$brut_2$	7	8.6	10.46	11.62	12.22	11.54	10.33	10.73	
$konz_1$	0.484	0.43	0.45	0.46	0.46	0.44	0.41	0.39	
$konz_2$	8	5.7	7.19	8.09	8.27	7.71	6.52	6.54	
$satt_1$	1.08	1.00	1.01	1.03	1.01	0.99	0.94	0.91	
$idso_1$	0.7	0.57	0.64	0.63	0.61	0.62	0.55	0.53	
$idso_2$	5.95	0.48	0.503	0.08	0.06	3.30	1.946	4.012	$\times 10^{-5}$
$idso_3$	1500	2369	2239	2801	2913	1702	1967	1813	
$izio_1$	0.43	0.42	0.35	0.32	0.35	0.38	0.44	0.47	
$izio_2$	11.5	16.44	10.42	9.07	11.67	11.87	16.76	20.62	
$prat_1$	1.2	0.26	0.4	0.87	0.76	0.46	0.38	0.24	
$prat_2$	3	4.75	5.19	4.51	4.21	4.91	3.93	4.41	
$prat_3$	0.5	0.42	0.40	0.42	0.43	0.4	0.42	0.37	
$dill_1$	59.38	29.43	58.18	66.24	61.73	36.5	29.10	22.96	
$dill_2$	113.7	124.6	114.4	91.5	97.7	140.8	128.2	130.3	
$dill_3$	96.96	119.2	102.41	129.71	122.34	88.11	98.02	97.21	

Table 5. Fitted parameters of the all-sky LDR parameterizations presented in Eqs. 21, 22 and 23. The clear-sky emissivity is estimated according to Konzelmann et al. (1994). The second line consists of the estimates when all stations are fitted simultaneously, while the first indicates the values estimated by Pirazzini et al. (2000).

	Eq. (21)		Eq. (22)			Eq. (23)		
	a	p_0	ϵ_{oc}	p_1	p_2	$\tilde{\epsilon}_{oc}$	$\tilde{p}_1$	$\tilde{p}_2$
Published	0.40	2.00	0.979	6.00	4.00			
All	0.34	1.00	0.957	0.29	0.42	0.968	3.77	2.97
OTL	0.29	1.41	0.980	2.68	2.25	0.985	2.05	1.61
PAY	0.33	1.20	1.003	0.48	0.60	0.940	4.08	2.94
DAV	0.30	1.06	0.993	0.47	0.56	0.928	3.28	2.57
CIM	0.37	0.95	1.025	0.65	0.70	0.987	2.05	1.78
WFJ	0.46	0.74	1.028	0.27	0.37	0.926	5.02	3.74
JUN	0.50	0.61	0.988	1.21	0.82	0.828	0.76	1.24

and Oerlemans, 2002; Mittaz et al., 2002; Machguth et al., 2008). Konzelmann et al. (1994) is preferred over the Brutsaert (1975) parameterization due to the additive constant representing the clear-sky emissivity of a dry atmosphere to include the effect of greenhouse gases.

4.2.2 Parameter estimation and validation of the all-sky LDR during daytime

The parameterizations of all-sky LDR are based on an estimated clear-sky emissivity coupled with the effect of cloudiness or cloud emissivity. Clear-sky emissivity is estimated according to Konzelmann et al. (1994) with the fitted parameter estimates (Table 4, second column). The fitted values of the parameters of the two parameterizations (Pirazzini et al. (2000), Eqs. 21 and 22) and the modified parameterization

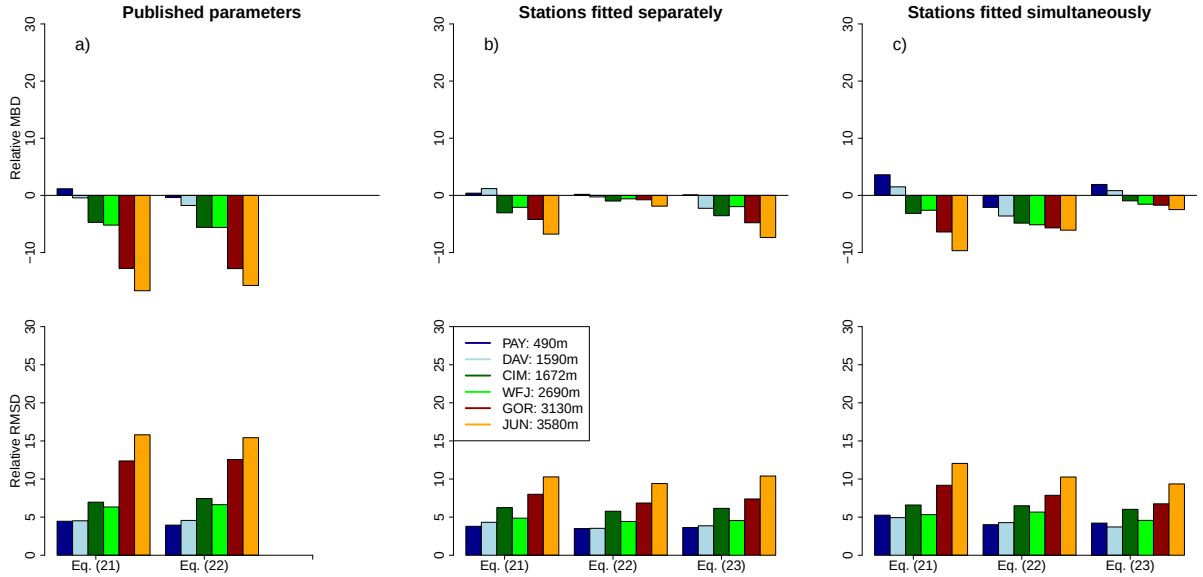

Fig. 8. MBD and RMSD for the LDR parameterizations using **(a)** the published parameter values by Pirazzini et al. (2000), **(b)** the parameter values when fitting the parameterizations to each station separately and **(c)** when fitting all stations together simultaneously. Clear-sky emissivity is estimated based on the Konzelmann et al. (1994) parameterization, using the parameters fitted for all stations simultaneously.

(Eq. 23) are presented in Table 5. The parameters reach values which are more or less comparable with those in the literature (Pirazzini et al., 2000, c.f. Table 3), however for CIM and WFJ, the estimated cloud emissivity ϵ_{oc} exceeds its physical range by being greater than 1. This problem does not arise for the modified parameterization (Eq. 23). MBD and RMSD are similar for all three parameterizations (Fig. 8), and slightly smaller for the modified version when fitting the stations simultanouesly. The relative MBD is less than 2 % for the latter, and RMSD is smaller than 10 %. Other than clear-sky LDR, all-sky LDR is overestimated at LOC and PAY, and underestimated at the higher elevation stations. The relative MBD and RMSD are comparable for clear-sky situations despite the greater uncertainties caused by cloud transmissivity. One reason for this is that LDR is around 30 to 50 W m^{-2} greater for cloudy than for clear skies, and therefore the absolute MBD and RMSD are divided by a greater number. All-sky LDR deviates more strongly from the measurements than clear-sky LDR (Fig. 9).

We proceed with the modified parameterization Eq. (23) for two reasons: (a) conversion from cloud transmittance τ_c to cloud cover N is not necessary and (b) the fitting to the measurements resulted in physically reasonable cloud emissivity values.

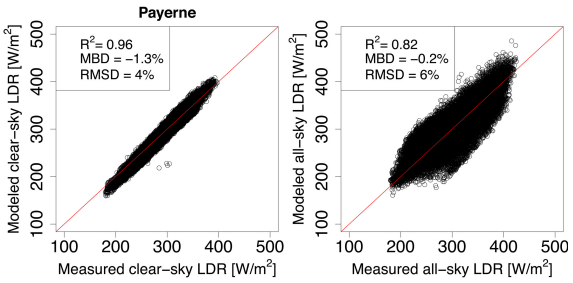

Fig. 9. Scatter plots of measured and modeled clear- and all-sky LDR according to Konzelmann et al. (1994) and Eq. 23.

4.2.3 Interpolation of cloud transmissivity during nighttime

The best all-sky LDR results during day- and nighttime were obtained by linearly interpolating the mean of the four cloud transmissivity values during the last hours in the afternoon preceeding the night, and the four hours in the following morning. For the simultaneous fitting, it resulted in a MBD of around 5 % and a RMSD up to 13 %, whereas the higher elevation stations have larger errors. Fitting the stations separately resulted in similar validation values. Constant interpolation resulted in errors that are around 2 % higher.

4.2.4 Sensitivity of the all-sky LDR

Modeled all-sky LDR (using Konzelmann et al. (1994) and Eq. 23) is sensitive to errors in air temperature, relative humidity and cloud transmissivity. The estimated parameters $x_1, x_2, \tilde{p_1}, \tilde{p_2}$ and $\tilde{\epsilon}_{\text{oc}}$ have, within their estimated *confidence intervals*, only a minor influence. Cloud transmissivity has the greatest influence on LDR (Fig. 10). Modeled LDR changes up to around 15 % (standard deviation of around 7.5 %) on cold (-30 to -10° C) and slightly cloudy ($0.8 < \tau_c < 1$) days for $\varepsilon_{\tau_c} \sim \mathcal{N}(0, 0.08)$, whereas the uncertainty decreases for increasing air temperature to around 2 % (for air temperatures above 20 °C) (Fig. 10a). The sensitivity in LDR to cloud transmissivity decreases with increasing relative humidity, and is around 5 % for slightly cloudy skies (Fig. 10b). Changes in low cloud transmissivity (i.e. when the sky is overcast) only provoke a standard deviation of about 1% in simulated LDR. Accurate measuring or modeling of cloud transmissivity (or cloud cover) is therefore more important for slightly cloudy skies. In absolute values, an uncertainty of 0.08 in cloud transmissivity results in errors of around 4 (overcast) to 25 W m^{-2} (cold, high relative humidity, only few clouds). An error of 0.2 °C in measured air temperature causes a relative standard deviation of around 0.5% for clear-sky LDR, and around 0.3% in overcast situations (Fig. 10c). The sensitivity decreases for increasing temperature, and varies only slightly for differing humidities (Fig. 10d). The sensitivity to errors of 5 % in measured relative humidity increases to 3 % on clear-days, and to almost 0 % for overcast situations (Fig. 10f). With respect to air temperature, the sensitivity increases slightly with increasing temperatures, and ranges around 0.5 % (Fig. 10e).

4.2.5 Uncertainty of the all-sky LDR

The uncertainty of the all-sky LDR was estimated for the Konzelmann et al. (1994) clear-sky parameterization together with the all-sky parameterization in Eq. (23). The parameters were fitted to all stations simultaneously. The cloud transmissivity was linearly interpolated during nighttime according to Sect. 4.2.3. The uncertainty is estimated similarly to the uncertainty in SDR by doing a Monte Carlo simulation for all input variables, the cloud transmissivity and the fitted parameters.

The all-sky LDR output uncertainty is below around 14 W m^{-2} at all locations. In relative terms, the 90 %-quantile of the uncertainty is smaller than 6 % at all locations. The median of the relative uncertainty for the all-sky LDR is around 3 %. A conservative estimate of the uncertainty of the all-sky LDR is:

$$\text{LDR}_{\text{all}} = \text{LDR}_{\text{all}}^{\text{est}} \cdot (1 + \varepsilon_{\text{LDR}_{\text{all, rel}}}), \quad (32)$$

$$\varepsilon_{\text{LDR}_{\text{all, rel}}} \sim \mathcal{N}(0, \sigma^2_{\text{LDR}_{\text{all, rel}}}),$$

with

$$\sigma_{\text{LDR}_{\text{all, rel}}} = 0.06, \quad (33)$$

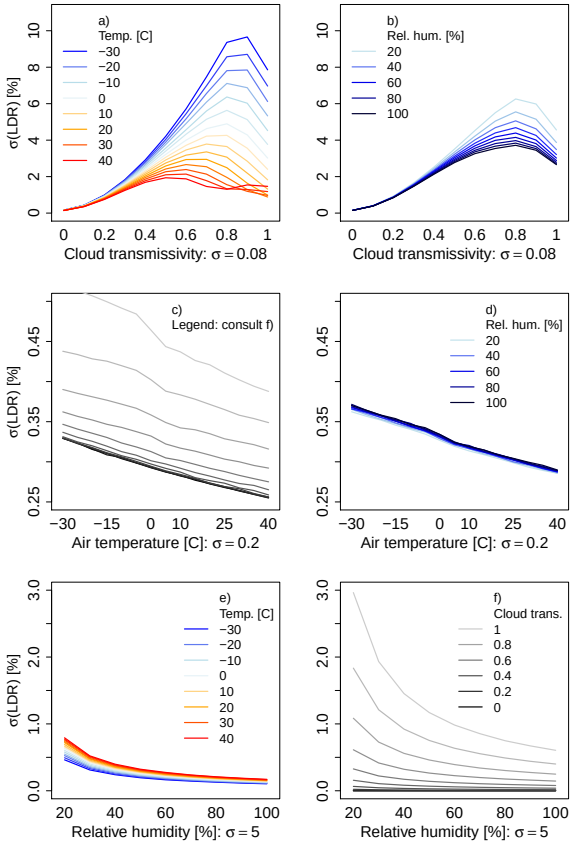

Fig. 10. LDR sensitivity to errors in estimated cloud transmissivity ($\sigma = 0.08$, **(a)** and **(b)**), measured air temperature ($\sigma = 0.2$ °C, **(c)** and **(d)**) and relative humidity ($\sigma = 5$ %, **(e)** and **(f)**). LDR sensitivity is expressed in the relative standard deviation of the simulated LDR using Monte Carlo. For air temperature for example, a mean value of 5 °C with an uncertainty of 0.2 °C results in a relative standard deviation of 0.45 % for clear-skies ($\tau_c = 1$) and 0.3% for overcast skies.

while the more confident estimate for the uncertainty in the LDR results in:

$$\sigma_{\text{LDR}_{\text{all, rel}}} = 0.03. \quad (34)$$

The function $f(\text{LDR}_{\text{all}}) = \sigma_{\text{LDR}_{\text{all, rel}}}$ was fitted through the relative uncertainties of the LDR using non-linear least-squares estimation, which results in:

$$\sigma_{\text{LDR}_{\text{all, rel}}} = \frac{1}{100} \frac{2681}{\text{LDR}_{\text{all}}^{1.21}}, \quad (35)$$

where $\sigma_{\text{LDR}_{\text{all, rel}}}$ is the standard deviation of the relative error $\varepsilon_{\text{LDR}_{\text{all, rel}}}$.

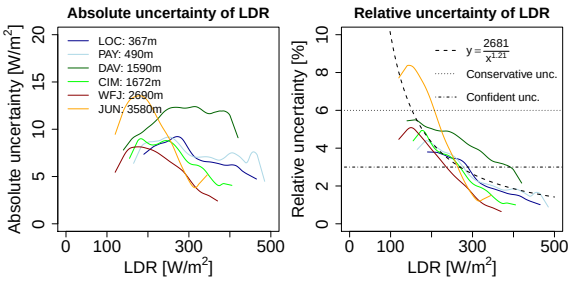

Fig. 11. Absolute and relative uncertainty of the modeled LDR. The clear-sky emissivity is estimated according to Konzelmann et al. (1994), and the all-sky parameterization is found in Eq. 23. The dashed black line denotes the fit of the function $f(\mathrm{LDR}) = \sigma_{\mathrm{LDR,\,rel}}$, where $x := \mathrm{LDR}$ and $y := \sigma_{\mathrm{LDR,\,rel}}$.

5 Discussion

The presented SDR and LDR models have been evaluated on many previous occasions (e.g. Gueymard, 1993, 2003b; Pirazzini et al., 2000; Klok and Oerlemans, 2002; Schillings, 2004; Sicart et al., 2006; Bilbao, 2006; Choi et al., 2008; Wang and Liang, 2009). The validation results for the clear-sky SDR and the all-sky LDR are in the range of these publications. We therefore only shortly comment our results with respect to some studies being of importance for the present study.

5.1 Evaluation of the clear-sky SDR model

According to Gueymard and Myers (2008), a clear-sky SDR model fits the measurements well if the MBD lies within ± 10 % and the RMSD< 20 % for global, and the MBD lies within ± 20 % and the RMSD<30 % for diffuse SDR. In Payerne, the Iqbal (1983) model C fulfills the even more stringent criteria by Badescu et al. (2012) (−5 % <MBD < +5 % and RMSD <15 % for global, and −10 % < MBD < +10 % and RMSD <30 % for diffuse SDR) if using measurements of the atmospheric variables in the model. In addition, the criteria are fulfilled for *global* SDR at all six stations even using *fixed* values of the atmospheric parameters. These findings are in agreement with Badescu et al. (2012) who tested the Iqbal (1983) model C together with 53 other clear-sky SDR models of diverse complexity on their performance and sensitivities in Cluy-Napoca and Bucharest, Romania. Badescu et al. (2012) however shows that the Iqbal (1983) model C for global SDR has some deficiencies in Cluy-Napoca for some of the sensitivity stages that were investigated. Model simulations of stage 11 for example, where measurements of precipitable water, ozone and ground albedo are assumed to be missing and therefore fixed (to values comparable to the ones used in this study), do not fulfill the quality criteria. However at Bucharest, global SDR is modeled well for most stages, being in agreement with the satisfying behaviour of the Iqbal (1983) model observed here. The diffuse SDR has greater problems when measurements of the atmospheric parameters are not available (Fig. 4, bottom and Badescu et al., 2012). A modeler with a special interest in diffuse SDR, but lacking measurements of the atmospheric parameters, is therefore recommended to use one of the well performing models as identified by Badescu et al. (2012) (e.g. ASHRAE2005 or King).

5.2 Calibration and evaluation of diverse clear- and all-sky LDR models

Wang and Liang (2009) resumed that the Brunt (1932) and Brutsaert (1975) are two of the best performing LDR parameterizations, which is in accordance with the findings of this study (and additionally Dilley and O'Brien, 1997). A very recent study (Marthews et al., 2012) shows that the Dilley and O'Brien (1997) clear-sky parameterization performs best for measurements in the tropics (Caxiuanã, Brasil), resulting in RMSD of between 12 and 22 $\mathrm{W\,m^{-2}}$. For the measurements in Switzerland, Brutsaert (1975) however performs better than Brunt (1932) and Dilley and O'Brien (1997) if applied with the published parameter values. Brunt (1932) underestimates LDR at the lower elevation stations, while Dilley and O'Brien (1997) overestimates LDR at the high elevation stations. When fitting the parameterizations to local conditions, the performance of Brunt (1932) and Brutsaert (1975); Dilley and O'Brien (1997) is similar, likewise the behaviour of some of the other parameterizations (Ångström, 1915; Konzelmann et al., 1994). This indicates that the key step for modeling LDR is not the selection of the parameterizations, but rather fitting the parameter values to local conditions, or using a parameterization developed or fitted at a place with comparable atmospheric conditions. This was also found by Bilbao (2006) who fitted the Brunt (1932); Swinbank (1963); Brutsaert (1975) and Idso (1981) parameterizations to measurements in central Spain.

Pirazzini et al. (2000) presented comparably high MBD and RMSD (MBD = −63 $\mathrm{W\,m^{-2}}$, RMSD = 64.5 $\mathrm{W\,m^{-2}}$) values using the Konzelmann et al. (1994) parameterization. We found that this is since Pirazzini et al. (2000) uses water vapor in Hectopascal instead of Pascal as originally published by Konzelmann et al. (1994). Using the correct unit for the water vapor, the Konzelmann et al. (1994) parameterizations performs acceptably (Fig. 7, left).

We have seen that transforming the estimated cloud transmissivity (Eq. 20) to cloud cover (Crawford and Duchon, 1998; Greuell et al., 1997; Sicart et al., 2006) to estimate all-sky LDR is not absolutely necessary (but does also provide reasonable results). By implementing the cloud transmissivity directly into the all-sky parameterization, errors from empirically estimated cloud conversions can be avoided. Similarly as for the clear-sky situation, fitting the parameterization to local conditions or using parameters estimated at similar locations is a crucial step to obtain reliable model

outputs. Wang and Liang (2009) validated the Brunt (1932) and Brutsaert (1975) parameterizations for all-sky conditions using $LDR_{all} = LDR_{cl} \cdot (1 - N) + N \cdot \sigma_{SB} \cdot T^{*4}$, where N is the cloud coverestimated from solar radiation according to Crawford and Duchon (1998). They found that all-sky LDR can be modeled with an average bias of 0.6 % and average standard deviation of 6 %, values which are comparable to the MBD and RMSD estimated in this study. The scatter of modeled clear-sky and all-sky LDR is large (Fig. 9), but seems to be in the order of other publications (Konzelmann et al., 1994; Crawford and Duchon, 1998; Wang and Liang, 2009).

5.3 Interpolation of cloud transmissivity during the night

The clear-sky index introduced by Marty and Philipona (2000) has the advantage to allow cloud detection during both day- and nighttime, in contrast to approaches using SDR. In contrast to global SDR, LDR is only rarely measured (cf. Alados-Arboledas et al., 1995; Wang and Liang, 2008) and needs often to be modeled to estimate the surface net radiation. The amount of clouds in the sky determines LDR, but cloud measurements are often error-prone and/or subjective. During daytime, cloud transmissivity is commonly estimated using modeled and measured global SDR (Greuell et al., 1997). We observed that during the night, linear interpolation using the mean cloud transmissivity estimated for the 4 to 6 hours of the preceeding afternoon and the following morning provided the best LDR estimates. Lhomme et al. (2007) used the mean cloud cover between 14 h and 16.30 h as a constant during the night, and observed errors in modeled LDR of around -7 $W m^{-2}$ (MBD) and 30 $W m^{-2}$ (RMSD) at the Andean Altiplano. In this study, we found that the constant interpolation provides around 2 % higher errors than linear interpolation.

5.4 Uncertainties of the clear-sky SDR and the all-sky LDR model

The validity of a clear-sky SDR model can be assessed using high quality and high sampling rate precipitable water and turbidity measurements, and great model performance can thereby be obtained. However, such measurements must often be inter- or extrapolated due to temporal or spatial incompleteness of the data source (Gueymard, 2003b). As mentioned above, a very detailed study investigating the sensitivity of 54 clear-sky SDR models on different sets of input data has only recently been published (Badescu et al., 2012), and determines models that behave satisfactorily even when not all the necessary input measurements are available. We think that it is worth to additionally quantify the error and the uncertainty that is thereby introduced as is presented in this study.

The energy in the atmosphere is a driving factor for any impact study concerned with the energy balance at the Earth's surface. Many impact models (Lehning et al., 2002; Klok and Oerlemans, 2002; Machguth et al., 2008) therefore incorporate SDR and LDR parameterizations. The downward radiation can be estimated and studied independently from any successive process at the Earth's surface and can be treated as an independent subsystem. A modeler dealing with model uncertainties can use the estimated uncertainties for the SDR (Eq. 28) and LDR (Eq. 32) by directly implementing them in his/her model, and propagating the uncertainties in SDR or LDR into the model output of interest. By direct implementing the presented uncertainty results, time and computational effort are reduced.

In accordance with earlier studies (Gueymard, 2003b; Schillings, 2004) we found that SDR is most sensitive to precipitable water and turbidity (Fig. 5). Errors in precipitable water can increase to 100 % due to atmospheric conditions or model discrepancies. The resultant uncertainty goes up to 10 % which is comparable to the errors of 2 to 15 % for direct SDR by Gueymard (2003b). Comparable results were also obtained for the direct SDR sensitivity to ozone, which are as low as 0.5 % for ozone (0.3 % for zenith angle zero degrees, and 1 % for zenith angle of 85° in Gueymard, 2003b). The greatest errors arise from variability in aerosols (−20 %). Sensitivity to nitrogen dioxide (NO_2) under polluted conditions is neglected since it is not explicitely modeled in Iqbal (1983), and since the NO_2 concentration in Switzerland is relatively low. In addition to the sensitivity in direct SDR, this study treats uncertainties of modeled diffuse and global SDR. We found that the sensitivity of direct and diffuse SDR to the Ångström parameters α and β are of opposite signs, and therefore compensate for each other when summed up to global SDR. *Modeled* global SDR is therefore *less uncertain* than would be expected after studying direct SDR alone. The confident total output uncertainty for global SDR is around 3 %, in comparison to 30 % uncertainty in diffuse and 10 % in direct SDR.

Concerning LDR, Sicart et al. (2006) found that clouds enhance LDR by around 16 % in Wolf Creek, Canada. On 90 % of the cloudy days, LDR increase was less than 30 %, and the maximal enhancement was found to be 50 %. Clouds thus predominantly determine LDR. We have shown that missing the correct cloud transmissivity value by around one tenth can result in differences of around 1 to 15 % in modeled LDR, in dependence of the atmospheric conditions. Therefore, accurate estimation or measuring the cloud cover or cloud transmissivity is of great importance to reduce errors in modeled LDR, especially when the sky is only partly cloudy.

We emphasize here that the presented uncertainties are in two ways subjective: (a) the selection of the parameters and input variables and (b) the prior distributions assigned to them. We tried to treat (a) and (b) as objectively as possible, however the reader should keep in mind that the assumptions influence the presented results.

6 Conclusions

The main findings of this study are shortly summarized:

- The Iqbal (1983) model reproduces clear-sky SDR well when using measurements of precipitable water and of the Ångström parameters α and β. Fixed atmospheric parameter values increase the errors in clear-sky global SDR from 2 % (MBD) and 3 % (RMSD) to around 5.5 % and 7 % at Payerne. The MBD and the RMSD of the clear-sky global SDR range from −3.3 to 5.5 % and from 2 to 12 % at the six locations, respectively, and therefore fulfill the quality criteria by Badescu et al. (2012). The Iqbal (1983) model is in a good linear agreement with measurements ($R^2 > 0.96$).
- The relative uncertainty for direct SDR is 10 %(20 %), for diffuse 30 %(40 %) and for global SDR 3 %(6 %) when estimating the relative uncertainty confidently (conservatively). In general, the uncertainty is greater for low sun elevations due to the larger path a sun ray traverses. The smaller relative uncertainty in clear-sky global SDR comes from the compensating effect of direct and diffuse SDR.
- The relative RMSD of the clear-sky LDR is less than 10 % for the best parameterizations (Dilley and O'Brien, 1997; Brutsaert, 1975; Konzelmann et al., 1994) and the MBD is around than 5 %. Fitting each location separately results in an elevation dependence of the parameters which could also be modeled in the future.
- Used with Konzelmann et al. (1994), the all-sky parameterization presented in Eq. 22 (Pirazzini et al., 2000) and similarly Eq. 23 perform best in order of MBD and RMSD, which are similar as for clear-skies. Conversion of cloud transmissivity to cloud cover is not necessary to estimate all-sky LDR.
- The study of the different interpolation techniques of the cloud transmissivity during nighttime has shown that a modeler preferably averages the cloud transmissivity estimated during 4 to 6 h before sunset and after sunrise and then linearly interpolates between the averages. This results in MBD of around 5 % and RMSD of 13 % for the resultant all-sky LDR.
- The output uncertainty of the all-sky LDR is less than 14 W m^{-2}, a conservative (confident) estimate of the relative uncertainty is 6 % (3 %). A trend with elevation is not observed.
- The key step when modeling LDR is not the selection of the parameterizations, but using a parameterization developed or fitted at a place with comparable atmospheric conditions.

7 Outlook

This study is focussed on the evaluation and uncertainty estimation of clear-sky SDR and all-sky LDR parameterizations at six locations in Switzerland due to unknown atmospheric parameters and errors in input data. Estimating the energy fluxes and their uncertainties at the place of potential input stations is certainly of value for further model applications in nearby locations. However, any model investigating the spatial distribution of a certain phenomenon comprises diverse formulae to extrapolate the measured input variables. The uncertainties due to these extrapolation techniques (such as the lapse rate for temperature) has not been studied. A further constraint of the presented study is the restriction to examine horizontal locations, neglecting thereby radiation from surrounding terrain and the topographical variability of model outputs. A study investigating these two issues would certainly deliver additional important information for further model applications.

Appendix A

Clear-sky global SDR

If not otherwise mentioned, all model formulations are from Iqbal (1983).

A1 Solar geometry

In a first step, the solar geometry for each location and time step is estimated according to the geometrical calculations by Corripio (2002). The eccentricity-corrected extraterrestrial solar radiation I_o is obtained by:

$$I_o = \rho \overline{I_o}, \tag{A1}$$

where $\rho \approx (\frac{r}{r_0})^2$, where r_0 is the actual and r the mean Sun–Earth distance, is an approximation of the relative distance traversed by the sun ray, and $\overline{I_o} = 1367\ \mathrm{W\,m^{-2}}$ is the solar constant. An approximation for ρ is (Spencer, 1971):

$$\begin{aligned}\rho =& 1.00011 + 0.034221\cos(\phi) + 0.00128\sin(\phi) \\ &+ 0.000719\cos(2\phi) + 0.000077\sin(2\phi),\end{aligned} \tag{A2}$$

where $\phi = 2\pi(d-1)/365$ is the day angle in radians and d is the day of the year.

A2 Direct radiation

The downward broadband SDR is given by

$$\mathrm{SDR_{dir}} = 0.9751 I_o \tau_r \tau_w \tau_o \tau_a \tau_g, \tag{A3}$$

where τ_r is the transmittance due to Rayleigh scattering, and τ_w, τ_o, τ_a and τ_g are the transmittances of water vapor, ozone,

aerosols and the uniformly mixed gases O_2 and CO_2, respectively. Attenuation due to dry air particles, aerosols and precipitable water is dependent on the length of the path a solar ray traverses before reaching the ground. Ignoring the Earth's curvature and under the assumption of a horizontal homogeneously distributed atmosphere the relative optical air mass m_r can be estimated as:

$$m_r = \frac{1}{\cos\Theta_Z}, \tag{A4}$$

where Θ_Z is the solar zenith angle. Attenuation increases with increasing zenith angle. Kasten (1966) developed an accurate estimation of the relative optical mass m_r considering the Earth's curvature and the refraction of the real atmosphere:

$$m_r = \frac{1}{cos\Theta_Z + 0.15(93.885 - \Theta_Z)^{-1.253}}. \tag{A5}$$

For non-standard pressures deviating from 1013.25 hPa at sea level, induced by weather or topography, the relative optical air mass m_r is modified to local condition air mass m_a:

$$m_a = m_r \frac{p^*}{1013.25}, \tag{A6}$$

where p^* is screen-level atmospheric pressure (hPa). Rayleigh scattering transmittance is:

$$\tau_r = \exp[-0.0903 m_a^{0.84}(1.0 + m_a - m_a^{1.01})]. \tag{A7}$$

Transmittance by ozone is given by:

$$\tau_o = 1.0 - [0.1611 U_1 (1.0 + 139.48 U_1)^{-0.3035} - 0.002715 U_1 (1.0 + 0.044 U_1 + 0.0003 U_1^2)^{-1}], \tag{A8}$$

where $U_1 = l m_r$ is the ozone relative optical path length, and l is the ozone column in cm. The transmittance by uniformly mixed gases is given by:

$$\tau_g = \exp[-0.0127 m_a^{0.26}], \tag{A9}$$

and the transmittance of water vapor is obtained from:

$$\tau_w = 1 - 2.4959 U_2 [(1.0 + 79.034 U_2)^{0.6828} + 6.385 U_2]^{-1}. \tag{A10}$$

Here, $U_2 = w m_r$ is the pressure-corrected relative optical path length of precipitable water. The parameter w denotes the precipitable water (cm). Aerosol transmittance is parameterized as proposed in Iqbal's model A:

$$\tau_a = (0.12445\alpha - 0.0162) + (1.003 - 0.125\alpha) \cdot \exp(-m_a \beta (1.089\alpha + 0.5123)),\ \beta < 0.5, \tag{A11}$$

where α is known as the Ångström parameter and β is the Ångström turbidity parameter.

A3 Diffuse radiation

Diffuse radiation is estimated as the sum of the Rayleigh-scattered, the aerosol-scattered and the multiple reflected irradiance, i.e.:

$$SDR_{dif} = SDR_{dif,r} + SDR_{dif,a} + SDR_{dif,rfl}. \tag{A12}$$

The Rayleigh-scattered diffuse irradiance is estimated as:

$$SDR_{dif,r} = 0.79 I_o \cos\Theta_z \frac{\tau_o \tau_g \tau_w \tau_{aa} 0.5(1 - \tau_r)}{1 - m_a + m_a^{1.02}}, \tag{A13}$$

where τ_{aa} is the estimated transmittance of direct radiation due to aerosol absorptance:

$$\tau_{aa} = 1 - (1 - \omega_0)(1 - m_a + m_a^{1.06})(1 - \tau_a), \tag{A14}$$

where ω_0 is the single-scattering albedo. We set $\omega_0 = 0.9$ (Bird and Hulstrom, 1980). Diffuse irradiance due to scattering of aerosols is:

$$SDR_{dif,a} = 0.79 I_o \cos\Theta_z \frac{\tau_o \tau_g \tau_w \tau_{aa} 0.84(1 - \tau_{as})}{1 - m_a + m_a^{1.02}}, \tag{A15}$$

where $\tau_{as} = \tau_a / \tau_{aa}$ is the fraction of the incident energy transmitted after scattering effects of aerosols. The between the Earth and the atmosphere multiply-reflected irradiance is:

$$SDR_{dif,rfl} = \frac{(SDR_{dir}\cos\Theta_z + SDR_{dif,r} + SDR_{dif,a})\rho_g \rho_a}{1 - \rho_g \rho_a}. \tag{A16}$$

The parameters ρ_g and ρ_a are ground albedo and albedo of the cloudless sky, respectively. The albedo of the cloudless sky is computed as:

$$\rho_a = 0.0685 + 0.16(1 - \tau_{as}). \tag{A17}$$

A4 Terrain reflected radiation

The terrain reflection radiation is estimated according to Dozier and Frew (1990):

$$SDR_{ter} = \rho_g \cdot (\frac{1 + \cos(slope)}{2} - svf) \cdot (SDR_{dir} + SDR_{dif}), \tag{A18}$$

where slope denotes the slope of the simulation point, and svf is the fraction of the sky visible at the simulation point. Since $\cos(slope) = \cos(0) = 1$ and the svf is large (between 0.97 and 1) for all simulation points, the terrain reflected radiation accounts only for a very small part of the global radiation.

A5 Global radiation

Global SDR is the sum of direct SDR (Sect. A2), diffuse radiation (Sect. A3) and the radiation reflected at surrounding terrain (Sect. A4), i.e. $SDR_{glob} = SDR_{dir} + SDR_{dif} + SDR_{ter}$.

Table B1. Mean and standarddeviation ($\mu|\sigma$) of the ground albedo from the MODIS/Terra+Aqua BRDF and Calculated Albedo data set, estimated at each location for a surrounding terrain of approximately 6.5^2 km^2 for each month of the year.

Month	CIM	DAV	GOR	JUN	OTL	PAY	WFJ
Jan	0.20|0.13	0.39|0.19	0.29|0.20	0.16|0.09	0.11|0.07	0.20|0.13	0.50|0.15
Feb	0.16|0.10	0.43|0.19	0.51|0.21	0.30|0.19	0.11|0.05	0.16|0.06	0.64|0.13
Mar	0.13|0.06	0.42|0.18	0.57|0.11	0.50|0.19	0.10|0.04	0.15|0.01	0.63|0.12
Apr	0.12|0.02	0.33|0.19	0.54|0.11	0.36|0.15	0.10|0.04	0.17|0.01	0.54|0.15
May	0.13|0.01	0.15|0.09	0.30|0.16	0.30|0.12	0.11|0.04	0.17|0.01	0.31|0.19
Jun	0.14|0.01	0.12|0.03	0.18|0.06	0.27|0.10	0.11|0.04	0.16|0.01	0.16|0.04
Jul	0.13|0.01	0.11|0.02	0.15|0.04	0.26|0.11	0.11|0.04	0.16|0.01	0.14|0.02
Aug	0.13|0.02	0.11|0.02	0.14|0.04	0.24|0.11	0.11|0.04	0.16|0.01	0.14|0.02
Sep	0.13|0.02	0.12|0.07	0.15|0.06	0.20|0.10	0.11|0.04	0.16|0.01	0.17|0.11
Oct	0.13|0.03	0.16|0.14	0.17|0.10	0.17|0.11	0.11|0.04	0.15|0.01	0.24|0.19
Nov	0.14|0.07	0.28|0.20	0.20|0.15	0.16|0.12	0.11|0.05	0.14|0.04	0.45|0.20
Dec	0.19|0.13	0.35|0.18	0.16|0.08	0.12|0.06	0.11|0.06	0.15|0.09	0.55|0.16

Appendix B

Estimated ground albedo distributions

The distribution of the ground albedo distribution for each station and each month of the year were estimated according to data from the MODIS/Terra+Aqua BRDF and Calculated Albedo dataset[1] (Table B1).

Acknowledgements. The authors are grateful to R. Philipona and L. Vuilleumier from MeteoSwiss for providing the high quality SACRaM and ASRB data together with the information about measurement uncertainty. We thank S. Endrizzi for extensive discussions about modeling the energy fluxes, and C. Gueymard for giving great advise and answering many questions. Comments from two anonymous reviewers helped to strongly improve the present manuscript. This study was funded by the Swiss National Science Foundation (SNSF) via the NCCR MICS project PermaSense, and further supported by X-Sense, funded through www.nano-tera.ch. All computational and statistical analyses were performed with R (www.cran.r-project.org).

Edited by: P. Monks

References

Aase, J. K. and Idso, S. B.: A comparison of two formula types for calculating long-wave radiation from the atmosphere, Water Resour. Res., 14, 623–625, 1978.

Alados-Arboledas, L., Vida, J. and Olmo, F. J.: The estimation of thermal atmospheric radiation under cloudy conditions, Int. J. Climatol., 15, 107–116, 1995.

[1]MODIS download information for Cimetta: Product: MCD43A Location Centered on: Latitude [46.201], Longitude [8.7908] Size: Approximately 6.5 km wide and 6.5 km high time Period: 18 February 2000 to 20 July 2010 Selected Solar Zenith Angle is local Selected Optical Depth is 0.2

Andreas, E. L. and Ackley, S. F.: On the differences in ablation seasons of Arctic and Antarctic sea ice-sheet, J. Atmos. Sci., 39, 440–447, 1982.

Ångström, A.: A study of the radiation of the atmosphere, Smithsonian Miscellaneous Collection, 65, 1–159, 1915.

Ångström, A.: On the atmospheric transmission of sun radiation and on dust in the air, Geografiska Annaler, 11, 156–166, 1929.

Ångström, A.: On the atmospheric transmission of sun radiation, Geografiska Annaler, 12, 130–159, 1930.

Asklöf, S.: Über den Zusammenhang zwischen der nächtlichen Wärmeaustrahlung, der Bewölkung und der Wolkenart, Geografiska Annaler, 2, 253–259, 1920.

Badescu, V., Gueymard, C., Cheval, S., Oprea, C., Baciu, M., Dumitrescu, A., Iacobescu, F., Milos, I. and Rada, C.: Computing global and diffuse solar hourly irradiation on clear sky. Review and testing of 54 models, Renew. Sustain. Energ. Rev., 16, 1636–1656, 2012.

Bates, D. M. and Chambers, J. M.: Nonlinear models, Chap. 10, Wadsworth and Brooks/Cole, Pacific Grove, CA, USA, 1992.

Bates, D. M. and Watts, D. G.: Nonlinear regression analysis and its applications, Wiley, New York, USA, 1988.

Battles, F. J., Olmo, F. J., Tovar, J. and Alados-Arboledas, L.: Comparison of cloudless sky parameterizations of solar irradiance at various Spanish midlatitude locations, Theor. Appl. Climatol., 66, 81–93, 2000.

Beck, M. B.: Water quality modeling: a review of the analysis of uncertainty, Water Resour. Res., 23, 1393–1442, 1987.

Beven, K.: Prophecy, reality and uncertainty in distributed hydrological modelling, Adv. Water Resour., 16, 41–51, 1993.

Bilbao, J. and de Miguel, A. H.: Estimation of daylight downward longwave atmospheric irradiance under clear-sky and all-sky conditions, J. Appl. Meteorol. Climatol., 46, 878–889, 2006.

Bird, R. E. and Hulstrom, R. L.: Direct insolation models, Tech. Report, Solar Energy Research Institute, Colorado, USA, 1980.

Bird, R. E. and Hulstrom, R. L.: Simplified clear sky model for direct and diffuse insolation horizontal surfaces, Solar Energy Research Institute, Colorado, USA, 1981.

Brunt, D.: Notes on radiation in the atmosphere, Q. J. Roy. Meteorol. Soc., 58, 389–420, 1932.

Brutsaert, W.: On a derivable formula for long-wave radiation from clear skies, Water Resour. Res., 11, 742–744, 1975.

Choi, M., Jacobs, J. M. and Kustas, W. P.: Assessment of clear and cloudy sky parameterizations for daily downwelling longwave radiation over different land surfaces in Florida, USA, Geophys. Res. Lett., 35, L20402, doi:10.1029/2008GL035731, 2008.

Cooter, E. and Dhakhwa, G.: A solar radiation model for use in biological applications in the South and Southeastern USA, Agric. Forest Meteorol., 79, 31–51, 1996.

Corripio, J. G.: Vectorial algebra algorithms for calculating terrain parameters from DEMs and solar radiation modelling in mountainous terrain, Geogr. Inf. Sci., 17, 1–23, 2002.

Crawford, T. M. and Duchon, C. E.: An improved parameterization for estimating effective atmospheric emissivity for use in calculating daytime downwelling longwave radiation, J. Appl. Meteorol., 38, 474–480, 1998.

Dilley, A. C. and O'Brien, D. M.: Estimating downward clear sky long-wave irradiance at the surface from screen temperature and precipitable water, Q. J. Roy. Meteorol. Soc., 124a, 1391–1401, 1997.

Dines, W. H.: Observations on radiation from the sky, and an attempt to determine the atmospheric constant of radiation, Meteorological Observations, Geophys. Mem., 18, 1921.

Dozier, J.: A clear-sky spectral solar radiation model for snow-covered mountainous terrain, Water Resour. Res., 16, 709–718, 1980.

Dozier, J. and Frew, J.: Rapid calculation of terrain parameters for radiation modeling from digital elevation data, IEEE T. Geosci. Remote, 28, 963–969, 1990.

Dürr, B. and Philipona, R.: Automatic cloud amount detection by surface longwave downward radiation measurements, J. Geophys. Res., 109, D05201, doi:10.1029/2003JD004182, 2004.

Efimova, N. A.: On methods of calculating monthly values of net long-wave radiation, Meteor. Gidrol., 10, 28–33, 1961.

Flatau, P. J., Walko, R. L., and Cotton, W. R.: Polynomial fits to saturation vapor pressure, J. Appl. Meteorol., 31, 1507–1513, 1992.

Foster, J., Bevis, M., and Raymond, W.: Precipitable water and the lognormal distribution, J. Geophys. Res., 111, D15102, doi:10.1029/2005JD006731, 2006.

Fung, I. Y., Harrison, D. E., and Lacis, A. A.: On the variability of the net longwave radiation at the ocean surface, Rev. Geophys. Space Phys., 22, 177–193, 1984.

Greuell, W., Knap, W. H., and Smeets, P. C.: Elevational changes in meteorological variables along a midlatitude glacier during summer, J. Geophys. Res., 102, 941–954, 1997.

Gruber, S.: Mountain permafrost: Transient spatial modelling, model verification and the use of remote sensing, Ph.D. Thesis, University of Zurich, Zurich, Switzerland, 2005.

Gueymard, C.: Critical analysis and performance assessment of clear sky solar irradiance models using theoretical and measured data, Sol. Energy, 51, 121–138, 1993.

Gueymard, C.: Direct solar transmittance and irradiance predictions with broadband models. Part I: detailed theoretical performance assessment, Solar Energy, 74, 355–379, 2003a.

Gueymard, C.: Direct solar transmittance and irradiance predictions with broadband models: Part II: validation with high-quality measurements, Sol. Energy, 74, 381–395, 2003b.

Gueymard, C. and Myers, D. R.: Validation and ranking methodologies for solar radiation models, In: Badescu, V. (Ed.), Modeling solar radiation at the earth surface, Berlin, Springer, 20, 479–509, 2008.

Gueymard, C.: Clear-sky irradiance predictions for solar resource mapping and large-scale applications: Improved validation methodology and detailed performance analysis of 18 broadband radiative models, Sol. Energy, in press, 2011.

Gupta, H. V., Beven, K., and Wagener, T.: Model calibration and uncertainty estimation, In: Anderson, M. G. (Ed.), Encyclopedia of Hydrological Sciences, John Wiley & Sons, Chichester, UK, 2005.

Hebeler, F. and Purves, R. S.: The impact of parametric uncertainty and topographic error in ice sheet modelling, J. Glaciol., 45, 899–919, 2008.

Helbig, N., Löwe, H., and Lehning, M.: Radiosity approach for the shortwave surface radiation balance in complex terrain, J. Atmos. Sci., 66, 2900–2912, 2009.

Idso, S. B. and Jackson, R. D.: Thermal radiation from the atmosphere, J. Geophys. Res., 74, 4167–4178, 1969.

Idso, S. B.: A set of equations for full spectrum and 8 to 14 µm and 10.5 to 12.5 µm thermal radiation from cloudless skies, Water Resour. Res., 17, 295–304, 1981.

Iqbal, M.: An Introduction to Solar Radiation, Academic Press, Toronto, Canada, 1983.

Iziomon, M. G., Mayer, H., and Matzarakis, A.: Downward atmospheric longwave irradiance under clear and cloudy skies: measurement and parameterization, J. Atmos. Solar-Terr. Phys., 65, 1107–1116, 2003.

JCGM: Evaluation of measurement data – Guide to the expression of uncertainty in measurement, Joint Committee for Guides in Metrology, Bureau International de Poids et Mesures, 2008.

Kasten, F.: A new table and approximate formular for relative optical air mass, Theor. Appl. Climatol., 14, 206–223, 1966.

Kavetski, D., Franks, S. W., and Kuczera, G.: Confronting input uncertainty in environmental modeling, Water Sci. Appl. Ser., 6, 49–68, 2003.

Klok, E. J. and Oerlemans, J.: A model study of the energy and mass balance of the Morteratschgletscher, Switzerland, J. Glaciol., 48, 505–518, 2002.

König-Langlo, G. and Augstein, E.: Parameterization of the downward long-wave radiation at the Earth's surface in polar regions, Meteorol. Z., 3, 343–347, 1994.

Konzelmann, T., van de Wal, R. S. W., Greuell, W., Bintanja, R., Henneken, E. A. C., and Abe-Ouchi, A.: Parameterization of global and longwave incoming radiation for the Greenland Ice Sheet, Global Planet. Change, 9, 143–164, 1994.

Leckner, B.: The spectral distribution of solar radiation at the Earth's surface–elements of a model, Solar Energy, 20, 143–150, 1978.

Lehning, L., Bartelt, P., Brown, B., and Fierz, C.: A physical SNOWPACK model for the Swiss avalanche warning Part III: meteorological forcing, thin layer formation and evaluation, Cold Reg. Sci. Technol., 35, 169–184, 2002.

Lhomme, J. P., Vacher, J. J., and Rocheteau, A.: Estimating downward long-wave radiation on the Andean Altiplano, Agric. Forest Meteorol., 145, 139–148, 2007.

Longman, R. J., Giambelluca, T. W., and Frazier, A. G.: Comparing the use of input parameters at different temporal resolutions, J. Geophys. Res., 117, D02201, doi:10.1029/2011JD016388, 2012.

Machguth, H., Purves, R. S., Oerlemans, J., Hoelzle, M., and Paul, F.: Exploring uncertainty in glacier mass balance modelling with Monte Carlo simulation, The Cryosphere, 2, 191–204, doi:10.5194/tc-2-191-2008, 2008.

Marshunova, M. S.: Principal characteristics of the radiation balance of the underlying surface, Soviet Data on the Arctic Heat Budget and its Climate Influence, Santa Monica, California, USA, 1966.

Marthews, T. R., Malhi, Y., and Iwata, H.: Calculating downward longwave radiation under clear and cloudy conditions over a tropical lowland forest site: an evaluation of model schemes for hourly data, Theor. Appl. Climatol., 107, 461–477, doi:10.1007/s00704-011-0486-9, 2012.

Marty, C. and Philipona, R.: The clear-sky index to separate clear-sky from cloudy-sky situations in climate research, Geophys. Res. Lett., 27, 2649–2652, 2000.

Maykut, G. A. and Church, P. E.: Radiation climate of Barrow, Alaska, 1962–1966, J. Appl. Meteorol., 12, 620–628, 1973.

Mittaz, C., Imhof, M., Hoelzle, M., and Haeberli, W.: Snowmelt evolution mapping using an energy balance approach over an Alpine terrain, Arctic, Antarctic, and Alpine Research, 34, 274–281, 2002.

Mulrooney, M. K. and Matney, M. J.: Derivation and application of a global albedo yielding an optical brightness to physical size transformation free of systematic errors, Advanced Maui Optical and Space Surveillance Technologies Conference, 12–15, 2007.

Nimielä, S., Räisänen, P., and Savijärvi, H.: Comparison of surface radiative flux parameterizations: Part I: Longwave radiation, Atmos. Res., 58, 1–18, 2001a.

Nimielä, S., Räisänen, P., and Savijärvi, H.: Comparison of surface radiative flux parameterizations: Part II: Shortwave radiation, Atmospheric Research, 58, 141–154, 2001b.

Okulov, O., Ohvril, H., and Kivi, R.: Atmospheric precipitable water in Estonia, 1990–2001, Boreal Environ. Res., 7, 291–200, 2002.

Oreopoulos, L. and Davies, R.: Plane parallel albedo biases from satellite observations. Part II: Parameterizations for bias removal, Am. Meteorol. Soc., 11, 933–944, 1998.

ORNL DAAC: Oak Ridge National Laboratory Distributed Active Archive Center, MODIS subsetted land products, Collection 5, ORNL DAAC, Oak Ridge, Tennessee, USA, 2010, available at: http://daac.ornl.gov/MODIS/modis.html, last access: March 2010.

Philipona, R., Fröhlich, C., and Betz, Ch.: Characterization of pyranometers and the accuracy of atmospheric longwave radiation measurements, Appl. Opt., 34, 1598–1605, 1995.

Philipona, R., Marty, C., Fröhlich, C., and Heimo, A.: Measurements of the longwave radiation budget in the Alps, in IRS 96: Current Problems in Atmospheric Radiation, edited by: Smith, W. L. and Stamnes K., A. Deepak Publishing, Hampton, Virginia, USA, 786–789, 1996.

Pirazzini, R., Nardino, M., Orsini, A., Calzolari, F., Georgiadis, T., and Levizzani, V.: Parameterization of the downward longwave radiation from clear and cloudy skies at Ny Alesund (Svalbard), in IRS 2000: Current Problems in Atmospheric Radiation, edited by: Smith, W. L. and Timofeyev, Y. A., A. Deepak Publishing, Hampton, Virginia, USA, 559–562, 2000.

Plüss, C. and Ohmura, A.: Longwave radiation on snow-covered mountainous surfaces, J. Appl. Meteorol., 36, 818–824, 1997.

Prata, A. J.: A new long-wave formula for estimating downward clearsky radiation at the surface, Q. J. Roy. Meteorol. Soc., 122, 1127–1151, 1996.

Reitan, C.: Surface dew point and water vapor aloft, J. Appl. Meteorol., 2, 776–779, 1963.

Robinson, G. D.: Notes on the measurement and estimation of atmospheric radiation, Q. J. Roy. Meteorol. Soc, 73,127–150, 1947.

Robinson, G. D.: Notes on the measurement and estimation of atmospheric radiation 2, Q. J. Roy. Meteorol. Soc, 76, 37–51, 1950.

Satterlund, D. R.: An improved equation for estimating longwave radiation from the atmosphere, Water Resour. Res., 15, 1649–1650, 1979.

Schillings, C.: Bestimmung langjähriger stündlicher Zeitreihen und räumlich hochaufgelöster Karten der Direkt-Normal-Strahlung auf der Basis von Meteosat-Daten und Atmosphärenparametern für die Nutzung in konzentrierenden Solarkraftwerken, Ph.D. thesis, Philipps-Universität Marburg, Marburg, Germany, 2004.

Sicart, J. E., Pomeroy, J. W., Essery, R. L. H., and Bewley, D.: Incoming longwave radiation to melting snow: observations, sensitivity and estimation in northern environments, Hydrol. Proc., 20, 3697–3708, 2006.

Spencer, J. W.: Fourier series representation of the position of the sun, Search, 2, 172 pp., 1971.

Staehelin, J., Renaud, A., Bader, J., McPeters, R., Viatte, P., Hoegger, B., Bugnion, V., Giroud, M., and Schill, H.: Total ozone series at Arosa (Switzerland): Homogenization and data comparison, J. Geophys. Res., 103, 5827–5841, 1998.

Swinbank, W. C.: Long-wave radiation from clear skies, Q. J. Roy. Meterol. Soc., 89, 330–348, 1963.

Wang, K. and Liang, S.: Estimation of daytime net radiation from shortwave radiation measurements and meteorological observations, Journal of Applied Meteorology and Climatology, 48, 634–643, 2008.

Wang, K. and Liang, S.: Global atmospheric downward longwave radiation over land surface under all-sky conditions from 1973 to 2008, J. Geophys. Res., 114, D19101, doi:10.1029/2009JD011800, 2009.

Yamamoto, G.: On nocturnal radiation, Sci. Rep. Tohoku Universitiy, 2, 27–43, 1950.

Zillman, J. and Commonwealth Bureau of Meteorology (Australia): A study of some aspects of the radiation and heat budgets of the Southern Hemisphere oceans, Meteorological Study, Canberra: Australian Government Publishing Service, 1972.

Publication IV

Gubler, S., S. Endrizzi, S. Gruber, and R. S. Purves (2013), Sensitivities and uncertainties of modeled ground temperatures in mountain environments, *Geoscientific Model Development*, *6*, 1319–1336, doi: 10.5194/gmd-6-1319-2013

Contributions:

- Design of model simulation set-up
- Assessment of parameter prior distributions with S. Endrizzi and S. Gruber
- Interpretation and visualization of results

Geosci. Model Dev., 6, 1319–1336, 2013
www.geosci-model-dev.net/6/1319/2013/
doi:10.5194/gmd-6-1319-2013

Geoscientific Model Development
Open Access

Sensitivities and uncertainties of modeled ground temperatures in mountain environments

S. Gubler, S. Endrizzi, S. Gruber, and R. S. Purves

Department of Geography, University of Zurich, Zurich, Switzerland

Correspondence to: S. Gubler (stefanie.gubler@geo.uzh.ch)

Received: 19 December 2012 – Published in Geosci. Model Dev. Discuss.: 6 February 2013
Revised: 27 June 2013 – Accepted: 12 July 2013 – Published: 23 August 2013

Abstract. Model evaluation is often performed at few locations due to the lack of spatially distributed data. Since the quantification of model sensitivities and uncertainties can be performed independently from ground truth measurements, these analyses are suitable to test the influence of environmental variability on model evaluation. In this study, the sensitivities and uncertainties of a physically based mountain permafrost model are quantified within an artificial topography. The setting consists of different elevations and exposures combined with six ground types characterized by porosity and hydraulic properties. The analyses are performed for a combination of all factors, that allows for quantification of the variability of model sensitivities and uncertainties within a whole modeling domain.

We found that model sensitivities and uncertainties vary strongly depending on different input factors such as topography or different soil types. The analysis shows that model evaluation performed at single locations may not be representative for the whole modeling domain. For example, the sensitivity of modeled mean annual ground temperature to ground albedo ranges between 0.5 and 4 °C depending on elevation, aspect and the ground type. South-exposed inclined locations are more sensitive to changes in ground albedo than north-exposed slopes since they receive more solar radiation. The sensitivity to ground albedo increases with decreasing elevation due to shorter duration of the snow cover. The sensitivity in the hydraulic properties changes considerably for different ground types: rock or clay, for instance, are not sensitive to uncertainties in the hydraulic properties, while for gravel or peat, accurate estimates of the hydraulic properties significantly improve modeled ground temperatures. The discretization of ground, snow and time have an impact on modeled mean annual ground temperature (MAGT) that cannot be neglected (more than 1 °C for several discretization parameters). We show that the temporal resolution should be at least 1 h to ensure errors less than 0.2 °C in modeled MAGT, and the uppermost ground layer should at most be 20 mm thick.

Within the topographic setting, the total parametric output uncertainties expressed as the length of the 95 % uncertainty interval of the Monte Carlo simulations range from 0.5 to 1.5 °C for clay and silt, and ranges from 0.5 to around 2.4 °C for peat, sand, gravel and rock. These uncertainties are comparable to the variability of ground surface temperatures measured within 10 m × 10 m grids in Switzerland. The increased uncertainties for sand, peat and gravel are largely due to their sensitivity to the hydraulic conductivity.

1 Introduction

Models are important tools for investigating natural processes and providing scenarios relating to future environments. Physically based or empirical models can predict spatial or temporal variation of measured attributes and related phenomena of interest, and derived products may serve as a basis for political or economical decisions. Since every model is an abstraction and simplification of reality, and since therefore model outputs are strongly dependent on the modeler's perception of the system, any model must in a first step be evaluated for its fit to an intended purpose (Rykiel, 1996). Model evaluation forms an important part of the development process (e.g., Beven, 1993; Gupta et al., 2005). It aims at (a) determining the degree of accordance of a model output with the respective measured quantity (e.g., Rykiel, 1996; Beck et al., 1997; Anderson and Bates, 2001;

Stow et al., 2009), (b) quantifying the related model uncertainty (e.g., Beck, 1987; Beven and Binley, 1992; Beven, 1993; Davis and Keller, 1997; Crosetto and Tarantola, 2001), (c) identifying parameters and input variables that account for the largest parts of this uncertainty (e.g., Cukier et al., 1977; Sobol, 1993; Saltelli et al., 2004, 2008) and (d) eventually calibrating the model to local conditions (e.g., Beven and Binley, 1992; Chen et al., 2000; Gupta et al., 2005).

Uncertainties and errors come from processes that are not represented in the model, unknown physical properties, errors in input data, numerical errors and the modeler's perception when selecting the processes to be represented, among others (Gupta et al., 2005). Uncertainty can be defined as limits in modeling due to lack of knowledge (e.g., unknown physical properties), while errors may arise from numerical approximations, for example (AIAA, 1998).

Models are often applied to make predictions for large spatial areas. However, model evaluation is typically restricted to only one or, in the best case, a few evaluation points due to lack of observed data for validation. In turn, this implicitly assumes that validation at a single point suffices to inform on decisions about model performance in different environmental conditions because the model is physically based (and thus representativity at one point implies representativity over a domain). However, the implications of this assumption when modeling phenomena in highly variable terrain or over long distances has been the subject of limited research. This paper is focused on a sensitivity and uncertainty analysis of a physically based mountain permafrost model to serve as a case study for examining the role of environmental variability in model evaluation.

The validity of a model cannot be determined based only on sensitivity and uncertainty analyses, since the model outputs are not compared to measured values. However, model sensitivities and uncertainties can be analyzed independently of such ground truth measurements. Sensitivity and uncertainty analyses are one valuable way of exploring the potential influence of different environmental settings on model evaluation, without requiring spatially distributed measurements. Since the processes determining the occurrence and characteristics of mountain permafrost are highly complex and nonlinear, a mountain permafrost model is a suitable tool to investigate the variability of model sensitivities and uncertainties in a highly variable environment.

The focus of this study lies on the variability of sensitivities and uncertainties for different topographic and other environmental conditions (Table 1). Here, sensitivity analysis quantifies the variation of the modeled output due to variation in single model parameters, while an uncertainty analysis quantifies the total parametric model output uncertainty due to errors or uncertainties in model parameters. A preliminary parameter calibration (i.e., a minimization of the differences between the model outputs and given values) is performed on selected parameters that influence snow duration most strongly. The object of investigation in this study is

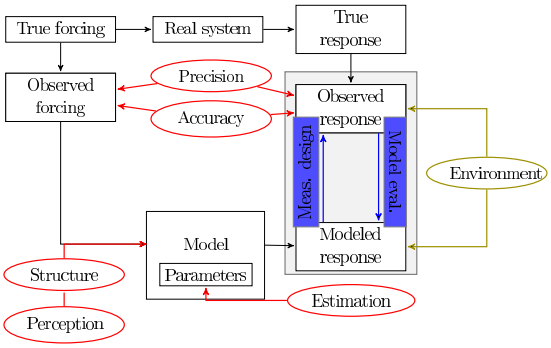

Fig. 1. Model uncertainties and errors has diverse sources (red) such as unknown parameters, errors in input data, numerical errors due to discretization, etc. Uncertainty and sensitivity studies investigate the effect of these possible sources of errors on model outputs (adapted from Gupta et al., 2005). Observed and modeled responses as well as model sensitivities are subject to strong environmental variation.

an energy- and mass-balance model with a primary focus on exploring variables and processes relating to permafrost, i.e., those influencing ground temperatures (GTs). GTs are interesting because they are influenced by highly nonlinear environmental processes such as the energy balance at the Earth's surface, snow cover distribution and snow melting, as well as heat conduction in the ground, which is determined by the thermal properties of the ground constituents and its water content and phase state (e.g., Williams and Smith, 1989). In mountain regions, GTs are strongly coupled to air temperature in summer, and are influenced by solar radiation, snow cover in winter and the ground material (e.g., Haeberli, 1973; Hoelzle, 1996; Keller and Gubler, 1993; Luetschg et al., 2008; Gruber and Hoelzle, 2008). Within a mountainous environment, these variables and processes vary within short distances (e.g., Hoelzle et al., 2003; Gubler et al., 2011), which makes interpolation of model outputs difficult. Similarly, results obtained from model evaluation cannot simply be transferred to other locations. To summarize, the main goals of this study are as follows: (a) to examine the influence of environmental variability on model sensitivity and uncertainty, and discuss the importance of representative model evaluation; (b) to quantify the sensitivity of mean annual ground temperature (MAGT) due to errors in discretization, numerical and model specific parameters and uncertainties in physical parameters; and (c) to discuss the influence of environmental variability on a physically based energy- and mass-balance model.

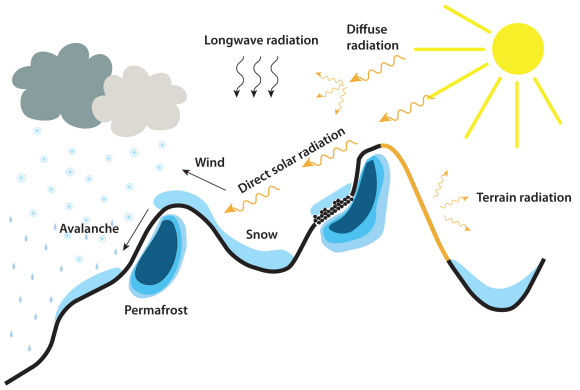

Fig. 2. Processes that influence permafrost are highly variable in mountain areas. The energy balance, shading from surrounding terrain and snow redistribution by wind or avalanches influence permafrost occurrence in high-mountain regions. The scale determines the importance of the influencing processes (Etzelmüller et al., 2001; Hoelzle et al., 2001).

2 Model and data description

2.1 The energy- and mass-balance model GEOtop

GEOtop is a physically based model originally developed for hydrological research. It couples the ground heat and water budgets, represents the energy exchange with the atmosphere, has a multilayer snow pack and represents the water and energy budget of the snow cover (Bertoldi et al., 2006; Rigon et al., 2006; Endrizzi, 2007; Dall'Amico, 2010). GEOtop simulates the temporal evolution of the snow depth and its effect on ground temperature. It solves the heat conduction equation in one dimension and the Richard's equation for water transport in one or three dimensions describing water infiltration in the ground as well as freezing and thawing processes. GEOtop is therefore a suitable tool to model permafrost relevant variables such as snow and ground temperatures (Fig. 2). It can be applied in high-mountain regions and allows topographic and other environmental variability to be accounted for. This study is performed using the GEOtop version number 1.225-9.

2.2 Input and validation measurements

Input data consist of measured air temperature, wind velocity and direction, relative humidity, global radiation and precipitation recorded by the MeteoSwiss meteorological stations. The experiment is run at Piz Corvatsch, Upper Engadine, Switzerland, where a meteorological station of MeteoSwiss is located at 3315 m a.s.l. A preliminary model analysis is performed at the 40 locations of ground surface temperature measurements around Piz Corvatsch (Gubler et al., 2011). The two main target variables are the mean annual ground surface temperature (MAGST) and the melt-out date of the snow (MD) (Schmid et al., 2012). The study was performed for two years of data, i.e., from summer 2009 to summer 2011.

2.3 Model parameters

2.3.1 Numerical parameters

In GEOtop, ground discretization is given as the thickness dz of each ground layer. Close to the surface, the ground is resolved in finer detail due to the greater temperature gradients. To reduce the number of degrees of freedom, the thickness of the ground layers is parameterized as an exponential function, describing the ground layer i as

$$dz_i = dz_{\min} \cdot (1+b)^{i-1}, \quad (1)$$

where $dz_{\min}$ is the thickness of the first layer, b is the growth rate and i is the layer index, being one at the ground surface and increasing downwards. In addition, the maximal depth $z_{\max}$ of the modeled ground must be set as a parameter.

Snow resolution is higher close to the snow surface (snow–atmosphere interface) and to the ground (snow–ground interface). Snow portions at the top (referred to as the top region) and at the bottom (bottom region) are defined that are discretized with snow layers that never exceed a specified snow water equivalent ($\mathrm{swe_m}$). The top and bottom regions are defined by their maximum snow water equivalent content, respectively given by $n_\mathrm{t} \cdot \mathrm{swe_m}$ and $n_\mathrm{b} \cdot \mathrm{swe_m}$, where n_t and n_b are integers. However, the portion of the snow pack not included in the top and bottom regions constitutes the middle region, which is discretized with a maximum number n_m of layers with minimum snow water equivalent content equal to $\mathrm{swe_m}$ and no maximum. The layering algorithm prevents the formation of significant snow water equivalent differences across the layers when the value $\mathrm{swe_m}$ is exceeded.

The heat and Richards' equations are solved with the Newton–Raphson method (Kelley, 2003). Significant numerical parameters are the time step dt of numerical integration of the equations and the residual tolerance at which the iterations are terminated. The sensitivity of the GEOtop model to both these parameters are also quantified in this study. The time step has been made to vary in the range from 7.5 min to 4 h. The higher the time step and residual tolerance are, the longer the computing time is. The optimal parameters for the simulation are the highest time step, and residual tolerance for which a decrement of their value does not result in a significant numerical solution difference.

2.3.2 Model-specific parameters

An initial condition of the state variables, namely temperature and total (= ice + liquid water) soil moisture initial profiles, must be assigned to run the model. Since there is always a certain degree of arbitrariness in this, the simulations

are then run for a long time so that they lose memory of the initial values and will assume values in equilibrium with the meteorological forcings and the ground properties. The ground column in the model is 10 m deep, and is initialized by repeatedly modeling GT down to 1 m (40 yr), then using the modeled GTs as initial condition to repeatedly simulate GT down to 5 m (40 yr) and finally simulating GTs down to 10 m depth. Preliminary analyses have shown that this procedure produces stable initial conditions of the ground. To test possibly different responses that may take place if the initial condition is given by unfrozen and frozen ground, a sensitivity study with negative (−1 °C) and positive (+1 °C) initial ground temperatures is performed. The initial total soil moisture profile is obtained from the retention curve after assigning a hydrostatic water pressure profile, and then the total soil moisture in ice and liquid water is split according to ground temperature and the freezing soil characteristic curve (e.g., Dall'Amico, 2010).

Although this study deals with one-dimensional simulations, it is possible to represent lateral water drainage between the surface and a depth referred to as z_f, while below this depth the ground can be filled with water until it is saturated. Depending on the interests of the modeler, the *water balance* can be turned off if no information on the ground hydraulic properties are available in order to save computation time or to study the influence of water balance on model outputs.

The longwave downward radiation (LDR) parameterizations implemented in GEOtop are based on the Stefan–Boltzmann law:

$$\mathrm{LWR_{in}} = \epsilon_{\mathrm{atm}} \cdot \sigma_{\mathrm{SB}} \cdot T_{\mathrm{atm}}^4, \tag{2}$$

where $\sigma_{\mathrm{SB}} = 5.67 \times 10^{-8}\,\mathrm{W\,m^{-2}\,K^{-4}}$ denotes the Stefan–Boltzmann constant, ϵ_{atm} the bulk emissivity and T_{atm} the effective temperature of the overlying atmosphere. In practice, T_{atm} is replaced by the temperature at screen-level height temperature T, and the atmospheric emissivity is parameterized as a function of air temperature and/or vapor pressure. Diverse LDR parameterizations can be found in the literature (Brutsaert, 1975; Idso, 1981; Konzelmann et al., 1994; Prata, 1996, among others). GEOtop includes a switch to select one out of nine parameterizations. Gubler et al. (2012) calibrated these parameterizations to measured longwave radiation in Switzerland. The sensitivity on the different LDR parameterizations, as well as on the calibrated Konzelmann et al. (1994) parameterization, is tested.

The turbulent fluxes of sensible and latent heat are calculated using the Monin–Obukhov similarity theory (Obukhov, 1946; Monin and Obukhov, 1954), which represents the effect of buoyancy with corrections to the logarithm profile of wind speed, valid only in a neutral atmosphere. However, the theory only determines the functional dependence of the corrections. Their mathematical formulation has to be found empirically. For this reason, in the present study the possibility to represent the turbulent fluxes assuming a neutral atmosphere is also considered. This becomes very important when the atmosphere is stable, because in this case the Monin–Obukhov corrections may improperly suppress turbulence and, as a result, the surface may be decoupled from the atmosphere, causing significant errors. If the wind speed is very small, such decoupling may also occur. Therefore, a minimum wind speed (V_{min}) has been added as a parameter. A minimum relative humidity ($\mathrm{RH_{min}}$) has also been added to prevent unrealistic turbulent fluxes. Temperature thresholds for rain $T_{\mathrm{r},0}$ and snow $T_{\mathrm{s},0}$ determine the temperature above which all precipitation is rain and below which all precipitation is snow. Between the two thresholds, the amount of precipitation that is rain or snow is interpolated linearly. They are set from 0 to 4 °C for rain, and −3 to 0 °C for snow (Kienzle, 2008).

2.3.3 Physical parameters

The parameters considered for ground are its aerodynamical roughness, ground albedo and emissivity, as well as its hydraulic properties presented in Sect. 2.4.2. The ground roughness influences the turbulent fluxes, and ranges from few millimeters up to half a meter or more depending on terrain obstacles (Wieringa, 1993). The albedo of a dry ground surface $\alpha_{\mathrm{g,dry}}$ is assumed to range from 0.1 to 0.4, values that are typically found in the literature (e.g., Ångström, 1925; Tetzlaff, 1983; Ineichen et al., 1990; Scharmer and Greif, 2000; Markvart and Castañer, 2003; Polo et al., 2012), with an average of 0.2. The reflection of wet ground $\alpha_{\mathrm{g,wet}}$ is smaller than for dry ground (Ångström, 1925), modeled as

$$\alpha_{\mathrm{g,wet}} = \alpha_{\mathrm{g,dry}} \cdot f_{\alpha_{\mathrm{g,wet}}}, \tag{3}$$

where $0.4 \leq f_{\alpha_{\mathrm{g,wet}}} \leq 1$. Emissivity of the different ground types is assumed between 0.8 and 0.99 with an average of 0.96 (e.g., Sutherland, 1986; Ogawa and Schmugge, 2004; Jin and Shunlin, 2006). The heat flux at the bottom of the ground profile determines the lower boundary condition of the heat conduction. The deep ground heat flux is $0.07\,\mathrm{W\,m^{-2}}$ (Medici and Rybach, 1995). Due to geometrical effects in high-mountain regions, the density of the ground heat flux in complex topographies varies (Kohl, 1999; Nötzli et al., 2007), and is hence assumed to have an average value of 0.05.

Diverse parameters concerning snow such as the snow reflectance, its emissivity, roughness, viscosity and the snow compaction rate can be set in GEOtop, determining the outgoing longwave radiation, the turbulent fluxes and the snow densification, They influence snow melt and the duration of the snow cover in spring. For shallow snow packs, snow albedo decreases since a significant portion of incoming shortwave radiation is actually absorbed by the ground surface (Tarboton and Luce, 1996). In GEOtop, this is represented by the albedo extinction parameter c_α. If the snow

Table 1. Environmental attributes determining the locations for which the sensitivity and uncertainty analyses are performed. The sky view factor (SVF) is a function of slope. For each combination of attributes, a separate sensitivity and uncertainty analysis is performed, resulting in a total of 200 simulation locations per ground type. In total, 1200 sensitivity and uncertainty analyses were performed.

Attribute	Unit	Min.	Max.	Step
Elevation	m	500	4000	500
Aspect	deg.	0	360	45
Slope	deg.	0	30	10
SVF		0.93	1	
Ground		1	6	e.g., Table 2

height z is smaller than c_α, ground and snow albedo are linearly interpolated. Snow emissivity ranges from 0.94 to 0.99, with an baseline value of 0.98 (e.g., Dozier and Warren, 1982; Zhang, 2005; Hori et al., 2006). The albedo of fresh snow for visible light is between 0.8 and 0.96 (e.g., Markvart and Castañer, 2003). The uncertainties in the atmospheric parameters that determine the attenuation of solar radiation are according to Gubler et al. (2012).

2.3.4 Input measurements and extrapolation

Air temperature is extrapolated at different elevations using a lapse rate. Analogous to air temperature, dew point temperature and precipitation are also distributed at different elevations using an elevation-related lapse rate. Precipitation measurements can have a negative bias due to wetting loss or wind-induced undercatch (Legates and DeLiberty, 1993; Goodison et al., 1998), for example. To deal with this systematic measurement error that has great effect on snow accumulation and soil moisture, GEOtop considers a precipitation correction factor. Hence, all precipitation measurements used as input to the model are multiplied with the correction factor. The value of the correction factor is assigned before running the model, and may be used for tuning.

The height of the sensor at which a temperature or wind speed is measured influences the calculation of the turbulent fluxes. While the exact height of the meteorological station can be measured precisely, the topography of the station in mountain regions may influence the equivalent height with respect to an infinite planar surface (Fig. 3). As a consequence, its determination is partly arbitrary. In this study, the height is varied between 0.5 and 16 m.

2.4 Experimental setting

The sensitivity study is performed for six different ground types (Sect. 2.4.2), which are varied within a topographical setting typical for mountain areas (Table 1). GEOtop is run for all combinations of ground types and topographical attributes that are assumed important when modeling mountain permafrost.

Fig. 3. The height of the meteorological station at Piz Corvatsch is assumed uncertain, ranging from 0.5 to 16 m. Within mountain topography, the actual height in relation with the surroundings at the top of a mountain cannot be accurately determined. In the figure, the meteorological station is just above the "tsch" of "Corvatsch".

2.4.1 Topography

The modeling study is performed within an artificial set of topographic attributes to evaluate the sensitivities of GEOtop for diverse topographical situations (Table 1). We model elevations in steps of 500 m from 500 to 4000 m a.s.l. Slope varies from 0° to 30° in steps of 10°, and aspect is varied in steps of 45°, thereby covering the most important exposure to the sun. In total, this topography sampling results in a total of 1200 simulation points. All locations where snow did not melt in summer were excluded from the analysis.

2.4.2 Ground types

Different ground types and ground surface covers influence the ground thermal regime substantially. Liquid water influences the thermal conductivity of the ground as well as the latent heat transfer during freezing and thawing of a specific ground layer (Williams and Smith, 1989). The study was performed for six different ground types: clay, sand, silt, peat, gravel and rock. For each of these ground types, typical values for the residual water content θ_r, the saturated water content θ_s, the parameters n_{vG} and α_{vG} determining the shape of the water retention curve parameterized according to van Genuchten (1980) and the saturated hydraulic conductivity K_h are determined (Table 2). The lateral hydraulic conductivity is assumed to be the same as the normal hydraulic conductivity. The thermal conductivity K_T is set to $2.5\,W\,m^{-1}\,K^{-1}$ and the thermal capacity C of the mineral particles to $2.25 \times 10^6\,J\,m^{-3}\,K^{-1}$ for the

Table 2. Parameters of the different ground types. In the sensitivity analysis, the hydraulic parameters are assumed to change by ±20 % for θ_{sat}, ±10 % for θ_{res}, ±50 % for n_{vG} and ±25 % for α_{vG}, and goes from 0.01 to 100 times the original value for K_h. The thermal conductivity changes by 50 % and the heat capacity changes by 20 % as shown in Table 3). The values are modified by the respective factors presented in Table 3.

Parameter	Symbol	Unit	Clay	Silt	Sand	Peat	Gravel	Rock
Residual water content	θ_r		0.072	0.057	0.055	0.2	0.055	0.002
Saturated water content	θ_s		0.475	0.487	0.374	0.85	0.374	0.05
van Genuchten α	α_{vG}	mm^{-1}	0.001	0.001	0.003	0.03	0.1	0.001
van Genuchten n	n_{vG}		1.4	1.6	3.2	1.8	2	1.2
Hydraulic conductivity	K_h	$mm\ s^{-1}$	0.0019	0.0051	0.0825	0.3	10	0.000001
Thermal conductivity	K_T	$W\,m^{-1}\,K^{-1}$	2.5	–	–	–	–	–
Thermal capacity	C	$J\,m^{-3}\,K^{-1}$	2.25×10^6	–	–	–	–	–

mineral particles (e.g., Cermák and Rybach, 1982; Wegmann et al., 1998; Šafanda, 1999). Ground is defined here as the volume below Earth's surface for which temperature is studied. Coarse blocks such as typically found on rock glaciers are important to model permafrost in the Alps. In this setting, we parameterize them with the hydrologic conductivity of gravel and a high porosity. This allows for a free drainage of the pore space, and the corresponding air content is accounted for in the calculation of ground thermal conductivity that constitutes one element of the importance of coarse blocks for permafrost (Gruber and Hoelzle, 2008). The advection of air in blocky surfaces, which is a complex problem that we are not yet in the position to address, is not included in the model.

The parameter values for silt, sand and clay are taken from Twarakavi et al. (2010, Table 2). For peat, the parameter values come from Carey et al. (2007) and Quinton et al. (2008). Residual and saturated water content for gravel is assumed to be similar to sand. The van Genuchten parameters and the hydraulic conductivity for gravel are approximated from Maier et al. (2009). For rock, they are assumed to be the same as for clay, and the hydraulic conductivity, and θ_r and θ_s are assumed to be very small. Measurements of the van Genuchten parameters for rock were not found in the literature.

2.5 Target variable

Ground temperatures are linearly interpolated between the simulation nodes that represent layers in the numerical scheme. Thereby, the modeled MAGT are compared at the same depths. The annual mean, minimum and maximum values at 10 cm, 1 m, 5 m and 10 m depth are calculated.

3 Experiments

This sensitivity and uncertainty study was performed based on the energy- and mass-balance model GEOtop (Rigon et al., 2006) (Sect. 2.1). A local sensitivity analysis (Sect. 4.2) on individual parameters was performed with a special focus on variations within topographically variable terrain (Sect. 2.4.1). Then, a subset of sensitive physical parameters was selected to quantify the total parametric output uncertainty of GEOtop (Sect. 3.3).

3.1 Preliminary analysis

The parameters that predominantly influence the duration of snow cover were calibrated in a preliminary analysis, since snow exerts great influence on ground temperatures through insulation (Zhang, 2005; Goodrich, 1982). The error of simulated melt-out day (MD) is compared to MD observed at 39 locations around Piz Corvatsch (Gubler et al., 2011; Schmid et al., 2012). MD is simulated for diverse parameter sets obtained by globally varying the most important parameters that influence MD. The simulations are calibrated with the observations to obtain parameter values that minimize the difference between model outputs and observations.

3.2 Sensitivity analysis

A model can be regarded as a black box represented by a function $f(x_1, x_2, \ldots, x_n) = (y_1, y_2, \ldots, y_m)$, where $(x_1, x_2, \ldots, x_n)$ are the model parameters and $(y_1, y_2, \ldots, y_m)$ are the model outputs. To evaluate GEOtop, a sensitivity analysis on 52 individual parameters is performed to (a) quantify the influence of each parameter on the output variables of interest and (b) to determine the most important physical parameters for the subsequent uncertainty analysis. The sensitivity of a parameter x_j is determined by keeping all parameters $x_i, i \neq j$ fixed at their baseline value $X_{j0} = (x_{10}, x_{20}, \ldots, x_{(j-1)0}, x_{(j+1)0}, \ldots, x_{n0})$, and varying x_j within values that are physically plausible. The ranges of the parameters are determined based on review of the literature and/or expert opinion. However, it must be kept in mind that, even though intended to be as objective as possible, the selection of a parameter range has a subjective part that influences the results and conclusions that are obtained from the analysis. The variation of the model outputs $y_k, k = 1, \ldots, m$ is evaluated to quantify the local sensitivities $s_{j,k}$ that are defined here as the range of the 95 % of the simulated outputs.

Local sensitivities are obtained when each parameter is varied separately and all others are kept fixed. This procedure contrasts to global sensitivities, where all parameters are changed simultaneously (e.g., Saltelli et al., 2004, 2008).

The parameters are categorized into (a) very sensitive parameters, (b) sensitive parameters and (c) nonsensitive parameters. Category (a) includes all parameters that are tuned in a preliminary analysis (Sect. 3.1). The second category includes all parameters having non-negligible influence to the model outputs. All physical parameters changing MAGT by at least 0.5 °C in the sensitivity analysis are included in the uncertainty analysis.

3.3 Uncertainty analysis

A prior distribution is assigned to each of the selected physical parameters. If a parameter has only positive values, it is assumed to be log-normally distributed, otherwise it follows a normal distribution. All parameters are assumed independent from each other. Since the study setting is synthetic, spatial autocorrelation of the parameters are not taken into account. The location parameter is the average of the parameter values determined for the local sensitivity analysis (e.g., Table 3), and the standard deviation is chosen such that the range encloses 95 % of the values for a normally distributed parameter. If a parameter is log-normally distributed (e.g., $x \sim \mathcal{L}(\mu, \sigma^2)$), the expected value $E[X]$ is the baseline value , and the variance Var$[X]$ is chosen appropriately representing the variability of the parameter. The statistical parameters of the log-normal distribution are

$$\sigma = \log\left(\frac{\mathrm{Var}[X]}{E[X]} + 1\right), \tag{4}$$

$$\mu = \log\left(E[X]\right) - \frac{\sigma^2}{2}. \tag{5}$$

Each parameter is sampled according to its prior distribution, and a GEOtop simulation is performed for each parameter set. In total, 1500 model simulations were performed to ensure convergence of the output probability distribution (Fig. 10). The results are depicted as relative frequency histograms to evaluate the total model output uncertainty, and are quantified as the length of the 95 % uncertainty interval of the simulations.

3.4 Model simulations

The sensitivity and uncertainty analyses were performed systematically for different ground types within a setting representing the topographic variability encountered in mountain regions (Sect. 2.4). In total, 1200 locations were simulated. The sensitivity analysis required 256 simulations, and the uncertainty analysis a total of 1500 simulations at each location. In total, more than 2 million GEOtop simulations were performed. The simulations are visually analyzed using small-multiple plots (Tufte, 1983, 1990) (e.g., Fig. 7), and are summarizedat least one ground in box plots for the different locations and ground types.

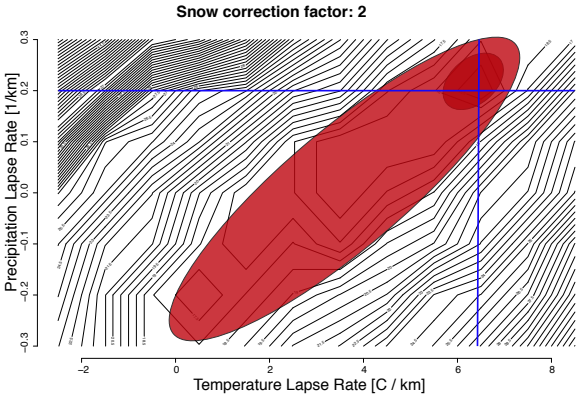

Fig. 4. Contour plot of the RMSD for simulated compared to observed MD around Piz Corvatsch, Switzerland (Gubler et al., 2011; Schmid et al., 2012). The smallest RMSDs are obtained for a a temperature lapse rate 6.5 °C km^{-1}, a snow correction factor of 2 and a precipitation lapse rate of 0.2 km^{-1} (indicated by the blue lines).

4 Results

4.1 Preliminary analysis

A preliminary analysis was conducted to extract reasonable values of the parameters that most considerably influence snow duration (i.e., the melt-out day (MD)). The temperature and precipitation lapse rates and the snow correction factor were calibrated using MD derived from ground surface temperature measurements around Piz Corvatsch (Gubler et al., 2011; Schmid et al., 2012). Due to a compensating effect, different parameter combinations lead to similar results (Beven and Freer, 2000) (Fig. 4). We chose to set the temperature lapse rate to its most commonly used value of -6.5 °C km^{-1}, resulting in an optimal precipitation lapse rate of 0.2 km^{-1} and a snow correction factor of 2 (Fig. 4). That results in an average MD error of zero days with a root-mean-squared error of less than 20 days for both study years 2010 and 2011. Precipitation lapse rate in mountain areas are normally negative accounting for greater snow accumulation in high-elevation areas (e.g., Barringer, 1989). Downward transportation of snow by avalanches or wind in the study area, processes that are not represented in GEOtop, may be the reason for the positive precipitation lapse rate. The sensitivity to different LDR parameterizations was reduced using the calibration performed by Gubler et al. (2012).

Table 3. Parameters selected for the sensitivity study. The minimum and the maximum indicate the range from which the parameters are sampled, and base indicates the standard choice used in, e.g., local sensitivity studies. The columns below "Uncertainty" indicate the properties of the prior distributions of the parameters considered in the uncertainty analysis. The values of the two LDR parameters (Konzelmann et al., 1994) change between 0.484 and 0.43, and 5.7 and 8 (Gubler et al., 2012).

Parameter	Symbol	Unit	Base	Sensitivity		Uncertainty		
				Min.	Max.	Distr.	Par_1	Par_2
Numerical parameter								
Thickness of first ground layer	dz_{min}	mm	20	5	640			
Growth rate ground depth	b		0.5	0	1			
Maximal ground depth	z_{max}	m	10	1.25	20			
Number of top snow layers	n_{t}		4	1	10			
Number of bottom snow layers	n_{b}		2	1	10			
Number of snow layers in middle	n_{m}		4	1	64			
Typical SWE	swe_{m}	mm	10	1.25	40			
Time discretization	dt	h	1	0.125	4			
Richard's tolerance	tol_{r}	mm	10^{-4}	10^{-8}	10^{-4}			
Heat equation tolerance	tol_{h}	J m^{-2}	10^{-4}	10^{-8}	10^{-4}			
Model parameter								
Minimal wind velocity	V_{min}	m s^{-1}	0.5	0.01	1.28			
Minimal relative humidity	RH_{min}	%	10	1	10			
LDR calibration	$\text{LDR}_{\text{in,K}}$							
Monin–Obukhov param.	MO		1	1	4			
Water balance	WB		1	0	1			
Physical parameter								
Initial ground temperature	T_{i}	°C	1	−1	1			
Depth above which water drains	z_f	m	10	0.01	10	Unif	0	10
Extinction parameter snow albedo	c_α	mm	10	0	200	Log-N	1.71	1.09
Ground roughness	r_{g}	mm	10	0.01	100	Log-N	1.96	0.83
Dry ground albedo	$\alpha_{\text{g,dry}}$		0.2	0.1	0.4	Norm	0.25	0.05
Divisor wet ground albedo	$f_{\alpha_{\text{g,wet}}}$		1	1	2.5	Norm	1.75	0.25
Ground emissivity	ϵ_{g}		0.96	0.81	0.99	Norm	0.93	0.02
Ground heat flux	Q_{g}	W m^{-2}	0.05	−0.1	0.1			
Snow roughness	r_{s}	mm	0.1	0.01	10	Log-N	−2.64	0.83
Fresh snow albedo (vis)	$\alpha_{\text{s,vis}}$		0.96	0.8	0.96	Norm	0.93	0.02
Fresh snow albedo (nir)	$\alpha_{\text{s,NIR}}$		0.65	0.6	0.7	Norm	0.65	0.02
Snow emissivity	ϵ_{s}		0.98	0.96	0.99			
Snow viscosity	v_{s}	N s m^{-2}	10^6	10^6	8×10^6	Norm	4×10^6	2×10^6
Ground-snow roughness threshold	$c_{\text{s,r}}$	mm	1	0.5	1			
Irreducible water saturation snow	$s_{\text{w,irr}}$		0.02	0.005	0.08	Log-N	−4.02	0.47
Snow density cutoff	$d_{\text{s,cut}}$	kg m^{-3}	100	75	175	Log-N	4.58	0.2
Dry snow deformation rate	$df_{\text{s,dry}}$	%	1	0.75	1.25			
Wet snow deformation rate	$df_{\text{s,wet}}$	%	1.5	1.25	2.5			
Temperature threshold rain	$T_{\text{r,0}}$	°C	3	0	4	Norm	2	0.5
Temperature threshold snow	$T_{\text{s,0}}$	°C	−1	−3	0	Norm	−1.75	0.5
Ozone	O_3	mm	0.314	0.238	0.39			
Ångström α	$\alpha_{\mathring{A}}$		1.38	0.46	2.30			
Ångström β	$\beta_{\mathring{A}}$		0.039	0.010	0.139	Log-N	−3.73	0.99
Albedo to determine SDR	α_c		0	0	1			
Residual water content (F)	$f_{\theta_{\text{res}}}$		1	0.8	1.2			
Saturated water content (F)	$f_{\theta_{\text{sat}}}$		1	0.9	1.1	Norm	1	0.05
van Genuchten parameter α (F)	$f_{\alpha_{\text{vG}}}$		1	0.75	1.25			
van Genuchten parameter n (F)	$f_{n_{\text{vG}}}$		1	0.5	1.5	Norm	1	0.25
Hydraulic conductivity (F)	$f_{K_{\text{h}}}$		1	0.01	100	Norm	0	1
Thermal capacity (F)	f_{C}		1	0.8	1.2			
Thermal conductivity (F)	f_{K_T}		1	0.5	1.5	Norm	1	0.25
Input								
Temperature lapse rate	Γ_T	°C km^{-1}	6.5	5.5	7.5			
Dew point temperature lapse rate	Γ_{DT}	°C km^{-1}	2.5	1.5	3.5			
Precipitation lapse rate	Γ_{P}	km^{-1}	0.2	−0.1	0.3			
Correction factor for precip.	c_{P}		2	1.6	2.4			
Sensor height wind velocity	h_{w}	m	2	0.5	16	Log-N	0.66	0.25
Sensor height temperature	h_T	m	2	0.5	16	Log-N	0.66	0.25

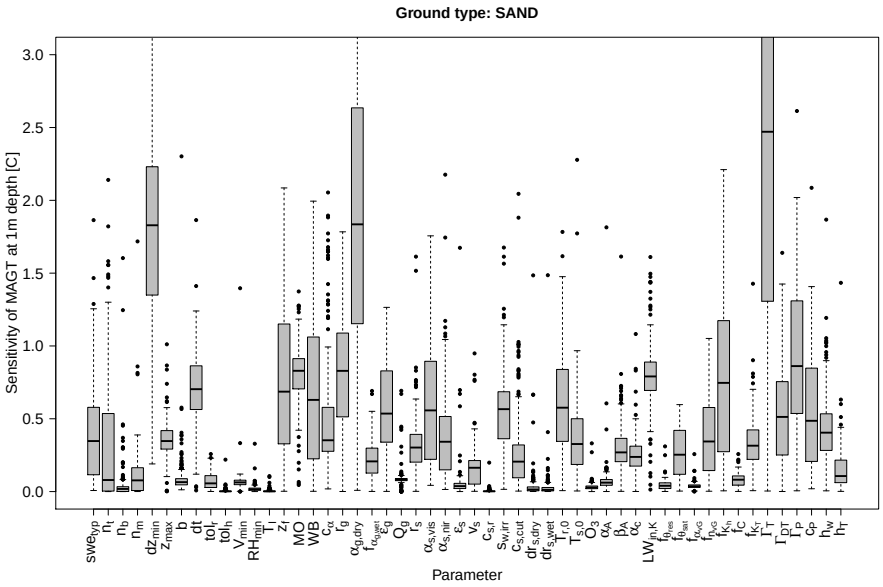

Fig. 5. Sensitivities of the target variable MAGT at 1 m depth [°C] for sandy ground. The sensitivities of the topographic locations are summarized as box plots. The greater the spread of the box, the higher the variability of the sensitivity within the topographic setting. The range of the box plots is equivalent to the "potential of being mislead" by the results of a sensitivity analysis performed at one single location. See Table 3 for an explanation of parameter names.

4.2 Summarized sensitivities

4.2.1 Topographic setting

MAGT sensitivities at different depths correlate strongly, and hence all the presented results concern MAGT modeled at 1 m depth. The sensitivities to the individual parameters vary strongly for different topographic factors (Fig. 5). Differences in the temperature lapse rate Γ_T of $2\,^{\circ}\mathrm{C\,km^{-1}}$ (5.5 to $7.5\,^{\circ}\mathrm{C\,km^{-1}}$) result in maximal ground temperature differences of up to 5 °C for an elevation distance of 1000 m between the modeled location and the meteorological station. The minimal sensitivity to Γ_T is less than 0.2 °C at locations of similar elevation as the meteorological station. The sensitivity to the temperature lapse rate increases linearly with the distance to the meteorological station.

The sensitivity to the dry ground albedo increases at south-exposed slopes that receive more solar radiation than adjacent slopes exposed to the north (Fig. 7). Further, low-elevation sites are more sensitive to the dry ground albedo since the snow duration is shorter there. The opposite is the case for the snow albedo, which has an enhanced sensitivity at high elevations. The sensitivity to ground roughness, the height at which wind velocity is measured, and the dew point temperature lapse rate increases for decreasing elevations. This indicates the increased importance of the turbulent fluxes in the energy balance for locations of increasing air temperatures and decreasing solar radiation.

4.2.2 Discretization errors

Ground

The sensitivity to the thickness of the first layer $dz_{\min}$ increases linearly with increasing $dz_{\min}$ for ground types sand, peat and gravel (Fig. 6). For clay, silt and rock, the sensitivity to $dz_{\min}$ increases only for $dz_{\min} \geq 40$ mm, while below that threshold it is zero. The sensitivity to $dz_{\min}$ is smaller for MAGT close to 0 °C, i.e., at high elevations. The highest sensitivities to $dz_{\min}$ are obtained for peat, gravel and rock (Fig. 9). For rock, this results in changes of almost 4 °C. Up to 20–40 mm, the median sensitivity to $dz_{\min}$ is relatively small (Fig. 8, bottom right figure) for all environmental conditions studied here, and it increases linearly for greater values. The maximal ground thickness $z_{\max}$ is not sensitive (except for few locations in rock). The ground layer thickness parameter b is insensitive to all ground types and topographic settings.

Time

The time step for which the numerical equations are solved results in maximal MAGT differences of 0.9 to 1.3 °C changes. The minimal sensitivity to the time step is around 0.2 °C. The sensitivity to the time step is negligible up to 15 min, and then increases linearly (Fig. 8, top left figure). We conclude that, if computation time is no issue, the heat

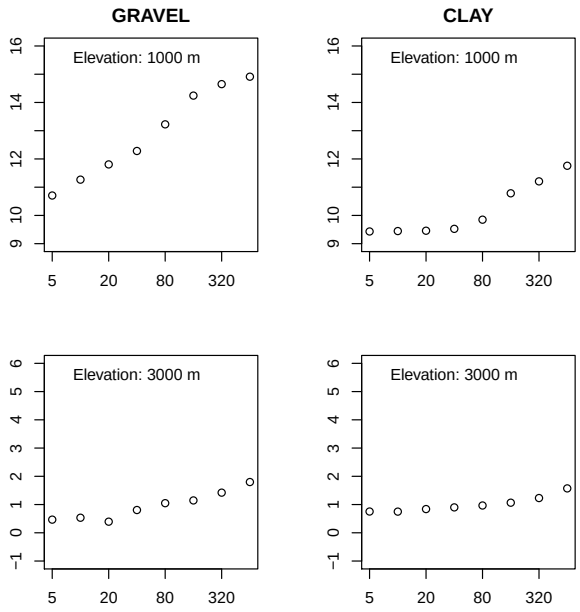

Fig. 6. Sensitivities of MAGT modeled at 10 cm depth to the thickness of the first ground layer for gravel (left) and clay (right). Modeled MAGT in gravel increase linearly for increasing ground thickness (note the logarithmic x axis), while MAGT in clay are constant for $dz_{\min} \leq 20$ mm. The sensitivity to $dz_{\min}$ decreases for ground temperatures closer to 0 °C (bottom figures).

conduction and the Richards equation should be solved at maximally half-hour resolution. Hourly resolution leads to average differences of around 0.2 °C in the solutions. The sensitivity to dt increases linearly with increasing dt, with changes of 0.8 °C for a resolution of 4 h in average.

Snow

The number of top layers in the snow module should be set to at least two, and the maximal value of $\mathrm{swe_m}$ should not exceed 10 mm to ensure stable ground temperatures. A few individual locations react nonlinearly to changes in the snow discretization parameters. We were, however, not able to explain the nonlinear response at these individual points.

All discretization parameters converge to stable solutions with average errors between 0.001 and 0.06 °C between the finest resolutions, allowing for quantification of average discretization errors (Table 4). The initial ground temperature is not sensitive under all environmental conditions, which indicates that the ground initialization is reliable.

4.2.3 Model-specific parameters

The calibrated LDR parameterization by Konzelmann et al. (1994) results in difference of 0.6 to 1.2 °C with respect to the published, original value of the parameterization. Neglecting the water balance results in changes of 1.5 °C in MAGST in sandy ground, while for rock or clay, the water balance is not important. Hence, in these ground types, the water balance might be neglected to save computational time. The Richard tolerance, which influences the convergence of the Richard's equation for movement of liquid water in ground, is important in gravel (more than 0.5 °C), whereas for the other ground types it is insignificant. When modeling ground with high hydraulic conductivity, the tolerance of the Richard's equation should be set sufficiently small (e.g., 10^{-8}).

4.2.4 Physical parameters influencing the energy balance

The dry ground albedo is the most sensitive parameter. Depending on the location, the sensitivity to the dry ground albedo (0.1 to 0.4) varies from around 0.5 to more than 2.5 °C for clay, for example. It is greatest at south-exposed slopes, and decreases by around 1.3 °C at north-exposed slopes. A slight decrease of the sensitivity is observed for 30° steep slopes facing north, while 30° south-facing slopes are more sensitive than flat slopes. The increased sensitivity stays in direct relation to the amount of solar radiation received at a locations. The sensitivity to the dry ground albedo increases strongly with decreasing elevation for all ground types because the snow duration is shorter at low-elevation sites. The minimal MAGT change is 0.5 °C at high elevation, inclined north-exposed slopes, while the maximal sensitivity to the dry ground albedo varies from 2.5 (clay, silt) to almost 4 °C (rock and gravel) (Fig. 9). The wet ground albedo is less sensitive than the dry ground albedo for all ground types. It ranges from 0.2 (gravel, sand, peat) to 1.3 °C (rock). In GEOtop, the value of the wet ground albedo is used if the water content equals θ_{sat}. Since θ_{sat} is very small in rock, the value of the wet albedo is more important than for other ground types, which explains its higher sensitivity. That simplification leads to the greater sensitivity of rock to the wet ground albedo, which in reality is likely not the case. The snow height for which the snow-ground albedo is interpolated has a maximal sensitivity of more than 1 °C, very similar to the fresh snow albedo. In summary, the surface albedo determined either by snow, ground or a composition of both has the greatest influence on MAGT. This supports the importance of the solar radiation in the energy balance determining snow melt and the available energy warming the ground in this environment.

Ground roughness changes MAGT at 1 m depth maximally by around 1.2 to 2 °C (rock). The height of the wind velocity meteorological station, the Monin–Obhukov parameterization and the dew point temperature lapse rate result in differences of around 1 °C in MAGT. Turbulent fluxes as well as longwave radiation have an increased importance during the night, when no radiation from the Sun reaches Earth. Snow roughness is less important (0.5 °C) than ground roughness since the snow surface is more homogeneous.

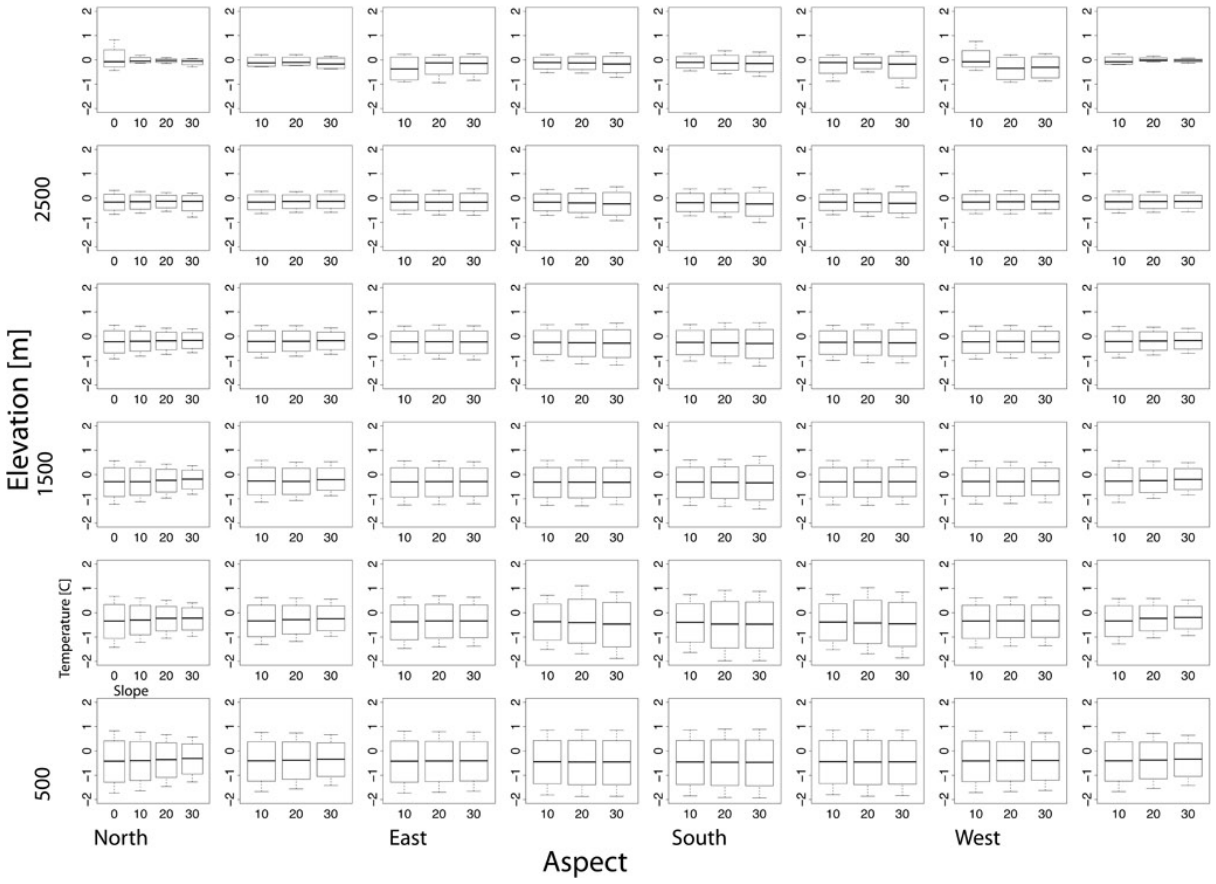

Fig. 7. Small multiple plots of normalized box plots of MAGT at 1 m depth [°C], simulated at all topographic locations for different ground albedo values. The box plots represent the different model outputs. The length of the 95 % uncertainty range of each box plot indicates the sensitivity to dry ground albedo at each location.

Table 4. Average discretization error ε [°C] of MAGT modeled at 1 m depth due to the different discretization parameters.

dt	1800	3600	7200	14 400							
ε_{dt}	0	0.027	0.113	0.226							
n_m	64	32	16	8	4	2	1				
$\varepsilon_{n_\mathrm{m}}$	0	0	0	0.001	0.013	0.004	0.023				
$\mathrm{swe_m}$	1.25	2.5	5	10	20	40					
$\varepsilon_{\mathrm{swe_m}}$	0	−0.025	−0.032	−0.02	0.093	0.225					
n_b	10	9	8	7	6	5	4	3	2	1	
$\varepsilon_{n_\mathrm{b}}$	0	0	0	0	0	0	0	0	0	0.001	
n_t	10	9	8	7	6	5	4	3	2	1	
$\varepsilon_{n_\mathrm{t}}$	0	0	0	0	0	0.001	0.002	0.004	0.004	0.172	
dz_min	5	10	20	40	80	160	320	640			
$\varepsilon_{dz_\mathrm{min}}$	0	0.061	0.138	0.231	0.444	0.749	1.11	1.535			
z_max	20 000	10 000	5000	2500	1250						
$\varepsilon_{z_\mathrm{max}}$	0	−0.004	−0.001	−0.002	−0.098						
b	1	1.1	1.2	1.3	1.4	1.5	1.6	1.7	1.8	1.9	2
ε_b	0	−0.001	0.002	0.001	−0.006	−0.003	−0.001	−0.001	−0.033	−0.022	−0.014

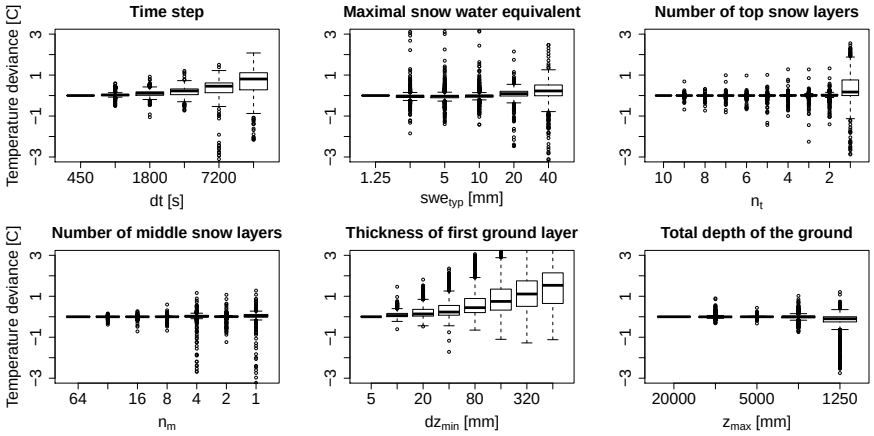

Fig. 8. Sensitivities of MAGT modeled at 1 m depth to the six sensitive discretization parameters d_t (top left), swe_m (top middle), n_t (top right), n_m (bottom left), dz_{min} (bottom middle) and z_{max} (bottom right), normalized with MAGT modeled with the finest resolution of each parameter. The sensitivities are summarized as box plots for all topographic properties and the six ground types.

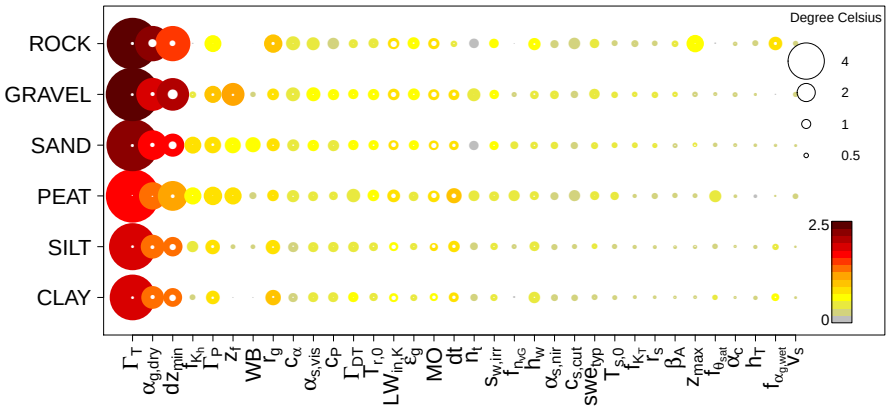

Fig. 9. Sensitivities of topographic sensitivity summarized as the 5, 50 and 95 % percentiles of MAGT modeled at 1 m depth for all ground types. The area of the circle indicates the 95 % percentile, and the area of the white dot the 5 % percentile of the sensitivity, summarized for all topographic locations. The color indicates the median sensitivity.

Other parameters such as temperature threshold for snow, the thermal conductivity, the Ångström parameter β and the snow viscosity change MAGT by around 0.5 °C. The remaining parameters have a maximal sensitivity that is less than 0.5 °C for all studied locations and ground types. These parameters, as well as the very sensitive parameters, were excluded from the subsequent comprehensive uncertainty analysis to reduce the parameter space.

4.2.5 Hydraulic properties of different ground types

The sensitivity of parameters influencing the water content in the ground such as the hydraulic conductivity K_h, the surface above which all water drains z_f, the saturated water content and the van Genuchten parameter n vary strongly for the different ground types (Fig. 9). The sensitivities range from 0.2 (rock) to 2 °C (sand and peat) differences at 1 m depth for z_f, from 0.3 (rock) to 0.5 (clay, sand, gravel) to 1.2 °C (peat) for θ_{sat}, and from 0.2 (rock) to 1.2 °C (peat) for n_{vG}.

4.3 Uncertainties in modeled MAGT

Two arguments support the parameter selection for the uncertainty analysis: (a) we exclude all numerical, discretization and model specific parameters since these parameters add to model error and not to model uncertainty and (b) include only parameters that influence ground temperature for more than 0.5 °C and at least one ground type (Fig. 9). All other

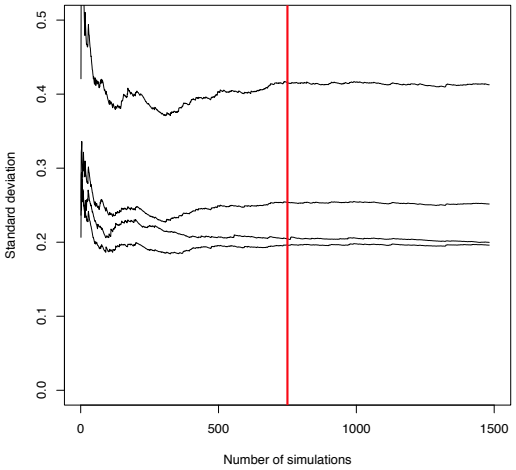

Fig. 10. Standard deviation of the model MAGT at 10 cm depth for increasing number of simulations (sand) at four arbitrarily selected points. Convergence is reached at approximately 750 simulations (indicated by the red line).

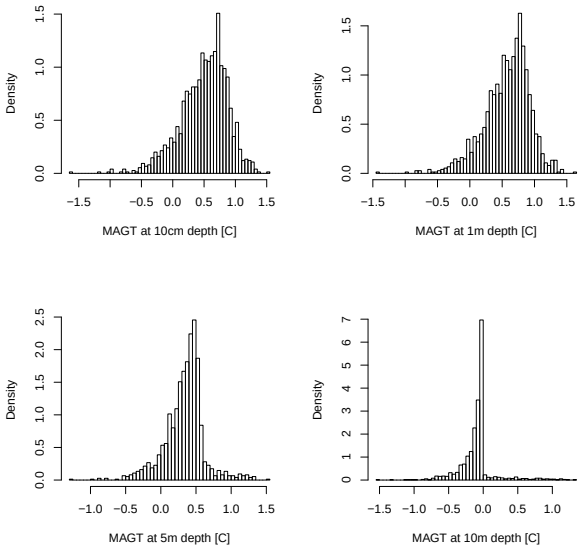

Fig. 11. Density histograms of modeled MAGT at a north-facing slope at 3500 m elevation at the four depths. At the greatest depths (right bottom), the soil remains frozen for most of the simulations, which indicates a cold initialization period. At points closer to the surface, the soil has thawed for most simulation.

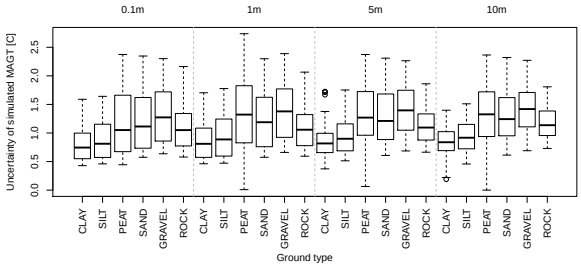

Fig. 12. Boxplots of the total output uncertainty for all topographic locations, presented for all ground types and depths. The parametric uncertainty is increased for sand, peat, gravel and rock.

parameters are fixed at their baseline value. The remaining parameters are sampled randomly according to their prior distribution (Table 3). In total, 1500 simulations were run; however 750 would suffice to ensure convergence (Fig. 10).

A plot of the frequency histograms at a location at 3500 m for the different depths is given in Fig. 11 (in the year 2010). At 10 m depth, we observe a non-Gaussian temperature distribution with values mostly below the freezing point of water. Closer to the surface, the simulated temperatures are higher than 0 °C. Since the initialization (1995–2000) of the ground temperature was done in a period of cold air temperatures, the ground was frozen. In the time after, air temperatures increased and the ground thawed. However, not enough energy was available to melt the ground column down to the bottom, which we observe in the distribution of the simulations at the lowest node. We can see that if ground temperatures are close to the freezing point, the frequency histogram of model simulations may be non-Gaussian. For this reason, the parametric model output uncertainty is expressed as the length of the 95 % uncertainty interval.

The parametric uncertainty varies from 0.4 to 1.5 °C for MAGT modeled in clay and silt. It is higher in sand, peat, gravel and rock (Fig. 12). In rock, the uncertainty decreases with increasing depth, as would be expected if integrating over a larger surface area. The increased uncertainty in sand, peat and gravel underlines the importance of accurate estimates of the hydraulic properties in these ground types. The parametric output uncertainty decreases for increasing elevation for all ground types. This can be attributed to the increased sensitivity to parameters influencing the energy balance at low-elevation sites, i.e., the ground albedo or roughness (Sect. 4.2). The environmental variability of the model uncertainties is not as pronounced as in the sensitivities, but differences between individual locations can still be observed.

Ground temperatures at greater depths integrate over larger surface areas (Gold and Lachenbruch, 1973), and are hence expected to be less variable than at the surface. Since the heat conduction is solved in one dimension in GEOtop, integration over large areas is not represented in these simulations. This may explain the constant size of the uncertainties at different depths. To study the influence of depth on model uncertainties, an uncertainty analysis should be performed solving the heat conduction in three dimensions.

However, the spatial autocorrelation of the parameters would have to be taken into account.

Model uncertainty at the surface is comparable with variability of ground surface temperatures measured within 10 m × 10 m cells. These range from approximately 0.25 at homogeneous grass sites to 2.5 °C in block fields, expressed as the total range (Gubler et al., 2011). The fine-scale environmental variability is similar to the parametric uncertainty found for modeled MAGT at 10 cm depth.

5 Discussion

5.1 The relevance of representative model evaluation

The synthetic environment allowed for us to quantify model sensitivity and uncertainty under differing environmental conditions. The selected setting allowed for quantification of the influence of individual parameters for different environmental conditions, as well as identification of locations where model sensitivities and uncertainties are largest. These findings can inform future measurement campaigns. Model uncertainty (for a given location, time and variable) can be interpreted as one metric for the benefit of an individual measurement. It does, however, not provide information on the correspondence of model results with reality, and should therefore be treated with care, and as one of several metrics to inform the design of measurement campaigns. Spatially distributed ground albedo measurements would, especially at low-elevation and south-exposed sites, strongly decrease the uncertainty of mountain permafrost models, and result in more-accurate model outputs. Other parameters are sensitive only under specific conditions, such as, for example, the hydraulic properties of the ground. A study on rock faces alone results in an insignificant influence of the hydraulic properties on modeled ground temperatures. Applied to other ground types such as sand, peat or gravel, this conclusion that the hydraulic properties are insignificant is wrong. Hence, evaluation of spatially distributed models should cover the main environmental properties of the modeling domain, since otherwise important model features could be missed. A recent study obtained similar results concerning the variability of model sensitivities and uncertainties due to differing topographic and climatic conditions for a snow model (He et al., 2011).

Thus, the presented environmental setting allowed for us to draw representative conclusions about the sensitivity and uncertainties of modeled MAGT in mountain regions. The results could be extended to modeling lowland areas, where the environmental variability may be, for example, expressed as differences in vegetation. The study contributes to the request by Gupta et al. (2008) for more representative model evaluation.

5.2 Sensitivities and uncertainties of the physically based model GEOtop

Snow is important in determining the thermal state of the ground (Goodrich, 1982; Keller and Gubler, 1993; Ishikawa, 2003; Luetschg et al., 2008). Parameters such as the temperature lapse rate or the correction factor for the precipitation measurement strongly influence snow duration, but have opposite effects. A higher lapse rate, for example, leads to warmer air temperature at low-elevation sites (if the meteorological station is located above the simulated locations), and results hence in faster melt-out. This is compensated by enhanced snow accumulation due to a greater precipitation lapse rate or higher precipitation correction factor. This compensating effect between different parameters is widely known as equifinality (Beven and Freer, e.g., 2000). A similar result was obtained by Essery and Etchevers (2004) for the influence of the radiative and turbulent fluxes on snow melt, for which different parameter combinations provided equally well behaving model outputs. Combination of different measured quantities could reduce the problem and lead to arguments for model improvement if conflicting results are obtained (Essery and Etchevers, 2004). GEOtop, and probably any physically based permafrost model, would benefit from validation with distributed time series of snow height (or SWE) in order to distinguish between snow accumulation and melting processes. Similarly, mountain permafrost models could benefit from individual calibration of parameters influencing the energy balance such as the roughness length (e.g., Andreadis et al., 2009) or ground albedo (e.g., Hoelzle, 1996; Gruber, 2005).

The ground albedo, which determines the net shortwave radiation at Earth's surface in summer, was the most important parameter when modeling MAGT. The importance of ground albedo in permafrost models has already been investigated by Hoelzle (1996), Ling and Zhang (2004) and Gruber (2005). Similarly, snow albedo is important since it strongly influences snow melting (Etchevers et al., 2004). Here, changes in the snow albedo changed MAGT by around 1 °C. The parameters influencing the turbulent fluxes determine snow melt (e.g., Etchevers et al., 2004) and change MAGT by around 0.5 to 1.5 °C. Calibration of the Konzelmann et al. (1994) LDR parameterization (e.g., Gubler et al., 2012) changes MAGT also by around 1 °C. This supports the relevance of calibrating physically based models (e.g., Beven and Binley, 1992; Gupta et al., 1998), and underlines the importance of evaluating individual processes separately if used in impact models, as, for example, done by Stocker-Mittaz et al. (2002) for mountain permafrost research. Some of the discretization parameters such as the time step at which equations are solved, as well as the thickness of the ground and snow-pack layers change MAGT by more than 1 °C. The temporal resolution should optimally be half an hour to ensure an error of less than 0.1 °C. Thickness of the uppermost ground layer of 20 mm results in 0.1 °C difference from the

smallest discretization chosen (e.g., 5 mm). The findings concerning the time step and the thickness of the uppermost soil layer are comparable to the findings by Romanovsky et al. (1997), who compared the behavior of three numerical permafrost models with analytical solutions of the heat conduction.

The sensitivity of the hydraulic parameters that determine the shape of the water retention curve varies strongly for the different ground types. For clay and rock, the sensitivity is almost negligible, while for sand or gravel, the van Genuchten parameter n, θ_{sat} and the hydraulic conductivity play a major role. Seaman et al. (2009) found that n, θ_{sat} and θ_{res} are the most important parameters to predict water retention in sand. The hydraulic conductivity K_h, θ_{sat} and θ_{res} were most important to estimate ground moisture in Mertens et al. (2005), while Jhorar et al. (2002) recommended fitting α, n and θ_{sat} when using the van Genuchten parameterization. The sensitivity of the van Genuchten parameters are hence controversial in the literature (e.g., Pollaco and Mohanty, 2012). In this study, we found that the hydraulic conductivity, the shape parameter n and the porosity most strongly influence MAGT for sand, peat and gravel. The variable sensitivity observed for the different soil types may by a reason for the controversial sensitivities found in the literature. These results underline the importance of systematic model evaluation for different environmental settings, since otherwise important model features are missed and would lead to wrong conclusions. Extrapolation of model uncertainties to locations of different environmental conditions is not feasible unless a systematic analysis spanning the environmental variability is performed.

The total parametric uncertainty goes from 0.5 to 1.5 °C for clay and silt, and increases up to around 2.4 °C for peat, sand, gravel and rock. This underlines the importance of hydraulic properties of ground types having high hydraulic conductivity and high porosity. In general, uncertainty is greater at low-elevation sites since the sensitivity to the ground albedo, as well as the turbulent fluxes, increases at low-elevation sites. Parametric uncertainty of MAGT at different depth is almost constant. The parametric model uncertainty is comparable to small-scale environmental variability of ground surface temperatures measured in Switzerland (Gubler et al., 2011).

This analyses performed in this study are of theoretical and practical relevance. The synthetic model setting allowed for quantification of the variability of model uncertainties within highly variable terrain as typically encountered when modeling mountain permafrost. To use GEOtop operationally, it should, however, be validated with spatially distributed measurements after an in-depth evaluation of all processes in the field. The diverse model parameters should be calibrated to local conditions to increase the accuracy of the model. Combination of both uncertainty and validation studies would provide additional insights on the model's ability to reproduce the processes that are relevant for mountain permafrost.

6 Conclusions

6.1 Environmental variability

Sensitivity and uncertainty studies are widely known to inform model use and model improvement. We have shown that model sensitivities and uncertainties can vary strongly as a function of the geographic location at which the modeling study is performed. The results support the importance of systematic and representative model evaluation (e.g., Gupta et al., 2008) such as to evaluate models within a setting that represents typical situations of the modeling domain. The systematic setting allows for comparison of our physical understanding of key processes for a variety of test cases. We conclude that considering environmental variability when analyzing model uncertainties is important to gain confidence in the conclusions made about the model and the modeled outputs. Before applying a model in a certain setting, a modeler should therefore determine the most important environmental variables (topography, differing soils, plants, etc.) that may influence model outputs. However, it is also important to note that in determining the most important variables, the modeler makes assumptions about how to abstract particular processes that may not reflect reality. Nonetheless, by carrying out a systematic model assessment, it is possible to evaluate the influence of model parameters on the processes being represented.

Based on these input factors that represent the modeling domain, a systematic model assessment should be undertaken. Otherwise, if model evaluation is done at few points in the modeling domain, important model features might be missed, and misleading conclusions might be drawn. For example, model sensitivities assessed at a south-exposed location might lead to an overestimation of the sensitivity to ground albedo in comparison to north-exposed locations. The possibility of detecting model deficiencies is increased when systematic and representative model evaluations are performed. The methods presented in this study proved useful in the study of the uncertainties of a distributed physical model used in mountain permafrost research within highly variable terrain. The high computational effort undertaken by simulating all combinations of environmental variables provided reliable results. The effort could, for future studies, however be reduced by using a probabilistic approach (e.g., Latin hypercube sampling).

6.2 GEOtop sensitivities and uncertainties

Uncertainties in modeled MAGT mainly come from uncertainties in the snow conditions and the individual components of the energy balance. The sensitivities are highly variable in variable topographies. To improve modeling results, spatially distributed measurements of snow, the components of the energy balance and ground conditions are required at locations of greatest uncertainties. These uncertainties

include both modeling and measurement uncertainties due to heterogenous environmental conditions (e.g., Gubler et al., 2011). These spatially distributed measurements should be used to validate and calibrate physically based models such as GEOtop in order to improve the general ability to model ground temperatures in mountain regions.

Accurate estimates of the hydraulic properties are required for soil types peat, sand and gravel to reduce MAGT modeled with GEOtop. While the result about the sensitivity of the soil types may differ for other permafrost models, it again underlines the importance of a representative model evaluation setting. Finally, missing processes, such as advection in blocky terrain, should be integrated into future versions of GEOtop.

Acknowledgements. We would like to thank R. Essery, M. Hoelzle and an anonymous referee for their constructive comments, which helped to improve this manuscript. This work was supported by the AAA/SWITCH-funded Swiss Multi-Science Computing Grid project (www.smscg.ch) with computational infrastructure and support. Customized libraries (ggeotop and GC3Pie) and user support were kindly provided by GC3: Grid Computing Competence Center (www.gc3.uzh.ch). The authors are grateful for the support by S. Maffioletti, who patiently answered any questions concerning the grid computing. This project was funded by the Swiss National Science Foundation (SNSF) via the NCCR MICS project PermaSense and via the project X-Sense (www.nano-tera.ch). All statistical analyses were performed with R (www.cran.r-project.org). We thank MeteoSwiss for supporting the work financially during the reviewing process.

Edited by: P. Huybrechts

References

AIAA: Guide for the verification and validation of computational fluid dynamics simulations, American Institute of Aeronautics and Astronautics, Reston, VA, USA, 1998.

Anderson, M. G. and Bates, P. D. (Eds).: Model Validation: Perspectives in Hydrological Science, Wiley, New York, USA, 2001.

Andreadis, K. M., Storck, P., and Lettenmaier, D. P.: Modeling snow accumulation and ablation processes in forested environments, Water Resour. Res., 45, W05429, doi:10.1029/2008WR007042, 2009.

Ångström, A.: The albedo of various surfaces of ground, Geograf. Ann., 7, 323–342, 1925.

Barringer, J. R. F.: A variable lapse rate snowline model for the remarkables, Central Otago, New Zealand, J. Hydrol., 28, 32–46, 1989.

Beck, M. B.: Water quality modeling: a review of the analysis of uncertainty, Water Resour. Res., 23, 1393–1442, 1987.

Beck, M. B., Ravetz, J. R., Mulkey, L. A., and Barnwell, T. O.: On the problem of model validation for predictive exposure assessments, Stoch. Hydrol. Hydraul., 11, 229–254, 1997.

Bertoldi, G., Rigon, R., and Over, T. M.: Impact of watershed geomorphic characteristics on the energy and water budgets, J. Hydrometeorol., 7, 389–403, 2006.

Beven, K.: Prophecy, reality and uncertainty in distributed hydrological modelling, Adv. Water Resour., 16, 41–51, 1993.

Beven, K. and Binley, A.: The future of distributed models: model calibration and uncertainty prediction, Hydrol. Process., 6, 279–298, 1992.

Beven, K. and Freer, J.: Equifinality, data assimilation, and uncertainty estimation in mechanistic modelling of complex environmental systems using the GLUE methodology, J. Hydrol., 249, 11–29, 2000.

Brutsaert, W.: On a derivable formula for long-wave radiation from clear skies, Water Resour. Res., 11, 742–744, 1975.

Carey, S. K., Quinton, W. L., and Goeller, N. T.: Field and laboratory estimates of pore size properties and hydraulic characteristics for subarctic organic soils, Hydrol. Process., 21, 2560–2571, doi:10.1002/hyp.6795, 2007.

Cermák, V. and Rybach, L.: Thermal conductivity and specific heat of minerals and rocks, in: Landolt-Börnstein Zahlenwerte und Funktionen aus Naturwissenschaften und Technik, Physikalische Eigenschaften der Gesteine, Springer, New York, 305–343, 1982.

Chen, M. H., Shao, Q. M., and Ibrahim, J. G.: Monte Carlo Methods in Bayesian Computation, Springer Verlag, New York, 2000.

Crosetto, M. and Tarantola, S.: Uncertainty and sensitivity analyses: tools for GIS-based model implementation, Int. J. Geograph. Inf. Sci., 15, 415–437, 2001.

Cukier, R. I., Levine, H. B., and Shuler, K. E.: Nolinear sensitivity analysis of multiparameter model systems, J. Phys. Chem., 81, 2365–2366, 1977.

Dall'Amico, M.: Coupled water and heat transfer in permafrost modeling, Ph.D. Thesis, Institute of Civil and Environmental Engineering, Universita degli Studi di Trento, Trento, 2010.

Davis, T. J. and Keller, C. P.: Modelling uncertainty in natural resource analysis using fuzzy sets and Monte Carlo simulation: slope stability prediction, Geogr. Inf. Sci., 11, 409–434, 1997.

Dozier, J. and Warren, S. G.: Effect of viewing angle on the infrared brightness temperature of snow, Water Resour. Res., 18, 1424–1434, 1982.

Endrizzi, S.: Snow cover modelling at local and distributed scale over complex terrain, Ph.D. thesis, Institute of Civil and Environmental Engineering, Universita degli Studi di Trento, Trento, 2007.

Essery, R. and Etchevers, P.: Parameter sensitivity in simulation of snowmelt, J. Geophys. Res., 109, D20111, doi:10.1029/2004JD005036, 2004.

Etchevers, P., Martin, E., Brown, R., Fierz, C., Lejeune, Y., Bazile, E., Boone, A., Dai, Y. J., Essery, R., Fernandez, A., Gusev, Y., Jordan, R., Koren, V., Kowalczyk, E., Nasonova, N. O., Pyles, R. D., Schlosser, A., Shmakin, A. B., Smirnova, T., Strasser, U., Verseghy, D., Yamazaki, T., and Yang, Z. L.: Validation of the energy budget of an alpine snowpack simulated by several snow models (SnowMIP project), Ann. Glaciol., 38, 150–158, 2004.

Etzelmüller, B., Hoelzle, M., Heggem, E. S. F., Isaksen, K., Stocker-Mittaz, C., Ødegård, R. S., Haeberli, W., and Sollid, J. L.: Mapping and modelling the occurrence and distribution of mountain permafrost, Norsk Geograf. Tidsskr., 55, 186–194, 2001.

Gold, L. W. and Lachenbruch, A. H.: Thermal conditions in permafrost – a review of North American literature, in: Proceedings of the 2nd International Conference on Permafrost, Yakutsk, USSR, 3–25, 13–28 July 1973.

Goodison, B. E., Louie, P. Y. T., and Yang, D.: WMO solid precipitation measurement intercomparison, Tech. Rep., World Meteorological Organization, Geneva, Switzerland, 1998.

Goodrich, L. E.: The influence of snow cover on the ground thermal regime, Can. Geotech. J., 19, 421–432, doi:10.1139/t82-047, 1982.

Gruber, S.: Mountain Permafrost: Transient Spatial Modelling, Model Verification and the Use of Remote Sensing, Ph.D. thesis, University of Zurich, Zurich, 2005.

Gruber, S. and Hoelzle, M.: The cooling effect of coarse blocks revisited: a modeling study of a purely conductive mechanism, in: 9th International Conference on Permafrost, Fairbanks, Alaska, 557–561, 28 June –3 July 2008.

Gubler, S., Fiddes, J., Keller, M., and Gruber, S.: Scale-dependent measurement and analysis of ground surface temperature variability in alpine terrain, The Cryosphere, 5, 431–443, doi:10.5194/tc-5-431-2011, 2011.

Gubler, S., Gruber, S., and Purves, R. S.: Uncertainties of parameterized surface downward clear-sky shortwave and all-sky longwave radiation., Atmos. Chem. Phys., 12, 5077–5098, doi:10.5194/acp-12-5077-2012, 2012.

Gupta, H. V., Sorooshian, S., and Patrice, O. Y.: Toward improved calibration of hydrologic models: Multiple and noncommensurable measures of information, Water Resour. Res., 34, 751–763, 1998.

Gupta, H. V., Beven, K., and Wagener, T.: Model Calibration and Uncertainty Estimation, John Wiley & Sons, New York, 2005.

Gupta, H. V., Wagener, T., and Liu, Y.: Reconciling theory with observations: elements of a diagnostic approach to model evaluation, Hydrol. Process., 22, 3802–3813, 2008.

Haeberli, W.: Die Basis-Temperatur der winterlichen Schneedecke als möglicher Indikator für die Verbreitung von Permafrost in den Alpen, Z. Gletscherk. Glaziol., 9, 221–227, 1973.

He, M., Hogue, T. S., Franz, K. J., Margulis, S. A., and Vrugt, J. A.: Characterizing parameter sensitivity and uncertainty for a snow model across hydroclimatic regimes, Adv. Water Resour., 34, 114–127, 2011.

Hoelzle, M.: Mapping and modelling of mountain permafrost distribution in the Alps, Norsk Geograf. Tidsskr., 50, Ho11–15, 1996.

Hoelzle, M., Mittaz, C., Etzelmüller, B., and Haeberli, W.: Surface energy fluxes and distribution models of permafrost in European mountain areas: an overview of current developments, Permafrost Periglac. Process., 12, 53–68, 2001.

Hoelzle, M., Haeberli, W., and Mittaz, C.: Miniature ground temperature data logger measurements 2000–2002 in the Murtèl-Corvatsch area, Eastern Swiss alps, in: 8th International Conference on Permafrost, Proceedings, edited by: Phillips, M., Springman, S., and Arenson, L., Swets & Zeitlinger, Lisse, Zürich, 419–424, 21–25 July 2003.

Hori, M., Aoki, T., Tanikawa, T., Motoyoshi, H., Hachikubo, A., Siugiura, K., Yasunari, T. J., Eide, H., Storvold, R., Nakajima, Y., and Takahashi, F.: In-situ measured spectral directional emissivity of snow and ice in the 8–14 µm atmospheric window, Remote Sens. Environ., 100, 486–502, 2006.

Idso, S. B.: A set of equations for full spectrum and 8 to 14 µm and 10.5 to 12.5 µm thermal radiation from cloudless skies, Water Resour. Res., 17, 295–304, 1981.

Ineichen, P., Guisan, O., and Perez, R.: Ground-reflected radiation and albedo, Solar Energy, 44, 207–214, 1990.

Ishikawa, M.: Thermal regine at the snow-ground interface and their implications for permafrost investigation, Geomorphology, 52, 105–120, 2003.

Jhorar, R. K., Bastiaanssen, W. G. M., Feddes, R. A., and Van Dam, J. C.: Inversely estimating soil hydraulic functions using evapotranspiration fluxes, J. Hydrol., 258, 198–213, 2002.

Jin, M. and Shunlin, L.: An improved land surface emissivity parameter for land surface models using global remote sensing observations, J. Climate, 19, 2867–2881, 2006.

Keller, F. and Gubler, H. U.: Interaction between snow cover and high mountain permafrost at Murtél Corvatsch, Swiss Alps, in: The Sixth International Conference on Permafrost, Beijing, 332–337, 5–9 July, 1993.

Kelley, C. T.: Solving Nonlinear Equations with Newton's method, Society for Industrial and Applied Mathematics, SIAM, Philadelphia, USA, 2003.

Kienzle, S. W.: A new temperature based method to separate rain and snow, Hydrol. Process., 22, 5067–5085, 2008.

Kohl, T.: Transient thermal effects below complex topographies, Tectonophysics, 306, 311–324, 1999.

Konzelmann, T., van de Wal, R. S. W., Greuell, W., Bintanja, R., Henneken, E. A. C., and Abe-Ouchi, A.: Parameterization of global and longwave incoming radiation for the Greenland Ice Sheet, Global Planet. Change, 9, 143–164, 1994.

Legates, D. R. and DeLiberty, T. L.: Precipitation measurement biases in the United States, J. Am. Water Resour. Assoc., 29, 855–861, doi:10.1111/j.1752-1688.1993.tb03245.x, 1993.

Ling, F. and Zhang, T.: A numerical model for surface energy balance and thermal regime of the active layer and permafrost containing unfrozen water, Cold Reg. Sci. Technol., 38, 1–15, 2004.

Luetschg, M., Lehning, M., and Haeberli, W.: A sensitivity study of factors influencing warm/thin permafrost in the Swiss Alps, J. Glaciol., 54, 696–704, 2008.

Maier, U., de Biase, C., Baeder-Bederski, O., and Bayer, P.: Estimation of Van Genuchten and preferential flow parameters by inverse modelling for large scale vertical flow constructed wetlands, Geophys. Res. Abstr., EGU General Assembly, p. 12916, Vienna, Austria, 2009.

Markvart, T. and Castañer, L.: Practical Handbook of Photovoltaics: Fundamentals and Applications, Elsevier, Amsterdam, 2003.

Medici, F. and Rybach, L.: Geothermal map of Switzerland 1995 (heat flow density), Matériaux pour la Géologie de la Suisse, Géophysique Nr. 30, Schweizerische Geophysikalische Kommision, 1995.

Mertens, J., Madsen, H., Kristensen, M., Jaques, D., and Feyen, J.: Sensitivity of soil parameters in unsaturated zone modeling and the relation between effective, laboratory and in situ measurements, Hydrol. Process., 19, 1611–1633, 2005.

Monin, A. S. and Obukhov, A. M.: Basic laws of turbulent mixing in the surface layer of the atmosphere, Tr. Akad. Nauk SSSR Geophiz. Inst., 24, 163–187, 1954.

Nötzli, J., Gruber, S., Kohl, T., Salzmann, N., and Haeberli, W.: Three-dimensional distribution and evolution of permafrost temperatures in idealized high-mountain topography, J. Geophys. Res., 112, F02S13, doi:10.1029/2006JF000545, 2007.

Obukhov, A. M.: Turbulence in an atmosphere with a non-uniform temperature, Bound.-Lay. Meteorol., 2, 7–29, 1946.

Ogawa, K. and Schmugge, T.: Mapping surface broadband emissivity of the Sahara desert using ASTER and

MODIS data, Earth Interact., 8, 1–14, doi:10.1175/1087-3562(2004)008<0001:MSBEOT>2.0.CO;2, 2004.

Pollaco, J. A. P., and Mohanty, B. P.: Uncertainties of water fluxes in soil-vegetation-atmosphere transfer models: inverting surface soil moisture and evapotranspiration retrieved from remote sensing, Vadose Zone J., 11, vzj2011.0167, doi:10.2136/vzj2011.0167, 2012.

Polo, J., Martín, L., and Cony, M.: Revision of ground albedo estimation in Heliosat scheme for deriving solar radiation from SEVIRI HRV channel of Meteosat satellite, Solar Energy, 86, 275–282, 2012.

Prata, A. J.: A new long-wave formula for estimating downward clearsky radiation at the surface, Q. J. R. Meteorol. Soc., 122, 1127–1151, 1996.

Quinton, W. L., Hayashi, M., and Carey, S. K.: Peat hydraulic conductivity in cold regions and its relation to pore size and geometry, Hydrol. Process., 22, 2829–2837, doi:10.1002/hyp.7027, 2008.

Rigon, R., Bertoldi, G., and Over, T. M.: GEOtop: a distributed hydrological model with coupled water and energy budget, J. Hydrometeorol., 7, 371–388, 2006.

Romanovsky, V. E., Osterkamp, T. E., and Duxbury, N. S.: An evaluation of three numerical models used in simulations of the active layer and permafrost temperature regimes, Cold Reg. Sci. Technol., 26, 195–203, 1997.

Rykiel, J. E. J.: Testing ecological models: the meaning of validation, Ecol. Model., 90, 299–244, 1996.

Saltelli, A., Tarantola, S., and Campolongo, F.: Sensitivity Analyses in Practice, doi:10.1002/0470870958, John Wiley and Sons, New York, 2004.

Saltelli, A., Ratto, M., Andres, T., Campolongo, F., Cariboni, J., Gatelli, D., Saisana, M., and Tarantola, S.: Global Sensitivity Analysis, The Primer, John Wiley & Sons, New York, 2008.

Scharmer, K. and Greif, J.: The European Solar Radiation Atlas, Vol. 1: Fundamentals and Maps, Les Presses de l'École des Mines, Paris, France, 2000.

Schmid, M.-O., Gubler, S., Fiddes, J., and Gruber, S.: Inferring snowpack ripening and melt-out from distributed measurements of near-surface ground temperatures, The Cryosphere, 6, 1127–1139, doi:10.5194/tc-6-1127-2012, 2012.

Seaman, J., Singer, J., and Aburime, S.: Evaluating the relative importance of the van Genuchten–Mualem parameters, in: Proceedings of the 2009 Georgia Water Resources Conference, 27–29 April 2009.

Sobol, I. M.: Sensitivity analysis for non-linear mathematical model, Math. Model. Comput. Exp., 1, 407–414, 1993.

Stocker-Mittaz, C., Hoelzle, M., and Haeberli, W.: Modelling alpine permafrost distribution based on energy-balance data: a first step, Permafrost Periglac. Process., 13, 271–282, doi:10.1002/ppp.426, 2002.

Stow, C., Jollif, J., McGillicuddy Jr., D. J., Doney, S. C., Allen, J. I., Friedrichs, M. A. M., Rose, K. A., and Wallhead, P.: Skill assessment for coupled biological/physical models of marine systems, J. Mar. Syst., 76, 4–15, 2009.

Sutherland, R. A.: Broadband and spectral emissivities (2–18 µm) of some natural soils and vegetation, J. Atmos. Ocean. Technol., 3, 199–202, 1986.

Tarboton, D. G. and Luce, C. H.: Utah Energy Balance Snow Accumulation and Melt Model (UEB), Tech. rep., Utah Water Research Laboratory Utah State University and USDA Forest Service Intermountain Research Station, Utah, USA, 1996.

Tetzlaff, G.: Albedo of the Sahara, in: Satellite measurements of radiation budget parameters, edited by: Raschke, E., 60–63, Bonn, 1983.

Tufte, E.: The Visual Display of Quantitative Information, Graphics Press, Cheshire, Connecticut, USA, 1983.

Tufte, E.: Envisioning Information, Graphics Press, Cheshire, Connecticut, USA, 1990.

Twarakavi, N. K. C., Simunek, J., and Schaap, M. G.: Can texture-based classification optimally classify soils with respect to soil hydraulics?, Water Resour. Res., 46, doi:10.1029/2009WR007939, 2010.

van Genuchten, M. T.: A closed-form equation for predicting the hydraulic conductivity of unsaturated soils, Soil Sci. Soc. Am. J., 44, 892–898, 1980.

Šafanda, J.: Ground surface temperature as a function of the slope angle, Tectonophysics, 360, 367–375, 1999.

Wegmann, M., Gudmundsson, G. H., and Haeberli, W.: Permafrost changes in rock walls and the retreat of Alpine glaciers: a thermal modelling approach, Permafrost Periglac. Process., 9, 23–33, 1998.

Wieringa, J.: Representative roughness parameters for homogeneous terrain, Bound.-Lay. Meteorol., 63, 323–363, 1993.

Williams, P. and Smith, M.: The Ground Thermal Regime, Chap. 4, Cambridge University Press, Cambridge, 83–121, 1989.

Zhang, T.: Influence of the seasonal snow cover in the ground thermal regime: an overview, Rev. Geophys., 43, doi:10.1029/2004RG000157, 2005.

Part III

Appendix

Curriculum Vitae (short version)

Personal details

Name:	Stefanie Patricia Gubler
Date of birth:	17 November, 1981
Citizenship:	Swiss

Education

08/1996–05/2001	Matura Typus D, Grammar School at the Literar-Gymnasium Kirchenfeld, Bern, Switzerland
10/2001–03/2007	Master of Science in Mathematics, ETHZ Thesis: *Biased positional games*
01/2004–01/2009:	Diplom Didaktischer Ausweis in Mathematik, ETHZ
01/2009–01/2011:	MAS Weiterbildungslehrgang in angewandter Statistik, ETHZ
09/2008– 01/2013	PhD student at the Department of Geography, University of Zurich

Employment

08/2007–07/2008	High school teacher, Colegio Helvetia de Bogotá, Colombia

Acknowledgements

This thesis would not exist without the immense support and help from many persons to which I would like to express my deepest gratitude. The greatest thanks goes to my two supervisors Stephan Gruber and Ross S. Purves. During the whole process, Stephan and Ross supported me with profound scientific discussions and advice on how to proceed, kept me motivated, and helped me through the many problems that arise when writing a doctoral thesis. I am very grateful that their doors were always open for any kind of question, and that I could always count on their assistance. I have learned so many things from Stephan and Ross for which I am very thankful.

I also thank Wilfried Haeberli for his guidance in writing this thesis. Wilfried impressed me with his huge knowledge of glaciers and mountain permafrost, and I greatly enjoyed (many) discussions with him on the history of and the diverse approaches to mountain permafrost research. Wilfried always supported and helped me not lose the greater picture of my research.

I would also like to express my gratitude to the whole PermaSense team for its great collaboration. Starting with a two-day retreat at the foot of the Matterhorn where I barely understood a word, I greatly enjoyed the inter-disciplinary work of the team. My biggest thanks goes to Matthias Keller and his collaborators for developing the iAssist, a tool that made fieldwork at Corvatsch manageable. Good food, wine, and pleasant chats with the TIK-Team of Jan Beutel made the NCCR MICS retreats not only interesting but also lots of fun. A "grazie mille" also goes to the GEOtop developers team, and especially to Stefano Endrizzi who patiently explained me the important processes and parameters of GEOtop. Their great work done with the model GEOtop made this PhD possible. Thanks also to Sergio Maffioletti from the Grid Computing Competence Center for making high-performance simulations of GEOtop possible. Further, I would like to thank Joël Fiddes, Marcol Schmid, Vanessa Wirz, Christina Lauper, Brunell Gugelmann, Lorenz Böckli and many others that organized, conducted and accompanied the yearly field trips to Corvatsch.

I would like to thank my office mates Andi Hasler, Holger Frey, Raymond Le Bris, Nico Mölg, Marlene Scheel, Annik Reissig, and the whole 3G group for the very enjoyable working atmosphere, fruitful scientific discussions, the chats during coffee breaks and at lunch on free-time activities and child rearing, as well as for the many fun yoga and sport outings together. Special thanks go to Jeanette Nötzli, Danaë Perez and Alice Gugelmann for reading and correcting the content and grammar of this manuscript. Alain Hauser installed and upgraded software on my personal computer many times, and answered countless questions about R, linux and programming in general. I also

thank Christian Blum for helping me improving many illustrations used in presentations.

Last but not least, I thank my parents for giving me an excellent education, for always supporting me in my different activities, and encouraging me in my life. This also goes for my whole family, brothers and sisters, grandparents, godmothers and godfathers, and all my friends. Lastly, a very special thank-you goes to Christian and to Laurin, who make my life beautiful and complete.